

Die approbierte Originalversion dieser  
Dissertation ist in der Hauptbibliothek der  
Technischen Universität Wien aufgestellt und  
zugänglich.

<http://www.ub.tuwien.ac.at>



The approved original version of this thesis is  
available at the main library of the Vienna  
University of Technology.

<http://www.ub.tuwien.ac.at/eng>



TECHNISCHE  
UNIVERSITÄT  
WIEN

VIENNA  
UNIVERSITY OF  
TECHNOLOGY

Doctoral thesis

**Viscous interfaces as source of material creep: New,  
micromechanics-based, perspectives on liquid crystal  
physics, rheology, and thixotropy**

submitted in satisfaction of the requirements for the degree of Doctor of Science  
in Civil Engineering of the Vienna University of Technology, Faculty of Civil  
Engineering

---

Dissertation

**Viskose Grenzflächen als Quelle von Materialkriechen:  
Neue, mikromechanisch fundierte Sichtweise auf  
Flüssigkeitskristallphysik, Rheologie und Thixotropie**

ausgeführt zum Zwecke der Erlangung des akademischen Grades eines Doktors  
der technischen Wissenschaft eingereicht an der Technischen Universität Wien  
Fakultät für Bauingenieurwesen

von

Mehran Shahidi, M.Sc.

Matrikelnummer: 1125233

Prüfer und Betreuer: Univ.-Prof. Dipl.Ing. Dr. techn. Christian Hellmich  
Institut für Mechanik der Werkstoffe und Strukturen,  
Technische Universität Wien

Prüfer: Prof. Dr. Vikas Tomar  
School of Aeronautics and Astronautics,  
Purdue University

---

## Acknowledgment

I would like to acknowledge the financial support of the MICROBONE project (grant number 257032), granted by the European Research Council (ERC), which enabled my employment as a research assistant at the Vienna University of Technology.

It has been such a privilege to work under the supervision of Univ.-Prof. Dipl.-Ing. Dr. techn. CHRISTIAN HELLMICH. I thank Prof. HELLMICH for his tremendous support, competent guidance, commitment, and openness for new ideas during the last years. Prof. HELLMICH not only shared his valuable knowledge and experience with me, he also contributed a lot to my personal development. I especially thank my co-supervisor Associate Prof. Priv.-Doz. Dipl.-Ing. Dr. techn. BERNHARD PICHLER for his patient guidance, encouragement and advice that he has provided throughout my study. I have been extremely lucky to have a co-supervisor who cared so much about my work. Many thanks to Associate Prof. VIKAS TOMAR from Purdue University, who agreed to be the co-examiner of this thesis.

Thanks to each and every employee of Institute for Mechanics of Materials and Structures. It has been joyful to work in such a calm and friendly atmosphere, which facilitated by our Dean Univ.-Prof. Dipl.-Ing. Dr. techn. DDr. h.c. JOSEF EBERHARDSTEINER. Talking about colleagues, I firstly thank Ass. Prof. Dipl.-Ing. Dr. techn. MEHDI AMINBAGHAI who has not been only sharing the office with me, but has always been there for me with a helping hand when it was necessary. Thanks to Dipl.-Ing. Dr. techn. KRZYSZTOF WOJCIECH LUCZYNSKI and Dipl.-Ing. ALEXANDER DEJACO for sharing their time with me, not only at the university. Thanks to everybody from the “bone-group”, the “wood-group”, and, the “stability-group”. All three ladies Mag. (FH) MARTINA PÖLL, GABRIELE OSTROWSKI and ASTRID SCHUH deserve a huge appreciation for dealing promptly and professionally with all administrative issues.

I thank all my friends, who supported me or influenced me along the way. It would be impossible to list every name, but some of those that come to mind include HADI, OMID, EHSAN, MAJID, DAVAR, MOSTAFA, AMIN and ALI. Among all I especially thank FARIBORZ for his strong scientific support. I also thank my international friends in Vienna ONNO, RENATA, KRISTINA, JULIO, SELMAN and DANIEL.

A very special thank goes to my parents. Despite the long distance separating me from my family, I have always felt their support in achieving anything I aimed at. For that constant help, I am very grateful to my parents, grandparents, and to my sisters. A final acknowledgement goes to MARIE, who stuck with me during hard working time.

---

## Abstract

It is well accepted that absorption of water (or other fluids) at interfaces within the microstructures and nano-structures of hydrated biomaterials or geomaterials are a very probably origin of their macroscopic creep and relaxation behavior; which has been studied particularly intensively for, e.g., concrete or bone. At the same time, the macroscopic creep behavior is standardly given in terms of classical rheological models (Kelvin-Voigt, Maxwell, Zener, chain models) with a number of regression parameters obtained from some fitting algorithms, while the actual micromechanical origin of the creep process remains fully unconsidered. The present thesis aims at delivering a first remedy to this somehow unsatisfactory situation. It is divided into five chapters, relating to articles published or prepared for publication in scientific journals, documenting the development of a new theoretical approach for the upscaling of interface viscosities to bulk material creep properties - and its first confrontation to experimental results as well.

Chapter 1 introduces the novel theoretical concept: Interfaces are perceived as zero-thickness limit cases of spheroidal, eigenstressed inclusions in an elastic matrix, and the limit case-driven eigentractions are inserted into viscosity laws, relating them to interface dislocation rates. In this way, the rich theoretical heritage of continuum micromechanics based on Eshelby problems and their derivatives for cracks, as developed over the last decades, can be triggered, so as to mathematically derive compact analytical formulae showing how macroscopic creep rates depend on interface density, size, and viscosity.

Chapter 2 extends the discussion to the case of more than one interface characteristic, i.e. to interfaces differing in size, density, and/or viscosity. The mathematical expenditures increase significantly, however, an elegant combination of advanced solution methods of differential equations, such as Laplace transforms, elimination schemes, and non-dimensionalization, do finally allow for the arrival at very elegant analytical formulae for the relaxation function of materials embedding differing interfaces - showing clearly the mutual interaction of these interfaces when governing macroscopic relaxation times or capacities.

Chapter 3 provides a link between the novel micromechanics-derived creep and relaxation functions, and those obtained from classical rheological models. Based on the structure of the underlying differential equation, a full analogy between matrix-interface composites with only one interface type and classical Kelvin-Voigt

and Maxwell models is developed, and independently proven by the dissipation expressions for both the micromechanical and the rheological systems.

Chapter 4 extends this analogy to the case of arbitrarily many (countable) interface types. Particularly, the Kelvin-Voigt parameters can be easily linked to interface and matrix properties.

Chapter 5 finally uses the newly developed methods in the light of real materials. A carefully experimentally validated hierarchical micromechanics model for bone viscoelasticity is complemented by an additional homogenization step, downscaling from the mineral clusters found in the extrafibrillar space, to the interfaces probably present within these clusters. The downscaled interface viscosity is (surprisingly) 14 orders of magnitude larger than that obtained from molecular dynamics. On a second glance, this huge discrepancy can be traced back to the 16 orders of magnitude difference between dislocation rates appearing during bone creep, and those used (for computational reasons) in molecular dynamics simulations. Glassy water in inter-crystalline interfaces in bone obviously show very pronounced thixotropy, i.e. viscosity decrease with increasing shear rate.

# Contents

<b>Contents</b>	<b>iv</b>
<b>List of Figures</b>	<b>ix</b>
<b>List of Tables</b>	<b>xii</b>
<b>Introduction</b>	<b>1</b>
<b>Methodology and key results</b>	<b>6</b>
<b>1 Viscous interfaces as source for material creep: a continuum micromechanics approach</b>	<b>11</b>
1.1 Introduction	11
1.2 General strategy for interface modeling	12
1.3 Auxiliary material system I: micromechanics of eigenstressed oblate phase in solid elastic matrix	13
1.3.1 General fundamentals of micromechanical representation	13
1.3.2 Determination of influence and concentration tensors from matrix-(spheroidal) inclusion problems	17
1.4 Auxiliary material system II: elastic matrix containing slits with eigentractions	20
1.4.1 Conversion of strains into dislocations	20
1.4.2 Concentration and influence tensors, as functions of interface density	22
1.4.3 Homogenized stiffness and Biot tensors	25
1.4.4 Macrostress-related concentration and influence relations	25
1.5 Upscaling from viscous interfaces to creeping materials	27
1.5.1 Interface behavior	27
1.5.2 Macroscopic viscoelasticity I: relaxation	28
1.5.3 Macroscopic viscoelasticity II: creep	33
1.6 Discussion and Conclusions	38
1.7 Nomenclature	40
<b>2 How interface size, density, and viscosity affect creep and relaxation functions of matrix-interface composites – a micromechanical study</b>	<b>45</b>

---

2.1	Introduction . . . . .	45
2.2	Matrix-interface micromechanics for different interface families and review of creep functions . . . . .	46
2.2.1	State equations for uniform strain boundary conditions . . . . .	48
2.2.2	State equations for uniform stress boundary conditions . . . . .	49
2.2.3	Review of creep functions . . . . .	50
2.3	Derivation of relaxation functions for interacting interfaces of different size, viscosity, and density . . . . .	52
2.3.1	Determination of dislocation histories based on Laplace transformation . . . . .	54
2.3.2	Revisiting dislocation histories based on an elimination scheme combined with the method of non-dimensionalization . . . . .	58
2.3.3	Relaxation functions . . . . .	63
2.3.4	Study of interface interaction in a relaxation test . . . . .	66
2.4	Identification of the mechanism responsible for interaction among interfaces, and concluding remarks . . . . .	69
2.5	Nomenclature . . . . .	72
<b>3</b>	<b>Interfacial micromechanics assessment of classical rheological models I: Single interface size and viscosity</b>	<b>75</b>
3.1	Introduction . . . . .	75
3.2	Review of rheological “spring-dashpot” models . . . . .	77
3.2.1	Kelvin-Voigt representation of standard linear solid . . . . .	77
3.2.2	Maxwell representation of standard linear solid . . . . .	80
3.3	Matrix-interface micromechanics . . . . .	82
3.3.1	Materials representation and constitutive relations . . . . .	82
3.3.2	Elastic energy and dissipation . . . . .	85
3.4	Interfacial micromechanics assessment of classical rheological models	87
3.4.1	Micromechanical explanation of rheological parameters . . . . .	87
3.4.2	Micromechanical interpretation of stress and strain contributions of individual springs and dashpots of the rheological models . . . . .	87
3.4.3	Micromechanical illustration of energy dissipating in dashpots of the rheological models . . . . .	90
3.5	Discussion and conclusion . . . . .	91
3.6	Nomenclature . . . . .	93
<b>4</b>	<b>Interfacial micromechanics assessment of classical rheological models II: Multiple interface sizes and viscosities</b>	<b>96</b>
4.1	Introduction . . . . .	96
4.2	Review of rheological chain models: derivation of governing differential equations . . . . .	97
4.2.1	Kelvin-Voigt chain models . . . . .	98
4.2.2	Maxwell chain models . . . . .	102
4.3	Matrix-interface representation and constitutive relations . . . . .	106
4.4	Interface micromechanics assessment of rheological models . . . . .	113

4.4.1	Relations between Kelvin Voigt chain parameters and micromechanical quantities . . . . .	114
4.4.2	Relations between Maxwell chain parameters and viscosities as well as micromechanical quantities . . . . .	115
4.4.3	Relation between parameters characterizing Kelvin-Voigt and Maxwell chains, respectively . . . . .	116
4.5	Discussion and conclusion . . . . .	117
4.6	Nomenclature . . . . .	118
<b>5</b>	<b>Viscosity of water interfaces adjacent to Hydroxyapatite crystals: Shear thinning as source for significant viscosity change</b>	<b>121</b>
5.1	Introduction . . . . .	121
5.2	Reuss bound-based estimation of creep tensor for interfaced materials with random orientation of interfaced building blocks . . . . .	122
5.3	Top-down identification of interface density, interface viscosity, and bulk viscosity of adsorbed water filling interfaces between hydroxyapatite crystals . . . . .	124
5.4	Top-down identification of typical interfacial dislocation speeds in relaxation tests on bone, starting from macroscopic three-point bending tests . . . . .	125
5.5	Thixotropy of adsorbed water allows for explaining differences in top-down and bottom-up identified viscosities: an outlook to bridging continuum micromechanics and molecular dynamics simulations	126
5.6	Nomenclature . . . . .	127
<b>A</b>	<b>Proof of limit case of strain concentration tensor of inclusion at infinity</b>	<b>130</b>
<b>B</b>	<b>Consideration of two parallel interface phases exhibiting <i>different</i> sizes</b>	<b>131</b>
<b>C</b>	<b>Components of homogenized elastic stiffness tensor, interface morphology tensor, as well as concentration and influence tensors</b>	<b>136</b>
C.1	Components of homogenized elastic stiffness tensor, interface morphology tensor, as well as concentration and influence tensors . . . . .	136
<b>D</b>	<b>Creep and relaxation study of rheological models, as well as matrix-interfaces composites</b>	<b>140</b>
D.1	Defintion of elastic stiffness of solid, identity tensor, and so-called T-tensor . . . . .	140
D.2	Kelvin-Voigt formulation: Creep and relaxation study . . . . .	141
D.2.1	Creep test . . . . .	141
D.2.2	Relaxation test . . . . .	142
D.3	Maxwell formulation: Creep and relaxation study . . . . .	143
D.3.1	Creep study . . . . .	143
D.3.2	Relaxation study . . . . .	144

---

D.4	Micromechanics formulation: Creep and relation study . . . . .	145
D.4.1	Creep test . . . . .	145
D.4.2	Relaxation test . . . . .	146
<b>E</b>	<b>Expanded version of generalized chain models</b>	<b>148</b>
E.1	Expanded version of generalized Kelvin-Voigt model . . . . .	148
E.2	Expanded version of generalized Maxwell model . . . . .	149
<b>F</b>	<b>Interpenetration of randomly oriented viscous interfaces</b>	<b>150</b>
F.1	Micromechanics of polycrystals with eigenstressed interface phases of isotropic orientation . . . . .	150
F.2	Determination of concentration and influence tensors from matrix- inclusion problems . . . . .	154
F.2.1	Transition from almost flat oblate spheroids to 2D interfaces	159
F.2.2	Introduction of eigentraction vector for flat interfaces . . . . .	161
F.2.3	Remarks on macroscopic loading in form of controlled stress	162
F.3	Constitutive behavior of viscous interfaces in local, interface-related components . . . . .	163
F.4	Specification of eigentraction-based micromechanics model for vis- cous interface behavior . . . . .	164
<b>G</b>	<b>Mechanics of organic-inorganic bio-interfaces – Implications for     strength and creep properties</b>	<b>166</b>
	<b>Bibliography</b>	<b>192</b>

# List of Figures

1.1	Nanostructure of hydrated materials containing parallel, fluid-filled interfaces made up of layered fluids (also called liquid crystals): (a) Calcium-silicate-hydrate, after [1, 2]; (b) extrafibrillar minerals in bone, after [3, 4, 5]; copyright permissions requested on July 31, 2013	13
1.2	Real (a) and auxiliary (b) material system: 2D flat parallel, spherical interfaces (a) and parallel oblate inclusions (b), embedded in a linear elastic solid matrix; 2D sketches of 3D representative volume elements . . . . .	15
1.3	Eshelby-Laws-type matrix-inclusion problem including an eigenstressed inclusion with vanishing elastic stiffness, 2D sketch of a 3D problem	18
1.4	Lateral view on an oblate spheroid with radius $a$ , half-opening $c$ , and aspect ratio $\omega = c/a$ . . . . .	18
1.5	Evolution of dimensionless microscopic average displacement jumps with dimensionless time: results of sensitivity analysis regarding Poisson's ratio of the matrix, $\nu_s$ , and the interface density parameter $d$	30
1.6	Evolution of dimensionless interface shear traction with dimensionless time: results of sensitivity analysis regarding Poisson's ratio of the matrix, $\nu_s$ , and the interface density parameter $d$ . . . . .	31
1.7	Evolution of dimensionless macroscopic shear stress with dimensionless time: results of sensitivity analysis regarding Poisson's ratio of the matrix, $\nu_s$ , and the interface density parameter $d$ . . . . .	34
1.8	Evolution of dimensionless microscopic average displacement jump with dimensionless time: results of sensitivity analysis regarding Poisson's ratio of the matrix, $\nu_s$ . . . . .	36
1.9	Evolution of dimensionless interface shear traction with dimensionless time: results of sensitivity analysis regarding Poisson's ratio of the matrix, $\nu_s$ . . . . .	36
1.10	Evolution of dimensionless macroscopic shear strain with dimensionless time: results of sensitivity analysis regarding Poisson's ratio of the matrix, $\nu_s$ , and the interface density parameter $d$ . . . . .	39
2.1	Matrix-interface composite consisting of continuous isotropic solid matrix and two families of parallel 2D interfaces; 2D sketch of a 3D representative volume element . . . . .	47

2.2	Sensitivity study regarding relaxation function (2.97): (a) characteristic relaxation times according to (2.103) as a function of interface densities (2.107), (b) relaxation capacities according to (2.99) and (2.100) as a function of interface densities (2.107), and (c) relaxation function (2.97) as a function of time, for four different partitions of interface density; $E_s = 114$ GPa, $\nu_s = 0.27$ , $a_1 \eta_{i,1} = 62.5$ GPa·h, $a_2 \eta_{i,2} = 2 \times a_1 \eta_{i,1}$ , $d_1 + d_2 = 0.3$ . . . . .	68
2.3	Sensitivity study regarding relaxation function (2.97): (a) characteristic relaxation times according to (2.103) as a function of interface densities (2.107), (b) relaxation capacities according to (2.99) and (2.100) as a function of interface densities (2.107), and (c) relaxation function (2.97) as a function of time, for four different partitions of interface density; $E_s = 114$ GPa, $\nu_s = 0.27$ , $a_1 \eta_{i,1} = 62.5$ GPa·h, $a_2 \eta_{i,2} = 5 \times a_1 \eta_{i,1}$ , $d_1 + d_2 = 0.3$ . . . . .	68
2.4	Sensitivity study regarding relaxation function (2.97): (a) characteristic relaxation times according to (2.103) as a function of interface densities (2.107), (b) relaxation capacities according to (2.99) and (2.100) as a function of interface densities (2.107), and (c) relaxation function (2.97) as a function of time, for four different partitions of interface density; $E_s = 114$ GPa, $\nu_s = 0.27$ , $a_1 \eta_{i,1} = 62.5$ GPa·h, $a_2 \eta_{i,2} = 10 \times a_1 \eta_{i,1}$ , $d_1 + d_2 = 0.3$ . . . . .	68
3.1	Matrix-interface composite consisting of continuous isotropic solid matrix and parallel 2D interfaces; 2D sketch of 3D representative volume elements . . . . .	76
3.2	Kelvin-Voigt representation of standard linear solid, used to model time-dependent behavior under pure shear see (3.4) . . . . .	78
3.3	Maxwell representation of standard linear solid . . . . .	80
3.4	Dimensionless dashpot viscosity of Kelvin-Voigt and Maxwell models, $\eta_I$ and $\eta_T$ , over the dimensionless interface density parameter $d$ . . . . .	89
4.1	Kelvin-Voigt representation of standard linear solid, used to model time-dependent behavior under pure shear . . . . .	98
4.2	Maxwell representation of standard linear solid, used to model time-dependent behavior under pure shear . . . . .	102
4.3	2D flat, parallel, spherical interfaces; 2D sketch of 3D representative volume elements . . . . .	107
F.1	Polycrystalline material comprising one spherical solid phase and an infinite amount of almost flat, circular interface phases with isotropic spatial orientation; 2D sketch of a 3D representative material volume $\Omega$ . . . . .	151
F.2	Orientation of an interface phase as well as interface-related base vectors . . . . .	152

---

F.3	Eshelby-type matrix-inclusion problems including infinite 3D matrices with isotropic stiffness, and eigenstress as well as one inclusion (a): oriented, almost flat spheroid with vanishing solid stiffness and eigenstresses, and (b): spherical inclusion with isotropic solid stiffness and vanishing eigenstresses . . . . .	155
-----	--	-----

# List of Tables

3.1	Relations between spring stiffness and dashpot viscosities of the Kelvin-Voigt and Maxwell representations of the standard linear solid model and micromechanical quantities of a matrix-interface composite . . . . .	88
F.1	15 Stroud orientations [6] . . . . .	164
F.2	28 Stroud orientations [6] . . . . .	165

# Introduction

Creep is slow, progressive deformation of materials under constant load. In 1874, Boltzmann introduced the concept of creep functions as well as the associated superposition principle, and he confirmed these groundbreaking ideas by an initial experimental campaign [7]. Ever since, these ideas have remained the fundament of the theory of viscoelasticity, which has been developed up to high mathematical maturity [8, 9, 10]. One of the parameters, which plays a major role in the creep behavior of materials comprising heterogeneous microstructures, is water. It is shown in different materials, with water being embedded into heterogeneous microstructures; as is encountered, among others, in the realm of geophysics [11, 12, 13], in cementitious materials like concrete [14, 15, 16, 17, 18], alcohol-based surfactant-water system [19, 20], or hard biomedical materials like bone or bone cements [17, 21, 22]. Hence, it is consistent with the macroscopic experimental observations, that creep in (bio or geo-)material increases with increasing the water content, as described for bone in [23], or for cementitious material in [24]. More precisely, water layers in a somewhat ice-like structured (or “glassy” [25]) state qualify as “liquid crystals”, referring to matter which is right inbetween the long-range positional and orientational order found in solids and the long-range disorder found in liquids. The creep phenomena in liquid crystal systems have been extensively studied also beyond the presence of water, e.g. for polymers [26, 27, 28] or ferroelectrics [29]. In more detail, it has been shown in various experimental and computational chemistry studies [15, 16, 17, 30], that the origin of the creep process is the intimate bounding of water molecules to electrically charged solid surfaces (and the “lubricant effect” of the fluid once the solid surfaces start to glide along the water sheets). In this context, the explicit mathematical consideration of how the lubrication effect of water on 2D interfaces results in creep properties of a bulk of material hosting such surfaces, is missing. To this end, a micromechanical framework which allows for translation of creep laws for interfaces, into the resulting creep laws at the continuum scale of materials hosting creeping interfaces as well as non-creeping solid phases inbetween, is introduced. More specifically,

we consider a linear relationship between (i) average interface dislocations and (ii) corresponding interface tractions, with an interface viscosity as the proportionality constant. Based on the homogenization schemes for eigenstressed heterogeneous materials, the interface behavior is upscaled to the much larger observation scale of a matrix-inclusion composite comprising an isotropic and linear elastic solid matrix, as well as interacting circular and parallel viscous interfaces embedded into the aforementioned matrix. The studied creep and relaxation of matrix-interface composites described in Chapter 1, shows both the obtained characteristic creep and relaxation times, describing exponentially decaying viscoelastic phenomena, increase with increasing interface size and viscosity, as well as with decreasing elastic stiffness of the solid matrix; while only the relaxation time decreases with increasing interface density. Accordingly, non-asymptotic creep of hydrated (quasi-)crystalline materials at higher load intensities may be readily explained through non-stationarity, i.e. spreading, of liquid crystal interfaces throughout solid elastic matrices [31].

Matrix-inclusion composites are well known to exhibit interaction among the inclusions [32, 33, 34, 35, 36, 37, 38]. In the special case of inclusions in form of flat interfaces, i.e. in the special case of *matrix-interface* composites, interaction among interfaces would be clearly expected. However, the two-dimensional nature of interfaces is responsible for particularly surprising interaction properties [39, 40]. This situation is reminiscent of the one encountered with microcracked materials [41, 42]. This is the motivation to study how interaction among microscopic interfaces affects the overall macroscopic creep and relaxation functions of matrix-interface composites. Extending the analysis of [31] – where we mainly focused on identical interfaces – we consider interaction among *two classes* of interfaces (referred to as “interface families”), differing in interface size, viscosity, and density. Starting point for the analysis are fundamental state equations established in the aforementioned continuum micromechanics framework. These state equations describe the time-dependent behavior of matrix-interface composites under uniform strain boundary conditions and under uniform stress boundary conditions, respectively. They allow for studying relaxation and creep scenarios. While derivation of the creep functions is a quite simple mathematical task, the derivation of relaxation functions turns out as formidable mathematical challenge. This calls for a carefully selection of solution methods, including Laplace transformation, a decoupling strategy in time-domain based on an elimination scheme, and the method of non-dimensionalization. Comparing creep and relaxation functions, a seeming paradox is obtained: no interface interaction can be identified

---

from the mathematical structure of the creep functions, while interface interaction is clearly manifested in the relaxation functions. The solution to this dilemma is provided by recalling the stress and strain average rules for materials hosting interfaces.

Engineers challenged to model creep and relaxation phenomena in scientific research or in the civil engineering practice typically try to keep things simple. Therefore, they frequently employ exponential creep and relaxation functions which are standardly related to the simple rheological models composed of linear springs and dashpots, such as the so-called “standard linear solid models” consisting of two springs and one dashpot. However, such simple models do not contain any direct information on microstructural origins of creep. The obvious question arising then is: How does such a micromechanical formulation and the microstructural quantities appearing therein relate to the classical rheological models made up of springs and of dashpots? As an answer to this question, we establish relations between microstructural quantities, such as interface size, interface density, interface viscosity, as well as elastic properties of the solid material phase, on the one hand, and spring stiffnesses and dashpot viscosities of macroscopic rheological models, on the other hand. This is accomplished by (i) deriving differential equations describing the material behavior in terms of overall stresses and strains defined on representative volume elements, and by (ii) carrying out a dissipation analysis. These two points will be tackled for the Kelvin-Voigt representation of the standard linear solid model, for the Maxwell representation of the standard linear solid model, and for a matrix-interface composite. Comparing the analytical results allows (i) for relating rheological spring stiffnesses and the dashpot viscosities of standard linear solid models, to microstructural features of a matrix-interface composite, and (ii) for a micromechanical interpretation of the stresses and strains which are formally associated with the rheological springs and dashpots, and (iii) for a micromechanical illustration of the energy dissipating in the dashpots.

Standard linear solid models often appear as too simple when it comes to the representation of the actual material behavior, such as typically observed in creep and relaxation tests. This was realized already in the 19th century when the field of creep mechanics was initiated [43]. The problem was tackled by the introduction of rheological chain models, such as Maxwell chains and Kelvin-Voigt chains, respectively. Ever since, such models have enjoyed great popularity in a variety of applications, concerning, e.g. the creep of aging cementitious materials [44], of soft biomaterials such as intervertebral discs [45], or of different types of polymers and

plastics [46]. It is the logic next step to pose the question whether also rheological chain models can be directly related to the mechanics of microstructural systems consisting of an elastic solid matrix and viscous interfaces, now with differing viscosities and differing sizes. We compare (i) coefficients of macroscopic stress-strain relations of rheological chains models with  $N$  Maxwell units (or  $N$  Kelvin-Voigt units, respectively), with (ii) coefficients of stress-strain relations characterizing a matrix-interface composite consisting of a contiguous, isotropic, and linear elastic solid matrix, as well as of  $N$  families of parallel interfaces. When it comes to deriving stress-strain relations linking shear stresses and their time-derivatives, to shear strains and their time-derivatives, we start with two rheological units or two interface families ( $N = 2$ ), respectively. Then we extend the derivation to three rheological units or three interface families ( $N = 3$ ), respectively; and, finally, we tackle the case of  $N$  rheological units or  $N$  interface families, respectively. A micromechanical interpretation of Maxwell chain models and Kelvin-Voigt chain models becomes possible by comparing the  $2N + 1$  independent coefficients occurring in the constitutive equations derived for the Kelvin-Voigt chain models, the Maxwell chain models, and the micromechanics models with different viscous interfaces families, respectively. These results relate spring stiffnesses and dash-pot viscosities to microstructural features such as interface size, interface density, interface viscosity, as well as elastic properties of the solid material phase and, hence, can be understood as a justification for frequently used phenomenological models.

Finally, we apply the developed continuum micromechanics framework to creep and relaxation of the hierarchically organized multiscale material “bone”. “Universal” mechanical properties of bone’s elementary constituents (hydroxyapatite, collagen, and water with non-collagenous organics), their “universal” interaction patterns across multiple length scales, and corresponding “universal” composition rules for extracellular bone matrices allow for the prediction of the large variety of mechanical properties of different bone tissues observed at the macroscopic scale, see, e. g. [47, 48, 49, 50]. In this context, the viscoelasticity of interface-penetrated extrafibrillar mineral clusters were identified from downscaling of different, independent macroscopic creep and relaxation tests. They can be quantified by isotropic Kelvin-Voigt parameters. We here expand on how to downscale this bulk viscosity value further, i. e. down to the level of the individual interfaces. To this end, we first use so-called Reuss bounds in order to derive, from knowledge on anisotropic creep tensors of matrix-interface composites with parallel interfaces, the *isotropic* creep tensor of a new material system which comprises *randomly*

*oriented* RVEs of matrix-interface composites with parallel interfaces. This opens the door to top-down identification of interface density, interface viscosity, and bulk viscosity of “glassy” water filling interfaces between hydroxyapatite crystals. As for the comparison of the top-down identified bulk viscosity with a corresponding quantity derived in a bottom-up approach resting on molecular dynamics simulations, it turns out to be useful to estimate the dislocation speeds from macroscopic relaxation experiments on bone. Top-down identified and bottom-up identified bulk viscosity of adsorbed water and speeds of interfacial dislocations, respectively, differ by several orders of magnitude. This seeming paradox can be explained based on the pronounced thixotropic behavior of “glassy water”, the viscosity of which decreases with increasing dislocation rate, whereby both physical quantities covering 14 and 16 orders of magnitude, respectively.

# Methodology and key results

## Chapter 1

This chapter is based on a joint publication of Mehran Shahidi, Bernhard Pichler, and Christian Hellmich published in the *European Journal of Mechanics A/Solid*, (2014), vol. 45, pp. 41-58.

Christian Hellmich and Bernhard Pichler set up the overall research strategy, using micromechanics for eigenstressed phases as a fundament for upscaling interface viscosities to macroscopic bulk creep properties. They supervised the research progress, checked key results, and supported the documentation process. Mehran Shahidi developed Maple codes for the analytical calculations and documented the research results.

### DIGEST:

It is generally agreed upon that fluids may play a major role in the creep behavior of materials comprising heterogeneous microstructures and fluid-filled porosity at small length scales. In more detail, nanoconfined fluid-filled interfaces are typically considered to act as a lubricant, once electrically charged solid surfaces start to glide along fluid sheets, while the fluid is typically in a liquid crystal state, which refers to an “adsorbed”, “ice-like”, or “glassy” structure of fluid molecules. Here, we aim at translating this interface behavior into apparent creep laws at the continuum scale of materials consisting of one non-creeping solid matrix with embedded fluid-filled interfaces. To this end, we consider a linear relationship between (i) average interface dislocations and (ii) corresponding interface tractions, with an interface viscosity as the proportionality constant. Homogenization schemes for eigenstressed heterogeneous materials are used to upscale this interface behavior to the much larger observation scale of a matrix-inclusion composite comprising an isotropic and linear elastic solid matrix, as well as interacting circular and parallel interfaces embedded into the aforementioned matrix. Both the obtained

---

characteristic creep and relaxation times, describing exponentially decaying viscoelastic phenomena, increase with increasing interface size and viscosity, as well as with decreasing elastic stiffness of the solid matrix; while only the relaxation time decreases with increasing interface density. Accordingly, non-asymptotic creep of hydrated (quasi-)crystalline materials at higher load intensities may be readily explained through non-stationarity, i.e. spreading, of liquid crystal interfaces throughout solid elastic matrices.

## Chapter 2

This chapter is based on a joint publication of Mehran Shahidi, Bernhard Pichler, and Christian Hellmich to be submitted to the Journal of Acta Mechanica.

All authors developed the structure of the differential equations to be solved. Bernhard Pichler and Mehran Shahidi developed the elimination scheme and the non-dimensionalization-based solutions, and Mehran Shahidi developed the Laplace transform-based strategy.

DIGEST:

Matrix-inclusion composites are known to exhibit interaction among the inclusions. When it comes to the special case of inclusions in form of flat interfaces, interaction among interfaces would be clearly expected, but the two-dimensional nature of interfaces is responsible for surprising interaction properties. This is the motivation to analyze how interaction among two different classes of microscopic interfaces manifests in macroscopic creep and relaxation functions of matrix-interface composites. To this end, we analyze composites consisting of a linear-elastic solid matrix hosting parallel interfaces, and we consider that creep and relaxation of such composites results from micro-sliding within adsorbed fluid layers filling the interfaces. The latter idea was recently elaborated in the framework of continuum micromechanics, exploiting eigenstress homogenization schemes, see [Eur J Mech Sol/A: 41-58, 2014]. After a rather simple mathematical exercise, it becomes obvious that creep functions do not reflect any interface interaction. Mathematical derivation of relaxation functions, however, turns out to be much more challenging because of pronounced interface interaction. Based on a careful selection of solution methods, including Laplace transforms and the method of non-dimensionalization, we analytically derive a closed-form expression of the relaxation functions, which provides the sought insight into interface interaction. The seeming paradox that no interface interaction can be identified from creep

---

functions, while interface interaction manifests itself very clearly in the relaxation functions of matrix-interface materials, is finally resolved based on stress and strain average rules for interfaced composites. They clarify that uniform stress boundary conditions lead to a direct external control of average stress and strain states in the solid matrix, and this prevents interaction among interfaces. Under uniform strain boundary conditions, in turn, interfacial dislocations influence the average stress and strain states in the solid matrix, and this results in pronounced interface interaction.

### Chapter 3

This chapter is based on a joint publication of Mehran Shahidi, Bernhard Pichler, and Christian Hellmich to be submitted to the Journal of Engineering Mechanics.

Bernhard Pichler and Christian Hellmich set up the overall research strategy, looking for analogies between micromechanics and classical rheological models. They supervised the research progress, checked key results, and supported the documentation process. Mehran Shahidi developed Maple codes for the analytical calculations and documented the research results.

#### DIGEST:

Creep functions are often represented by “rheological models” consisting of springs and dashpots, while the actual microscopic origins of creep, such as micro-sliding along interfaces, has only recently been explicitly considered in a continuum mechanics framework [Eur J Mech Sol 45A : 41-58, 2014]. The question arises whether formal analogies between the former and the latter can be derived: This question is answered here for the rheological models of the Kelvin-Voigt and Maxwell type. Thereby, it appears a full analogy between shear stresses and strains acting on the rheological models, and those acting on a micromechanical representative volume element consisting of an elastic solid matrix with embedded viscous interfaces, whereby the respective viscosity arises from layered polar fluids absorbed at these interfaces. The Kelvin-Voigt parameters appear as being much simpler and more intuitively related to the micromechanical quantities, when compared to the Maxwell parameters. More specifically, rheological spring parameters are always related to the shear stiffness of the elastic solid matrix, while they may additionally depend on the Poisson’s ratio of the elastic solid matrix, and on the interface density. On the other hand, dashpot viscosities are always related to interface viscosities, interface radii, and interface densities; and they may even depend on

the Poisson's ratio of the elastic solid matrix.

## Chapter 4

This chapter is based on a joint publication of Mehran Shahidi, Bernhard Pichler, and Christian Hellmich to be submitted to the Journal of Engineering Mechanics.

Bernhard Pichler and Christian Hellmich set up the overall research strategy, looking for analogies between micromechanics and classical rheological models. They supervised the research progress, checked key results, and supported the documentation process. Mehran Shahidi developed Maple codes for the analytical calculations and documented the research results.

DIGEST:

While the companion paper provided a micromechanical explanation of the spring and dashpot parameters occurring in the rheological models of the Kelvin-Voigt and Maxwell type, we here extend this discussion towards rheological chain models. Therefore, the considered micromechanical system is extended from one interface phase to  $N$  interface phases differing in size and viscosity. Elimination schemes allow for deriving differential equations with only overall stresses and strains and their derivatives as unknowns, rather than microstresses and microstrains in case of micromechanics, or spring/dashpot-related stresses and strains in case of the rheological chain models. Companion of corresponding coefficients reveals a full analogy between the chain models, and also between the latter and the micromechanics model. For the Kelvin-Voigt chain, this analogy is even identical to the one of the Zener model of companion paper Part I. The Maxwell chain-related analogy is much more complex, and analytical solutions only exist in the case of very few chain members.

## Chapter 5

This work is the outgrowth of a cooperation with Prof. Vikas Tomar, Devendra Verma, and Tao Qu from Purdue University. They conducted a series of molecular dynamics studies, the results of which were compared to micromechanics-based viscosity results derived for bone. Supervised by Christian Hellmich and Bernhard Pichler, Mehran Shahidi performed the computations, and documented the results. They became part of a topical issue paper for the MRS Bulletin, prepared in

---

cooperation with the colleagues from Purdue University, and attached as Appendix G the present thesis.

DIGEST:

After having elaborated the theoretical basis for matrix-interface composites in Chapter 1, after having studied interaction among interfaces of different size, density, and viscosity in Chapter 2, and after having identified links between micromechanical quantities and parameters of rheological models widely used in the engineering research and practice, see Chapters 3 and 4, we here come into the position to apply of all of these theoretical developments to a real interfaced material. We consider the hierarchically organized biomaterial “bone”, and we aim at top-down identification (i) of interface density and interface viscosity of water-filled interfaces between hydroxyapatite crystals and (ii) of the characteristic speed of interface dislocation in a macroscopic relaxation test on a bone specimen. To this end, we consider a new material system consisting of randomly arranged building blocks which are RVEs of the matrix-interface composites with one family of parallel interfaces. In order to derive an isotropic creep tensor for the new material system, we start from the anisotropic creep tensor of the matrix-interface materials studied in Chapters 1 and 3, and we apply the mixture rule, i. e. we evaluate the so-called Reuss bound by carrying out a complete spatial average. The here-derived micromechanics-related isotropic creep tensor is compared with a Kelvin-Voigt creep tensor for interfaced hydroxyapatite, taken from the literature, and this allows for top-down identification of the interface density and interface viscosity. Multiplying the latter with the characteristic thickness of interfaces, delivers a bulk viscosity of water filling the interfaces between hydroxyapatite crystals. This bulk viscosity is similar to the one of molten glass, hence the name “glassy” water. As for the comparison of this quantity with corresponding results from a bottom-up approach resting on molecular dynamics simulations (provided by colleagues from Purdue University, IN, USA), it turns out to be useful to estimate the dislocation speed from macroscopic relaxation experiments on bone. The top-down identified viscosity of adsorbed water is by 14 orders of magnitude larger than the bottom-up identified viscosity. Similarly, the typical speed of interfacial dislocations in a relaxation test on bone is by 16 order of magnitude smaller than the one realized in the molecular dynamics simulation. This results indicate a pronounced thixotropic effect of adsorbed water, i. e. the viscosity decreases with increasing speed of interfacial dislocations.

# Chapter 1

## Viscous interfaces as source for material creep: a continuum micromechanics approach

### 1.1 Introduction

It is generally agreed upon that water may play a major role in the creep behavior of materials comprising heterogeneous microstructures with water being embedded into those; as is encountered, among others, in the realm of geophysics [11, 12, 13], in cementitious materials like concrete [14, 15, 16, 17, 18], alcohol-based surfactant-water system [19, 20], or hard biomedical materials like bone or bone cements [17, 21, 22]. Hence, creep increases with increasing water content, as described for bone in [23]. Water layers in a somewhat ice-like structured (or “glassy” [25]) state qualify as “liquid crystals”, referring to matter which is right inbetween the long-range positional and orientational order found in solids and the long-range disorder found in liquids. The creep phenomena in liquid crystal systems have been extensively studied also beyond the presence of water, e.g. for polymers [26, 27, 28] or ferroelectrics [29]. More specifically, the intimate bounding of water molecules to electrically charged solid surfaces (and the “lubricant effect” of the fluid once the solid surfaces start to glide along the water sheets) is thought of as the origin of the creep process, as is supported by various experimental and computational chemistry studies [15, 16, 17, 30]. What is somehow lacking in this respect, is the explicit mathematical consideration of how the lubrication effect of water on 2D interfaces results in creep properties of a bulk of material hosting

such surfaces. As a contribution to this somehow open problem, the present paper describes a micromechanical framework which allows for translation of creep laws for interfaces, into the resulting creep laws at the continuum scale of materials hosting creeping interfaces as well as non-creeping solid phases inbetween.

## 1.2 General strategy for interface modeling

When aiming at concise, yet efficient modeling of interface behavior, we need to consider their peculiar, *two-dimensional* nature, because of which no “fluid bulk stiffness” can be defined on them. Namely, bulk stiffnesses are (by definition) related to volume changes, while the 2D interfaces do not exhibit any volume. Accordingly, neither stress nor strain tensors are defined on the interfaces. Instead, traction forces act on the interface planes; and the interfaces also exhibit dislocations, i.e. the in-plane displacements show jumps when crossing the interface perpendicular to its plane.

When fictitiously cutting out each and every interface from the surrounding solid matrix, then the (in-plane) tractions acting on the interface surfaces are related, via the viscosity of the infinitesimally thin liquid crystal membrane, to the in-plane displacement jumps or dislocations. We reserve the corresponding mathematical formulation for Section 1.5.1, and first focus on the remaining material system consisting of the solid matrix with infinitesimally thin slits (the latter being the remnants of the fictitiously removed liquid crystal interfaces). The action of the interfaces is replaced by free tractions (or eigentractions) acting on the slit walls. The relation between these eigentractions and the corresponding dislocations or displacement jumps across the slits now depends on the elastic properties of the solid matrix surrounding the slits (defined through so-called concentration tensors, given in Section 1.4), but also on the macroscopic strains prescribed to the overall material system, i.e. the representative material volume of a piece of matter with interfaces (or slits) in between. The latter dependency is quantified in terms of so-called concentration tensors, given also in Section 1.4. However, this quantification is not straightforward, but requires an additional, auxiliary mathematical step which is inspired by a strategy proposed by Pensée et al. [51] for the case of sharp cracks: Namely, in order to find compact analytical expressions for the aforementioned concentration and influence tensors (having their conceptual roots in the so-called transformation field analysis [52, 53]), we consider the slits as limit cases of oblate spheroids, for which analytical solutions are available, i.e. we first

introduce an auxiliary material system consisting of an elastic matrix with oblate spheroidal zero-stiffness inclusions subjected to eigenstresses. This is developed in Section 1.3, based on the general concentration-influence relation concept of Pichler and Hellmich [54]. When finally setting the eigenstrains at the slit walls identical to the tractions acting on the viscous interface, while enforcing equilibrium of all forces in the material system, we arrive at relations between macroscopic strains and macroscopic stresses, i.e. at the creep or relaxation characteristics of the overall material, as well as at the corresponding traction and dislocation evolutions at the interface level. Illustrative examples are given in Sections 1.5.2 and 1.5.3. All mathematical developments contained in the present paper are restricted to parallel interfaces, a case which is e.g. encountered in hydrated calcium silicate as it occurs in cementitious materials, see Figure 1(a), or in the hydrated mineral crystal clusters found in the extrafibrillar spaces of bone tissues, see Figure 1(b).

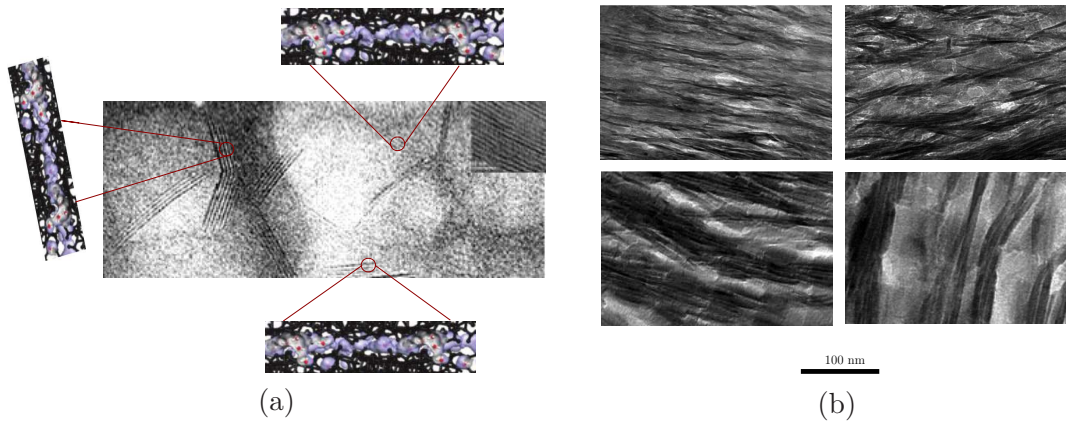


Figure 1.1: Nanostructure of hydrated materials containing parallel, fluid-filled interfaces made up of layered fluids (also called liquid crystals): (a) Calcium-silicate-hydrate, after [1, 2]; (b) extrafibrillar minerals in bone, after [3, 4, 5]; copyright permissions requested on July 31, 2013

### 1.3 Auxiliary material system I: micromechanics of eigenstressed oblate phase in solid elastic matrix

#### 1.3.1 General fundamentals of micromechanical representation

In order to finally arrive at compact analytical expressions for the targeted material system consisting of an elastic matrix with embedded viscous interfaces, we first introduce an auxiliary material system in the framework of continuum micromechanics [32, 55, 56]: In this context, a material is considered as the matter

filling a representative volume element (RVE) with volume  $\Omega$ , which fulfills the standard separation-of-scales requirement [57, 58]: The material volume needs to be much smaller than the structure built up by this material, and much larger than the inhomogeneities found within this material. Working in the framework of continuum micromechanics [55, 56], we do not resolve each and every detail within the material volume, but introduce mechanically relevant sub-domains called material phases, namely one solid phase and one “auxiliary inclusion phase” [see Fig. 1.2(b)], which will finally give access, in the Section 1.5, to the physical nature of all the fluid (or liquid crystal) layers depicted in Figure 1.2(a). The inclusion phase (labelled by index  $i$ ) is characterized by eigen-microstresses  $\underline{\underline{\underline{\underline{\sigma}}}}_i^E$

$$\underline{\underline{\underline{\underline{\sigma}}}}_i = \underline{\underline{\underline{\underline{\sigma}}}}_i^E \quad (1.1)$$

These inclusion eigenstresses are “free” from elastic effects, and they will be converted into interface eigentractions in Section 1.4, before the latter tractions will be related to liquid crystal viscosity in Section 1.5. Furthermore, since the bulk stiffness of a 2D viscous interface is, by definition, zero, the inclusion phase is assigned a vanishing bulk stiffness,

$$\underline{\underline{\underline{\underline{C}}}}_i = 0 \quad (1.2)$$

On the other hand, the solid phase of Figure 1.2(b) is characterized by an elastic stiffness tensor  $\underline{\underline{\underline{\underline{C}}}}_s$  and no eigenstress

$$\underline{\underline{\underline{\underline{\sigma}}}}_s = \underline{\underline{\underline{\underline{C}}}}_s : \underline{\underline{\underline{\underline{\varepsilon}}}}_s \quad (1.3)$$

with  $\underline{\underline{\underline{\underline{\sigma}}}}_s$  and  $\underline{\underline{\underline{\underline{\varepsilon}}}}_s$  as the average microstresses and the average microstrains in the solid. In the following, we restrict ourselves to an isotropic solid stiffness

$$\underline{\underline{\underline{\underline{C}}}}_s = 3k_s \underline{\underline{\underline{\underline{I}}}}_{vol} + 2\mu_s \underline{\underline{\underline{\underline{I}}}}_{dev} \quad (1.4)$$

where  $\underline{\underline{\underline{\underline{I}}}}_{vol} = \frac{1}{3} \underline{\underline{\underline{\underline{1}}}} \otimes \underline{\underline{\underline{\underline{1}}}}$  and  $\underline{\underline{\underline{\underline{I}}}}_{dev} = \underline{\underline{\underline{\underline{I}}}} - \underline{\underline{\underline{\underline{I}}}}_{vol}$ , respectively, denote the volumetric and the deviatoric part of the symmetric fourth-order identity tensor  $\underline{\underline{\underline{\underline{I}}}}$ , with components  $I_{ijkl} = \frac{1}{2}(\delta_{ik} \delta_{jl} + \delta_{il} \delta_{kj})$ , and with  $\delta_{ij}$  denoting the Kronecker delta being equal to 1 if  $i = j$  and 0 otherwise. In addition,  $\underline{\underline{\underline{\underline{1}}}}$  is the second-order identity tensor with components being equal to the Kronecker delta. In (1.4),  $k_s$  and  $\mu_s$  denote the bulk modulus and the shear modulus of the solid phase, respectively. They are related to Young’s modulus  $E_s$  and Poisson’s ratio  $\nu_s$  via the isotropic elasticity relations

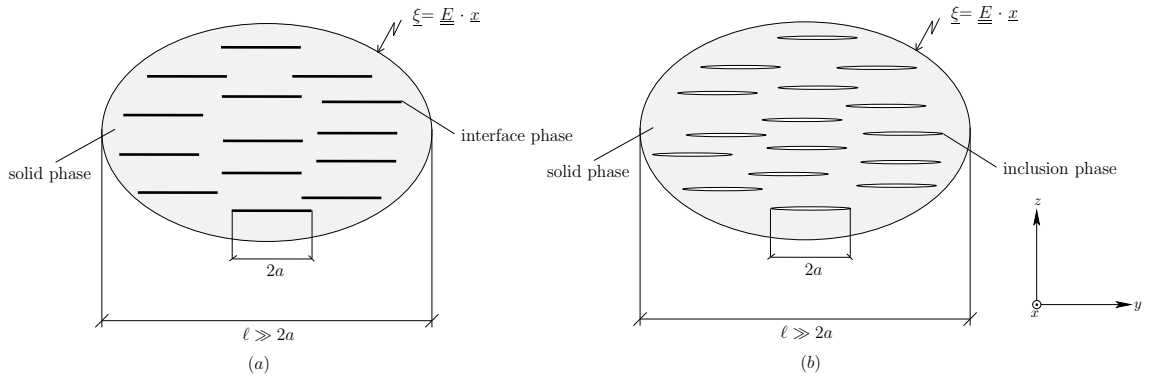


Figure 1.2: Real (a) and auxiliary (b) material system: 2D flat parallel, spherical interfaces (a) and parallel oblate inclusions (b), embedded in a linear elastic solid matrix; 2D sketches of 3D representative volume elements

$$\begin{aligned}
 k_s &= \frac{E_s}{3(1-2\nu_s)} & \mu_s &= \frac{E_s}{2(1+\nu_s)} \\
 E_s &= \frac{9k_s\mu_s}{3k_s + \mu_s} & \nu_s &= \frac{3k_s - 2\mu_s}{6k_s + 2\mu_s}
 \end{aligned} \tag{1.5}$$

Uniform strain boundary conditions are considered, i. e. the RVE of Figure 1.2 is subjected to macroscopic strains  $\underline{E}$  [55] being applied in terms of displacement vectors  $\underline{\xi}$  at the boundary of the RVE,  $\partial\Omega$ ,

$$\underline{\xi}(\underline{x}) = \underline{E} \cdot \underline{x} \quad \text{on} \quad \partial\Omega \tag{1.6}$$

with  $\underline{x}$  as the position vector labelling geometrical points at this boundary. The prescribed macroscopic strains  $\underline{E}$  are independent of  $\underline{x}$ . Furthermore, we consider the resulting microscopic strains

$$\underline{\underline{\varepsilon}}(\underline{x}) = \frac{1}{2} \left[ \underline{\underline{\nabla}}\underline{\xi}(\underline{x}) + {}^t\underline{\underline{\nabla}}\underline{\xi}(\underline{x}) \right] \tag{1.7}$$

inside the RVE to be kinematically compatible, which entails the validity of the strain averaging rule [55] in the form

$$\underline{E} = \frac{1}{\Omega} \int_{\Omega} \underline{\underline{\varepsilon}}(\underline{x}) d\Omega \quad \Rightarrow \quad \underline{E} = f_s \underline{\underline{\varepsilon}}_s + f_i \underline{\underline{\varepsilon}}_i \tag{1.8}$$

with  $\underline{\underline{\varepsilon}}_i$  as the average strains in the inclusion phase and  $f_i$  as its volume fraction; while  $\underline{\underline{\varepsilon}}_s$  and  $f_s$  denote the average strain and the volume fraction of the solid material compartment. Linear elasticity law (1.3) and the linear strain-displacement relation (1.7) together with eigenstresses (1.1) and macroscopic strains (1.6) imply

the following linear influence-concentration relations [52, 54]

$$\underline{\underline{\varepsilon}}_i = \underline{\underline{A}}_i : \underline{\underline{E}} + \underline{\underline{D}}_{ii} : \underline{\underline{\sigma}}_i^E \quad (1.9)$$

$$\underline{\underline{\varepsilon}}_s = \underline{\underline{A}}_s : \underline{\underline{E}} + \underline{\underline{D}}_{si} : \underline{\underline{\sigma}}_i^E \quad (1.10)$$

with  $\underline{\underline{A}}_i$  and  $\underline{\underline{A}}_s$  as the strain concentration tensors of inclusion and solid phase, respectively, as well as with  $\underline{\underline{D}}_{ii}$  and  $\underline{\underline{D}}_{si}$  as the influence tensors quantifying the effect of eigen-microstresses  $\underline{\underline{\sigma}}_i^E$  on the microstrains of the inclusion phase and the solid phase, respectively. For defining the macroscopic stress  $\underline{\underline{\Sigma}}$ , we consider that work done by the RVE-related macrostress  $\underline{\underline{\Sigma}}$  on the macrostrain  $\underline{\underline{E}}$ , is equal to the work done by all microstresses *within* the RVE, on all microstrains:

$$\underline{\underline{\Sigma}} : \underline{\underline{E}} = \frac{1}{\Omega} \int_{\Omega} \underline{\underline{\sigma}}(\underline{\underline{x}}) : \underline{\underline{\varepsilon}}(\underline{\underline{x}}) d\Omega \quad (1.11)$$

When considering the strain average rule (1.8) and an equilibrated microscopic stress field ( $\text{div } \underline{\underline{\sigma}}(\underline{\underline{x}}) = 0$ ), the integral in (1.11) can be transformed into [59]

$$\frac{1}{\Omega} \int_{\Omega} \underline{\underline{\sigma}}(\underline{\underline{x}}) : \underline{\underline{\varepsilon}}(\underline{\underline{x}}) d\Omega = \frac{1}{\Omega} \int_{\Omega} \underline{\underline{\sigma}}(\underline{\underline{x}}) d\Omega : \frac{1}{\Omega} \int_{\Omega} \underline{\underline{\varepsilon}}(\underline{\underline{x}}) d\Omega \quad (1.12)$$

which is standardly referred to as Hill's lemma. From combination of (1.11) and (1.12) with (1.8) it follows that the macrostress is the average of the microstresses over the RVE,

$$\underline{\underline{\Sigma}} = \frac{1}{\Omega} \int_{\Omega} \underline{\underline{\sigma}}(\underline{\underline{x}}) d\Omega \quad \Rightarrow \quad \underline{\underline{\Sigma}} = f_s \underline{\underline{\sigma}}_s + f_i \underline{\underline{\sigma}}_i^E \quad (1.13)$$

Eq. (1.13) is standardly referred to as the stress average rule. As to arrive at an elegant alternative expression for the macroscopic stress, we follow Dormieux [59] in splitting the loading of the RVE into two separate parts, namely (i) the macroscopic strains  $\underline{\underline{E}}$  and (ii) the inclusion eigenstresses  $\underline{\underline{\sigma}}_i^E$ , labelling corresponding physical quantities with “I” and “II”, respectively. Accordingly,  $\underline{\underline{E}}_I = \underline{\underline{E}}$ ,  $\underline{\underline{E}}_{II} = 0$ ,  $\underline{\underline{\sigma}}_{i,I}^E = 0$ , and  $\underline{\underline{\sigma}}_{i,II}^E = \underline{\underline{\sigma}}_i^E$ . Insertion of Eqs. (1.1), (1.3), and (1.10), into Eq. (1.13), and specifying the result for load case I, yields

$$\underline{\underline{\Sigma}}_I = \underline{\underline{C}}_{hom} : \underline{\underline{E}} \quad (1.14)$$

with the so-called homogenized stiffness tensor

$$\underline{\underline{C}}_{hom} = f_s \underline{\underline{C}}_s : \underline{\underline{A}}_s \quad (1.15)$$

As for calculation of the macrostress in load case  $II$ , we let microscopic stresses  $\underline{\underline{\sigma}}_{s,II}$  and  $\underline{\underline{\sigma}}_{i,II}^E$  do work on microscopic strains  $\underline{\underline{\varepsilon}}_{s,I}$  and  $\underline{\underline{\varepsilon}}_{i,I}$ , which, upon twofold application of Hill's lemma (1.11) and (1.12), yields [59]

$$\underline{\underline{\Sigma}}_{II} = f_i \underline{\underline{\sigma}}_i^E : \underline{\underline{A}}_i \quad (1.16)$$

which is referred to as Levin's theorem [60]. Adding (1.14) and (1.16) yields the sought alternative expression for the macroscopic stresses,

$$\underline{\underline{\Sigma}} = \underline{\underline{C}}_{hom} : \underline{\underline{E}} + f_i \underline{\underline{\sigma}}_i^E : \underline{\underline{A}}_i \quad (1.17)$$

### 1.3.2 Determination of influence and concentration tensors from matrix-(spheroidal) inclusion problems

For the sake of simplicity, we restrict ourselves to one inclusion phase in form of separated (aligned) inclusions which are adjacent only to an isotropic solid matrix phase [see Fig. 1.2(b)], i.e. the inclusions do not intersect each other. For this matrix-inclusion morphology the so-called Mori-Tanaka scheme [33, 61] is appropriate. Accordingly, we estimate the inclusion phase strains  $\underline{\underline{\varepsilon}}_i$  by means of an auxiliary matrix-inclusion problem (see Fig. 1.3), namely we set them equal to the uniform strains occurring in an eigenstressed ellipsoidal inclusion (with eigenstresses  $\underline{\underline{\sigma}}_i^E$ ), embedded in an infinite matrix of stiffness  $\underline{\underline{C}}_s$  subjected to fictitious strains  $\underline{\underline{E}}_\infty$  at its infinitely remote boundary, the latter strains being chosen in a way which allows for fulfillment of the strain average rule (1.8). In detail, the inclusion strains follow the analytical relation [32, 62]

$$\underline{\underline{\varepsilon}}_i = \underline{\underline{A}}_i^\infty : \left[ \underline{\underline{E}}_\infty - \underline{\underline{P}}_i : \underline{\underline{\sigma}}_i^E \right] \quad (1.18)$$

with

$$\underline{\underline{A}}_i^\infty = \left[ \underline{\underline{I}} - \underline{\underline{P}}_i : \underline{\underline{C}}_s \right]^{-1} \quad (1.19)$$

In (1.18) and (1.19), the Hill tensor  $\underline{\underline{P}}_i$  is determined from the Eshelby tensor  $\underline{\underline{S}}_i$ , through

$$\underline{\underline{P}}_i = \underline{\underline{S}}_i : \underline{\underline{C}}_s^{-1} \quad (1.20)$$

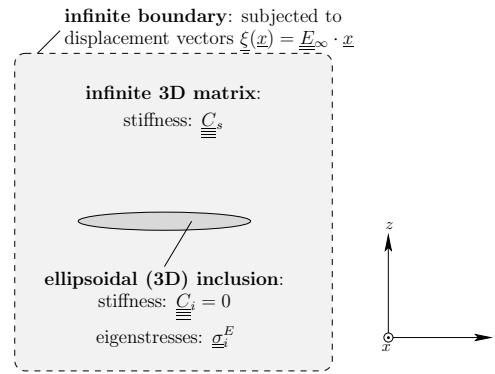


Figure 1.3: Eshelby-Laws-type matrix-inclusion problem including an eigenstressed inclusion with vanishing elastic stiffness, 2D sketch of a 3D problem

and the Eshelby tensor components for oblate spheroidal inclusions with radius  $a$  and half-opening  $c$  (see Fig. 1.4), can be found in [62]. Given our interest in flat spheroids, characterized by very small aspect ratio  $\omega = c/a \ll 1$ , we develop these components into Taylor series around  $\omega = 0$ , which we then truncate after the term which is linear in  $\omega$ . This leads to the following non-vanishing components, provided that the normal to the mid-plane of the flat spheroid is pointing in the  $z$ -direction:

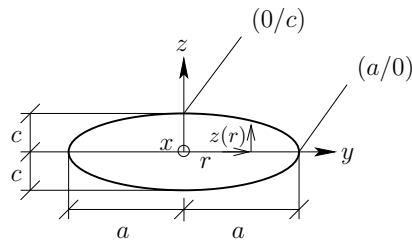


Figure 1.4: Lateral view on an oblate spheroid with radius  $a$ , half-opening  $c$ , and aspect ratio  $\omega = c/a$

$$\begin{aligned}
 S_{i,xxxx} &= S_{i,yyyy} = \frac{13 - 8v_s}{32(1 - v_s)} \pi \omega, \\
 S_{i,xyxy} &= S_{i,yyxx} = \frac{8v_s - 1}{32(1 - v_s)} \pi \omega, \\
 S_{i,xxzz} &= S_{i,yyzz} = \frac{2v_s - 1}{8(1 - v_s)} \pi \omega, \\
 S_{i,zzxx} &= S_{i,zzyy} = \frac{v_s}{(1 - v_s)} \left( 1 - \frac{4v_s + 1}{8v_s} \pi \omega \right), \\
 S_{i,xyxy} &= S_{i,yxyx} = S_{i,yxyx} = S_{i,xyyx} = \frac{7 - 8v_s}{32(1 - v_s)} \pi \omega, \\
 S_{i,yzyz} &= S_{i,zyyz} = S_{i,yzzy} = S_{i,zyzy} = S_{i,xzxx} = S_{i,xzzx} = \\
 &= S_{i,zxzx} = S_{i,zxzx} = \frac{1}{2} \left( 1 + \frac{(v_s - 2)}{(1 - v_s)} \frac{\pi}{4} \omega \right), \\
 S_{i,zzzz} &= 1 - \frac{1 - 2v_s}{1 - v_s} \frac{\pi}{4} \omega
 \end{aligned} \tag{1.21}$$

In Eq. (1.21),  $v_s$  denotes Poisson's ratio of the isotropic matrix with stiffness  $\underline{\underline{C}}_s$  (see Fig. 1.3). When formally choosing an inclusion with stiffness  $\underline{\underline{C}}_s$  in an infinite matrix of the same stiffness subjected to  $\underline{\underline{E}}_\infty$  at the infinity remote boundary, it follows that

$$\underline{\underline{\varepsilon}}_s = \underline{\underline{E}}_\infty \tag{1.22}$$

Use of (1.18) and (1.22) in the strain average rule (1.8) yields a relation between the strains  $\underline{\underline{E}}$  subjected at the boundary of the RVE and the (fictitious) strains  $\underline{\underline{E}}_\infty$  acting at the infinitely remote boundary of the auxiliary matrix of the problem shown in Fig. 1.3,

$$\underline{\underline{E}}_\infty = \left[ f_s \underline{\underline{I}} + f_i \underline{\underline{A}}_i^\infty \right]^{-1} : \left( \underline{\underline{E}} + f_i \underline{\underline{A}}_i^\infty : \underline{\underline{P}}_i : \underline{\underline{\sigma}}_i^E \right) \tag{1.23}$$

Backsubstitution of (1.23) into (1.18) and (1.22) yields

$$\underline{\underline{\varepsilon}}_i = \underline{\underline{A}}_i^\infty : \left[ f_s \underline{\underline{I}} + f_i \underline{\underline{A}}_i^\infty \right]^{-1} : \left( \underline{\underline{E}} + f_i \underline{\underline{A}}_i^\infty : \underline{\underline{P}}_i : \underline{\underline{\sigma}}_i^E \right) - \underline{\underline{A}}_i^\infty : \underline{\underline{P}}_i : \underline{\underline{\sigma}}_i^E \tag{1.24}$$

$$\underline{\underline{\varepsilon}}_s = \left[ f_s \underline{\underline{I}} + f_i \underline{\underline{A}}_i^\infty \right]^{-1} : \left( \underline{\underline{E}} + f_i \underline{\underline{A}}_i^\infty : \underline{\underline{P}}_i : \underline{\underline{\sigma}}_i^E \right) \tag{1.25}$$

Comparing (1.24) and (1.25) to (1.9) and (1.10) allows for identification of the concentrations tensors of the INCLUSION and solid phases,  $\underline{\underline{A}}_i$  and  $\underline{\underline{A}}_s$ , as

$$\underline{\underline{A}}_i = \underline{\underline{A}}_i^\infty : \left[ f_s \underline{\underline{I}} + f_i \underline{\underline{A}}_i^\infty \right]^{-1} \quad (1.26)$$

$$\underline{\underline{A}}_s = \left[ f_s \underline{\underline{I}} + f_i \underline{\underline{A}}_i^\infty \right]^{-1} \quad (1.27)$$

and of the influence tensors for inclusion-inclusion and inclusion-solid interactions,  $\underline{\underline{D}}_{ii}$  and  $\underline{\underline{D}}_{si}$ , as

$$\underline{\underline{D}}_{ii} = \left( f_i \underline{\underline{A}}_i - \underline{\underline{I}} \right) : \underline{\underline{A}}_i^\infty : \underline{\underline{P}}_i = -f_s \underline{\underline{A}}_s : \underline{\underline{A}}_i^\infty : \underline{\underline{P}}_i \quad (1.28)$$

$$\underline{\underline{D}}_{si} = \underline{\underline{A}}_s : f_i \underline{\underline{A}}_i^\infty : \underline{\underline{P}}_i \quad (1.29)$$

where we made use of the volume average rule for strain concentration tensors [59], which results from insertion of Eqs. (1.9) and (1.10) into Eq. (1.8), while considering  $\underline{\underline{\sigma}}_i^E = 0$ ,

$$\underline{\underline{I}} = f_i \underline{\underline{A}}_i + f_s \underline{\underline{A}}_s \quad (1.30)$$

## 1.4 Auxiliary material system II: elastic matrix containing slits with eigentractions

### 1.4.1 Conversion of strains into dislocations

Next, we discuss the transition from oblate spheroidal inclusions, as introduced in Section 1.3.2, to *flat*, i.e. 2D, circular interfaces, extending the idea of Pensée et al. [51] to (zero-stiffness) inclusions *with eigenstresses*. Given an inclusion radius  $a$  and an initial half-opening  $c$  (see Fig. 1.4), this transition is related to the limit of the aspect ratio  $\omega = c/a$  going to zero. As a consequence, the displacement field across the resulting 2D interface becomes discontinuous, and this discontinuity can be quantified as follows: We start from the displacement field in an spheroidal interface inclusion (see Fig. 1.4), which, given the linear strain-displacement relations (1.7), can be derived from the uniform strains  $\underline{\underline{\epsilon}}_i$  prevailing in this inclusion, through

$$\underline{\underline{\xi}}(\underline{\underline{x}}) = \underline{\underline{\epsilon}}_i \cdot \underline{\underline{x}} \quad \forall \underline{\underline{x}} \in \Omega_i \quad (1.31)$$

where  $\Omega_i$  refers to the volume of the inclusion. In order to label the boundary of such an inclusion, we choose cylindrical coordinates for quantifying corresponding location vectors  $\underline{x}$  (see Fig. 1.4),

$$\underline{x} = x \underline{e}_x + y \underline{e}_y + z \underline{e}_z = r \cos \phi \underline{e}_x + r \sin \phi \underline{e}_y + z \underline{e}_z \quad (1.32)$$

so that all points of the upper boundary of the inclusion, denoted as  $\underline{x}^+$ , fulfill

$$\forall \underline{x}^+ \in \partial\Omega_i^+ : \quad z = \omega \sqrt{a^2 - r^2} \quad (1.33)$$

while those at the lower boundary of the inclusion, denoted as  $\underline{x}^-$ , fulfill

$$\forall \underline{x}^- \in \partial\Omega_i^- : \quad z = -\omega \sqrt{a^2 - r^2} \quad (1.34)$$

Relations (1.32), (1.33), and (1.34) allow us to quantify the displacement increment  $\Delta \underline{\xi}_i$  between the upper and the lower inclusion boundary, as

$$\Delta \underline{\xi}_i = \underline{\underline{\xi}}_i \cdot (\underline{x}^+ - \underline{x}^-) = 2 \omega \underline{\underline{\xi}}_i \cdot \underline{e}_z \sqrt{a^2 - r^2} = \Delta \underline{\xi}_i(r) \quad (1.35)$$

where  $\underline{e}_z$  is the unit vector in  $z$ -direction (see Fig. 1.4). Obviously, the displacement increment is not uniform across the inclusion boundary, but depends on the radial coordinate  $r$ , i.e. on the distance from the inclusion center. In order to replace this function by a constant value characterizing the displacement state in the inclusion, we introduce the average displacement increment of the interface phase as

$$\Delta \underline{\underline{\xi}}_i = \frac{1}{a^2 \pi} \int_0^a 2 \omega \underline{\underline{\xi}}_i \cdot \underline{e}_z \sqrt{a^2 - r^2} 2\pi r dr \quad (1.36)$$

In order to solve the integral in (1.36), we use the following substitution:

$$a^2 - r^2 = u^2 \quad (1.37)$$

In order to identify the link between the differentials  $dr$  and  $du$ , we derive the left-hand-side of (1.37) with respect to  $r$ , and the right-hand-side of (1.37) with respect to  $u$  delivering:

$$-2r dr = 2u du \quad \Rightarrow \quad r dr = -u du \quad (1.38)$$

Finally, integration bounds  $r = 0$  and  $r = a$ , see (1.36), are related, by (1.37), to  $u = a$  and  $u = 0$ , respectively. Specifying the integral in (1.36) for (1.37) and

(1.38), while considering the aforementioned integration bounds, yields:

$$\int_0^a \sqrt{a^2 - r^2} r dr = \int_a^0 \sqrt{u^2} (-u du) = \int_a^0 -u^2 du = \left. \frac{-u^3}{3} \right|_a^0 = \frac{a^3}{3} \quad (1.39)$$

Specifying (1.36) for (1.39) yields the average displacement increment as:

$$\Delta \underline{\xi}_i = \frac{4a}{3} \omega \underline{\varepsilon}_i \cdot \underline{e}_z \quad (1.40)$$

Insertion of concentration-influence relation (1.9) into displacement increment expression (1.40) yields

$$\Delta \underline{\xi}_i = \frac{4a}{3} \omega \left( \underline{\underline{A}}_i : \underline{E} + \underline{\underline{D}}_{ii} : \underline{\underline{\sigma}}_i^E \right) \cdot \underline{e}_z \quad (1.41)$$

We now consider the transition from spheroidal inclusions to flat, “sharp” interfaces, through the limit case  $\omega \rightarrow 0$ , so that displacement increment  $\Delta \underline{\xi}_i$  becomes a displacement jump (“dislocation”) across the infinitely thin interface,

$$\begin{aligned} \llbracket \underline{\xi} \rrbracket_i &= \frac{4a}{3} \lim_{\omega \rightarrow 0} \omega \left( \underline{\underline{A}}_i : \underline{E} + \underline{\underline{D}}_{ii} : \underline{\underline{\sigma}}_i^E \right) \cdot \underline{e}_z \\ &= \frac{4a}{3} \left( \lim_{\omega \rightarrow 0} \omega \underline{\underline{A}}_i : \underline{E} + \lim_{\omega \rightarrow 0} \omega \underline{\underline{D}}_{ii} : \underline{\underline{\sigma}}_i^E \right) \cdot \underline{e}_z \\ &= \frac{4a}{3} \left( \underline{\underline{A}}_i^{lim} : \underline{E} + \underline{\underline{D}}_{ii}^{lim} : \underline{\underline{\sigma}}_i^E \right) \cdot \underline{e}_z \end{aligned} \quad (1.42)$$

#### 1.4.2 Concentration and influence tensors, as functions of interface density

Eq. (1.42) highlights the need for calculating the limits  $\lim_{\omega \rightarrow 0} \omega \underline{\underline{A}}_i$  and  $\lim_{\omega \rightarrow 0} \omega \underline{\underline{D}}_{ii}$ . The former limit involves the strain concentration tensor  $\underline{\underline{A}}_i$ , and it follows under consideration of (1.19), (1.20), and (1.26), as well as of the limit rule for products (of tensor components) as

$$\lim_{\omega \rightarrow 0} \omega \underline{\underline{A}}_i = \underline{\underline{A}}_i^{lim} = \underline{\underline{T}}_i : \left[ \underline{\underline{I}} + \frac{4\pi d}{3} \underline{\underline{T}}_i \right]^{-1} \quad (1.43)$$

where we followed Dormieux and Kondo [63] in introducing the notation

$$\underline{\underline{T}}_i = \lim_{\omega \rightarrow 0} \omega \underline{\underline{A}}_i^\infty = \lim_{\omega \rightarrow 0} \omega \left[ \underline{\underline{I}} - \underline{\underline{S}}_i(\omega) \right]^{-1} \quad (1.44)$$

Given flat interfaces with normal vectors pointing in the  $z$ -direction, the non-vanishing components of  $\underline{\underline{T}}_i$  follow from specification of (1.44) for (1.21) as

$$\left. \begin{aligned} T_{i,xzzz} = T_{i,zzxz} = T_{i,xzzx} = T_{i,zzxx} \\ T_{i,yzyz} = T_{i,zyyz} = T_{i,yzzy} = T_{i,zyzy} \end{aligned} \right\} = \frac{2(1-\nu_s)}{\pi(2-\nu_s)} \quad (1.45)$$

$$\left. \begin{aligned} T_{i,zzxx} \\ T_{i,zzyy} \end{aligned} \right\} = \frac{4\nu_s(1-\nu_s)}{\pi(1-2\nu_s)} \quad (1.46)$$

$$T_{i,zzzz} = \frac{4(1-\nu_s)^2}{\pi(1-2\nu_s)} \quad (1.47)$$

For the limit case operation (1.43)-(1.47), the volume fraction of the interface phase was considered as

$$f_i = \frac{\mathcal{N}}{\Omega} \frac{4\pi}{3} a^2 c = \frac{4\pi}{3} d \omega, \quad f_s = 1 - f_i \quad (1.48)$$

In (1.48),  $(4\pi/3)a^2c$  stands for the volume of one spheroidal interface,  $\mathcal{N}$  denotes the number of single interfaces inside the volume  $\Omega$  of the RVE, and  $d$  denotes the interface density parameter, defined in analogy to the crack density parameter [64, 65], as

$$d = \frac{\mathcal{N}a^3}{\Omega} \quad (1.49)$$

Thanks to the tensor definition (1.44), to volume fraction expressions (1.48), and to the result  $\lim_{\omega \rightarrow 0} \omega \underline{\underline{A}}_i^\infty : \underline{\underline{P}}_i = \underline{\underline{C}}_s^{-1} : \underline{\underline{T}}_i^t$  (see Appendix. A for the related proof), the influence tensor limit,  $\lim_{\omega \rightarrow 0} \omega \underline{\underline{D}}_{ii}$  follows from (1.27) as

$$\lim_{\omega \rightarrow 0} \omega \underline{\underline{D}}_{ii} = \underline{\underline{D}}_{ii}^{lim} = -\underline{\underline{A}}_s : \underline{\underline{C}}_s^{-1} : \underline{\underline{T}}_i^t \quad (1.50)$$

The non-vanishing components of this influence tensor  $\underline{\underline{D}}_{ii}^{lim}$  read as

$$\begin{aligned} D_{ii,xzzz}^{lim} = D_{ii,zzxz}^{lim} = D_{ii,xzzx}^{lim} = D_{ii,zzxx}^{lim} = D_{ii,yzyz}^{lim} = D_{ii,yzzy}^{lim} = \\ = D_{ii,zzyz}^{lim} = D_{ii,zyyz}^{lim} = -\frac{6(1-\nu_s^2)}{E_s \pi [3(2-\nu_s) + 16d(1-\nu_s)]} \end{aligned} \quad (1.51)$$

and

$$D_{ii,zzzz}^{lim} = -\frac{12(1-\nu_s^2)(1-2\nu_s)}{E_s \pi [3(1-2\nu_s) + 16d(1-\nu_s)^2]} \quad (1.52)$$

It follows from the format of the influence tensor components (1.51) and (1.52) that the displacement jump expression (1.42) involves only three components of the eigenstress tensor, namely  $\sigma_{i,zz}^E = \sigma_{i,xz}^E$ ,  $\sigma_{i,zy}^E = \sigma_{i,yz}^E$ , and  $\sigma_{i,zz}^E$ . These components build up an eigentraction vector  $\underline{T}_i^E$  according to

$$\underline{T}_i^E = \underline{\underline{\sigma}}_i^E \cdot \underline{e}_z \quad (1.53)$$

This provides the motivation to replace  $\underline{\underline{D}}_{ii}^{lim}$  in (1.42) by a second-order influence tensor  $\underline{\underline{D}}_{ii}^{lim}$  in the format

$$\frac{4a}{3} \left( \underline{\underline{D}}_{ii}^{lim} : \underline{\underline{\sigma}}_i^E \right) \cdot \underline{e}_z = \underline{\underline{D}}_{ii}^{lim} \cdot \underline{T}_i^E \quad (1.54)$$

The non-vanishing components of  $\underline{\underline{D}}_{ii}^{lim}$  read as

$$D_{ii,xx}^{lim} = D_{ii,yy}^{lim} = -\frac{16(1-\nu_s^2)a}{E_s \pi [3(2-\nu_s) + 16d(1-\nu_s)]}, \quad (1.55)$$

$$D_{ii,zz}^{lim} = -\frac{16(1-\nu_s^2)(1-2\nu_s)a}{E_s \pi [3(1-2\nu_s) + 16d(1-\nu_s)^2]} \quad (1.56)$$

By analogy to (1.53) and (1.54), we replace  $\underline{\underline{A}}_i^{lim}$  in (1.42) by a third-order concentration tensor  $\underline{\underline{A}}_i^{lim}$ , describing the influence of macrostrain  $\underline{E}$  on the average displacement jumps  $[[\xi]]_i$ , as

$$\frac{4a}{3} \left( \underline{\underline{A}}_i^{lim} : \underline{E} \right) \cdot \underline{e}_z = \underline{\underline{A}}_i^{lim} : \underline{E} \quad (1.57)$$

The non-vanishing components of  $\underline{\underline{A}}_i^{lim}$  read as

$$A_{i,xxz}^{lim} = A_{i,xxx}^{lim} = A_{i,yyz}^{lim} = A_{i,yzy}^{lim} = \frac{8(1-\nu_s)a}{\pi [3(2-\nu_s) + 16d(1-\nu_s)]} \quad (1.58)$$

$$A_{i,zzx}^{lim} = A_{i,zyy}^{lim} = \frac{16\nu_s(1-\nu_s)a}{\pi [3(1-2\nu_s) + 16d(1-\nu_s)^2]} \quad (1.59)$$

$$A_{i,zzz}^{lim} = \frac{1-\nu_s}{\nu_s} A_{i,xxx}^{lim} \quad (1.60)$$

Concentration and influence tensors  $\underline{\underline{A}}_i^{lim}$  and  $\underline{\underline{D}}_{ii}^{lim}$  allow for rewriting the concentration-influence relation (1.42) in the format

$$[[\xi]]_i = \underline{\underline{A}}_i^{lim} : \underline{E} + \underline{\underline{D}}_{ii}^{lim} \cdot \underline{T}_i^E \quad (1.61)$$

### 1.4.3 Homogenized stiffness and Biot tensors

When it comes to the macroscopic elasticity law (1.17), we need to evaluate the limit  $\omega \rightarrow 0$  for the homogenized stiffness  $\underline{\underline{C}}_{hom}$ . It follows from (1.15), (1.19), (1.20), (1.27), and (1.48), when considering (1.44), that

$$\lim_{\omega \rightarrow 0} \underline{\underline{C}}_{hom} = \underline{\underline{C}}_{hom}^{lim} = \underline{\underline{C}}_s : \left[ \underline{\underline{I}} + \frac{4\pi d}{3} \underline{\underline{T}}_i \right]^{-1} \quad (1.62)$$

In analogy to the new tensor definitions (1.54) and (1.57), we define a third-order tensor  $\underline{\underline{B}}_i^{lim}$  (in analogy to the ‘‘Biot tensor’’ in poroelasticity [59, 66]) describing the effect of the eigentraction vector  $\underline{\underline{T}}_i^E$  on the macrostress  $\underline{\underline{\Sigma}}$ . Under consideration of the limit  $\omega \rightarrow 0$ , and of  $\underline{\underline{\sigma}}_i^E : \underline{\underline{A}}_i = (\underline{\underline{\sigma}}_i^E : \underline{\underline{A}}_i)^t = \underline{\underline{A}}_i^t : \underline{\underline{\sigma}}_i^{f,t} = \underline{\underline{A}}_i^t : \underline{\underline{\sigma}}_i^E$  it follows that

$$\lim_{\omega \rightarrow 0} \left[ \frac{4\pi d}{3} \omega \underline{\underline{A}}_i^t : \underline{\underline{\sigma}}_i^E \right] = \underline{\underline{B}}_i^{lim} \cdot \underline{\underline{T}}_i^E \quad (1.63)$$

The non-vanishing components of  $\underline{\underline{B}}_i^{lim}$  read as

$$B_{i,xxx}^{lim} = B_{i,xzx}^{lim} = B_{i,zyy}^{lim} = B_{i,yzy}^{lim} = \frac{16d(1-\nu_s)}{3(2-\nu_s) + 16d(1-\nu_s)} \quad (1.64)$$

$$B_{i,xxz}^{lim} = B_{i,yyz}^{lim} = -\frac{16d\nu_s(1-\nu_s)}{3(1-2\nu_s) + 16d(1-\nu_s)^2} \quad (1.65)$$

$$B_{i,zzz}^{lim} = \frac{16d(1-\nu_s)^2}{3(1-2\nu_s) + 16d(1-\nu_s)^2} \quad (1.66)$$

Stiffness tensor (1.62) and ‘‘Biot tensor’’ (1.63)-(1.66) allow for re-formulation of the macroscopic state equation (1.17) in the following format

$$\underline{\underline{\Sigma}} = \underline{\underline{C}}_{hom}^{lim} : \underline{\underline{E}} + \underline{\underline{B}}_i^{lim} \cdot \underline{\underline{T}}_i^E \quad (1.67)$$

### 1.4.4 Macrostress-related concentration and influence relations

We now consider that a material with eigenstressed interfaces is subjected to a given macroscopic stress state  $\underline{\underline{\Sigma}}$ , such that the macrostrain  $\underline{\underline{E}}$  is a dependent quantity. This is the motivation for solving state equation (1.67) for  $\underline{\underline{E}}$

$$\begin{aligned} \underline{\underline{E}} &= (\underline{\underline{C}}_{hom}^{lim})^{-1} : \underline{\underline{\Sigma}} - (\underline{\underline{C}}_{hom}^{lim})^{-1} : \underline{\underline{B}}_i^{lim} \cdot \underline{\underline{T}}_i^E \\ &= (\underline{\underline{C}}_{hom}^{lim})^{-1} : \underline{\underline{\Sigma}} - \underline{\underline{B}}_i^{\Sigma,lim} \cdot \underline{\underline{T}}_i^E \end{aligned} \quad (1.68)$$

where we introduced a third-order influence tensor  $\underline{\underline{B}}_i^{\Sigma,lim}$  describing the influence of eigentraction vector  $\underline{T}_i^E$  on the macrostrains  $\underline{E}$ ,

$$\underline{\underline{B}}_i^{\Sigma,lim} = (\underline{\underline{C}}_{hom}^{lim})^{-1} : \underline{\underline{B}}_i^{lim} \quad (1.69)$$

The non-vanishing components of  $\underline{\underline{B}}_i^{\Sigma,lim}$  read as

$$B_{i,zzx}^{\Sigma,lim} = B_{i,xzx}^{\Sigma,lim} = B_{i,zyy}^{\Sigma,lim} = B_{i,yzy}^{\Sigma,lim} = \frac{16 d (1 - \nu_s^2)}{3 E_s (2 - \nu_s)} \quad (1.70)$$

$$B_{i,zzz}^{\Sigma,lim} = \frac{16 d (1 - \nu_s^2)}{3 E_s} \quad (1.71)$$

Subsequently, we use the expression (1.68) to replace  $\underline{E}$ , in the concentration-influence relation (1.61), by  $\underline{\underline{\Sigma}}$ , which results in the relation

$$\begin{aligned} \llbracket \xi \rrbracket_i &= \underline{\underline{A}}_i^{lim} : (\underline{\underline{C}}_{hom}^{lim})^{-1} : \underline{\underline{\Sigma}} + \left( \underline{\underline{D}}_{ii}^{lim} - \underline{\underline{A}}_i^{lim} : \underline{\underline{B}}_i^{\Sigma,lim} \right) \cdot \underline{T}_i^E \\ &= \underline{\underline{A}}_i^{\Sigma,lim} : \underline{\underline{\Sigma}} + \underline{\underline{D}}_{ii}^{\Sigma,lim} \cdot \underline{T}_i^E \end{aligned} \quad (1.72)$$

where we introduced the third-order influence tensor  $\underline{\underline{A}}_i^{\Sigma,lim}$  describing the influence of macrostress  $\underline{\underline{\Sigma}}$  on the average displacement jumps  $\llbracket \xi \rrbracket_i$

$$\underline{\underline{A}}_i^{\Sigma,lim} = \underline{\underline{A}}_i^{lim} : (\underline{\underline{C}}_{hom}^{lim})^{-1} \quad (1.73)$$

The non-vanishing components of  $\underline{\underline{A}}_i^{\Sigma,lim}$  read as

$$\begin{aligned} A_{i,xzx}^{\Sigma,lim} = A_{i,xzx}^{\Sigma,lim} = A_{i,yyz}^{\Sigma,lim} = A_{i,yzy}^{\Sigma,lim} &= \frac{16 a (1 - \nu_s^2)}{3 \pi E_s (2 - \nu_s)}, \\ A_{i,zzz}^{\Sigma,lim} &= \frac{16 a (1 - \nu_s^2)}{3 \pi E_s} \end{aligned} \quad (1.74)$$

Furthermore, we introduced, in (1.72), the second-order influence tensor  $\underline{\underline{D}}_{ii}^{\Sigma,lim}$  describing the influence of  $\underline{T}_i^E$  on the average displacement jump  $\llbracket \xi \rrbracket_i$

$$\underline{\underline{D}}_{ii}^{\Sigma,lim} = \underline{\underline{D}}_{ii}^{lim} - \underline{\underline{A}}_i^{lim} : \underline{\underline{B}}_i^{\Sigma,lim} \quad (1.75)$$

The non-vanishing components of  $\underline{\underline{D}}_{ii}^{\Sigma,lim}$  read as

$$D_{ii,xx}^{\Sigma,lim} = D_{ii,yy}^{\Sigma,lim} = -\frac{16 a (1 - \nu_s^2)}{3 \pi E_s (2 - \nu_s)}, \quad D_{ii,zz}^{\Sigma,lim} = -\frac{16 a (1 - \nu_s^2)}{3 \pi E_s} \quad (1.76)$$

Eqs. (1.68) and (1.72), together with (1.69)-(1.71) and (1.73)-(1.76), are well-suited to study macroscopic creep of microheterogeneous materials comprising eigenstressed interfaces.

## 1.5 Upscaling from viscous interfaces to creeping materials

### 1.5.1 Interface behavior

So far, the forces and deformations of the interface phase, quantified through traction force  $\underline{T}_i^E$  and displacement jump  $[[\xi]]_i$ , have been introduced independently from each other. Now is the time to define the constitutive behavior of the interface phase:

- In normal direction  $\underline{e}_z$ , we consider that molecular ordering-related joining forces prevent the interfaces from opening (or closing):

$$[[\xi_z]]_i = 0 \quad (1.77)$$

Eq. (1.77) is referred to as a “glueing condition”.

- The tangential components of the traction force drive, in a linear viscous behavior, the tangential displacement jump rates,

$$\eta [[\dot{\xi}_\alpha]]_i = T_{i,\alpha} \quad \alpha = x, y \quad (1.78)$$

where  $\eta$  denotes a viscosity constant with physical dimension [Stress×Time/Length], and where a dot stands for the partial derivative with respect to time  $t$

$$\dot{\bullet} = \frac{\partial \bullet}{\partial t} \quad (1.79)$$

Specifying the concentration-influence relations (1.61) and (1.72), respectively, for interface properties (1.77) and (1.78), results in partial differential equations for the time-evolution of the in-plane displacement jumps. This will be detailed in

the sequel, where we consider matrix-inclusion composites containing parallel fluid-filled interfaces, and where we investigate how anisotropic local interface properties (1.77) and (1.78) influence the macroscopic material behavior.

### 1.5.2 Macroscopic viscoelasticity I: relaxation

The RVE of Fig. 1.2(a) with isotropic elastic matrix and viscous interfaces according to (1.77) and (1.78) is considered to be subjected (at time  $t = 0$ ) to a general three-dimensional strain state which is kept constant (time-independent) thereafter ( $t > 0$ ):

$$\underline{\underline{E}} = \sum_{j=x,y,z} \sum_{k=x,y,z} E_{jk} \underline{e}_j \otimes \underline{e}_k, \quad (1.80)$$

with symmetries  $E_{jk} = E_{kj}$  and where  $\underline{e}_x, \underline{e}_y$ , and  $\underline{e}_z$  stand for the Cartesian unit base vectors according to Fig. 1.2. Specification of concentration-influence relation (1.61) for (1.58)-(1.60) and (1.55)-(1.56) delivers the following components of the average displacement jumps

$$\llbracket \xi_\alpha \rrbracket_i = \frac{16(1-\nu_s)a}{\pi[3(2-\nu_s)+16d(1-\nu_s)]} \left[ E_{\alpha z} - \frac{(1+\nu_s)}{E_s} T_{i,\alpha} \right], \quad \alpha = x, y \quad (1.81)$$

$$\begin{aligned} \llbracket \xi_z \rrbracket_i &= \frac{16(1-\nu_s)a}{\pi[3(1-2\nu_s)+16d(1-\nu_s)^2]} \times \\ &\times \left[ \nu_s(E_{xx} + E_{yy}) + (1-\nu_s)E_{zz} - \frac{(1+\nu_s)(1-2\nu_s)}{E_s} T_{i,z} \right] \end{aligned} \quad (1.82)$$

Eq. (1.81) shows that the average in-plane displacement jumps depend on corresponding shear components of both the macrostrain tensor and the interface traction vector. Eq. (1.82) shows that the average out-of-plane displacement jump is a function of all three macroscopic normal strain components as well as of the normal components of the interface traction vectors. Specifying (1.82) for the out-of-plane glueing condition (1.77), as well as (1.81) for in-plane viscous interface behavior (1.78), and rearranging terms in the resulting expressions yields

$$\llbracket \dot{\xi}_\alpha \rrbracket_i + \frac{E_s \pi [3(2-\nu_s) + 16d(1-\nu_s)]}{16a\eta(1-\nu_s^2)} \llbracket \xi_\alpha \rrbracket_i = \frac{E_s}{\eta(1+\nu_s)} E_{\alpha z}, \quad \alpha = x, y \quad (1.83)$$

$$\llbracket \xi_z \rrbracket_i = 0 \Rightarrow T_{i,z} = \frac{E_s}{(1+\nu_s)(1-2\nu_s)} \left[ \nu_s(E_{xx} + E_{yy}) + (1-\nu_s)E_{zz} \right] \quad (1.84)$$

Eq. (1.83) represents two viscosity-related, ordinary, first-order, inhomogeneous differential equations with constant coefficients, for the time-evolution of the average in-plane displacement jumps. Eq. (1.84) shows a glueing condition-related

link between the macroloading (in terms of  $E_{xx}$ ,  $E_{yy}$ , and  $E_{zz}$ ) and the normal components of the interface interface traction vector,  $T_{i,z}$ . Considering the initial condition ( $[[\xi]]_i = 0$  for  $t = 0$ ), the solution for the average in-plane displacement jumps follows from (1.83) as:

$$[[\xi_\alpha]]_i(t) = [[\xi_{relax}]]_i^\infty \times \left[ 1 - \exp\left(-\frac{t}{\tau_{relax}}\right) \right], \quad \alpha = x, y \quad (1.85)$$

with the asymptotically reached displacement jump or dislocation reading as

$$[[\xi_{relax}]]_i^\infty = \frac{16(1 - \nu_s) a E_{\alpha z}}{\pi [3(2 - \nu_s) + 16d(1 - \nu_s)]} \quad (1.86)$$

and with the characteristic relaxation time  $\tau_{relax}$  reading as

$$\tau_{relax} = \frac{a \eta}{E_s} \frac{16(1 - \nu_s^2)}{\pi [3(2 - \nu_s) + 16d(1 - \nu_s)]} \quad (1.87)$$

According to (1.85), together with (1.86) and (1.87), the micromechanical model of Fig. 1.2(a) with linearly viscous interfaces entails an increase of in-plane displacement jumps with increasing time, up to an asymptotic value which increases with increasing interface radius  $a$ , with increasing macroscopic shear strain  $E_{\alpha z}$ , with decreasing interface density  $d$ , and with decreasing Poisson's ratio of the solid matrix,  $\nu_s$ , see Fig. 5 for dimensionless evaluations.

It follows from the characteristic time (1.87), together with the exponent in (1.85), that the asymptotic displacement jump is reached the faster, the larger both the interface density  $d$  and the Young's modulus of the solid matrix,  $E_s$ , as well as the smaller both the interface radius  $a$  and the viscosity constant  $\eta$ . The influence of Poisson's ratio  $\nu_s$  depends on the value of the interfaces density parameter, i.e. for interface densities larger than  $9/16 = 0.5625$ , the asymptotic displacement jump is reached the faster, the smaller Poisson's ratio of the solid matrix. For smaller interface densities, the asymptotic displacement jump is reached the slower, the closer Poisson's ratio is to the value  $[2(3 + 8d) - \sqrt{3(9 + 32d)}]/(3 + 16d)$ .

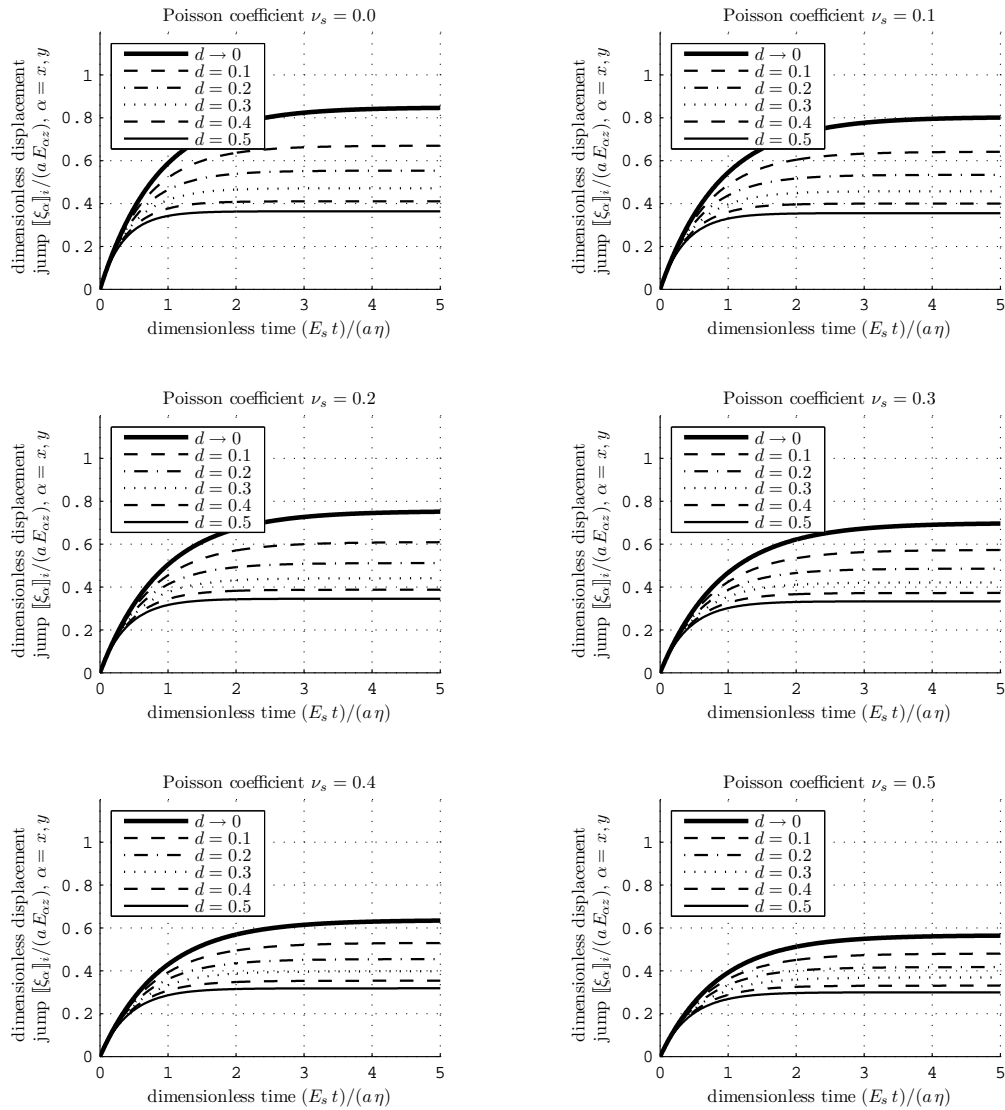


Figure 1.5: Evolution of dimensionless microscopic average displacement jumps with dimensionless time: results of sensitivity analysis regarding Poisson's ratio of the matrix,  $\nu_s$ , and the interface density parameter  $d$

The time-evolutions (relaxation) of the interface shear traction components follow from insertion of the temporal derivative of (1.85), together with (1.86) and (1.87), into (1.78), as

$$T_{i,\alpha}(t) = \frac{E_s}{(1 + \nu_s)} E_{\alpha z} \exp\left(-\frac{t}{\tau_{relax}}\right), \quad \alpha = x, y \quad (1.88)$$

with the relaxation time still following (1.87). It follows from (1.88) that  $T_{i,\alpha}$  decreases exponentially with increasing time, starting from the initial value  $E_s E_{\alpha z} / (1 + \nu_s)$  at  $t = 0$ , down to zero, which is the asymptotic value reached after infinite time, see Fig. 6.

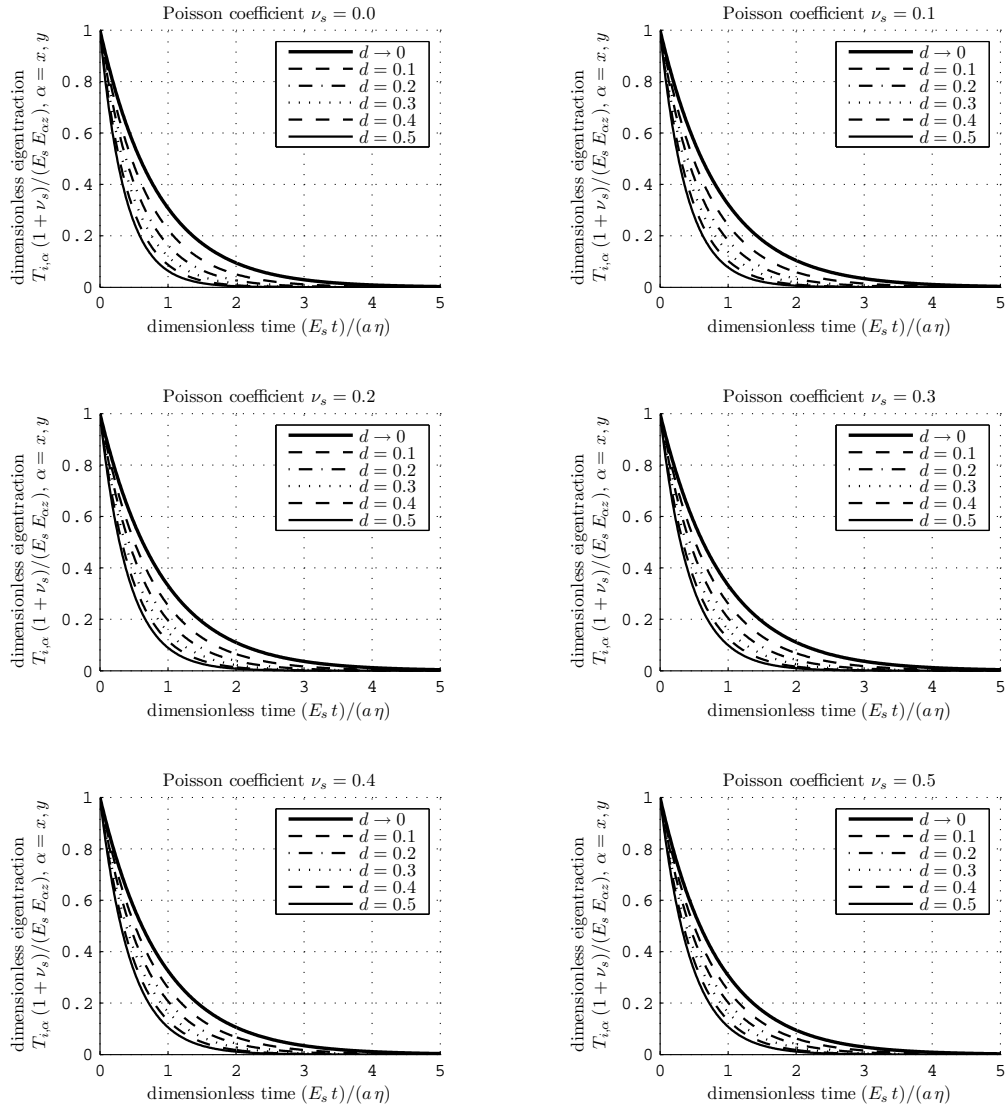


Figure 1.6: Evolution of dimensionless interface shear traction with dimensionless time: results of sensitivity analysis regarding Poisson's ratio of the matrix,  $\nu_s$ , and the interface density parameter  $d$

In order to study the macroscopic stress relaxation, we evaluate (1.67) for (1.62), (1.4), (1.5), and (1.45)-(1.47) as well as for (1.64)-(1.66), yielding

$$\begin{aligned}\Sigma_{xx} &= \frac{E_s [(1 - \nu_s) (3 + 16 d) E_{xx} + \nu_s [3 + 16 d(1 - \nu_s)] E_{yy} + 3 \nu_s E_{zz}]}{(1 + \nu_s) [3(1 - 2 \nu_s) + 16 d(1 - \nu_s)^2]} \\ &+ \frac{16 d \nu_s (1 - \nu_s) T_{i,z}}{3(1 - 2 \nu_s) + 16 d(1 - \nu_s)^2}\end{aligned}\quad (1.89)$$

$$\begin{aligned}\Sigma_{yy} &= \frac{E_s [\nu_s (3 + 16 d(1 - \nu_s)) E_{xx} + (1 - \nu_s) (3 + 16 d) E_{yy} + 3 \nu_s E_{zz}]}{(1 + \nu_s) [3(1 - 2 \nu_s) + 16 d(1 - \nu_s)^2]} \\ &+ \frac{16 d \nu_s (1 - \nu_s) T_{i,z}}{3(1 - 2 \nu_s) + 16 d(1 - \nu_s)^2}\end{aligned}\quad (1.90)$$

$$\Sigma_{zz} = \frac{3 E_s [\nu_s (E_{xx} + E_{yy}) + (1 - \nu_s) E_{zz}]}{(1 + \nu_s) [3(1 - 2 \nu_s) + 16 d(1 - \nu_s)^2]} + \frac{16 d(1 - \nu_s)^2 T_{i,z}}{3(1 - 2 \nu_s) + 16 d(1 - \nu_s)^2}\quad (1.91)$$

$$\Sigma_{xy} = \frac{E_s E_{xy}}{1 + \nu_s}\quad (1.92)$$

$$\Sigma_{\alpha z} = \frac{E_s 3(2 - \nu_s) E_{\alpha z}}{(1 + \nu_s) [3(2 - \nu_s) + 16 d(1 - \nu_s)]} + \frac{16 d(1 - \nu_s) T_{i,\alpha}}{3(2 - \nu_s) + 16 d(1 - \nu_s)}, \alpha = x, y \quad (1.93)$$

It follows from Eqs. (1.89)-(1.93) that all macrostress components except  $\Sigma_{xy}$  are influenced by the interfaces. Specification of (1.89)-(1.91) for the glueing condition-related value of  $T_{i,z}$  according to (1.84), as well as of (1.93) for the time-evolutions of  $T_{i,x}(t)$  and  $T_{i,y}(t)$  according to (1.88) yields

$$\Sigma_{xx} = \frac{E_s [(1 - \nu_s) E_{xx} + \nu_s (E_{yy} + E_{zz})]}{(1 + \nu_s)(1 - 2 \nu_s)}\quad (1.94)$$

$$\Sigma_{yy} = \frac{E_s [(1 - \nu_s) E_{yy} + \nu_s (E_{xx} + E_{zz})]}{(1 + \nu_s)(1 - 2 \nu_s)}\quad (1.95)$$

$$\Sigma_{zz} = \frac{E_s [(1 - \nu_s) E_{zz} + \nu_s (E_{xx} + E_{yy})]}{(1 + \nu_s)(1 - 2 \nu_s)}\quad (1.96)$$

$$\Sigma_{xy} = \frac{E_s E_{xy}}{1 + \nu_s}\quad (1.97)$$

as well as

$$\Sigma_{\alpha z}(t) = \Sigma^0 - \Delta \Sigma^\infty \times \left[ 1 - \exp\left(-\frac{t}{\tau_{relax}}\right) \right], \quad \alpha = x, y \quad (1.98)$$

with the relaxation time still following (1.87), while the initial macrostress  $\Sigma^0$  and the asymptotically relaxed stress increment  $\Delta \Sigma^\infty$  read as

$$\Sigma^0 = \frac{E_s E_{\alpha z}}{1 + \nu_s} \quad \Delta \Sigma^\infty = \Sigma^0 \frac{16 d(1 - \nu_s)}{3(2 - \nu_s) + 16 d(1 - \nu_s)}\quad (1.99)$$

Eqs. (1.84) and (1.96) entail that  $T_{i,z} = \Sigma_{zz}$ , i.e. that the microscopic field of the normal stress component in  $z$ -direction is, at any time  $t$ , uniform, including  $\sigma_{s,zz}(\underline{x}) = \Sigma_{zz}$ ,  $\forall \underline{x} \in \Omega_s$ . As a consequence, all the macroscopic normal stress components are independent of the interfaces, see (1.94)-(1.96). In addition, Eqs.

(1.88) and (1.98) show that under sudden load increase at  $t = 0$ , the interface tractions result (only at that time instant) in an entirely uniform microscopic stress field  $\underline{\underline{\sigma}}_s(\underline{x}, t = 0) = \underline{\underline{\Sigma}}, \forall \underline{x} \in \Omega_s$ , and  $\underline{T}_i(t = 0) = \underline{\underline{\Sigma}} \cdot \underline{e}_z$ , such that the material behaves macroscopically as if no interfaces would exist. With progress of time, the average displacement jumps (1.85) increase with decelerating speed, such that interface shear traction components (1.88) progressively decrease, resulting in a monotonous decrease (relaxation) of the shear macrostress components (1.98), until an asymptotic value is reached, see Fig. 7. The intensity of stress relaxation increases with increasing interface density  $d$  and with decreasing Poisson's ratio of the solid. The relaxation behavior of the material system of Figure 1.2(a) can be quantified also in a general format, by means of the fourth-order relaxation tensor  $\underline{\underline{\underline{R}}}$ , with only four time-dependent components, namely

$$R_{\alpha z \alpha z} = R_{\alpha z z \alpha} = R_{z \alpha \alpha z} = R_{z \alpha z \alpha} = \frac{\Sigma^0}{2 E_{\alpha z}} - \frac{\Delta \Sigma^\infty}{2 E_{\alpha z}} \times \left[ 1 - \exp\left(-\frac{t}{\tau_{relax}}\right) \right], \alpha = x, y \quad (1.100)$$

with  $\Sigma^0$  and  $\Delta \Sigma^\infty$  still following from (1.99). All other relaxation tensor components are identical to the components of the solid stiffness tensor,  $R_{ijkl} = C_{s,ijkl}$ . Also, for infinite viscosity,  $\eta \rightarrow \infty$  in Eq. (1.100), the time dependency in the relaxation function is lost; then, the material system behaves just identical to the elastic solid matrix.

### 1.5.3 Macroscopic viscoelasticity II: creep

The RVE of Fig. 1.2(a) is considered to be subjected (at time  $t = 0$ ) to a general three dimensional stress state which is kept constant (time-independent) thereafter ( $t > 0$ ):

$$\underline{\underline{\Sigma}} = \sum_{j=x,y,z} \sum_{k=x,y,z} \Sigma_{jk} \underline{e}_j \otimes \underline{e}_k, \quad (1.101)$$

with symmetries  $\Sigma_{jk} = \Sigma_{kj}$ . Specification of concentration-influence relation (1.72) for (1.74) and (1.76) delivers the following components of the average displacement jumps

$$\llbracket \xi_\alpha \rrbracket_i = \frac{16(1-\nu_s^2)a}{3\pi E_s(2-\nu_s)} [\Sigma_{\alpha z} - T_{i,\alpha}], \quad \alpha = x, y \quad (1.102)$$

$$\llbracket \xi_z \rrbracket_i = \frac{16(1-\nu_s^2)a}{3\pi E_s} [\Sigma_{zz} - T_{i,z}] \quad (1.103)$$

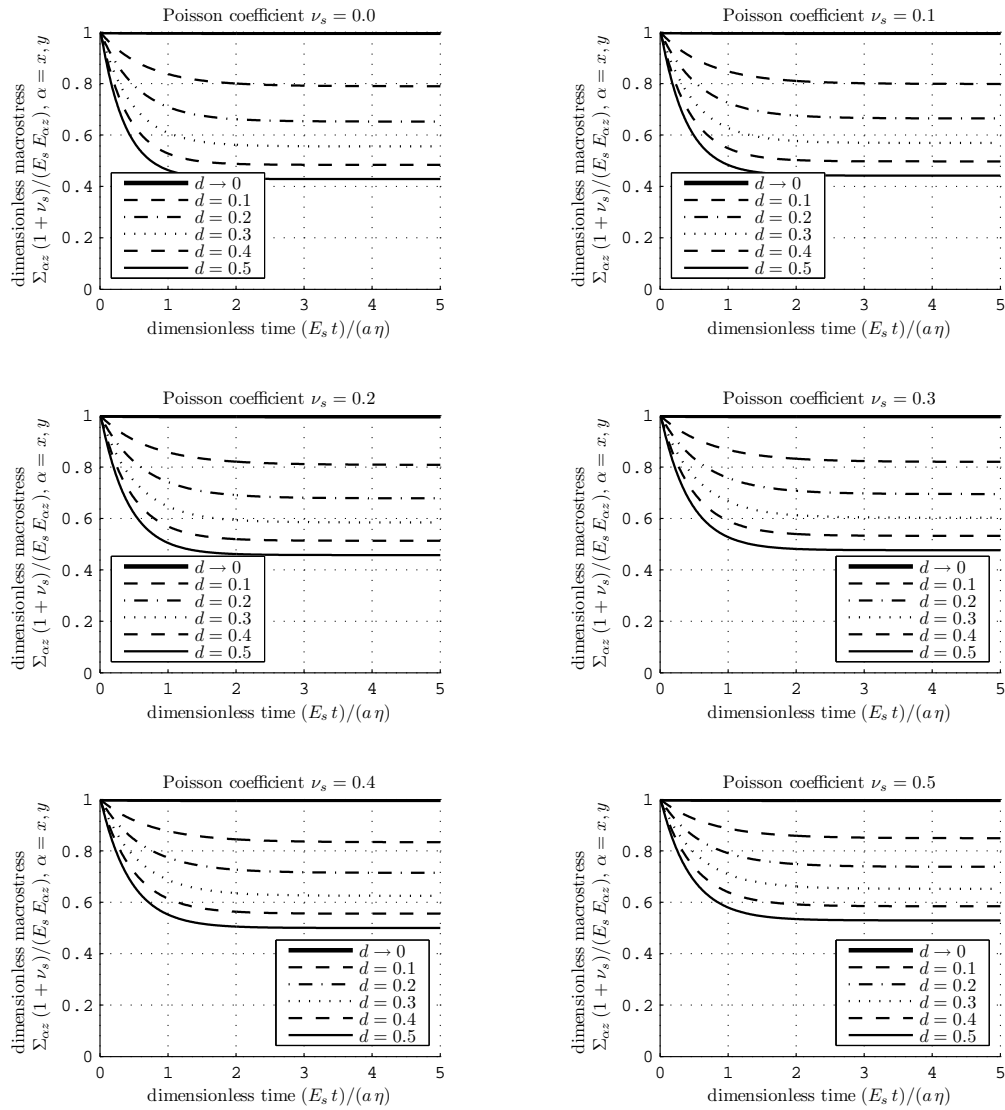


Figure 1.7: Evolution of dimensionless macroscopic shear stress with dimensionless time: results of sensitivity analysis regarding Poisson's ratio of the matrix,  $\nu_s$ , and the interface density parameter  $d$

Eqs. (1.102)-(1.103) imply that the average in-plane displacement jumps depend on corresponding shear components both of the macrostress and of the interface traction vector. The average out-of-plane displacement jump is a function of the macroscopic normal stress component aligned with the normal to the interface as well as of the normal component of the interface traction vectors. Specifying (1.103) for the out-of-plane glueing condition (1.77), as well as (1.102) for in-plane viscous interface behavior (1.78), and rearranging terms in the resulting expression

yields

$$\llbracket \dot{\xi}_\alpha \rrbracket_i + \frac{3 E_s \pi (2 - \nu_s)}{16 a \eta (1 - \nu_s^2)} \llbracket \xi_\alpha \rrbracket_i = \frac{1}{\eta} \Sigma_{\alpha z}, \quad \alpha = x, y \quad (1.104)$$

$$\llbracket \xi_z \rrbracket_i = 0 \quad \Rightarrow \quad T_{i,z} = \Sigma_{zz} \quad (1.105)$$

Eqs. (1.104)-(1.105) contain two viscosity-related ordinary, first-order, inhomogeneous differential equations with constant coefficients for the time-evolution of the average in-plane displacement jumps, and a glueing condition-related link between the macroloading  $\Sigma_{zz}$  and the normal component of the interface traction vector  $T_{i,z}$ . Considering the initial condition ( $\llbracket \xi \rrbracket_i = 0$  for  $t = 0$ ), the solution for the average in-plane displacement jumps follows from (1.104) as:

$$\llbracket \xi_\alpha \rrbracket_i(t) = \llbracket \xi_{creep} \rrbracket_i^\infty \times \left[ 1 - \exp\left(-\frac{t}{\tau_{creep}}\right) \right], \quad \alpha = x, y \quad (1.106)$$

with the asymptotically reached displacement jump or dislocation reading as

$$\llbracket \xi_{creep} \rrbracket_i^\infty = \frac{16 (1 - \nu_s^2) a \Sigma_{\alpha z}}{3 \pi E_s (2 - \nu_s)} \quad (1.107)$$

and with the characteristic relaxation time  $\tau_{creep}$  reading as

$$\tau_{creep} = \frac{a \eta}{E_s} \frac{16 (1 - \nu_s^2)}{3 \pi (2 - \nu_s)} \quad (1.108)$$

Eq. (1.106), together with (1.107) and (1.108), implies an increase of in-plane displacement jumps with increasing time, up to an asymptotic value which increases with increasing shear macrostress  $\Sigma_{\alpha z}$ , with increasing interface radius  $a$ , and with decreasing Young's modulus of the solid (see Fig. 1.8). As for the influence of Poisson's ratio of the solid, the model implies that the asymptotic displacement jump value is the larger, the closer  $\nu_s$  to the value  $2 - \sqrt{3} = 0.268$ .

The characteristic relaxation time (1.108) together with the exponent in (1.106) implies that the asymptotic value is reached the faster, the larger Young's modulus of the solid,  $E_s$ , the smaller the interface radius  $a$  and the viscosity constant  $\eta$ , as well as the larger the distance of Poisson's ratio of the solid,  $\nu_s$ , from the numerical value  $2 - \sqrt{3} = 0.268$ . The model suggests that the interface density has no influence on the speed of creep.

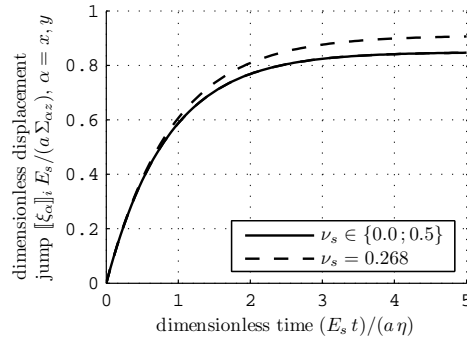


Figure 1.8: Evolution of dimensionless microscopic average displacement jump with dimensionless time: results of sensitivity analysis regarding Poisson's ratio of the matrix,  $\nu_s$

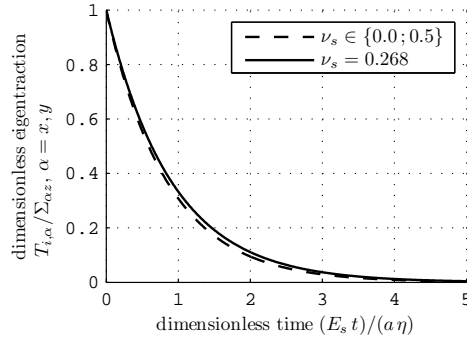


Figure 1.9: Evolution of dimensionless interface shear traction with dimensionless time: results of sensitivity analysis regarding Poisson's ratio of the matrix,  $\nu_s$

The time-evolutions (relaxation) of the interface shear traction components follow from insertion of the temporal derivative of (1.106) into (1.78), as

$$T_{i,\alpha}(t) = \Sigma_{\alpha z} \left[ \exp \left( -\frac{t}{\tau_{creep}} \right) \right], \alpha = x, y \quad (1.109)$$

with the characteristic creep time still following (1.108). Eq. (1.109) together with (1.108), implies that  $T_{i,\alpha}$  decreases with increasing time, starting from  $\Sigma_{\alpha z}$  at  $t = 0$ , down to zero which is the asymptotic value reached after infinite time (see Fig. 9).

Specification of the macroscopic elasticity law (1.68) for (1.62), (1.4), (1.5), and (1.45)-(1.47) as well as for (1.70)-(1.71), yields

$$E_{xx} = \frac{\Sigma_{xx} - \nu_s (\Sigma_{yy} + \Sigma_{zz})}{E_s} \quad (1.110)$$

$$E_{yy} = \frac{\Sigma_{yy} - \nu_s (\Sigma_{xx} + \Sigma_{zz})}{E_s} \quad (1.111)$$

$$E_{zz} = -\frac{3\nu_s (\Sigma_{xx} + \Sigma_{yy}) + (16d(1 - \nu_s^2) + 3)\Sigma_{zz}}{3E_s} - \frac{16d(1 - \nu_s^2)T_{i,z}}{3E_s} \quad (1.112)$$

$$E_{xy} = \frac{(1 + \nu_s)\Sigma_{xy}}{E_s} \quad (1.113)$$

$$E_{\alpha z} = \frac{(1 + \nu_s)[3(2 - \nu_s) + 16d(1 - \nu_s)]\Sigma_{\alpha z}}{3E_s(2 - \nu_s)} - \frac{16d(1 - \nu_s^2)T_{i,\alpha}}{3E_s(2 - \nu)}, \alpha = x, y \quad (1.114)$$

Eqs. (1.110)-(1.114) imply that the macrostrain components  $E_{xz}$ ,  $E_{yz}$ , and  $E_{zz}$  are influenced by the interfaces, while the components  $E_{xx}$ ,  $E_{yy}$ , and  $E_{xy}$  depend exclusively on the properties of the solid. Specification of Eq. (1.112) for the glueing condition-related value of  $T_{i,z} = \Sigma_{zz}$ , see (1.105), as well as of (1.114) for the time-evolution of  $T_{i,x}(t)$  and  $T_{i,y}(t)$  according to (1.109), yields the model-predicted solution of the macrostrain components as

$$E_{xx} = \frac{\Sigma_{xx} - \nu_s (\Sigma_{yy} + \Sigma_{zz})}{E_s}, \quad E_{yy} = \frac{\Sigma_{yy} - \nu_s (\Sigma_{xx} + \Sigma_{zz})}{E_s} \quad (1.115)$$

$$E_{zz} = \frac{\Sigma_{zz} - \nu_s (\Sigma_{xx} + \Sigma_{yy})}{E_s}, \quad E_{xy} = \frac{(1 + \nu_s)\Sigma_{xy}}{E_s} \quad (1.116)$$

and

$$E_{\alpha z}(t) = E^0 + \Delta E^\infty \times \left[ 1 - \exp\left(-\frac{t}{\tau_{creep}}\right) \right], \quad \alpha = x, y \quad (1.117)$$

with the instantaneous strain response  $E^0$  and the asymptotically reached creeping strain increment  $\Delta E^\infty$  reading as

$$E^0 = \frac{(1 + \nu_s)\Sigma_{\alpha z}}{E_s} \quad \Delta E^\infty = E^0 \frac{16d(1 - \nu_s)}{3(2 - \nu_s)} \quad (1.118)$$

By analogy to the relaxation problem, only the shear macrostrain components  $E_{xz}$  and  $E_{yz}$  exhibit time-dependent behavior, compare (1.115)-(1.118) with (1.94)-(1.99). The other macrostrain components are equal to time-independent values which depend on the macroscopic loading and on the elastic properties of the solid. In addition, Eqs. (1.109), (1.117), and (1.118) imply that under sudden load increase at  $t = 0$ , the interface tractions result in an entirely uniform microscopic stress field  $\underline{\underline{\sigma}}_s(\underline{x}, t = 0) = \underline{\underline{\Sigma}}$ ,  $\forall \underline{x} \in \Omega_s$  and  $\underline{\underline{T}}_i(\underline{x}, t = 0) = \underline{\underline{\Sigma}} \cdot \underline{e}_z$ ,  $\forall \underline{x} \in \Omega_i$ , such that the material behaves as if no interfaces exist. With progress of time, the

average displacement jumps (1.106) increase with decelerating speed such that interface shear traction components (1.109) progressively decrease, resulting in a monotonous increase (creep) of the shear macrostrain components (1.117) until an asymptotic value is reached (see Fig. 10). The asymptotically reached creep strains increase with increasing interface density  $d$ . In addition, as long as interface density is smaller than  $9/16 = 0.5625$ , asymptotic creep strains increase with increasing Poisson's ratio. For larger interface densities, the final creep strains are the larger, the closer Poisson's ratio to the numerical value  $2(3+16d-2\sqrt{3d(3+16d)})/(3+16d)$ . The creep behavior of the material system of Figure 1.2(a) can be also quantified in a general format, by means of the fourth-order creep tensor  $\underline{\underline{J}}$ , with only four time-dependent components, namely

$$J_{\alpha z \alpha z} = J_{\alpha z z \alpha} = J_{z \alpha \alpha z} = J_{z \alpha z \alpha} = \frac{E^0}{2 \Sigma_{\alpha z}} + \frac{\Delta E^\infty}{2 \Sigma_{\alpha z}} \times \left[ 1 - \exp\left(-\frac{t}{\tau_{creep}}\right) \right], \alpha = x, y \quad (1.119)$$

while all other components are identical to the components of the solid compliance tensor,  $J_{ijkl} = C_{s,ijkl}^{-1}$ . Also, for infinite viscosity,  $\eta \rightarrow \infty$  in Eq. (1.119), the time dependency in the creep function is lost; then, the material system behaves just identical to the elastic solid matrix.

## 1.6 Discussion and Conclusions

Our study combined the concept of influence and concentration tensors with viscous laws of thin layers made of liquid crystals, as to upscale the time-dependent layer behavior to the scale of a material system consisting of an elastic bulk matrix with embedded viscous layers. The question may arise why for this task, the use of the well-known correspondence principle [67] could have been an alternative, potentially more straightforward approach. In this context it is appropriate to remember that the key idea of the correspondence principle is to transform a viscoelastic problem into a sequence of linear elastic problems related to some "pseudo-time". That requires all components of the considered system to exhibit the features necessary for the definition of an elasticity tensor. One such key feature is the exhibition of a *volume*. However, our interface phases do not exhibit any volume; and this hinders a straightforward application of the correspondence principle to our material system. In addition, our alternative based on the concept of eigenstresses and influence-concentration tensors, turns out to be very efficient, in the sense that the solution of a (large) sequence of homogenization steps is not necessary.

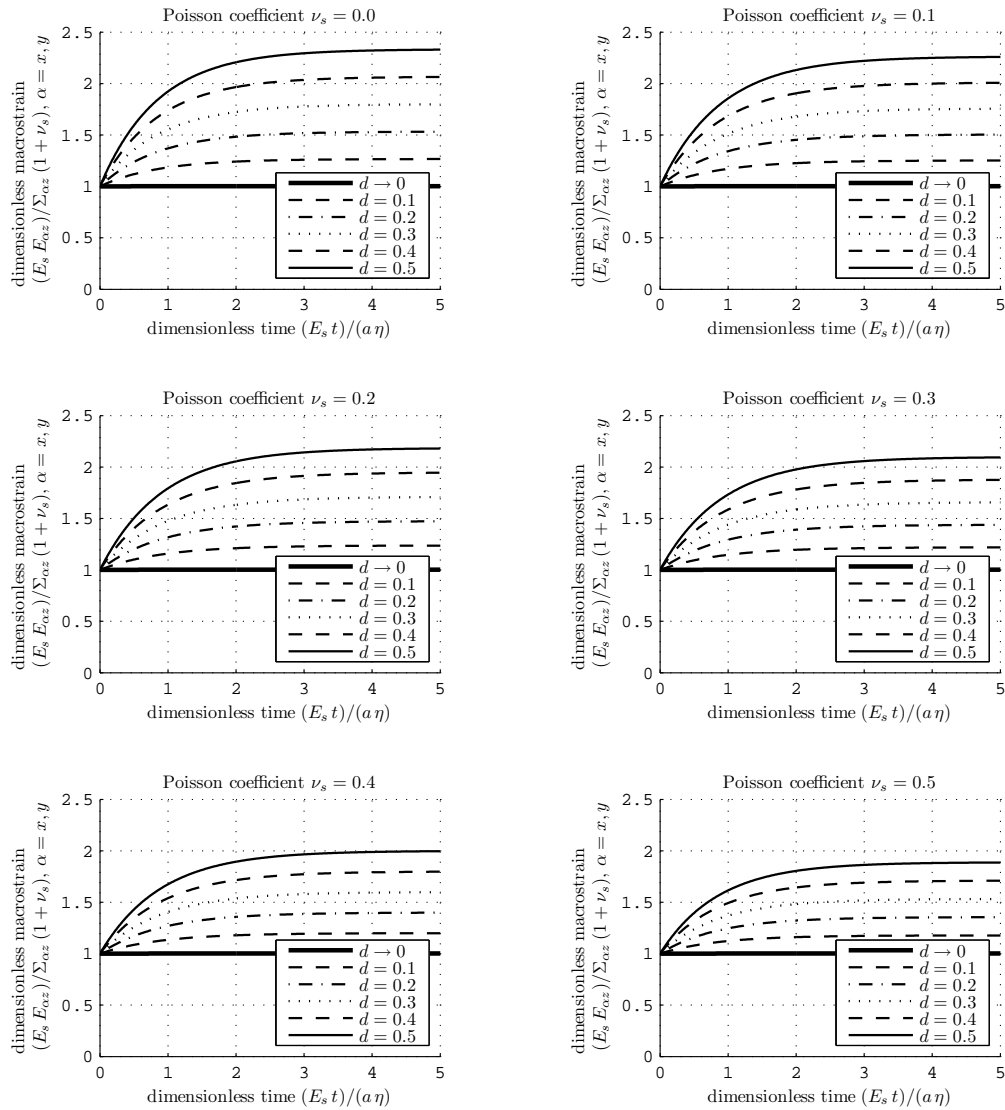


Figure 1.10: Evolution of dimensionless macroscopic shear strain with dimensionless time: results of sensitivity analysis regarding Poisson's ratio of the matrix,  $\nu_s$ , and the interface density parameter  $d$

This efficient method revealed that the linear viscous behavior of parallel (glassy, ice-like, or layered water-filled) interfaces embedded in an isotropically elastic solid matrix manifests itself, at the bulk material scale, as exponential strain and stress evolutions in a classical creep or relaxation test. Such stress and strain evolutions are restricted to shear deformations affecting solely the planes parallel to the interfaces, while all other deformation or stress modes exhibit the purely elastic behavior of the solid matrix phase. Creep and relaxation speeds increase with increasing Young's modulus of the solid phase, decreasing interface radius, and increasing distances of the solid phase's Poisson's ratio from creep and relaxation-specific optimum values. In addition, relaxation speed increases with increasing

interface density, while the latter does not influence the creep speed. However, the larger the interface density, the larger is the asymptotically reached macroscopic stress relaxation and the macroscopic creep strains, respectively. At this stage, it may be appropriate to remember that our model included only one type of interfaces, with only one characteristic size. The question arises whether the aforementioned features of elastic matrices with parallel viscous interfaces would change if interfaces of different sizes would occur. The mathematical relations related to the corresponding extension of our model are presented in Appendix. B, and they show that the creep response of the system appears as the “sum” of the responses of systems with only one interface size. This is reminiscent of the well-known “Maxwell-chain” models as they are widely used in engineering practice. At the same time, also the behavior of material systems with various interface sizes is of asymptotic nature – i.e. the creep strain rates tend to zero with creep duration going to infinity. Such asymptotic creep behavior is indeed observed in systems subjected at a moderate load level, as it has been shown e.g. for bone samples at different hydration states [68]. However, at higher load levels, often non-asymptotic creep behavior is observed, be it at very small time and length scales like in nanoindentation tests on concrete [69] or at very large time and length scales like reported in the context of “excessive creep” of long-span concrete bridges having deformed over several decades [70]. In view of our theoretical developments presented here, loss of asymptotic creep behavior could be readily explained by the interface size, which appears in the numerator of the formula for the characteristic creep times of Eq. (1.108), to *increase over time*. This would result in the characteristic creep time increasing itself while the creep process goes on, so that the latter may never come to an end. Such an “interface spreading” is perfectly consistent with higher load levels inducing higher microstress concentrations in the interface edges, which would then act as liquid crystal-glued “cracks”. This opens an interesting perspective of further developments combining the present approach with fracture mechanics, which in the end, promise to support, through a multi-disciplinary approach linking material physics with continuum mechanics, the quest for deciphering the scale-transitions from highly nanoconfined fluid layers to creeping microheterogeneous hydrated solids, such as concrete or bone.

## 1.7 Nomenclature

$a$	radius of an oblate spheroid
$\underline{\underline{A}}_i$	fourth-order strain concentration tensor of spheroidal interface phase

$\underline{\underline{\underline{A}}}_s$	fourth-order strain concentration tensor of solid
$\underline{\underline{\underline{A}}}_i^\infty$	fourth-order strain concentration tensor of spheroidal interface phase in Eshelby-Laws-type matrix-inclusion problem
$\underline{\underline{\underline{A}}}_i^{lim}$	limit of $\underline{\underline{\underline{A}}}_i$ for flat interfaces
$\underline{\underline{\underline{A}}}_i^{lim}$	third-order strain concentration tensor describing the influence of macroscopic strain on the average displacement jump of flat interfaces
$\underline{\underline{\underline{A}}}_i^{\Sigma,lim}$	third-order strain concentration tensor describing the influence of macroscopic stress on the average displacement jump of flat interfaces
$A_{i,jkm}^{lim}$	$ijk$ -th component of $\underline{\underline{\underline{A}}}_i^{lim}$ ; $j, k, m \in \{x, y, z\}$
$A_{i,jkm}^{\Sigma,lim}$	$ijk$ -th component of $\underline{\underline{\underline{A}}}_i^{\Sigma,lim}$ ; $j, k, m \in \{x, y, z\}$
$\underline{\underline{\underline{B}}}_i^{lim}$	third-order influence tensor describing the influence of interfacial eigenstrains of flat interfaces on the macroscopic stress
$\underline{\underline{\underline{B}}}_i^{\Sigma,lim}$	third-order influence tensor describing the influence of interfacial eigenstrains on the macroscopic strain
$B_{i,jkm}^{lim}$	$ijk$ -th component of $\underline{\underline{\underline{B}}}_i^{lim}$ ; $j, k, m \in \{x, y, z\}$
$B_{i,jkm}^{\Sigma,lim}$	$ijk$ -th component of $\underline{\underline{\underline{B}}}_i^{\Sigma,lim}$ ; $j, k, m \in \{x, y, z\}$
$c$	half opening of an oblate spheroid
$\underline{\underline{\underline{C}}}_i$	fourth-order stiffness tensor of interface phase
$\underline{\underline{\underline{C}}}_s$	fourth-order stiffness tensor of solid
$\underline{\underline{\underline{C}}}_{hom}$	fourth-order homogenized stiffness tensor
$\underline{\underline{\underline{C}}}_{hom}^{lim}$	limit case of $\underline{\underline{\underline{C}}}_{hom}$ for flat interfaces
$(\underline{\underline{\underline{C}}}_{hom}^{lim})^{-1}$	inversion of $\underline{\underline{\underline{C}}}_{hom}^{lim}$ , i.e. homogenized compliance tensor for flat interfaces
$d$	interface density parameter
$dr$	differential of $r$
$du$	differential of $u$
$d\Omega$	differential volume
$\underline{\underline{\underline{D}}}_{ii}$	fourth-order influence tensor describing the influence of eigenstresses in spheroidal interface phase on its total strains
$\underline{\underline{\underline{D}}}_{ii}^{lim}$	fourth-order limit of $\underline{\underline{\underline{D}}}_{ii}$ for flat interfaces
$\underline{\underline{\underline{D}}}_{ii}^{lim}$	second-order influence tensor describing the influence of interfacial eigenstrain on the average displacement jump
$\underline{\underline{\underline{D}}}_{ii}^{\Sigma,lim}$	second-order influence tensor describing the influence of interfacial eigenstrain on the average displacement jump
$\underline{\underline{\underline{D}}}_{si}$	fourth-order influence tensor describing the influence of eigenstresses in spheroidal interface phase on the total solid phase strains

$D_{ii,jkmn}^{lim}$	$ijklm$ -th component of $\underline{\underline{D}}_{ii}^{lim}; j, k, m, n \in \{x, y, z\}$
$D_{ii,jk}^{lim}$	$jk$ -th component of $\underline{\underline{D}}_{ii}^{lim}; j, k \in \{x, y, z\}$
$D_{ii,jk}^{\Sigma,lim}$	$jk$ -th component of $\underline{\underline{D}}_{ii}^{\Sigma,lim}; j, k \in \{x, y, z\}$
$\underline{e}_x, \underline{e}_y, \underline{e}_z$	unit base vectors of Cartesian coordinate system
$\underline{\underline{E}}$	macroscopic strain tensor
$\underline{\underline{E}}_\infty$	remote strain tensor of Eshelby-Laws-type matrix-inclusion problem
$\underline{\underline{E}}_I$	$\underline{\underline{E}}$ in first load case
$\underline{\underline{E}}_{II}$	$\underline{\underline{E}}$ in second load case
$E_s$	Young's modulus of the solid phase
$E_{jk}$	$jk$ -th component of $\underline{\underline{E}}; j, k \in \{\alpha, x, y, z\}$
$E^0$	INITIAL MACROSTRAIN IN A CREEP EXPERIMENT
$\Delta E^\infty$	ASYMPTOTICALLY REACHED CREEPING STRAIN INCREMENT
$f_i$	volume fraction of interface phase
$f_s$	volume fraction of solid phase
$i$	index for interface phase
$\underline{\underline{I}}$	symmetric fourth-order identity tensor
$\underline{\underline{I}}_{dev}$	DEVIATORIC PART OF $\underline{\underline{I}}$
$\underline{\underline{I}}_{vol}$	VOLUMETRIC PART OF $\underline{\underline{I}}$
$\underline{\underline{1}}$	second-order identity tensor
$j$	index $j \in \{x, y, z\}$
$\underline{\underline{J}}$	FOURTH-ORDER CREEP TENSOR
$J_{ijkl}$	$ijkl$ -TH COMPONENTS OF $\underline{\underline{J}}$
$k$	index $k \in \{x, y, z\}$
$k_s$	bulk modulus of solid phase
$\ell$	characteristic size of RVE
$m$	index $m \in \{x, y, z\}$
$n$	index $n \in \{x, y, z\}$
$\mathcal{N}$	number of interfaces inside the RVE, making up the interface phase
$\underline{\underline{P}}$	fourth-order Hill tensor, accounting for inclusion shape
$\underline{\underline{P}}_i$	fourth-order Hill tensor of interface phase
$r$	radial coordinate of a cylindrical coordinate system
RVE	Representative Volume Element
$\underline{\underline{R}}$	FOURTH-ORDER RELAXATION TENSOR
$R_{ijkl}$	$ijkl$ -TH COMPONENTS OF $\underline{\underline{R}}$
$s$	index for solid phase

$\underline{\underline{S}}_i$	fourth-order Eshelby tensor of interface phase
$S_{i,jkmn}$	$ijklmn$ -th component of $\underline{\underline{S}}_i$ ; $j, k, m, n \in \{x, y, z\}$
$\underline{\underline{T}}_i$	fourth-order morphology tensor for flat inclusions; abbreviation for $\lim_{\omega \rightarrow 0} \omega \underline{\underline{A}}_i^\infty$
$T_{i,jkmn}$	$ijklmn$ -th component of $\underline{\underline{T}}_i$ ; $j, k, m, n \in \{x, y, z\}$
$\underline{\underline{T}}_i^E$	viscous eigentractor vector of interface phase
$T_{i,j}^E$	$j$ -th component of $\underline{\underline{T}}_i^E$ ; $j \in \{\alpha, z\}$
$u$	integration variable
$x, y, z$	Cartesian coordinates
$\underline{x}$	position vector
$\underline{x}^+$	position vector labelling geometrical points at upper boundary of the spheroidal inclusion
$\underline{x}^-$	position vector labelling geometrical points at lower boundary of the spheroidal inclusion
$z(r)$	half opening of an oblate spheroid, measured relative to the midplane of the oblate spheroid, at a distance $r$ from the center on the long axis ( $z(0) = c$ )
$\alpha$	index $\alpha \in \{x, y\}$
$\delta$	Kronecker delta
$\underline{\underline{\varepsilon}}$	microscopic strain tensor
$\underline{\underline{\varepsilon}}_i$	average strains of interface phase
$\underline{\underline{\varepsilon}}_s$	average strains of solid phase
$\underline{\underline{\varepsilon}}_{i,I}$	$\underline{\underline{\varepsilon}}_i$ in first load case
$\underline{\underline{\varepsilon}}_{s,I}$	$\underline{\underline{\varepsilon}}_s$ in first load case
$\eta$	viscosity constant of flat interfaces
$\mu_s$	shear modulus of solid phase
$\nu_s$	Poisson's ratio of solid phase
$\underline{\underline{\xi}}$	displacement vector
$\Delta \underline{\underline{\xi}}_i$	displacement increment across spheroidal interface
$\llbracket \underline{\underline{\xi}} \rrbracket_i$	average displacement jump of flat interfaces
$\llbracket \underline{\xi}_z \rrbracket_i$	normal component of $\llbracket \underline{\underline{\xi}} \rrbracket_i$
$\llbracket \underline{\xi}_\alpha \rrbracket_i$	shear component of $\llbracket \underline{\underline{\xi}} \rrbracket_i$ in $\alpha$ -direction; $\alpha = x, y$
$\dot{\llbracket \underline{\underline{\xi}} \rrbracket}_i$	rate of $\llbracket \underline{\underline{\xi}} \rrbracket_i$
$\dot{\llbracket \underline{\xi}_\alpha \rrbracket}_i$	rate of $\llbracket \underline{\xi}_\alpha \rrbracket_i$
$\llbracket \underline{\xi}_{creep} \rrbracket_i^\infty$	asymptotic displacement jump in a creep test
$\llbracket \underline{\xi}_{relax} \rrbracket_i^\infty$	asymptotic displacement jump in a relaxation test
$\underline{\underline{\sigma}}$	microscopic stress tensor

$\underline{\underline{\sigma}}_i$	average stresses of interface phase
$\underline{\underline{\sigma}}_s$	average stresses of solid phase
$\underline{\underline{\sigma}}_i^E$	eigenstress tensor of interface phase, related to viscous effects
$\underline{\underline{\sigma}}_{i,I}^E$	$\underline{\underline{\sigma}}_i^E$ in first load case
$\underline{\underline{\sigma}}_{i,II}^E$	$\underline{\underline{\sigma}}_i^E$ in second load case
$\underline{\underline{\sigma}}_{s,II}$	$\underline{\underline{\sigma}}_s$ in second load case
$\underline{\underline{\Sigma}}$	macroscopic stress tensor
$\underline{\underline{\Sigma}}_I$	$\underline{\underline{\Sigma}}$ in first load case
$\underline{\underline{\Sigma}}_{II}$	$\underline{\underline{\Sigma}}$ in second load case
$\sigma_{i,jk}^E$	$jk$ -th component of $\underline{\underline{\sigma}}_i^E$ ; $j, k \in \{\alpha, x, y, z\}$
$\sigma_{s,jk}$	$jk$ -th component of $\underline{\underline{\sigma}}_s$ ; $j, k \in \{\alpha, x, y, z\}$
$\Sigma_{jk}$	$jk$ -th component of $\underline{\underline{\Sigma}}$ ; $j, k \in \{\alpha, x, y, z\}$
$\Sigma^0$	INITIAL MACROSTRESS IN A RELAXATION EXPERIMENT
$\Delta\Sigma^\infty$	ASYMPTOTICALLY RELAXED MACROSTRESS INCREMENT
$\tau_{creep}$	CHARACTERISTIC CREEP TIME
$\tau_{relax}$	CHARACTERISTIC RELAXATION TIME
$\phi$	azimuthal coordinate of a cylindrical coordinate system
$\partial\Omega$	boundary of RVE
$\partial\Omega_i^+$	upper boundary of the inclusion
$\partial\Omega_i^-$	lower boundary of the inclusion
$\Omega$	volume of the RVE
$\Omega_i$	volume of the interface phase
$\Omega_s$	volume of the solid phase
$\omega$	aspect ratio
$\partial$	partial derivative
$\cdot$	first-order tensor contraction
$:$	second-order tensor contraction
$\dot{\bullet}$	partial derivative with respect to time (“rate”), of quantity “ $\bullet$ ”
$\bullet^t$	transpose of fourth-order tensor “ $\bullet$ ”
$\bullet^{-1}$	inverse of fourth-order tensor “ $\bullet$ ”
$\in$	belongs to
$\nabla$	nabla operator
${}^t\nabla$	transpose of nabla operator
$\otimes$	dyadic product

## Chapter 2

# How interface size, density, and viscosity affect creep and relaxation functions of matrix-interface composites – a micromechanical study

### 2.1 Introduction

Matrix-inclusion composites are known to exhibit interaction among the inclusions [32, 33, 34, 35, 36, 37, 38]. When it comes to the special case of inclusions in form of flat interfaces, i.e. to that of *matrix-interface* composites, interaction among interfaces would be clearly expected as well, however, the two-dimensional nature of interfaces is responsible for particularly surprising interaction properties [39, 40], reminiscent of the situation encountered with microcracked materials [41, 42]. The present contribution tackles the question of how interaction among microscopic interfaces affects the overall macroscopic creep and relaxation functions of matrix-interface composites. To this end, we analyze matrix-interface composites consisting of a linear-elastic solid matrix and parallel viscous interfaces, and we consider that the creep and relaxation behavior of such composites results from micro-sliding within adsorbed fluid layers filling the interfaces. The latter idea was recently elaborated in the framework of continuum micromechanics [31], based on eigenstress homogenization schemes [54].

Extending the analysis of [31] – where we mainly focused on identical interfaces – we here consider interaction among *two classes* of interfaces (referred to as “interface families”), differing in interface size, viscosity, and density. The theoretical basis for our analysis is the topic of Section 2.2, where we briefly recall fundamental state equations governing the time-dependent behavior of matrix-interface composites comprising two-dimensional interfaces filled with viscous fluids [31]. This review comprises both types of so-called Hashin boundary conditions [55], i.e. uniform strain boundary conditions and uniform stress boundary conditions, as means for the study of relaxation and creep properties, respectively. The latter properties are comparatively simple to be derived from the microscopic interface behavior, and the corresponding result can be directly recalled from our previous study [31]. The derivation of relaxation functions turns out as formidable mathematical task, which Section 2.3 of the present paper is fully devoted to: In order to (i) derive a compact closed-form solution of the sought relaxation functions, and to (ii) provide derived insight into interface interaction, we carefully select solution methods for coupled systems of linear differential equations. They are: Laplace transformation, a decoupling strategy in time-domain based on an elimination scheme, and the method of non-dimensionalization. The analytically derived relaxation functions are evaluated numerically, in order to (i) study their sensitivity with respect to interface size, density, and viscosity of two interface families, and to (ii) provide insight into interface interaction. Comparing creep and relaxation functions with the aim to identify the reason for interface interaction is the focus of Section 2.4. There, we discuss the seemingly paradox situation that no interface interaction can be identified from the mathematical structure of the creep functions, while interface interaction is clearly manifested in the relaxation functions. In fact, this situation can be understood when recalling the stress and strain average rules for materials hosting interfaces, relating to loading in terms of uniform stress boundary conditions and uniform strain boundary conditions, respectively. Section 2.4 closes with final conclusions.

## 2.2 Matrix-interface micromechanics for different interface families and review of creep functions

We consider a matrix-interface composite consisting of a linear-elastic solid matrix and of two families of embedded 2D, circular interfaces which are parallel to the

$x,y$ -plane (Fig. 2.1). Mechanical properties of these microstructural constituents are described next.

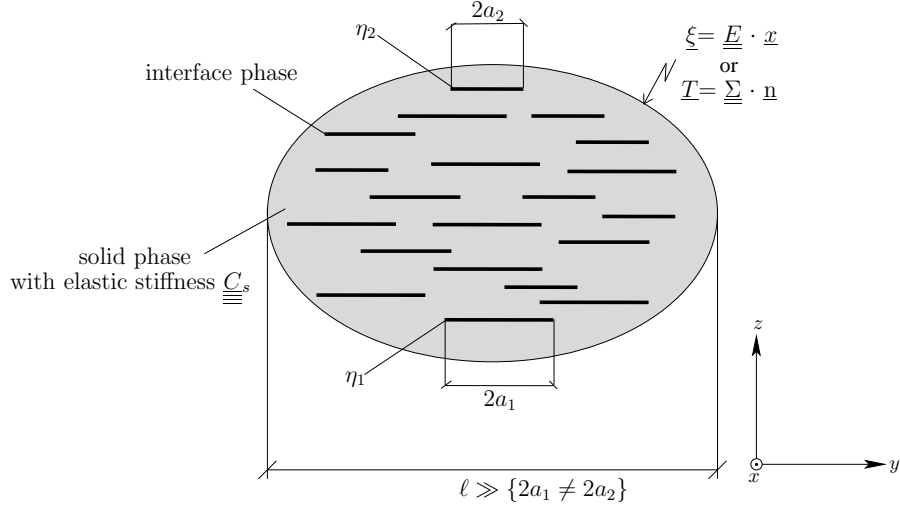


Figure 2.1: Matrix-interface composite consisting of continuous isotropic solid matrix and two families of parallel 2D interfaces; 2D sketch of a 3D representative volume element

The material behavior of the solid matrix follows the generalized Hooke's law

$$\underline{\underline{\sigma}}(\underline{x}) = \underline{\underline{C}}_s : \underline{\underline{\varepsilon}}(\underline{x}) \quad \forall \underline{x} \in \Omega_s \quad (2.1)$$

In Eq. (2.1),  $\underline{\underline{\sigma}}(\underline{x})$  and  $\underline{\underline{\varepsilon}}(\underline{x})$  denote Cauchy microstresses and linear microstrains at any position  $\underline{x}$  in the volume  $\Omega_s$  of the solid phase, and  $\underline{\underline{C}}_s$  denotes an isotropic elastic stiffness tensor

$$\underline{\underline{C}}_s = \frac{E_s}{(1 - 2\nu_s)} \underline{\underline{I}}_{vol} + \frac{E_s}{(1 + \nu_s)} \underline{\underline{I}}_{dev} \quad (2.2)$$

In Eq. (2.2),  $E_s$  and  $\nu_s$ , respectively, denote Young's modulus and Poisson's ratio of the isotropic matrix. In addition,  $\underline{\underline{I}}_{vol}$  and  $\underline{\underline{I}}_{dev}$  stand for the volumetric and the deviatoric part of the symmetric fourth-order identity tensor  $\underline{\underline{I}}$  (see Appendix C.1 for components of these tensors).

The two interface families are denoted with indexes 1 and 2, and they comprise interfaces with radius  $a_1$  and  $a_2$ , respectively (Fig. 2.1). Denoting the number of interfaces per unit volume of the composite as  $\mathcal{N}_1$  and as  $\mathcal{N}_2$ , respectively, the interface densities  $d_1$  and  $d_2$  read, according to Budiansy and O'Connell [65], as  $d_1 = \mathcal{N}_1 a_1^3$  and  $d_2 = \mathcal{N}_2 a_2^3$ . The interfaces are considered to host fluids adsorbed to electrically charged solid surfaces [31]. Accordingly, the fluids are ice-like structured, i. e. they are in a "glassy" or "liquid crystal" state, right in between the

long-range positional and orientational order found in solids and the long-range disorder found in liquids. The lubricant effect of such fluid layers promotes gliding of the solid surfaces along the fluid sheets [15, 16, 30, 71]. This fluid behavior is mathematically described through relations between components of (i) interfacial dislocation vectors  $[[\underline{\xi}]]_1$  and  $[[\underline{\xi}]]_2$  quantifying the displacement jumps across the interfaces, and of (ii) interfacial traction vectors acting on the interface planes,  $\underline{T}_1$  and  $\underline{T}_2$ . Molecular ordering-related joining forces prevent the interfaces from opening, i. e., displacement jumps in the interface normal direction  $\underline{e}_z$  (see Fig. 2.1) vanish in both interface families

$$[[\underline{\xi}]]_{j,z} = 0 \quad j = 1, 2 \quad (2.3)$$

As for the in-plane behavior, the adsorbed fluids are considered to result in linear viscous relations between the components of the traction vectors ( $T_{1,x}$  and  $T_{1,y}$  as well as  $T_{2,x}$  and  $T_{2,y}$ ), and the corresponding dislocation rates, with interface viscosities  $\eta_{i,1}$  and  $\eta_{i,2}$  as proportionality factors

$$T_{j,\alpha} = \eta_{i,j} [[\dot{\underline{\xi}}]]_{j,\alpha} \quad \begin{cases} j = 1, 2 \\ \alpha = x, y \end{cases} \quad (2.4)$$

In Eq. (2.4), the dot stands for the time derivative

$$\frac{d\bullet}{dt} = \dot{\bullet} \quad (2.5)$$

In the sequel, we recall fundamental relations of interfacial micromechanics [31], which were derived in the framework of eigenstress homogenization [54]. Thereby, we consider that the matrix-interface composite of Fig. 2.1 is subjected to a specific type of so-called Hashin boundary conditions [55], i. e. either to uniform strain boundary conditions or to uniform stress boundary conditions, respectively.

### 2.2.1 State equations for uniform strain boundary conditions

Consider that the boundary  $\partial\Omega$  of the studied matrix-interface composite (Fig. 2.1) is subjected to linear displacement functions which are related to a uniform macro-strain state  $\underline{E}$  by

$$\underline{\xi}(\underline{x}) = \underline{E} \cdot \underline{x} \quad \forall \underline{x} \in \partial\Omega \quad (2.6)$$

In addition, consider that traction forces  $\underline{T}_1$  and  $\underline{T}_2$  prevail in the interface phase.

The corresponding macroscopic state equation expresses the macrostress  $\underline{\underline{\Sigma}}$  as a function of the macrostrain  $\underline{\underline{E}}$  and of the interface traction vectors  $\underline{\underline{T}}_1$  and  $\underline{\underline{T}}_2$ , reading as [31]

$$\underline{\underline{\Sigma}} = \underline{\underline{C}}_{hom} : \underline{\underline{E}} + \underline{\underline{B}}_1 \cdot \underline{\underline{T}}_1 + \underline{\underline{B}}_2 \cdot \underline{\underline{T}}_2 \quad (2.7)$$

In Eq. (2.7),  $\underline{\underline{C}}_{hom}$  denotes the homogenized stiffness tensor, while  $\underline{\underline{B}}_1$  and  $\underline{\underline{B}}_2$ , respectively, denote influence tensors (see Appendix C.1 for components of these tensors).

The remaining two state equations establish relations between dislocation vectors of the two interface families,  $\llbracket \underline{\xi} \rrbracket_1$  and  $\llbracket \underline{\xi} \rrbracket_2$ , on the one hand, and the macrostrain  $\underline{\underline{E}}$  as well as the interface traction vectors  $\underline{\underline{T}}_1$  and  $\underline{\underline{T}}_2$ , on the other hand. These concentration-influence relations read as [31]

$$\llbracket \underline{\xi} \rrbracket_1 = \underline{\underline{A}}_1 : \underline{\underline{E}} + \underline{\underline{D}}_{11} \cdot \underline{\underline{T}}_1 + \underline{\underline{D}}_{12} \cdot \underline{\underline{T}}_2 \quad (2.8)$$

$$\llbracket \underline{\xi} \rrbracket_2 = \underline{\underline{A}}_2 : \underline{\underline{E}} + \underline{\underline{D}}_{21} \cdot \underline{\underline{T}}_1 + \underline{\underline{D}}_{22} \cdot \underline{\underline{T}}_2 \quad (2.9)$$

In Eqs. (2.8) and (2.9),  $\underline{\underline{A}}_1$  and  $\underline{\underline{A}}_2$  denote concentration tensors, while  $\underline{\underline{D}}_{11}$ ,  $\underline{\underline{D}}_{12}$ ,  $\underline{\underline{D}}_{21}$ , and  $\underline{\underline{D}}_{22}$  represent influence tensors (see Appendix C.1 for components of these tensors). Notably,  $\underline{\underline{D}}_{12}$  and  $\underline{\underline{D}}_{21}$  account for the interaction of the two interface families, i. e. the components of these two tensors quantify the influence of interface tractions of one interface family, on the dislocation evolution of the other interface family, and vice versa. This interaction will be the central topic of Section 2.3, where we derive relaxation functions of the matrix-interface composite of Fig. 2.1.

### 2.2.2 State equations for uniform stress boundary conditions

Consider that the boundary  $\partial\Omega$  of the studied matrix-interface composite (Fig. 2.1) is subjected to a field of traction vectors  $\underline{\underline{T}}$  which are related via Cauchy's formula to a uniform macrostress state  $\underline{\underline{\Sigma}}$

$$\underline{\underline{T}}(\underline{\underline{x}}) = \underline{\underline{\Sigma}} \cdot \underline{\underline{n}}(\underline{\underline{x}}) \quad \forall \underline{\underline{x}} \in \partial\Omega \quad (2.10)$$

where  $\underline{\underline{n}}(\underline{\underline{x}})$  denotes to outward unit normal at any point  $\underline{\underline{x}}$  of the boundary of the composite. In addition, consider that traction forces  $\underline{\underline{T}}_1$  and  $\underline{\underline{T}}_2$  prevail in the interface phase.

The corresponding macroscopic state equation expresses the macrostrain  $\underline{\underline{E}}$  as a function of the macrostress  $\underline{\underline{\Sigma}}$  and of the interface traction vectors  $\underline{\underline{T}}_1$  and  $\underline{\underline{T}}_2$ . It

follows from solving Eq. (2.7) for the macrostrain [31], and it reads as

$$\underline{\underline{E}} = \underline{\underline{C}}_{hom}^{-1} : \underline{\underline{\Sigma}} - \underline{\underline{B}}_1^\Sigma \cdot \underline{\underline{T}}_1 - \underline{\underline{B}}_2^\Sigma \cdot \underline{\underline{T}}_2 \quad (2.11)$$

In Eq. (2.11)  $\underline{\underline{B}}_1^\Sigma$  as well as  $\underline{\underline{B}}_2^\Sigma$ , respectively, denote influence tensors (see Appendix C.1 for components of these tensors).

The remaining two state equations establish relations between dislocation vectors of the two interface families,  $[\underline{\underline{\xi}}]_1$  and  $[\underline{\underline{\xi}}]_2$ , on the one hand, and the macrostress  $\underline{\underline{\Sigma}}$  as well as the interface traction vectors  $\underline{\underline{T}}_1$  and  $\underline{\underline{T}}_2$ , on the other hand. These concentration-influence relations follow from specifying Eqs. (2.8) and (2.9) for (2.11), and they read as

$$[\underline{\underline{\xi}}]_1 = \underline{\underline{A}}_1^\Sigma : \underline{\underline{\Sigma}} + \underline{\underline{D}}_{11}^\Sigma \cdot \underline{\underline{T}}_1 \quad (2.12)$$

$$[\underline{\underline{\xi}}]_2 = \underline{\underline{A}}_2^\Sigma : \underline{\underline{\Sigma}} + \underline{\underline{D}}_{22}^\Sigma \cdot \underline{\underline{T}}_2 \quad (2.13)$$

In Eqs. (2.12) and (2.13),  $\underline{\underline{A}}_1^\Sigma$ ,  $\underline{\underline{A}}_2^\Sigma$ ,  $\underline{\underline{D}}_{11}^\Sigma$ , and  $\underline{\underline{D}}_{22}^\Sigma$  represent influence tensors (see Appendix C.1 for components of these tensors). Very remarkably, Eqs. (2.12) and (2.13) do *not* contain influence tensors  $\underline{\underline{D}}_{12}^\Sigma$  and  $\underline{\underline{D}}_{21}^\Sigma$ , i. e. interface tractions of one interface family do *not* influence the evolution of the dislocations of the other interface family, and vice versa. This renders the situation with uniform stress boundary conditions (2.10), as fundamentally different from the situation encountered with uniform strain boundary conditions (2.6); compare the concentration influence relations (2.12) and (2.13), with those of (2.8) and (2.9). Clarification of the reason for this interesting difference is one of the central aims of this paper. To this end, we derive and compare macroscopic creep and relaxation functions defined on the homogenized matrix-interface composite. While relaxation functions are reserved for Section 2.3, we already here quickly recall the derivation of creep functions as anticipated in [31].

### 2.2.3 Review of creep functions

In order to derive the creep functions related to the matrix-interface composite of Fig. 2.1, we consider a stress state which is suddenly imposed at time  $t = 0$  and kept constant thereafter ( $t > 0$ ), see the uniform stress boundary conditions (2.10). Since time-dependent behavior of the composite is related to in-plane dislocations of the interfaces, see the viscous interface law (2.4), it is sufficient to study the

following pure shear stress state

$$\underline{\underline{\Sigma}} = \Sigma_{xz} (\underline{e}_x \otimes \underline{e}_z + \underline{e}_z \otimes \underline{e}_x) \quad (2.14)$$

Specifying the concentration-influence relations (2.12) and (2.13) for (2.14), considering the components of the involved influence tensors according to Appendix C.1, and consideration of the viscous interface behavior according to (2.4), deliver the following two differential equations for the time-evolutions of the in-plane dislocation functions  $[[\xi]]_{1,x}$  and  $[[\xi]]_{2,x}$

$$[[\xi]]_{1,x} = \frac{16 a_1 (1 - \nu_s^2)}{3 \pi E_s (2 - \nu_s)} \left[ \Sigma_{xz} - \eta_{i,1} [[\dot{\xi}]]_{1,x} \right] \quad (2.15)$$

$$[[\xi]]_{2,x} = \frac{16 a_2 (1 - \nu_s^2)}{3 \pi E_s (2 - \nu_s)} \left[ \Sigma_{xz} - \eta_{i,2} [[\dot{\xi}]]_{2,x} \right] \quad (2.16)$$

Since Eqs. (2.15) and (2.16) are uncoupled, the solution for the sought two dislocation histories is straightforward, and it reads as

$$[[\xi]]_{1,x} = \frac{16 (1 - \nu_s^2) a_1 \Sigma_{xz}}{3 \pi E_s (2 - \nu_s)} \left[ 1 - \exp \left( - \frac{3 \pi (2 - \nu_s)}{16 (1 - \nu_s^2)} \frac{E_s t}{a_1 \eta_{i,1}} \right) \right] \quad (2.17)$$

$$[[\xi]]_{2,x} = \frac{16 (1 - \nu_s^2) a_2 \Sigma_{xz}}{3 \pi E_s (2 - \nu_s)} \left[ 1 - \exp \left( - \frac{3 \pi (2 - \nu_s)}{16 (1 - \nu_s^2)} \frac{E_s t}{a_2 \eta_{i,2}} \right) \right] \quad (2.18)$$

The creep function is obtained in two steps. At first, interface traction histories  $T_{1,x}$  and  $T_{2,x}$  are calculated by specifying the viscous interface law (2.4) for the time-derivatives of the dislocation histories (2.15) and (2.16). After that, the macroscopic state equation (2.11) is specified for the imposed stress state (2.14) and for the interface traction histories  $T_{1,x}$  and  $T_{2,x}$  obtained in the first step. Considering the components of the homogenized stiffness tensor and the involved influence tensors according to Appendix C.1, and comparing the resulting expressions with

$$E_{xz} = J_{xzzz}(t) 2\Sigma_{xz} \quad (2.19)$$

delivers the sought creep functions as [31]

$$J_{xzzz}(t) = \frac{(1 + \nu_s)}{2 E_s} \left\{ 1 + \frac{16 d_1 (1 - \nu_s)}{3 (2 - \nu_s)} \left[ 1 - \exp \left( - \frac{3 \pi (2 - \nu_s)}{16 (1 - \nu_s^2)} \frac{E_s t}{a_1 \eta_{i,1}} \right) \right] + \frac{16 d_2 (1 - \nu_s)}{3 (2 - \nu_s)} \left[ 1 - \exp \left( - \frac{3 \pi (2 - \nu_s)}{16 (1 - \nu_s^2)} \frac{E_s t}{a_2 \eta_{i,2}} \right) \right] \right\} \quad (2.20)$$

The creep functions (2.20) contain two exponentials underlining the existence of two different characteristic creep times. They read as

$$\tau_{creep,I} = \frac{a_1 \eta_{i,1}}{E_s} \frac{16 (1 - \nu_s^2)}{3 \pi (2 - \nu_s)} \quad \tau_{creep,II} = \frac{a_2 \eta_{i,2}}{E_s} \frac{16 (1 - \nu_s^2)}{3 \pi (2 - \nu_s)} \quad (2.21)$$

Because the concentration-influence relations (2.12) and (2.13) are free of interaction terms, it was mathematically quite simple to derive the creep functions of the matrix-inclusion composite of Fig. 2.1. This will be different when it comes to determination of relaxation functions, as discussed next.

### 2.3 Derivation of relaxation functions for interacting interfaces of different size, viscosity, and density

In order to derive relaxation functions of the matrix-interface composite of Fig. 2.1, we consider a deformation state which is suddenly imposed at time  $t = 0$  and kept constant thereafter ( $t > 0$ ), see the uniform strain boundary conditions (2.6). Since time-dependent behavior of the composite is related to in-plane dislocations of the interfaces, see the viscous interface law (2.4), it is sufficient to study the following pure shear stress state (note the analogy to Eq. (2.14) considered for the derivation of the creep functions)

$$\underline{\underline{E}} = E_{xz} (\underline{e}_x \otimes \underline{e}_z + \underline{e}_z \otimes \underline{e}_x) \quad (2.22)$$

Specifying the concentration-influence relations (2.8) and (2.9) for (2.22) and consideration of the viscous interface behavior according to (2.4), deliver the following set of coupled, linear, inhomogeneous, first-order, ordinary differential equations (with constant coefficients) for the dislocation histories of the two interface families

$$\begin{aligned} \llbracket \dot{\xi} \rrbracket_{1,x} &= \frac{16 (1 - \nu_s) a_1}{\pi [3 (2 - \nu_s) + 16 (d_1 + d_2) (1 - \nu_s)]} \times \\ &\times \left[ E_{xz} - \frac{(1 + \nu_s) [3 (2 - \nu_s) + 16 d_2 (1 - \nu_s)]}{3 E_s (2 - \nu_s)} \eta_{i,1} \llbracket \dot{\xi} \rrbracket_{1,x} + \frac{16 d_2 (1 - \nu_s^2)}{3 E_s (2 - \nu_s)} \eta_{i,2} \llbracket \dot{\xi} \rrbracket_{2,x} \right] \end{aligned} \quad (2.23)$$

$$\begin{aligned} \llbracket \xi \rrbracket_{2,x} &= \frac{16(1-\nu_s)a_2}{\pi[3(2-\nu_s)+16(d_1+d_2)(1-\nu_s)]} \times \\ &\times \left[ E_{xz} - \frac{(1+\nu_s)[3(2-\nu_s)+16d_1(1-\nu_s)]}{3E_s(2-\nu_s)} \eta_{i,2} \llbracket \dot{\xi} \rrbracket_{2,x} + \frac{16d_1(1-\nu_s^2)}{3E_s(2-\nu_s)} \eta_{i,1} \llbracket \dot{\xi} \rrbracket_{1,x} \right] \end{aligned} \quad (2.24)$$

Notably, time-derivatives of *both* of the sought dislocation histories,  $\llbracket \dot{\xi} \rrbracket_{1,x}$  and  $\llbracket \dot{\xi} \rrbracket_{2,x}$ , appear in *both* of the Eqs. (2.23) and (2.24). This underlines the coupled nature of Eqs. (2.23) and (2.24). In order to simplify this situation, the differential equation (2.23) is solved for  $\llbracket \dot{\xi} \rrbracket_{1,x}$ , and the resulting expression is used for elimination of  $\llbracket \dot{\xi} \rrbracket_{1,x}$  from the differential equation (2.24). Vice versa, the differential equation (2.24) is solved for  $\llbracket \dot{\xi} \rrbracket_{2,x}$ , and the resulting expression is used for elimination of  $\llbracket \dot{\xi} \rrbracket_{2,x}$  from the differential equation (2.23). This yields

$$\llbracket \dot{\xi} \rrbracket_{1,x} + \frac{E_s \pi [3(2-\nu_s) + 16d_1(1-\nu_s)]}{16a_1\eta_{i,1}(1-\nu_s^2)} \llbracket \xi \rrbracket_{1,x} + \frac{E_s \pi d_2}{(1+\nu_s)a_2\eta_{i,1}} \llbracket \xi \rrbracket_{2,x} = \frac{2\mu_s}{\eta_{i,1}} E_{xz} \quad (2.25)$$

$$\llbracket \dot{\xi} \rrbracket_{2,x} + \frac{E_s \pi d_1}{(1+\nu_s)a_1\eta_{i,2}} \llbracket \xi \rrbracket_{1,x} + \frac{E_s \pi [3(2-\nu_s) + 16d_2(1-\nu_s)]}{16a_2\eta_{i,2}(1-\nu_s^2)} \llbracket \xi \rrbracket_{2,x} = \frac{2\mu_s}{\eta_{i,2}} E_{xz} \quad (2.26)$$

This set of differential equations can be brought into the more comfortable form

$$\dot{\gamma}_1(t) \eta_1 + \gamma_1(t)[\mu_1 + \mu_s] + \gamma_2(t) \mu_s = \gamma \mu_s \quad (2.27)$$

$$\dot{\gamma}_2(t) \eta_2 + \gamma_2(t)[\mu_2 + \mu_s] + \gamma_1(t) \mu_s = \gamma \mu_s \quad (2.28)$$

based on the following definitions of constant

$$\mu_s = \frac{E_s}{2(1+\nu_s)}, \quad \gamma = 2E_{xz}, \quad (2.29)$$

$$\mu_1 = \mu_s \frac{3(2-\nu_s)}{16d_1(1-\nu_s)}, \quad \eta_1 = \frac{a_1\eta_{i,1}}{2\pi d_1}, \quad \gamma_1(t) = \frac{2\pi d_1}{a_1} \llbracket \xi_1 \rrbracket \quad (2.30)$$

$$\mu_2 = \mu_s \frac{3(2-\nu_s)}{16d_2(1-\nu_s)}, \quad \eta_2 = \frac{a_2\eta_{i,2}}{2\pi d_2}, \quad \gamma_2(t) = \frac{2\pi d_2}{a_2} \llbracket \xi_2 \rrbracket \quad (2.31)$$

The most popular method for solving a system of differential equations like the one given through (2.27) and (2.28) is based on Laplace transformation. This is described next.

### 2.3.1 Determination of dislocation histories based on Laplace transformation

Let us recall that Laplace transformation of functions  $\gamma_i(t)$  yields functions  $\Gamma_i(s)$ , as follows from the definition

$$\Gamma_i(s) = \mathcal{L}\{\gamma_i(t)\} = \int_0^{\infty} \exp(-st) \gamma_i(t) dt \quad i = 1, 2 \quad (2.32)$$

where  $s$  is a complex number. Eq. (2.32) implies the following transformation rules for first-order and second-order time derivatives of functions  $\gamma_i(t)$  [72]

$$\mathcal{L}\{\dot{\gamma}_i(t)\} = s \Gamma_i(s) - \gamma_i(0) \quad \mathcal{L}\{\ddot{\gamma}_i(t)\} = s^2 \Gamma_i(s) - s \gamma_i(0) - \dot{\gamma}_i(0) \quad i = 1, 2 \quad (2.33)$$

Accordingly, determination of dislocation histories by means of Laplace transformation becomes more straightforward when considering the time-derivatives of Eqs. (2.27) and (2.28), resulting in the following set of coupled, linear, homogeneous, second-order, ordinary differential equations (with constant coefficients):

$$\ddot{\gamma}_1(t) + \dot{\gamma}_1(t) \frac{\mu_1 + \mu_s}{\eta_1} + \dot{\gamma}_2(t) \frac{\mu_s}{\eta_1} = 0 \quad (2.34)$$

$$\ddot{\gamma}_2(t) + \dot{\gamma}_2(t) \frac{\mu_2 + \mu_s}{\eta_2} + \dot{\gamma}_1(t) \frac{\mu_s}{\eta_2} = 0 \quad (2.35)$$

Relations (2.33) underline (i) that initial conditions are considered already during Laplace transformation, and (ii) that these initial condition need to be formulated in the dimensionless dislocations and their rates (according to (2.30)<sub>3</sub> and (2.31)<sub>3</sub>). At time  $t = 0$ , i.e. at the time instant of sudden loading, the dislocations vanish in all interfaces

$$\gamma_1(0) = \gamma_2(0) = 0 \quad (2.36)$$

The (dimensionless) dislocation rates right after sudden loading at time  $t = 0$ , follow simply from specification of (2.27) and (2.28) for (2.36), and from solving the resulting expressions for  $\dot{\gamma}_1(0)$  and  $\dot{\gamma}_2(0)$ , yielding

$$\dot{\gamma}_1(0) = \gamma \frac{\mu_s}{\eta_1} \quad \text{and} \quad \dot{\gamma}_2(0) = \gamma \frac{\mu_s}{\eta_2} \quad (2.37)$$

The Laplace transformation of Eqs. (2.34) and (2.35) is carried out under consideration of transformation rules (2.33), as well as of initial conditions (2.36) and

(2.37). This yields

$$s^2 \Gamma_1(s) - \gamma \left( \frac{\mu_s}{\eta_1} \right) + \left( \frac{\mu_1 + \mu_s}{\eta_1} \right) s \Gamma_1(s) + \left( \frac{\mu_s}{\eta_1} \right) s \Gamma_2(s) = 0 \quad (2.38)$$

$$s^2 \Gamma_2(s) - \gamma \left( \frac{\mu_s}{\eta_2} \right) + \left( \frac{\mu_2 + \mu_s}{\eta_2} \right) s \Gamma_2(s) + \left( \frac{\mu_s}{\eta_2} \right) s \Gamma_1(s) = 0 \quad (2.39)$$

Rearranging terms in (2.38) and (2.39) delivers the following system of two algebraic equations:

$$\begin{bmatrix} s^2 + \left( \frac{\mu_1 + \mu_s}{\eta_1} \right) s & \frac{\mu_s}{\eta_1} s \\ \frac{\mu_s}{\eta_2} s & s^2 + \left( \frac{\mu_2 + \mu_s}{\eta_2} \right) s \end{bmatrix} \cdot \begin{bmatrix} \Gamma_1(s) \\ \Gamma_2(s) \end{bmatrix} = \begin{bmatrix} \gamma \frac{\mu_s}{\eta_1} \\ \gamma \frac{\mu_s}{\eta_2} \end{bmatrix} \quad (2.40)$$

The solution of (2.40) yields the functions  $\Gamma_1(s)$  and  $\Gamma_2(s)$  as

$$\Gamma_1(s) = \frac{\left( \left[ s^2 + \left( \frac{\mu_2 + \mu_s}{\eta_2} \right) s \right] \gamma \left( \frac{\mu_s}{\eta_1} \right) - \frac{\gamma \mu_s^2}{\eta_1 \eta_2} s \right)}{\left[ s^2 + \left( \frac{\mu_1 + \mu_s}{\eta_1} \right) s \right] \left[ s^2 + \left( \frac{\mu_2 + \mu_s}{\eta_2} \right) s \right] - \frac{\mu_s^2}{\eta_1 \eta_2} s^2} \quad (2.41)$$

$$\Gamma_2(s) = \frac{\left( \left[ s^2 + \left( \frac{\mu_1 + \mu_s}{\eta_1} \right) s \right] \gamma \left( \frac{\mu_s}{\eta_2} \right) - \frac{\gamma \mu_s^2}{\eta_1 \eta_2} s \right)}{\left[ s^2 + \left( \frac{\mu_1 + \mu_s}{\eta_1} \right) s \right] \left[ s^2 + \left( \frac{\mu_2 + \mu_s}{\eta_2} \right) s \right] - \frac{\mu_s^2}{\eta_1 \eta_2} s^2} \quad (2.42)$$

Notably, the two solutions (2.41) and (2.42) are structurally identical. In other words, the solution for  $\Gamma_1(s)$  according to (2.41) can be converted into the solution for  $\Gamma_2(s)$  according to (2.42), and vice versa, simply by permutation of indexes, i.e. by setting  $1 \rightarrow 2$  and, at the same time,  $2 \rightarrow 1$ . Consequently, it is sufficient to back-transform only  $\Gamma_1(s)$  in order to obtain the solution for  $\gamma_1(t)$  in physical time domain, because  $\gamma_2(t)$  follows simply from subsequent index permutation.

For the back-transformation of  $\Gamma_1(s)$  from Laplace space to physical time domain, we will use the following basic rules [72]

$$\mathcal{L}^{-1} \left\{ \frac{\omega}{s} \right\} = \omega \quad (2.43)$$

$$\mathcal{L}^{-1} \left\{ \frac{s + \alpha}{(s + \alpha)^2 + \omega^2} \right\} = \exp(-\alpha t) \cos(\omega t) \quad (2.44)$$

$$\mathcal{L}^{-1} \left\{ \frac{\omega}{(s + \alpha)^2 + \omega^2} \right\} = \exp(-\alpha t) \sin(\omega t) \quad (2.45)$$

We are left with modifying  $\Gamma_1(s)$  according to (2.41), such that the back-transformation rules (2.43) to (2.45) can be applied. This is done in two steps. At first, we transform (2.41) into the format

$$\Gamma_1(s) = \frac{c_1}{s} - \frac{c_1 s - e_1}{s^2 + a s + b} \quad (2.46)$$

through definition of new coefficients  $a$ ,  $b$ ,  $c_1$ , and  $e_1$ , reading as

$$\begin{aligned} a &= \left( \frac{\mu_2 + \mu_s}{\eta_2} + \frac{\mu_1 + \mu_s}{\eta_1} \right), & b &= \left( \frac{\mu_2 \mu_s + \mu_1 \mu_2 + \mu_1 \mu_s}{\eta_1 \eta_2} \right) \\ c_1 &= \frac{\gamma}{\mu_1 \left( \frac{1}{\mu_1} + \frac{1}{\mu_2} + \frac{1}{\mu_s} \right)}, & e_1 &= -\frac{\gamma \mu_s [-\eta_2 \mu_1 \mu_s + \eta_1 \mu_2 (\mu_2 + \mu_s)]}{\eta_1 \eta_2 [\mu_2 \mu_s + \mu_1 \mu_2 + \mu_1 \mu_s]} \end{aligned} \quad (2.47)$$

In the second step, we expand the expression for  $\Gamma_1(s)$  according to (2.46), such that we arrive at the following expression:

$$\Gamma_1(s) = \frac{c_1}{s} - \frac{c_1 \left( s + \frac{a}{2} \right)}{\left( s + \frac{a}{2} \right)^2 + \left( b - \frac{a^2}{4} \right)} + \frac{e_1 + c_1 \frac{a}{2}}{\sqrt{b - \frac{a^2}{4}}} \frac{\sqrt{b - \frac{a^2}{4}}}{\left( s + \frac{a}{2} \right)^2 + \left( b - \frac{a^2}{4} \right)} \quad (2.48)$$

Back-transformation of (2.48) into physical time domain yields, based on transformation rules (2.43) to (2.45),

$$\gamma_1(t) = c_1 + \exp\left(-\frac{a}{2}t\right) \left\{ -c_1 \cos\left(\sqrt{b - \frac{a^2}{4}}t\right) + \frac{e_1 + c_1 \frac{a}{2}}{\sqrt{b - \frac{a^2}{4}}} \sin\left(\sqrt{b - \frac{a^2}{4}}t\right) \right\} \quad (2.49)$$

In order to replace the trigonometric functions in (2.49) by exponential functions, we use the following two Euler's formulas [72]

$$\cos(\omega t) = \frac{1}{2} \left[ \exp(i\omega t) + \exp(-i\omega t) \right] \quad (2.50)$$

$$\sin(\omega t) = \frac{1}{2i} \left[ \exp(i\omega t) - \exp(-i\omega t) \right] \quad (2.51)$$

Specifying (2.49) for (2.50) and (2.51), together with consideration of

$$i \sqrt{b - a^2/4} = \sqrt{a^2/4 - b} \quad (2.52)$$

yields

$$\begin{aligned} \gamma_1(t) = & c_1 + \exp\left(-\frac{a}{2}t\right) \left\{ -\frac{c_1}{2} \left[ \exp\left(\sqrt{\frac{a^2}{4} - bt}\right) + \exp\left(-\sqrt{\frac{a^2}{4} - bt}\right) \right] \right. \\ & \left. + \frac{e_1 + c_1 \frac{a}{2}}{2\sqrt{\frac{a^2}{4} - b}} \left[ \exp\left(\sqrt{\frac{a^2}{4} - bt}\right) - \exp\left(-\sqrt{\frac{a^2}{4} - bt}\right) \right] \right\} \end{aligned} \quad (2.53)$$

Finally, we consider that the product rule for exponential functions  $\exp(x) \exp(y) = \exp(x + y)$ , yielding  $\gamma_1(t)$  as

$$\begin{aligned} \gamma_1(t) = & c_1 + \frac{1}{2\sqrt{\frac{a^2}{4} - b}} \left[ -\left(e_1 - c_1 \left[-\frac{a}{2} - \sqrt{\frac{a^2}{4} - b}\right]\right) \exp\left(-\frac{a}{2} - \sqrt{\frac{a^2}{4} - bt}\right) \right. \\ & \left. + \left(e_1 - c_1 \left[-\frac{a}{2} + \sqrt{\frac{a^2}{4} - b}\right]\right) \exp\left(-\frac{a}{2} + \sqrt{\frac{a^2}{4} - bt}\right) \right] \end{aligned} \quad (2.54)$$

$\gamma_2(t)$  is derived from (2.54) by means of index permutation, i. e. by replacing index 1 by index 2 and at the same time, by replacing index 2 by index 1, which leads to

$$\begin{aligned} \gamma_2(t) = & c_2 + \frac{1}{2\sqrt{\frac{a^2}{4} - b}} \left[ -\left(e_2 - c_2 \left[-\frac{a}{2} - \sqrt{\frac{a^2}{4} - b}\right]\right) \exp\left(-\frac{a}{2} - \sqrt{\frac{a^2}{4} - bt}\right) \right. \\ & \left. + \left(e_2 - c_2 \left[-\frac{a}{2} + \sqrt{\frac{a^2}{4} - b}\right]\right) \exp\left(-\frac{a}{2} + \sqrt{\frac{a^2}{4} - bt}\right) \right] \end{aligned} \quad (2.55)$$

The coefficients  $c_2$  and  $e_2$  follow from  $c_1$  and  $d_1$  according to (2.47), by means of the same index permutation, so that we arrive at

$$c_2 = \frac{\gamma}{\mu_2 \left( \frac{1}{\mu_1} + \frac{1}{\mu_2} + \frac{1}{\mu_s} \right)}, \quad e_2 = -\frac{\gamma \mu_s [-\eta_1 \mu_2 \mu_s + \eta_2 \mu_1 (\mu_1 + \mu_s)]}{\eta_1 \eta_2 [\mu_2 \mu_s + \mu_1 \mu_2 + \mu_1 \mu_s]} \quad (2.56)$$

The two solutions (2.54) and (2.55) clearly indicate interaction among the two different interface families, but the mechanical reason remains somewhat obscure. In more details, we observe that:

- The square-root expressions in Eqs. (2.54) and (2.55) originate from preparation of  $\Gamma_1(s)$  according to (2.51), for back-transformation into physical time space, see (2.49). This square-root expression combines information on both

interface families and, therefore, represents a coupling term. The mechanical meaning of it, however, is not directly obvious, because of the markedly mathematical character of the derivation.

- The obtained solutions for the dislocation histories are still quite mathematically expanded, and more compact expressions appear to be out of direct reach.

Both aspects provide the motivation to deeper investigate the solution of Eqs. (2.27) and (2.28); to (i) solving the governing system of coupled differential equations (2.27) and (2.28) in physical time space through an uncoupling strategy based on an elimination scheme, and (ii) by combining this approach with the method of non-dimensionalization, in order to arrive at a compact closed-form solution of the relaxation function. This is described next.

### 2.3.2 Revisiting dislocation histories based on an elimination scheme combined with the method of non-dimensionalization

Our first aim is to combine the two governing differential equations (2.27) and (2.28), such that an uncoupled differential equation, exclusively in  $\gamma_1(t)$ , is obtained. To this end, we solve (2.27) for  $\gamma_2(t)$ , and we calculate its first-order time-derivative

$$\gamma_2(t) = -\dot{\gamma}_1(t) \frac{\eta_1}{\mu_s} - \gamma_1(t) \left[ \frac{\mu_1 + \mu_s}{\mu_s} \right] + \gamma \quad (2.57)$$

$$\dot{\gamma}_2(t) = -\ddot{\gamma}_1(t) \frac{\eta_1}{\mu_s} - \dot{\gamma}_1(t) \left[ \frac{\mu_1 + \mu_s}{\mu_s} \right] \quad (2.58)$$

Specifying (2.28) for (2.57) and (2.58) eliminates  $\gamma_2(t)$  as well as  $\dot{\gamma}_2(t)$ , and delivers a linear, inhomogeneous, second-order, ordinary differential equation exclusively in  $\gamma_1(t)$ , which reads, after rearranging and collecting terms, as

$$\ddot{\gamma}_1(t) + \dot{\gamma}_1(t) \underbrace{\left[ \frac{\mu_1 + \mu_s}{\eta_1} + \frac{\mu_2 + \mu_s}{\eta_2} \right]}_a + \gamma_1(t) \underbrace{\left[ \left( \frac{\mu_1 + \mu_s}{\eta_1} \right) \left( \frac{\mu_2 + \mu_s}{\eta_2} \right) - \frac{\mu_s^2}{\eta_1 \eta_2} \right]}_b = \gamma \frac{\mu_s \mu_2}{\eta_1 \eta_2} \quad (2.59)$$

It is interesting to interpret Eq. (2.59) from a mechanical viewpoint. To this end, we recall that the original problem is *coupled*, see (2.27) and (2.28). The used elimination scheme delivered an *uncoupled* differential equation for  $\gamma_1(t)$ , see (2.59), but this mathematical modification, of, does not change the underlying

physics. The coupled nature of the problem manifests itself in the coefficients of the uncoupled differential equation, see Eq. (2.59). Notably, the same two coefficients were found during the Laplace solution, compare the abbreviation  $a$  and  $b$  in (2.59) with the definitions (2.47).

The solution of differential equation (2.59) contains two parts: the particulate integral  $\gamma_{1p}(t)$  and the solution of the homogeneous differential equation, called complementary function  $\gamma_{1h}(t)$ ,

$$\gamma_1(t) = \gamma_{1p}(t) + \gamma_{1h}(t) \quad (2.60)$$

We start with the particulate integral  $\gamma_{1p}(t)$ . Since the right-hand-side of (2.59) is time-independent, also the sought particulate integral is a constant. It follows from specifying (2.59) for  $\gamma_1(t) = \gamma_{1p}$ , for  $\ddot{\gamma}_{1p}(t) = 0$ , and for  $\dot{\gamma}_{1p}(t) = 0$ , as well as from solving the resulting expression for  $\gamma_{1p}$ , as

$$\gamma_{1p} = \frac{\gamma}{\mu_1 \left( \frac{1}{\mu_1} + \frac{1}{\mu_2} + \frac{1}{\mu_s} \right)} \quad (2.61)$$

Notably,  $\ddot{\gamma}_{1p}(t) = 0$  and  $\dot{\gamma}_{1p}(t) = 0$  underline that  $\gamma_{1p}$  is a stationary (time-independent) solution, such that  $\gamma_{1p}$  can be interpreted as the dislocation which is asymptotically reached after infinite time, i.e. the dislocation which is finally reached once the relaxation process has come to an end. In addition, we note that  $\gamma_{1p}$  is identical to constant  $c_1$ , which we have introduced during the derivation of the Laplace solution, compare (2.61) with  $c_1$  in (2.47). We are left with determination of the complementary function  $\gamma_{1h}(t)$ . To this end, we rewrite the differential equation (2.59) under consideration  $a$  and  $b$  according to (2.47), and we set the right-hand-side equal to zero, in order to obtain a homogeneous differential equation

$$\ddot{\gamma}_{1h}(t) + a \dot{\gamma}_{1h}(t) + b \gamma_{1h}(t) = 0 \quad (2.62)$$

As for the solution of (2.62), we make the following ansatz involving an exponential function and two constants  $\beta$  and  $\lambda$

$$\gamma_{1h}(t) = \beta \exp(\lambda t) \quad (2.63)$$

Specifying differential equation (2.62) for ansatz (2.63) yields

$$\lambda^2 [\beta \exp(\lambda t)] + a \lambda [\beta \exp(\lambda t)] + b [\beta \exp(\lambda t)] = 0 \quad (2.64)$$

Dividing Eq. (2.64) by  $\beta \exp(\lambda t)$  results in the following quadratic equation for  $\lambda$

$$\lambda^2 + a \lambda + b = 0 \quad (2.65)$$

The two roots of the quadratic equation (2.65) are two independent solutions for  $\lambda$ , i. e.

$$\lambda = -\frac{a}{2} \pm \sqrt{\frac{a^2}{4} - b} \quad (2.66)$$

Eq. (2.66) implies that the sought complementary function  $\gamma_{1h}(t)$  consists of two terms, containing two exponentials which are multiplied by two integration constants  $C_1$  and  $D_1$

$$\gamma_{1h}(t) = C_1 \exp\left(\left[-\frac{a}{2} + \sqrt{\frac{a^2}{4} - b}\right] t\right) + D_1 \exp\left(\left[-\frac{a}{2} - \sqrt{\frac{a^2}{4} - b}\right] t\right) \quad (2.67)$$

The complete solution for the dislocation history  $\gamma_1(t)$  follows from specification of (2.60) for the particulate integral from Eq. (2.61) and the complementary function from Eq. (2.67) as

$$\gamma_1(t) = \gamma_{1p} + C_1 \exp\left(\left[-\frac{a}{2} + \sqrt{\frac{a^2}{4} - b}\right] t\right) + D_1 \exp\left(\left[-\frac{a}{2} - \sqrt{\frac{a^2}{4} - b}\right] t\right) \quad (2.68)$$

While noting that integration constants  $C_1$  and  $D_1$  are conceptually to be identified from the initial conditions (2.36) and (2.37), we emphasize that the solution (2.68) exhibits exactly the same structure as the solution derived with the Laplace transformation method, compare (2.68) with (2.54). Still, the used uncoupling strategy based on an elimination scheme provides valuable insight into the question why a square-root shows up in the exponential function. It stems from a quadratic function which needs to be solved during the derivation of the complementary function. Still, the square-root terms render the derivation of a compact version of a closed-form solution for the relaxation function difficult.

In order to further improve the situation, we revisit the derivation of the complementary function  $\gamma_{1h}(t)$  based on the method of non-dimensionalization. This approach allows for reducing the mathematical complexity of the solution to a possible minimum. Given that time  $t$  is the parameter of the studied relaxation problem, the idea of non-dimensionalization is to set the dimensional time  $t$  equal to dimensionless time  $\tau$ , multiplied with an arbitrary time constant  $t_c$

$$t = \tau t_c \quad (2.69)$$

Appropriate choice of the time constant  $t_c$  will allow us to reduce the mathematical complexity of the solution to the sought minimum. Considering of (2.69) in the form  $dt = d\tau t_c$  underlines that every derivative with respect to dimensional time  $t$  can be replaced by a derivative with respect to dimensionless time  $\tau$ , multiplied with  $1/t_c$ . Applying this strategy to the homogeneous differential equation (2.62) yields

$$\frac{\ddot{\gamma}_{1h}(\tau)}{t_c^2} + a \frac{\dot{\gamma}_{1h}(\tau)}{t_c} + b \gamma_{1h}(\tau) = 0 \quad (2.70)$$

Multiplying Eq. (2.70) by  $t_c^2$  delivers

$$\ddot{\gamma}_{1h} + (a t_c) \dot{\gamma}_{1h} + (b t_c^2) \gamma_{1h} = 0 \quad (2.71)$$

Since Eq. (2.71) is completely analogous to Eq. (2.62), and because (2.62) has led to the two solutions for  $\lambda$  according to (2.66), we conclude that avoiding a square-root expression in the solution function  $\gamma_{1h}(t)$  can be achieved by choosing the time constant  $t_c$  according to the following condition:

$$\sqrt{\frac{(a t_c)^2}{4} - (b t_c^2)} = 1 \quad (2.72)$$

Specifying condition (2.72) for  $a$  and  $b$  according to (2.70), respectively, and solving for the time constant  $t_c$  delivers

$$t_c = \frac{2}{\sqrt{\left[ \left( \frac{\mu_1 + \mu_s}{\eta_1} \right) - \left( \frac{\mu_2 + \mu_s}{\eta_2} \right) \right]^2 + \frac{4 \mu_s^2}{\eta_1 \eta_2}}} \quad (2.73)$$

With help of condition (2.72), and the corresponding special choice (2.73) for the time constant  $t_c$ , the solution of the differential equation (2.71) can now be retrieved in the much simpler form, and based on

$$\gamma_{1h}(\tau) = C_1 \exp \left[ - \left( \frac{a t_c}{2} + 1 \right) \tau \right] + D_1 \exp \left[ - \left( \frac{a t_c}{2} - 1 \right) \tau \right] \quad (2.74)$$

Whereby we followed the the same line of reasoning that has led us from Eq. (2.59) to Eq. (2.67). Notably,  $\gamma_{1h}(\tau)$  in Eq. (2.74) is a function of dimensionless time  $\tau$ . In order to obtain an expression for  $\gamma_{1h}(t)$ , i. e. a function where dimensional time  $t$  appears as the argument, we specify (2.74) for  $\tau = t/t_c$

$$\gamma_{1h}(t) = C_1 \exp \left[ - \left( \frac{a}{2} + \frac{1}{t_c} \right) t \right] + D_1 \exp \left[ - \left( \frac{a}{2} - \frac{1}{t_c} \right) t \right] \quad (2.75)$$

The complete solution for the dislocation history  $\gamma_1(t)$  follows from specification of (2.60) for the particulate integral from Eq. (2.61) and the complementary function from Eq. (2.75), yielding

$$\gamma_1(t) = \gamma_{1p} + C_1 \exp \left[ - \left( \frac{a}{2} + \frac{1}{t_c} \right) t \right] + D_1 \exp \left[ - \left( \frac{a}{2} - \frac{1}{t_c} \right) t \right] \quad (2.76)$$

The two integration constants  $C_1$  and  $D_1$  are identified from the initial conditions (2.36) and (2.37). To this end, we calculate the time-derivative of  $\gamma_1(t)$  given in Eq. (2.76) as

$$\dot{\gamma}_1(t) = -C_1 \left( \frac{a}{2} + \frac{1}{t_c} \right) \exp \left[ - \left( \frac{a}{2} + \frac{1}{t_c} \right) t \right] - D_1 \left( \frac{a}{2} - \frac{1}{t_c} \right) \exp \left[ - \left( \frac{a}{2} - \frac{1}{t_c} \right) t \right] \quad (2.77)$$

Specifying the initial conditions (2.36) and (2.37) for  $\gamma_1(t)$  given in (2.76) and for  $\dot{\gamma}_1(t)$  given in (2.77) yields the following two equations for  $C_1$  and  $D_1$  as

$$\gamma_1(t=0) = C_1 + D_1 + \gamma_{1p} = 0 \quad (2.78)$$

$$\dot{\gamma}_1(t=0) = -C_1 \left( \frac{a}{2} + \frac{1}{t_c} \right) - D_1 \left( \frac{a}{2} - \frac{1}{t_c} \right) = \frac{\gamma \mu_s}{\eta_1} \quad (2.79)$$

Solving the initial conditions (2.78) and (2.79) for the integration constants  $C_1$  and  $D_1$  delivers

$$C_1 = -\frac{\gamma \mu_s t_c}{2 \eta_1} + \left( \frac{a t_c}{2} - 1 \right) \frac{\gamma_{1p}}{2} \quad (2.80)$$

$$D_1 = +\frac{\gamma \mu_s t_c}{2 \eta_1} - \left( \frac{a t_c}{2} + 1 \right) \frac{\gamma_{1p}}{2} \quad (2.81)$$

The solution for  $\gamma_2(t)$  is found by analogy to (2.76), i.e. by permutation of indexes:

$$\gamma_2(t) = \gamma_{2p} + C_2 \exp \left[ - \left( \frac{a}{2} + \frac{1}{t_c} \right) t \right] + D_2 \exp \left[ - \left( \frac{a}{2} - \frac{1}{t_c} \right) t \right] \quad (2.82)$$

The integration constants  $C_2$  and  $D_2$  follow from initial conditions (2.36) and (2.37) and by analogy to  $C_1$  and  $D_1$  given in (2.80) and (2.81), respectively, as

$$C_2 = -\frac{\gamma \mu_s t_c}{2 \eta_2} + \left( \frac{a t_c}{2} - 1 \right) \frac{\gamma_{2p}}{2} \quad (2.83)$$

$$D_2 = +\frac{\gamma \mu_s t_c}{2 \eta_2} - \left( \frac{a t_c}{2} + 1 \right) \frac{\gamma_{2p}}{2} \quad (2.84)$$

The dislocation histories (2.76) and (2.82) exhibit a sufficiently compact mathematical form, ready for the derivation of a closed-form representation of the

relaxation function. This is described next.

### 2.3.3 Relaxation functions

Relaxation functions are obtained in two steps. At first, interface traction histories  $T_{1,x}$  and  $T_{2,x}$  are calculated. To this end, the relations between  $\gamma_1(t)$  and  $[\xi_1]$ , as well as between  $\gamma_2(t)$  and  $[\xi_2]$ , as defined in (2.31), are solved for the dislocation histories:

$$[\xi_1](t) = \frac{a_1}{2\pi d_1} \gamma_1(t) \quad [\xi_2](t) = \frac{a_2}{2\pi d_2} \gamma_2(t) \quad (2.85)$$

The sought interface traction components  $T_{1,x}$  and  $T_{2,x}$  follow from specifying the viscous interface law (2.4) for the time-derivatives of the dislocation histories (2.85):

$$T_{1,x} = \frac{\eta_{i,1} a_1}{2\pi d_1} \dot{\gamma}_1(t) \quad T_{2,x} = \frac{\eta_{i,2} a_2}{2\pi d_2} \dot{\gamma}_2(t) \quad (2.86)$$

In the second step, the macroscopic state equation (2.11) is specified for the imposed strain state (2.22), which yields, under consideration of the components of the homogenized stiffness tensor and the involved influence tensors according to Appendix C.1, the following scalar equation for the time-evolution of the macroscopic shear stress  $\Sigma_{xz}$

$$\begin{aligned} \Sigma_{xz} = & \frac{3 E_s (2 - \nu_s)}{(1 + \nu_s) [3 (2 - \nu_s) + 16 (d_1 + d_2) (1 - \nu_s)]} E_{xz} \\ & + \frac{16 d_1 (1 - \nu_s)}{3(2 - \nu_s) + 16 (d_1 + d_2) (1 - \nu_s)} T_{1,x} \\ & + \frac{16 d_2 (1 - \nu_s)}{3(2 - \nu_s) + 16 (d_1 + d_2) (1 - \nu_s)} T_{2,x} \end{aligned} \quad (2.87)$$

Specifying (2.87) for the tractions (2.86) yields, under consideration of the definitions (2.31), the following compact result

$$\begin{aligned} \Sigma_{xz} = & 2 E_{xz} \left( \frac{1}{\mu_s} + \frac{1}{\mu_1} + \frac{1}{\mu_2} \right)^{-1} \\ & - \left( \frac{1}{\mu_s} + \frac{1}{\mu_1} + \frac{1}{\mu_2} \right)^{-1} \left( \frac{C_1 \eta_1}{\mu_1} + \frac{C_2 \eta_2}{\mu_2} \right) \left( \frac{a}{2} + \frac{1}{t_c} \right) \exp \left[ - \left( \frac{a}{2} + \frac{1}{t_c} \right) t \right] \\ & - \left( \frac{1}{\mu_s} + \frac{1}{\mu_1} + \frac{1}{\mu_2} \right)^{-1} \left( \frac{D_1 \eta_1}{\mu_1} + \frac{D_2 \eta_2}{\mu_2} \right) \left( \frac{a}{2} - \frac{1}{t_c} \right) \exp \left[ - \left( \frac{a}{2} - \frac{1}{t_c} \right) t \right] \end{aligned} \quad (2.88)$$

Comparing Eq. (2.88) with

$$\Sigma_{xz} = R_{xzzz}(t) 2E_{xz} \quad (2.89)$$

delivers the sought relaxation functions as

$$\begin{aligned} R_{xzzz}(t) = & \left( \frac{1}{\mu_s} + \frac{1}{\mu_1} + \frac{1}{\mu_2} \right)^{-1} \\ & - \left( \frac{1}{\mu_s} + \frac{1}{\mu_1} + \frac{1}{\mu_2} \right)^{-1} \left( \frac{\bar{C}_1 \eta_1}{\mu_1} + \frac{\bar{C}_2 \eta_2}{\mu_2} \right) \left( \frac{a}{2} + \frac{1}{t_c} \right) \exp \left[ - \left( \frac{a}{2} + \frac{1}{t_c} \right) t \right] \\ & - \left( \frac{1}{\mu_s} + \frac{1}{\mu_1} + \frac{1}{\mu_2} \right)^{-1} \left( \frac{\bar{D}_1 \eta_1}{\mu_1} + \frac{\bar{D}_2 \eta_2}{\mu_2} \right) \left( \frac{a}{2} - \frac{1}{t_c} \right) \exp \left[ - \left( \frac{a}{2} - \frac{1}{t_c} \right) t \right] \end{aligned} \quad (2.90)$$

with

$$\bar{C}_1 = -\frac{\mu_s t_c}{2\eta_1} + \left( \frac{a t_c}{2} - 1 \right) \frac{1}{2\mu_1} \left( \frac{1}{\mu_s} + \frac{1}{\mu_1} + \frac{1}{\mu_2} \right)^{-1} \quad (2.91)$$

$$\bar{D}_1 = +\frac{\mu_s t_c}{2\eta_1} - \left( \frac{a t_c}{2} + 1 \right) \frac{1}{2\mu_1} \left( \frac{1}{\mu_s} + \frac{1}{\mu_1} + \frac{1}{\mu_2} \right)^{-1} \quad (2.92)$$

$$\bar{C}_2 = -\frac{\mu_s t_c}{2\eta_2} + \left( \frac{a t_c}{2} - 1 \right) \frac{1}{2\mu_2} \left( \frac{1}{\mu_s} + \frac{1}{\mu_1} + \frac{1}{\mu_2} \right)^{-1} \quad (2.93)$$

$$\bar{D}_2 = +\frac{\mu_s t_c}{2\eta_2} - \left( \frac{a t_c}{2} + 1 \right) \frac{1}{2\mu_2} \left( \frac{1}{\mu_s} + \frac{1}{\mu_1} + \frac{1}{\mu_2} \right)^{-1} \quad (2.94)$$

The relaxation functions (2.90) contain two exponentials which are underlining the existence of the following two different characteristic relaxation times

$$\tau_{relax,I} = \left( \frac{a}{2} + \frac{1}{t_c} \right)^{-1} \quad (2.95)$$

$$\tau_{relax,II} = \left( \frac{a}{2} - \frac{1}{t_c} \right)^{-1} \quad (2.96)$$

Eqs. (2.95) and (2.96) together with the characteristic evolution of a relaxation test (discussed in the sequel) provide the motivation to re-formulate the relaxation functions (2.90) finally as

$$R_{xzzz}(t) = \mu_s - \Delta\mu \left[ 1 - A_I \exp \left( - \frac{t}{\tau_{relax,I}} \right) - A_{II} \exp \left( - \frac{t}{\tau_{relax,II}} \right) \right] \quad (2.97)$$

with

$$\Delta\mu = \mu_s \left( \frac{1}{\mu_1} + \frac{1}{\mu_2} \right) \left( \frac{1}{\mu_s} + \frac{1}{\mu_1} + \frac{1}{\mu_2} \right)^{-1} \quad (2.98)$$

$$A_I = -\frac{1}{\mu_s} \left( \frac{1}{\mu_1} + \frac{1}{\mu_2} \right)^{-1} \left( \frac{a}{2} + \frac{1}{t_c} \right) \left( \frac{\bar{C}_1 \eta_1}{\mu_1} + \frac{\bar{C}_2 \eta_2}{\mu_2} \right) \quad (2.99)$$

$$A_{II} = -\frac{1}{\mu_s} \left( \frac{1}{\mu_1} + \frac{1}{\mu_2} \right)^{-1} \left( \frac{a}{2} - \frac{1}{t_c} \right) \left( \frac{\bar{D}_1 \eta_1}{\mu_1} + \frac{\bar{D}_2 \eta_2}{\mu_2} \right) \quad (2.100)$$

Noting that  $A_I + A_{II} = 1$ , allows for the following mechanical interpretation of Eq. (2.97). Specifying (2.97) for  $t = 0$  yields

$$R_{xxx}(t=0) = \mu_s \quad (2.101)$$

Eq. (2.101) states that the effective stiffness of the composite is equal to the solid stiffness at the *beginning* of a relaxation test. Specifying (2.97) for  $t = \infty$  yields

$$R_{xxx}(t=\infty) = \mu_s - \Delta\mu \quad (2.102)$$

Comparison of Eqs. (2.101) and (2.102) shows that  $\Delta\mu$  denotes the loss of effective stiffness of the composite during the relaxation test. Finally, we note that  $A_I$  and  $A_{II}$  stand for relaxation capacities associated with the two characteristic relaxation times.

For the transition to micromechanical quantities, i. e. to Young's modulus  $E_s$  and Poisson's ratio  $\nu_s$  of the solid matrix, to interface sizes  $a_1$  and  $a_2$ , to interface viscosities  $\eta_{i,1}$  and  $\eta_{i,2}$ , as well as to interface densities  $d_1$ , and  $d_2$ , consider the definitions of  $a$  according to (2.47), of  $t_c$  according to (2.73) and of  $\mu_s$ ,  $\mu_1$ ,  $\mu_2$ ,  $\eta_1$ ,  $\eta_2$  according to (2.31). Exemplarily, this transition is carried out for the two characteristic relaxation times (2.95) and (2.96). This delivers

$$\begin{aligned} \tau_{relax,I} &= \frac{2}{\bar{a} + \sqrt{\bar{b}^2 + \frac{4 E_s^2 \pi^2 d_1 d_2}{a_1 \eta_{i,1} a_2 \eta_{i,2} (1 + \nu_s)^2}}} \\ \tau_{relax,II} &= \frac{2}{\bar{a} - \sqrt{\bar{b}^2 + \frac{4 E_s^2 \pi^2 d_1 d_2}{a_1 \eta_{i,1} a_2 \eta_{i,2} (1 + \nu_s)^2}}} \end{aligned} \quad (2.103)$$

with  $\bar{a}$  and  $\bar{b}$  reading as

$$\bar{a} = \frac{E_s \pi \left[ 3(2 - \nu_s)(a_1 \eta_{i,1} + a_2 \eta_{i,2}) + 16(1 - \nu_s)(a_1 \eta_{i,1} d_2 + a_2 \eta_{i,2} d_1) \right]}{16(1 - \nu_s^2) a_1 \eta_{i,1} a_2 \eta_{i,2}} \quad (2.104)$$

$$\bar{b} = \frac{E_s \pi \left[ 3(2 - \nu_s)(a_2 \eta_{i,2} - a_1 \eta_{i,1}) + 16(1 - \nu_s)(a_2 \eta_{i,2} d_1 - a_1 \eta_{i,1} d_2) \right]}{16(1 - \nu_s^2) a_1 \eta_{i,1} a_2 \eta_{i,2}} \quad (2.105)$$

### 2.3.4 Study of interface interaction in a relaxation test

Because the concentration-influence relations (2.8) and (2.9) contain interaction terms, it was mathematically quite challenging to derive the relaxation functions of the matrix-inclusion composite of Fig. 2.1. In the following, we evaluate our analytical results with the aim to gain insight into interface interaction. To this end, we consider properties of the solid matrix which are representative for hydroxyapatite [21]

$$E_s = 114 \text{ GPa} \quad \nu_s = 0.27 \quad (2.106)$$

In order to study the sensitivity of the relaxation function (2.97) with respect to changes in size, viscosity, and density of two interface families, we consider that the sum of the two interface densities amounts to 0.3

$$d_1 + d_2 = 0.3 \quad (2.107)$$

We will investigate all cases between  $d_1 = 0.3$  and  $d_2 = 0.0$ , on the one hand, as well as  $d_1 = 0.0$  and  $d_2 = 0.3$ , on the other hand. Because interface radius  $a_1$  and interface viscosity  $\eta_{i,1}$  appear in the analytical expressions always multiplied with each other, we consider the product  $a_1 \eta_{i,1}$  to be a constant and to amount to

$$a_1 \eta_{i,1} = 62.5 \text{ GPa}\cdot\text{h} \quad (2.108)$$

In order to study interaction among two interface families exhibiting different interface sizes and viscosities, the corresponding product  $a_2 \eta_{i,2}$ , referring to the second interface family, is considered to be a multiple of (2.108)

$$a_2 \eta_{i,2} = n \times 62.5 \text{ GPa}\cdot\text{h} \quad (2.109)$$

where  $n$  will be set equal to 2, to 5, and to 10, respectively, see Figs. 2.2, 2.3, and 2.4. The multiplication factor  $n$  can be interpreted, in the sense of the following two special cases:

- $n$  is equal to the ratio of the two interface radii,  $n = a_2/a_1$ , provided that the two interface viscosities are the same  $\eta_{i,1} = \eta_{i,2}$ .
- $n$  is equal to the ratio of the two interface viscosities,  $n = \eta_{i,2}/\eta_{i,1}$ , provided that the two interface radii are the same  $a_1 = a_2$ .

As for discussing the characteristic relaxation times (2.95) and (2.96), see also (2.103), (2.104), and (2.105), and the corresponding relaxation capacities (2.99) and (2.100), it is useful to study limit cases  $d_1 \rightarrow 0$  and  $d_2 \rightarrow 0$ . Considering the limit case that all interfaces belong to the first family ( $d_2 \rightarrow 0$ ) yields

$$\lim_{d_2 \rightarrow 0} A_I = 1 \quad \lim_{d_2 \rightarrow 0} \tau_{relax,I} = \frac{a_1 \eta_{i,1}}{E_s} \frac{16(1 - \nu_s^2)}{\pi[3(2 - \nu_s) + 16d_1(1 - \nu_s)]} \quad (2.110)$$

$$\lim_{d_2 \rightarrow 0} A_{II} = 0 \quad \lim_{d_2 \rightarrow 0} \tau_{relax,II} = \frac{a_2 \eta_{i,2}}{E_s} \frac{16(1 - \nu_s^2)}{3\pi(2 - \nu_s)} \quad (2.111)$$

Eqs. (2.110) and (2.111) indicate that the relaxation function (2.97) degenerates, for  $d_2 \rightarrow 0$ , such that it contains only the one exponential involving  $\tau_{relax,I}$  and this characteristic time is equal to the one which was derived in [31] for interfaces of identical size and viscosity, see the white square in Figs. 2.2(a) and (b), 2.3(a) and (b), as well as 2.4(a) and (b). The second characteristic time,  $\tau_{relax,II}$ , has, in the limit  $d_2 \rightarrow 0$ , no physical meaning, because the related relaxation capacity  $A_{II}$  vanishes, see (2.111) and the black circles in Figs. 2.2(a) and (b), 2.3(a) and (b), as well as 2.4(a) and (b). Considering the other limit case that all interfaces belong to the second family ( $d_1 \rightarrow 0$ ) yields by analogy to (2.110) and (2.111)

$$\lim_{d_1 \rightarrow 0} A_I = 0 \quad \lim_{d_1 \rightarrow 0} \tau_{relax,I} = \frac{a_1 \eta_{i,1}}{E_s} \frac{16(1 - \nu_s^2)}{3\pi(2 - \nu_s)} \quad (2.112)$$

$$\lim_{d_1 \rightarrow 0} A_{II} = 1 \quad \lim_{d_1 \rightarrow 0} \tau_{relax,II} = \frac{a_2 \eta_{i,2}}{E_s} \frac{16(1 - \nu_s^2)}{\pi[3(2 - \nu_s) + 16d_2(1 - \nu_s)]} \quad (2.113)$$

Again, Eqs. (2.110) and (2.111) indicate that the relaxation function (2.97) degenerates, for  $d_1 \rightarrow 0$ , such that it contains only the one exponential involving  $\tau_{relax,II}$  and this characteristic time is equal to the one which was derived in [31] for interfaces of identical size and viscosity, see the white circle in Figs. 2.2(a)

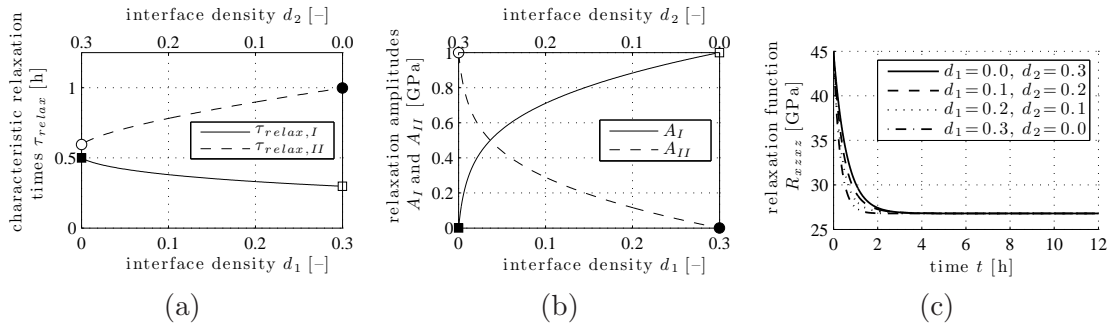


Figure 2.2: Sensitivity study regarding relaxation function (2.97): (a) characteristic relaxation times according to (2.103) as a function of interface densities (2.107), (b) relaxation capacities according to (2.99) and (2.100) as a function of interface densities (2.107), and (c) relaxation function (2.97) as a function of time, for four different partitions of interface density;  $E_s = 114$  GPa,  $\nu_s = 0.27$ ,  $a_1 \eta_{i,1} = 62.5$  GPa·h,  $a_2 \eta_{i,2} = 2 \times a_1 \eta_{i,1}$ ,  $d_1 + d_2 = 0.3$

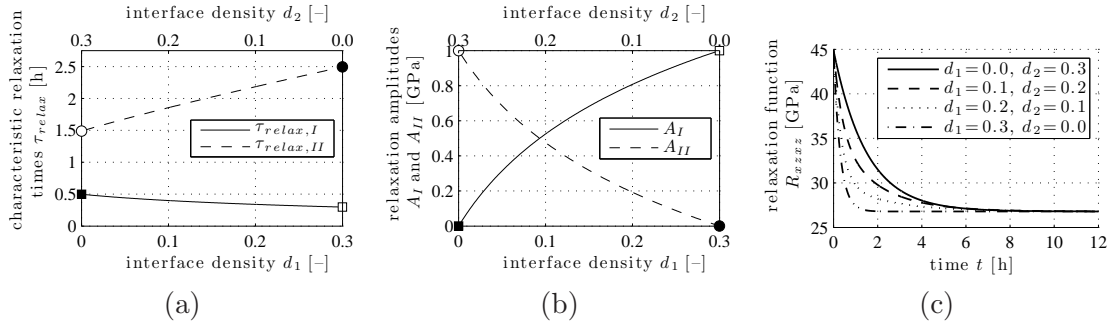


Figure 2.3: Sensitivity study regarding relaxation function (2.97): (a) characteristic relaxation times according to (2.103) as a function of interface densities (2.107), (b) relaxation capacities according to (2.99) and (2.100) as a function of interface densities (2.107), and (c) relaxation function (2.97) as a function of time, for four different partitions of interface density;  $E_s = 114$  GPa,  $\nu_s = 0.27$ ,  $a_1 \eta_{i,1} = 62.5$  GPa·h,  $a_2 \eta_{i,2} = 5 \times a_1 \eta_{i,1}$ ,  $d_1 + d_2 = 0.3$

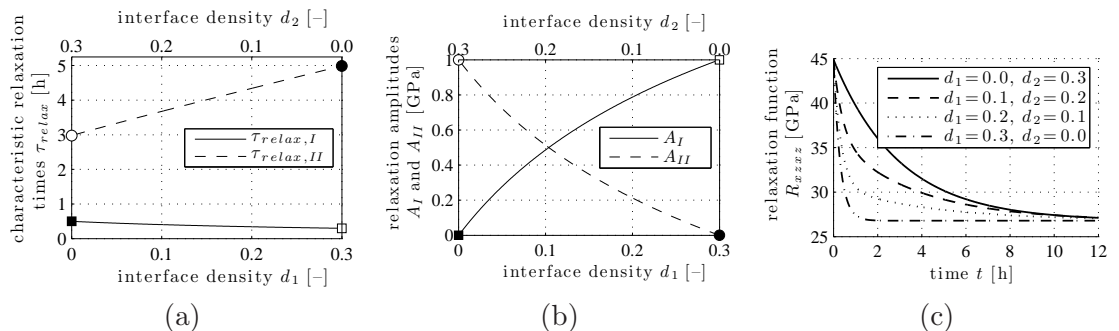


Figure 2.4: Sensitivity study regarding relaxation function (2.97): (a) characteristic relaxation times according to (2.103) as a function of interface densities (2.107), (b) relaxation capacities according to (2.99) and (2.100) as a function of interface densities (2.107), and (c) relaxation function (2.97) as a function of time, for four different partitions of interface density;  $E_s = 114$  GPa,  $\nu_s = 0.27$ ,  $a_1 \eta_{i,1} = 62.5$  GPa·h,  $a_2 \eta_{i,2} = 10 \times a_1 \eta_{i,1}$ ,  $d_1 + d_2 = 0.3$

and (b), 2.3(a) and (b), as well as 2.4(a) and (b). The first characteristic time,  $\tau_{relax,I}$ , has, in the limit  $d_1 \rightarrow 0$ , no physical meaning, because the corresponding relaxation capacity  $A_I$  vanishes, see (2.112) and the black squares in Figs. 2.2(a) and (b), 2.3(a) and (b), as well as 2.4(a) and (b). Between the two discussed limits, a continuous transition of characteristic relaxation times and corresponding relaxation capacities is obtained, see Figs. 2.2(a) and (b), 2.3(a) and (b), as well as 2.4(a) and (b).

Also the relaxation functions exhibits a continuous transition from the limit case  $d_1 = 0.0$  and  $d_2 = 0.3$ , i. e. from one interface family with a larger interface radius and/or larger interface viscosity, to the other limit case  $d_1 = 0.3$  and  $d_2 = 0.0$ , i. e. to one interface family with a smaller interface radius and/or smaller interface viscosity, see Figs. 2.2(c), 2.3(c), and 2.4(c). Since dislocation processes evolve faster at smaller scales and slower at larger scales, the asymptotic (“relaxed”) state is reached the faster, the smaller or less viscous interfaces are present at the microstructure of the composite.

In the mentioned transition regime from  $d_1 = 0.0$  and  $d_2 = 0.3$  to  $d_1 = 0.3$  and  $d_2 = 0.0$ , our analytical results strongly underline interaction between the two interface families. The reason for this behavior is discussed next.

## 2.4 Identification of the mechanism responsible for interaction among interfaces, and concluding remarks

In order to study interaction between interfaces of different size, viscosity, and density, we have recalled the derivation of creep functions, see (2.20), and we have newly derived relaxation functions, see (2.97), both for a matrix-interface composite containing two interface families. The creep functions (2.20) contain two exponentials underlining the existence of two different characteristic creep times, see Eqs. (2.21). The latter highlight that each of the two interface families is associated with one of the two characteristic creep times. In other words, the characteristic creep times suggest that the two interface families do not interact. The relaxation functions (2.90) also contain two exponentials which are – again – underlining the existence of two different characteristic relaxation times, see Eqs. (2.103). The latter highlight that properties of both interface families influence both characteristic relaxation times. In other words, the characteristic relaxation times suggest that the two interface families are interacting, see also Figs. 2.2, 2.3, and 2.4. These

results pose the questions why a matrix-interface composite exhibits interaction of interfaces provided that it is subjected to uniform strain boundary conditions, while interfaces are *not* interacting under uniform stress boundary conditions.

In order to clarify the interaction properties of different interfaces, it is useful to consider average rules for stresses and strains. For any multiphase composite with volume  $\Omega$ , which is subjected either to uniform stress or strain boundary conditions, they read as [56]

$$\underline{\underline{\Sigma}} = \frac{1}{|\Omega|} \int_{\Omega} \underline{\underline{\sigma}}(\underline{x}) dV \quad (2.114)$$

$$\underline{\underline{E}} = \frac{1}{|\Omega|} \int_{\Omega} \underline{\underline{\varepsilon}}(\underline{x}) dV \quad (2.115)$$

Next, we specify Eqs. (2.114) and (2.115) for a matrix-interface composite. In this context, it is important to consider that the interfaces are two-dimensional, i. e. interfaces occupy a vanishing volume such that the solid matrix fills the entire volume of the composite:  $\Omega = \Omega_s$ . Because finite interface tractions are acting in a vanishing interface volume, the stress average rule (2.114) simplifies to [73]

$$\underline{\underline{\Sigma}} = \frac{1}{|\Omega|} \int_{\Omega_s} \underline{\underline{\sigma}}(\underline{x}) dV \quad (2.116)$$

Note that the integral in (2.116) refers to the volume of the solid. Eq. (2.116) underlines that the macrostress  $\underline{\underline{\Sigma}}$  is equal to the average stress in the solid matrix. The situation is different when it comes to the strain average rule, where the dislocations contribute to the macrostrain [73]

$$\underline{\underline{E}} = \frac{1}{|\Omega|} \left( \int_{\Omega_s} \underline{\underline{\varepsilon}}(\underline{x}) dV + \sum_j \int_{C_j} \llbracket \underline{\xi} \rrbracket_j \otimes \underline{n}_j dS \right) \quad (2.117)$$

In Eq. (2.117), summation index  $j$  runs over all  $C_j$  interfaces of the studied composite, and  $\underline{n}_j$  is standing for the unit normal to the  $j$ -th interface. Eq. (2.117) underlines that the macrostrain is decomposed into (i) the average strain in the solid matrix and (ii) a contribution related to the dislocations of the interfaces. Notably, the average stress of the solid, see the stress average rule (2.116), and the average strain of the solid, see the strain average rule (2.117), are related via

generalized Hooke's law reading as

$$\left( \frac{1}{|\Omega|} \int_{\Omega_s} \underline{\underline{\sigma}}(\underline{x}) dV \right) = \underline{\underline{C}}_s : \left( \frac{1}{|\Omega|} \int_{\Omega_s} \underline{\underline{\varepsilon}}(\underline{x}) dV \right) \quad (2.118)$$

The stress average rule (2.116) and the strain average rule (2.117) allow for the sought interpretation of interface interaction, described next. Given the matrix-interface morphology illustrated in Fig. 2.1, each interface family “feels” the stress and strain states of the surrounding solid matrix, and they drive the evolution of interfacial dislocations and tractions. Under uniform stress or strain boundary conditions, the interaction between the interfacial dislocations, on the one hand, and the average stress and strain states of the solid matrix, on the other hand, are markedly different:

- Under uniform stress boundary conditions, average stresses and strains in the solid are controlled from outside of the composite; in more detail, the average stress of the solid matrix is equal to the externally controlled loading, see the stress average rule (2.116). Generalized Hooke's law (2.118), in turn, underlines that also the average strain in the solid matrix is directly proportional to the externally prescribed loading. This implies that the dislocation histories of both interface families evolve under the externally controlled average stress and strain states of the solid matrix. Hence, the interfaces do not interact, because increasing dislocations do not change the average stress and strain states of the solid matrix, but result only in an increase of the macrostrain, see (2.117).
- Under uniform strain boundary conditions, average stresses and strains in the solid are *not* controlled from outside of the composite. Instead, they are depending on the dislocation states of all interfaces, resulting in interface interaction. This situation becomes specifically clear, when considering the special case of relaxation, where a strain state is suddenly imposed on the composite at time  $t = 0$  and kept constant thereafter. At the time instant of sudden loading, the dislocations are equal to zero, because the viscous behavior of the interfaces requires finite time intervals for the development of dislocations. Given vanishing dislocations at  $t = 0$ , the average strain of the solid matrix is equal to the macrostrain; consider  $[\underline{\underline{\xi}}]_1 = [\underline{\underline{\xi}}]_2 = 0$  in the strain average rule (2.117). With increasing time, the dislocations increase, and they take over part of the imposed macrostrain, see (2.117), such that

the average strain of the solid matrix decreases. According to (2.118), also the average stress level in the solid matrix decreases (“relaxes”) proportionally. In other words, evolving dislocations of one specific interface result in a reduction of the average stress and strain states in the solid matrix, and this is “felt” by all other interfaces. This explains the interaction underlined by the coupled relaxation times (2.103).

We here investigated the interaction between two different interface families, but the conclusions can be extended to consideration of  $n$  interface families. The creep functions contain  $n$  exponentials with  $n$  different characteristic creep times, whereby each interface family influences just one characteristic creep time. Also the relaxation functions contain  $n$  exponentials with  $n$  different characteristic relaxation times, but all interface families influence each and every characteristic relaxation time. In the herein studied special case of two interface families, the characteristic times involve square-root expressions, stemming from the solution of a second-order polynomial. In the general case of  $n$  interface families, the characteristic relaxation times involve  $n$ th-order root expressions, stemming from the solution of a  $n$ th-order polynomial. This underlines that macroscopic creep tests are conceptually clearly preferable for top-down identification of interfacial properties.

## 2.5 Nomenclature

$a_1$	radius of first interface family
$a_2$	radius of second interface family
$\underline{\underline{A}}_j$	third-order strain concentration tensor describing the concentration of macroscopic strain into the dislocation of interfaces; $j = 1, 2$ refers to the two interface families
$\underline{\underline{A}}_j^\Sigma$	third-order influence tensor describing the influence of macroscopic stress on the dislocation of interfaces; $j = 1, 2$ refers to the two interface families
$\underline{\underline{B}}_j$	third-order influence tensor describing the influence of interface traction on the macroscopic stress; $j = 1, 2$ refers to the two interface families
$\underline{\underline{B}}_j^\Sigma$	third-order influence tensor describing the influence of interface traction on the macroscopic strain; $j = 1, 2$ refers to the two interface families
$\underline{\underline{C}}_s$	fourth-order elastic stiffness tensor of solid
$\underline{\underline{C}}_s^{-1}$	inverse of $\underline{\underline{C}}_s$

$\underline{\underline{C}}_{hom}$	fourth-order homogenized stiffness tensor of matrix-interface composite
$\underline{\underline{C}}_{hom}^{-1}$	inverse of $\underline{\underline{C}}_{hom}$
$d_j$	interface density parameter; $j = 1, 2$ refers to the two interface families
$\underline{e}_1, \underline{e}_3$	unit base vectors of Cartesian coordinate system
$\underline{\underline{E}}$	second-order tensor of macroscopic strain
$E_{xz}$	shear component of $\underline{\underline{E}}$
$E_s$	Young's modulus of the solid
$j$	index for interface phase
$\underline{\underline{I}}$	symmetric fourth-order identity tensor
$\underline{\underline{I}}_{dev}$	deviatoric part of $\underline{\underline{I}}$
$\underline{\underline{I}}_{vol}$	volumetric part of $\underline{\underline{I}}$
$J_{xzzz}$	creep function
$\mathcal{L}$	Laplace transformation operator
$\mathcal{L}^{-1}$	back transformation operator from Laplace space to time domain
$\mathcal{N}_j$	number of interfaces per unit volume of a matrix-interface composite; $j = 1, 2$ refers to the two interface families
$\underline{n}$	outward unit normal at any point of the boundary of the composite
$\underline{n}_j$	unit vector in normal direction of the interfaces; $j = 1, 2$ refers to the two interface families
$R_{xzzz}$	relaxation function
$s$	index for solid phase / Laplace space parameter
$\underline{T}_j$	interface traction vector; $j = 1, 2$ refers to the two interface families
$\underline{\underline{T}}_i$	fourth-order morphology tensor for 2D interface inclusion (“sharp crack” morphology)
$T_{j,1}$	shear component of traction vector $\underline{T}_j$ ; $j = 1, 2$ refers to the two interface families
$x, y, z$	Cartesian coordinates
$\underline{x}$	position vector
$\gamma$	constant related to $E_{xz}$
$\gamma_j$	function related to interface dislocation; $j = 1, 2$ refers to the two interface families
$\gamma_{j,h}$	solution of homogeneous differential equation for $\gamma_j$ ; $j = 1, 2$ refers to the two interface families
$\gamma_{j,p}$	particulate integral of inhomogeneous differential equation for $\gamma_j$ ; $j = 1, 2$ refers to the two interface families

---

$\Gamma_j$	Laplace transform of function $\gamma_j$ ; $j = 1, 2$ refers to the two interface families
$\delta$	Kronecker delta
$\underline{\underline{\varepsilon}}$	second-order tensor of microscopic linear strain
$\eta_{i,j}$	viscosity of the interfaces; $j = 1, 2$ refers to the two interface families
$\eta_j$	constant related to interface viscosity; $j = 1, 2$ refers to the two interface families
$\mu_s$	shear modulus of isotropic solid matrix
$\mu_j$	stiffness constant related to the interfaces; $j = 1, 2$ refers to the two interface families
$\nu_s$	Poisson's ratio of isotropic solid matrix
$\underline{\xi}$	displacement vector
$[\underline{\xi}]_j$	dislocation vector of interfaces; $j = 1, 2$ refers to the two interface families
$[\underline{\xi}]_{j,1}$	shear component of $[\underline{\xi}]_j$
$[\underline{\xi}]_{j,3}$	normal component of $[\underline{\xi}]_j$
$\underline{\underline{\sigma}}$	second-order tensor of microscopic Cauchy stresses
$\underline{\underline{\Sigma}}$	second-order tensor of macroscopic Cauchy stresses
$\Sigma_{xz}$	shear component of $\underline{\underline{\Sigma}}$
$\tau_{creep}$	characteristic time of creep function
$\tau_{relax}$	characteristic time of relaxation function
$\Omega$	volume of the matrix-interface composite
$\Omega_s$	volume occupied by the solid phase
$\partial$	partial derivative
:	second-order tensor contraction
$\bullet$	partial derivative with respect to time ("rate"), of quantity " $\bullet$ "
$\otimes$	dyadic product

## Chapter 3

# Interfacial micromechanics

## assessment of classical rheological models I: Single interface size and viscosity

### 3.1 Introduction

In 1874, Boltzmann introduced the concept of creep functions as well as the associated superposition principle, and he confirmed these groundbreaking ideas by an initial experimental campaign [7]. Ever since, these ideas have remained the fundament of the theory of viscoelasticity, which has been developed up to high mathematical maturity [8, 9, 10]. In order to keep things simple, often exponential creep functions are considered, and they are standardly related to the simple rheological models composed of linear springs and dashpots. Their simplest versions exhibit a parallel arrangement of one spring and one dashpot (the so-called Kelvin-Voigt model) [74, 75], or a serial arrangement of one spring and one dashpot (the so-called Maxwell model) [76]. Slightly more complex arrangements of spring and dashpots are normally called standard linear solid models. They can be either represented as a serial arrangement of a Kelvin-Voigt unit and an additional spring (Kelvin-Voigt representation or Zehner model [77]), or as a serial arrangement of a Maxwell unit and an additional spring (Maxwell representation). However, such simple models do not contain any direct information on microstructural effect at the origin of creep, such as the flow of water along thin layers within the texture of

hydrated bio- or geomaterials [11, 12, 13, 14, 15, 16, 18, 19, 20, 21, 22, 23, 71]. Aiming exactly at the aforementioned direct consideration of viscous “micro-” interfaces when mathematically describing macroscopic creep behaviors, we recently developed a micromechanical formulation for matrix-interface composites consisting (i) of a continuous isotropic linear elastic solid matrix and (ii) of embedded parallel interfaces filled by a liquid crystal exhibiting a linear viscous behavior [31], see also Fig. 3.1. The obvious question arising then is: How does such a micromechanical formulation and the microstructural quantities appearing therein relate to the classical rheological models made up of springs and of dashpots? As an answer to this question, we here aim at establishing relations between microstructural quantities, such as interface size, interface density, interface viscosity, as well as elastic properties of the solid material phase (see Fig. 3.1), on the one hand, and spring stiffnesses and dashpot viscosities of macroscopic rheological models (as illustrated in Figs. 3.2 and 3.3), on the other hand. Therefore, it suffices to consider macroscopic pure shear strains in planes orthogonal to the viscous interfaces (with normals  $\underline{e}_3$ ), i.e. in the  $\underline{x}_1, \underline{x}_3$ -plane or in the  $\underline{x}_2, \underline{x}_3$ -plane of Fig. 3.1. Namely, in the chosen base frame  $\underline{e}_1, \underline{e}_2, \underline{e}_3$ , only the aforementioned shear strain components are related to creep deformation, and hence, we here focus on relations between macroscopic strains

$$\underline{\underline{E}} = E_{13} (\underline{e}_1 \otimes \underline{e}_3 + \underline{e}_3 \otimes \underline{e}_1) \quad (3.1)$$

and corresponding stresses

$$\underline{\underline{\Sigma}} = \Sigma_{13} (\underline{e}_1 \otimes \underline{e}_3 + \underline{e}_3 \otimes \underline{e}_1) \quad (3.2)$$

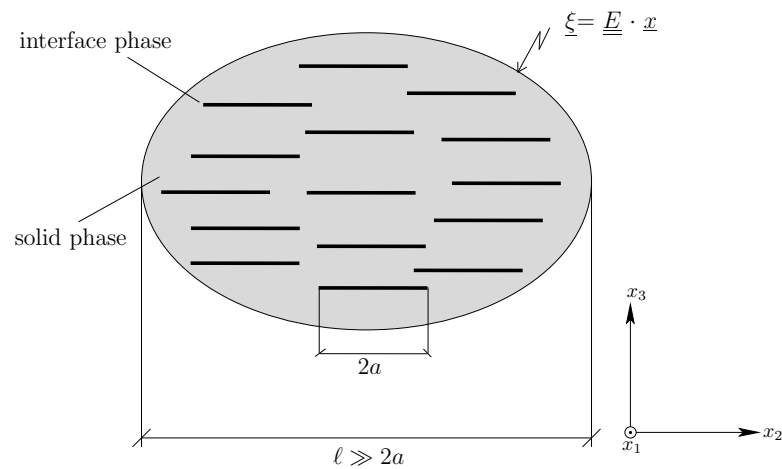


Figure 3.1: Matrix-interface composite consisting of continuous isotropic solid matrix and parallel 2D interfaces; 2D sketch of 3D representative volume elements

When it comes to the rheological models as depicted in Figs. 3.2 and 3.3, it is noteworthy that they refer to the behavior of a unit cube of a tested material, i.e. the “force” acting on the rheological model is equal to the shear traction acting on the material unit cube, and the “elongation” of the spring-dashpot model is equal to the engineering shear strain of the material unit cube.

In order to establish the aforementioned link between micromechanics and classical rheology, we will, in the remainder of this paper, (i) derive differential equations describing the material behavior in terms of overall stresses and strains defined on representative volume elements, and (ii) carry out a dissipation analysis, where we will consider the fundamental thermodynamics definition of the dissipation  $\mathcal{D}$ , which is equal to the rate of work of the external forces,  $\underline{\underline{\Sigma}} : \underline{\underline{\dot{E}}}$ , minus the rate of elastic or free “Helmholtz” energy  $\dot{\Psi}$

$$\mathcal{D} = \underline{\underline{\Sigma}} : \underline{\underline{\dot{E}}} - \dot{\Psi} \quad (3.3)$$

This will be developed, in three consecutive sections, for (i) the Kelvin-Voigt representation of the standard linear solid model, for (ii) the Maxwell representation of the standard linear solid model, and for (iii) a matrix-interface composite. Corresponding analytical formulations will allow us to relate rheological spring stiffnesses and the dashpot viscosities of standard linear solid models, to microstructural features of a matrix-interface composite. It will also allow for a micromechanical interpretation of the stresses and strains which are formally associated with the rheological springs and dashpots, and for a micromechanical illustration of the energy dissipating in the dashpots. Implications for preferential choices of rheological parameters, and their relation to experiments, will be covered, thereafter, in the Discussion section.

## 3.2 Review of rheological “spring-dashpot” models

### 3.2.1 Kelvin-Voigt representation of standard linear solid

The Kelvin-Voigt representation of the standard linear solid consists of a Kelvin-Voigt unit (i.e. parallelly set spring and dashpot elements) in series with an additional elastic spring (see Fig. 3.2). Here, we focus on pure shear deformation, so that rheological shear stresses  $\tau$  and strains  $\gamma$  are related to the following stress

and strain tensors by analogy to (3.2) and (3.1)

$$\underline{\underline{\Sigma}} = \tau (\underline{e}_1 \otimes \underline{e}_3 + \underline{e}_3 \otimes \underline{e}_1) \quad \text{and} \quad \underline{\underline{E}} = \frac{1}{2} \gamma (\underline{e}_1 \otimes \underline{e}_3 + \underline{e}_3 \otimes \underline{e}_1) \quad (3.4)$$

The overall shear deformation of the rheological model,  $\gamma$ , can be decomposed into

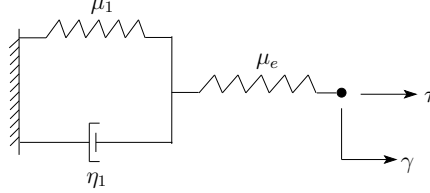


Figure 3.2: Kelvin-Voigt representation of standard linear solid, used to model time-dependent behavior under pure shear see (3.4)

a dissipative portion related to the Kelvin-Voigt unit ( $\gamma_1$ ) and an elastic portion related to the single spring ( $\gamma_e$ ),

$$\gamma = \gamma_1 + \gamma_e \quad (3.5)$$

The overall shear stress  $\tau$ , in turn, is transferred both through the Kelvin-Voigt unit ( $\tau_1 = \tau$ ) and through the elastic spring ( $\tau_e = \tau$ ),

$$\tau = \tau_1 = \tau_e \quad (3.6)$$

The shear stress acting on the Kelvin-Voigt unit,  $\tau_1$ , can be decomposed into the shear stress acting on the spring,  $\tau_1^\mu$ , and into the one acting on the dashpot,  $\tau_1^\eta$ ,

$$\tau_1 = \tau_1^\mu + \tau_1^\eta \quad (3.7)$$

where indexes  $\mu$  and  $\eta$  refer to the spring and to the dashpot, respectively.

Derivation of a differential equation in  $\sigma$  and  $\gamma$  describing the constitutive behavior of the rheological model requires individual constitutive laws for all three rheological devices. Denoting the spring stiffness of the additional elastic spring as  $\mu_e$ , and the one of the Kelvin-Voigt spring as  $\mu_1$ , as well as the dashpot viscosity as  $\eta_1$ , see Fig. (3.2), the individual constitutive laws read as

$$\tau_1^\mu = \mu_1 \gamma_1, \quad \tau_1^\eta = \eta_1 \dot{\gamma}_1, \quad \tau_e = \mu_e \gamma_e \quad (3.8)$$

where a dot is standing for the time derivative  $\dot{\bullet} = \partial \bullet / \partial t$ . The sought differential equation is obtained by combining Eqs. (3.5) to (3.8), with the aim to eliminate

the individual stress combinations  $\tau_1^\mu$  and  $\tau_1^\eta$  as well as the individual strain combinations  $\gamma_1$  and  $\gamma_e$ . To this end, Eq. (3.7) is specified for (3.5), (3.6), and (3.8), and the resulting expression is divided by  $\eta_1$

$$\frac{\tau}{\eta_1} = \frac{\mu_1}{\eta_1} \gamma_1 + \dot{\gamma}_1 \quad (3.9)$$

Next, the last Eq. (3.8) is specified for (3.6) and solved for  $\gamma_e$ , yielding  $\frac{\tau}{\mu_e} = \gamma_e$ . The equality is modified in two different directions: firstly, we consider its time derivative

$$\frac{\dot{\tau}}{\mu_e} = \dot{\gamma}_e \quad (3.10)$$

and, secondly, we consider it multiplied by  $\mu_1/\eta_1$

$$\frac{\tau \mu_1}{\mu_e \eta_1} = \frac{\mu_1}{\eta_1} \gamma_e \quad (3.11)$$

The differential equation describing the constitutive behavior of the rheological model follows from summing up Eqs. (3.9) to (3.11) and from consideration of (3.5) as well as of its time derivative,  $\dot{\gamma} = \dot{\gamma}_1 + \dot{\gamma}_e$ , as

$$\frac{\dot{\tau}}{\mu_e} + \tau \frac{\mu_1}{\eta_1} \left( \frac{1}{\mu_1} + \frac{1}{\mu_e} \right) = \dot{\gamma} + \frac{\mu_1}{\eta_1} \gamma \quad (3.12)$$

Eq. (3.12) is a first-order ordinary differential equation in the overall shear stress  $\tau$  and the overall shear strain  $\gamma$ .

Specification of the dissipation  $\mathcal{D}$  according to (3.3) for the Kelvin-Voigt representation of the standard linear solid model requires expressions for the rate of work of the external forces,  $\dot{W}_{ext}$ , and the rate of elastic internal energy  $\dot{\Psi}$ . The former is simply equal to “force”  $\tau$  acting on the rheological model times the “elongation rate”  $\dot{\gamma}$ , i.e. the shear stress  $\tau$  times the rate of the engineering strain,  $\dot{\gamma}$ ,

$$\dot{W}_{ext} = \tau \dot{\gamma} \quad (3.13)$$

Elastic internal energy  $\Psi$ , in turn, is stored in the two springs. In both cases the energy is equal to 1/2 times the spring’s force multiplied with its elongation; under consideration of (3.8) we obtain

$$\Psi = \frac{1}{2} \tau_1^\mu \gamma_1 + \frac{1}{2} \tau_e \gamma_e = \frac{1}{2} \gamma_1 \mu_1 \gamma_1 + \frac{1}{2} \gamma_e \mu_e \gamma_e \quad (3.14)$$

Taking the time derivative of (3.14), and consideration of (3.8), delivers the sought rate of elastic internal energy as

$$\dot{\Psi} = \mu_1 \gamma_1 \dot{\gamma}_1 + \mu_e \gamma_e \dot{\gamma}_e = \tau_1^\mu \dot{\gamma}_1 + \tau_e \dot{\gamma}_e \quad (3.15)$$

The dissipation finally follows from specification of (3.3) for (3.13) and (3.15). This yields, under consideration of (3.6), of (3.5) in the form  $\dot{\gamma} - \dot{\gamma}_e = \dot{\gamma}_1$ , and of (3.7) in the form  $\tau - \tau_1^\mu = \tau_1^\eta$ ,

$$\mathcal{D} = \tau (\dot{\gamma} - \dot{\gamma}_e) - \tau_1^\mu \dot{\gamma}_1 = (\tau - \tau_1^\mu) \dot{\gamma}_1 = \tau_1^\eta \dot{\gamma}_1 \quad (3.16)$$

Eq. (3.16) underlines that energy dissipates exclusively in the dashpot.

### 3.2.2 Maxwell representation of standard linear solid

The Maxwell representation of the standard linear solid consists of a Maxwell unit (i.e. serially set spring and dashpot elements) in parallel with an additional elastic spring (see Fig. 3.3). Here, it is considered to represent a piece of material under pure shear, see (3.4).

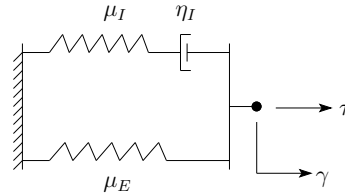


Figure 3.3: Maxwell representation of standard linear solid

The overall shear stress of the rheological model,  $\tau$ , can be decomposed into the shear stress of the Maxwell unit ( $\tau_I$ ) and into the one of the elastic spring ( $\tau_E$ ),

$$\tau = \tau_I + \tau_E \quad (3.17)$$

The overall shear deformation  $\gamma$ , in turn, is equal to the deformation of the Maxwell unit ( $\gamma_I = \gamma$ ) and to the deformation of the elastic spring ( $\gamma_E = \gamma$ ),

$$\gamma = \gamma_I = \gamma_E \quad (3.18)$$

The shear deformation of the Maxwell unit,  $\gamma_I$ , can be decomposed into the shear deformation of the spring,  $\gamma_I^\mu$ , and into the one of the dashpot,  $\gamma_I^\eta$ ,

$$\gamma_I = \gamma_I^\mu + \gamma_I^\eta \quad (3.19)$$

where indexes  $\mu$  and  $\eta$  refer to the spring and to the dashpot, respectively.

Derivation of a differential equation in  $\tau$  and  $\gamma$  describing the constitutive behavior of the rheological model requires individual constitutive laws for all three rheological devices. Denoting the spring stiffness of the additional elastic spring as  $\mu_E$ , and the one of the Maxwell spring as  $\mu_I$ , as well as the dashpot viscosity as  $\eta_I$ , the individual constitutive laws read by analogy to (3.8) as

$$\tau_I = \mu_I \gamma_I^\mu, \quad \tau_I = \eta_I \dot{\gamma}_I^\eta, \quad \tau_E = \mu_E \gamma_E \quad (3.20)$$

The sought differential equation is obtained by combining Eqs. (3.17) to (3.20), with the aim to eliminate the individual strain combinations  $\gamma_I^\mu$  and  $\gamma_I^\eta$ , as well as the individual stress combinations  $\tau_I$  and  $\tau_E$ . To this end, the time derivative of (3.19) is specified for  $\dot{\gamma}_I^\mu$  and  $\dot{\gamma}_I^\eta$  from (3.20), delivering under consideration of (3.18)

$$\frac{\dot{\tau}_I}{\mu_I} + \frac{\tau_I}{\eta_I} = \dot{\gamma} \quad (3.21)$$

Next, the last Eq. (3.20) is specified for (3.18), and the resulting equality,  $\tau_E = \mu_E \gamma$ , is modified in two different directions: firstly, we consider it multiplied with  $\frac{1}{\eta_I}$ ,

$$\frac{\tau_E}{\eta_I} = \frac{\mu_E \gamma}{\eta_I} \quad (3.22)$$

and, secondly, we consider its time derivative, multiplied with  $\frac{1}{\mu_I}$

$$\frac{\dot{\tau}_E}{\mu_I} = \frac{\mu_E \dot{\gamma}}{\mu_I} \quad (3.23)$$

The differential equation describing the constitutive behavior of the rheological model follows from summing up Eqs. (3.21) to (3.23) and from consideration of (3.17) as well as of its time derivative,  $\dot{\tau} = \dot{\tau}_I + \dot{\tau}_E$ , as

$$\frac{1}{\mu_I} \dot{\tau} + \frac{1}{\eta_I} \tau = \dot{\gamma} \left( 1 + \frac{\mu_E}{\mu_I} \right) + \frac{\mu_E}{\eta_I} \gamma \quad (3.24)$$

Eq. (3.24) is a first-order ordinary differential equation in the overall shear stress  $\tau$  and the overall shear strain  $\gamma$ .

Specification of the dissipation  $\mathcal{D}$  according to (3.3) for the Maxwell representation of the standard linear solid model requires expressions for the rate of work of the external forces,  $\dot{W}_{ext}$ , and the rate of elastic internal energy  $\dot{\Psi}$ . The former reads by analogy to (3.13) as

$$\dot{W}_{ext} = \tau \dot{\gamma} \quad (3.25)$$

Elastic internal energy  $\Psi$ , in turn, is stored in the two springs. In both cases the energy is equal to 1/2 times the spring's force multiplied with its elongation; under consideration of (3.20) we obtain

$$\Psi = \frac{1}{2} \tau_I \gamma_I^\mu + \frac{1}{2} \tau_E \gamma_E = \frac{1}{2} \gamma_I^\mu \mu_I \gamma_I^\mu + \frac{1}{2} \gamma_E \mu_E \gamma_E \quad (3.26)$$

Taking the time derivative of (3.26) and combining (3.20) delivers the sought rate of elastic internal energy as

$$\dot{\Psi} = \mu_I \gamma_I^\mu \dot{\gamma}_I^\mu + \mu_E \gamma_E \dot{\gamma}_E = \tau_I \dot{\gamma}_I^\mu + \tau_E \dot{\gamma}_E \quad (3.27)$$

The dissipation finally follows from specification of (3.3) for (3.25) and (3.27). This yields, under consideration of (3.18), of (3.17) in the form of  $\tau - \tau_E = \tau_I$ , and of (3.19) in the form  $\dot{\gamma}_I - \dot{\gamma}_I^\mu = \dot{\gamma}_I^\eta$

$$\mathcal{D} = \dot{\gamma}_I (\tau - \tau_E) - \tau_I \dot{\gamma}_I^\mu = \tau_I (\dot{\gamma}_I - \dot{\gamma}_I^\mu) = \tau_I \dot{\gamma}_I^\eta \quad (3.28)$$

Eq. (3.28) underlines that energy dissipates exclusively in the dashpot.

### 3.3 Matrix-interface micromechanics

#### 3.3.1 Materials representation and constitutive relations

Consider a matrix-interface composite consisting of one solid phase and of one interface phase comprising the entity of all viscous fluid layers (Fig. 3.1). The solid matrix phase exhibits linear elastic behavior characterized by an isotropic stiffness tensor  $\underline{\underline{C}}_s$

$$\underline{\underline{\sigma}}(\underline{x}) = \underline{\underline{C}}_s : \underline{\underline{\varepsilon}}(\underline{x}) \quad (3.29)$$

with  $\underline{\underline{\sigma}}(\underline{x})$  and  $\underline{\underline{\varepsilon}}(\underline{x})$  as Cauchy microstresses and linear microstrains at any position  $\underline{x}$  in the solid phase. As regards the interfaces, we consider that molecular ordering-related joining forces prevent the interfaces from opening, hence dislocations in interface normal direction  $\underline{e}_3$  vanish  $[[\xi_3]] = 0$ . The component of the traction

vector acting in the interface plane,  $T_1$ , is related by a linear viscous law to the dislocation rate  $[\dot{\xi}_1]$

$$T_1 = \eta [\dot{\xi}_1] \quad (3.30)$$

where  $\eta$  denotes a viscosity constant with physical dimension [Stress  $\times$  Time/Length], and where index 1 stands for the in-plane tangential direction aligned with the macroscopic loading, see (3.2) and (3.1).

In order to derive a differential equation describing the constitutive behavior of the studied composite in terms of macroscopic stress  $\Sigma_{13}$  and strain  $E_{13}$ , we recall two fundamental interfacial micromechanics relations [31], derived in the framework of eigenstress homogenization schemes [54]:

- The macroscopic state equation, expressing the macrostress  $\underline{\underline{\Sigma}}$  as a function of the macrostrain  $\underline{\underline{E}}$  and of the interface traction vector  $\underline{\underline{T}}$  reads as [31]

$$\underline{\underline{\Sigma}} = \underline{\underline{C}}_{hom} : \underline{\underline{E}} + \underline{\underline{B}} \cdot \underline{\underline{T}} \quad (3.31)$$

where  $\underline{\underline{C}}_{hom}$  denotes the homogenized stiffness tensor of the studied composite and  $\underline{\underline{B}}$  denotes a Biot-type tensor quantifying the influence of interface traction vector  $\underline{\underline{T}}$  on the macrostress  $\underline{\underline{\Sigma}}$ , provided that the macrostrain  $\underline{\underline{E}}$  is equal to zero. Specifying (3.31) for the matrix-interface composite shown in Fig. 3.1 and for loading in terms of pure macroscopic shear according to (3.1), allows for extracting the following scalar equation linking shear stress  $\Sigma_{13}$ , shear strain  $E_{13}$ , and the in-plane interface traction vector component  $T_1$  [31]

$$\Sigma_{13} = \frac{\mu_s 3(2 - \nu_s)}{3(2 - \nu_s) + 16 d (1 - \nu_s)} E_{13} + \frac{16 d (1 - \nu_s)}{3(2 - \nu_s) + 16 d (1 - \nu_s)} T_1 \quad (3.32)$$

In (3.32),  $\mu_s$  and  $\nu_s$  stand for the shear modulus and for Poisson's ratio of the isotropic solid matrix, and  $d$  denotes the interface density parameter [65]

$$d = \mathcal{N} a^3 \quad (3.33)$$

with  $\mathcal{N}$  and  $a$  standing for the number of the interfaces per unit volume of the composite, and for the radius of the interfaces, respectively.

- The concentration-influence relation expressing the dislocation vector  $[\underline{\underline{\xi}}]$  as a function of the macrostrain  $\underline{\underline{E}}$  and of the interface traction vector  $\underline{\underline{T}}$ , reads

as [31]

$$\llbracket \underline{\xi} \rrbracket = \underline{\underline{A}} : \underline{\underline{E}} + \underline{\underline{D}} \cdot \underline{\underline{T}} \quad (3.34)$$

where  $\underline{\underline{A}}$  denotes a concentration tensor quantifying the influence of macrostrain  $\underline{\underline{E}}$  on the dislocation vector  $\llbracket \underline{\xi} \rrbracket$  provided that the interface traction vector  $\underline{\underline{T}}$  vanishes, and  $\underline{\underline{D}}$  stands for an influence tensor quantifying the influence of the interface traction vector  $\underline{\underline{T}}$  on the dislocation vector  $\llbracket \underline{\xi} \rrbracket$ , provided that macrostrain  $\underline{\underline{E}}$  vanishes. Specifying (3.34) for the matrix-interface composite shown in Fig. 3.1 and for loading in terms of pure macroscopic shear according to (3.1), allows for extracting the following scalar equation linking in-plane dislocation  $\llbracket \xi_1 \rrbracket$ , the shear strain  $E_{13}$ , and the in-plane interface traction vector component  $T_1$  [31]

$$\llbracket \xi_1 \rrbracket = \frac{8(1-\nu_s)a}{\pi[3(2-\nu_s)+16d(1-\nu_s)]} \left[ 2E_{13} - \frac{T_1}{\mu_s} \right] \quad (3.35)$$

In order to derive the sought differential equation linking  $\Sigma_{13}$  and  $E_{13}$ , as well as their time derivatives  $\dot{\Sigma}_{13}$  and  $\dot{E}_{13}$ , we solve the concentration-influence relation (3.35) for the interface traction  $T_1$ , and we insert the resulting expression into (3.32), delivering

$$\Sigma_{13} = 2\mu_s E_{13} - \mu_s \frac{2\pi d}{a} \llbracket \xi_1 \rrbracket \quad (3.36)$$

Taking the time derivative of (3.36), multiplying  $\llbracket \dot{\xi}_1 \rrbracket$  by 1 in form of  $\frac{\eta}{\eta}$  yields, under consideration of (3.30),

$$\dot{\Sigma}_{13} = 2\mu_s \dot{E}_{13} - \mu_s \frac{2\pi d}{a\eta} T_1 \quad (3.37)$$

Solving (3.37) for  $T_1$  and inserting the resulting expression into (3.32), delivers the sought differential equation describing the constitutive behavior of the studied composite as

$$\dot{\Sigma}_{13} \frac{1}{\mu_s} + \Sigma_{13} \frac{\pi[3(2-\nu_s)+16d(1-\nu_s)]}{8a\eta(1-\nu_s)} = 2\dot{E}_{13} + 2E_{13} \frac{3(2-\nu_s)\pi\mu_s}{8(1-\nu_s)a\eta} \quad (3.38)$$

Eq. (3.38) is a first-order ordinary differential equation in the overall shear stress  $\Sigma_{13}$  and the overall shear strain  $E_{13}$ .

### 3.3.2 Elastic energy and dissipation

In order to quantify the elastic energy stored in the elastic solid matrix, it is convenient to replace the “eigencontractions”  $\underline{T}$  of the interface phase, by eigenstresses  $\underline{\sigma}_i^E$  of a flat spheroidal phase (whereby the limit case of the spheroid’s thickness going to zero would again relate to the two-dimensional interface). For such a system, state equations analogous to (3.31) and (3.34) read as [54, 78]

$$\underline{\underline{\Sigma}} = \underline{\underline{C}}_{hom} : \underline{\underline{E}} + \underline{\underline{\sigma}}_i^E : \underline{\underline{B}} \quad (3.39)$$

and

$$\underline{\underline{\Phi}} = \phi_i \underline{\underline{\varepsilon}}_i = \underline{\underline{B}} : \underline{\underline{E}} - \underline{\underline{N}}^{-1} : \underline{\underline{\sigma}}_i^E \quad (3.40)$$

with  $\phi_i$  and  $\underline{\underline{\varepsilon}}_i$  as volume fraction and the strains of the spheroidal phase, with  $\underline{\underline{C}}_{hom}$  as the homogenized stiffness tensor,  $\underline{\underline{B}}$  as the tensor of Biot coefficients, and  $\underline{\underline{N}}^{-1}$  as the inverse of the tensor of Biot moduli. The latter quantities are defined as [78]

$$\begin{aligned} \underline{\underline{C}}_{hom} &= \underline{\underline{C}}_s : \left[ \underline{\underline{I}} + \frac{4\pi d}{3} \underline{\underline{T}}_i \right]^{-1} \\ \underline{\underline{B}} &= \underline{\underline{I}} - \underline{\underline{C}}_s^{-1} : \underline{\underline{C}}_{hom} \\ \underline{\underline{N}}^{-1} &= \underline{\underline{B}} : \underline{\underline{C}}_s^{-1} \end{aligned} \quad (3.41)$$

see also Appendix D.1 for more details, in particular as concern the morphology tensor  $\underline{\underline{T}}$ . The portion of elastic energy  $\psi_s$  stored per time increment in the purely elastically behaving solid matrix is equal to the external power  $\mathcal{L}_s^{ext}$  supplied to this elastic matrix. This reads mathematically as [78]

$$\dot{\psi}_s = \mathcal{L}_s^{ext} = \int_{V_s} \underline{\underline{\sigma}} : \underline{\underline{\dot{\varepsilon}}} dV = \int_{V_{RVE}} \underline{\underline{\sigma}} : \underline{\underline{\dot{\varepsilon}}} dV - \int_{V_i} \underline{\underline{\sigma}} : \underline{\underline{\dot{\varepsilon}}} dV = \underline{\underline{\Sigma}} : \underline{\underline{\dot{E}}} - \underline{\underline{\sigma}}_i^E : \underline{\underline{\dot{\Phi}}} \quad (3.42)$$

with  $\underline{\underline{\sigma}}$  and  $\underline{\underline{\varepsilon}}$  denoting the microscopic stress and strain fields within a representative volume element hosting an elastic matrix with spheroidal inclusions; and  $V_{RVE}$ ,  $V_s$ , and  $V_i$ , respectively, denoting the volume of such an RVE, and of its subvolumes hosting solid matrix and spheroidal inclusions, respectively.

In order to quantify the dissipation in matrix-interface composites, it is noteworthy that the elastic energy stored in the composite,  $\Psi$ , is equal to the elastic energy stored in the solid matrix,  $\psi_s$ , because the viscous interfaces do neither exhibit any elastic properties, nor do they, due to their 2D nature, occupy any significant

volume within the RVE. Specification of the dissipation inequality (3.3) for  $\dot{\Psi} = \dot{\psi}_s$  according to (3.42), yields the dissipation of the matrix-interface composite as

$$\mathcal{D} = \underline{\underline{\Sigma}} : \underline{\underline{\dot{E}}} - \dot{\psi}_s = \underline{\underline{\sigma}}_i^E : \underline{\underline{\dot{\Phi}}} \quad (3.43)$$

The aim is now to transform (3.43) into a function of the variables characterizing the dissipative interfaces, namely  $\underline{T}$  and  $[[\underline{\xi}]]$ . Therefore,  $\underline{\underline{\dot{\Phi}}}$  follows from temporal derivation of (3.40),

$$\underline{\underline{\dot{\Phi}}} = \underline{\underline{B}} : \underline{\underline{\dot{E}}} - \underline{\underline{N}}^{-1} : \underline{\underline{\dot{\sigma}}}_i^E \quad (3.44)$$

When additionally considering the actual two-dimensional nature of the interface phase, the eigenstress tensor degenerates to

$$\underline{\underline{\sigma}}_i^E = T_1 (\underline{e}_1 \otimes \underline{e}_3 + \underline{e}_3 \otimes \underline{e}_1) \quad (3.45)$$

and  $\underline{\underline{\dot{\Phi}}}$  simplifies to

$$\underline{\underline{\dot{\Phi}}} = \dot{\Phi}_{13} (\underline{e}_1 \otimes \underline{e}_3 + \underline{e}_3 \otimes \underline{e}_1) \quad (3.46)$$

$\dot{\Phi}_{13}$  in (3.46) follows from specification of (3.44) for (3.1) and (3.45), resulting in

$$\dot{\Phi}_{13} = \frac{16 d (1 - \nu_s)}{3 (2 - \nu_s) + 16 d (1 - \nu_s)} \dot{E}_{13} - \frac{8 d (1 - \nu_s)}{[3 (2 - \nu_s) + 16 d (1 - \nu_s)] \mu_s} \dot{T}_1 \quad (3.47)$$

whereby  $\dot{T}_1$ , through consideration of (3.35), can be expressed in terms of  $\dot{E}_{13}$  and  $[[\dot{\xi}_1]]$  as

$$\dot{T}_1 = 2 \mu_s \dot{E}_{13} - \frac{\mu_s \pi [3 (2 - \nu_s) + 16 d (1 - \nu_s)]}{8 a (1 - \nu_s)} [[\dot{\xi}_1]] \quad (3.48)$$

Accordingly, insertion of (3.48) into (3.47) yields

$$\underline{\underline{\dot{\Phi}}} = \frac{[[\dot{\xi}_1]] d \pi}{a} (\underline{e}_1 \otimes \underline{e}_3 + \underline{e}_3 \otimes \underline{e}_1) \quad (3.49)$$

Finally, use of (3.49), and of (3.45) for transforming the expression (3.43) allows us to identify the dissipation as

$$\mathcal{D} = \frac{2 d \pi}{a} [[\dot{\xi}_1]] T_1 \quad (3.50)$$

Eq. (3.50) expresses explicitly that the energy dissipates exclusively in the viscous interfaces.

## 3.4 Interfacial micromechanics assessment of classical rheological models

### 3.4.1 Micromechanical explanation of rheological parameters

Summarizing Sections 3.2 and 3.3, we have derived equations describing, in terms of the overall shear stress and the overall shear strain, the constitutive behavior of the Kelvin-Voigt representation of the standard linear solid model, see (3.12), of the Maxwell representation of the standard linear solid model, see (3.24), and of a matrix-interface composite, see (3.38). These differential equations are valid for any type of prescribed loading history, including the special cases of a creep scenario (vanishing shear stress rate) and of a relaxation scenario (vanishing shear strain rate), see also Appendix D.2, D.3, and D.4. Notably, the structure of the three differential equations is the same, i.e. an analogy can be established through comparison of (3.2), (3.1), and (3.4), by setting equal

$$\tau = \Sigma_{13} \quad \text{and} \quad \gamma = 2 E_{13} \quad (3.51)$$

In order to complete the analogy, also the factors of the stress and strain variables, as appearing in (3.12), (3.24), and (3.38), need to be set equal. In other words, comparison of these coefficients delivers the sought relations between spring stiffnesses and dashpot viscosities, on the one hand, and micromechanical quantities, such as interface density, size, and viscosity, as well as shear modulus and Poisson's ratio of the solid matrix, on the other hand; see Table 3.1 for the result of this comparison and Figure 3.4 for further illustration of these relations.

### 3.4.2 Micromechanical interpretation of stress and strain contributions of individual springs and dashpots of the rheological models

The established relations between the rheological models and the micromechanical description of the matrix-interface composite, see (3.51) and Table 3.1, open the door to a novel, micromechanics-based interpretation of the rheological models. Accordingly, we will now express the stresses and strains acting in individual springs and dashpots, as functions of micromechanical quantities.

As for the Kelvin-Voigt representation of the standard linear solid model, such expressions concern the strain in the Kelvin-Voigt unit,  $\gamma_1$ , the strain in the additional spring,  $\gamma_e$ , the stress acting on the Kelvin-Voigt spring,  $\tau_1^\mu$ , and the stress acting on the dashpot,  $\tau_1^\eta$ . As for the expression for  $\gamma_1$  and  $\gamma_e$ , we specify the constitutive law of the additional spring,  $\tau = \mu_e \gamma_e$ , see (3.8), for  $\gamma_e = \gamma - \gamma_1$ , see (3.5), yielding  $\tau = \mu_e (\gamma - \gamma_e)$ , and we compare this relation with (3.36). Under consideration of (3.51) and the relations listed in Table 3.1, we then obtain

$$\gamma_1 = \frac{2 \pi d}{a} \llbracket \xi_1 \rrbracket \quad \text{and} \quad \gamma_e = 2 E_{13} - \frac{2 \pi d}{a} \llbracket \xi_1 \rrbracket = \frac{\Sigma_{13}}{\mu_s} \quad (3.52)$$

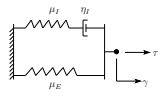
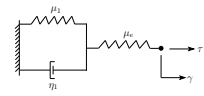
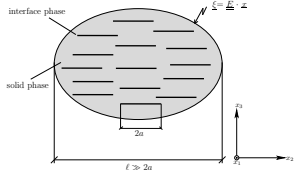
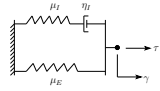
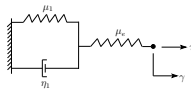
Next, we relate  $\tau_1^\mu = \mu_1 \gamma_1$  to micromechanical quantities, by specifying this equality for  $\mu_1$  according to Table 3.1, and for  $\gamma_1$  from (3.52)

$$\tau_1^\mu = \frac{3 \mu_s \pi (2 - \nu_s)}{8 a (1 - \nu_s)} \llbracket \xi_1 \rrbracket \quad (3.53)$$

Finally the micromechanical analogon for  $\tau_1^\eta$  follows from first solving both (3.32) and (3.35) with respect to  $E_{13}$ , and from setting equal the corresponding results, yielding

$$\Sigma_{13} = T_3 + \frac{3 \mu_s \pi (2 - \nu_s)}{8 a (1 - \nu_s)} \llbracket \xi_1 \rrbracket \quad (3.54)$$

Table 3.1: Relations between spring stiffness and dashpot viscosities of the Kelvin-Voigt and Maxwell representations of the standard linear solid model and micromechanical quantities of a matrix-interface composite

Models			
	$\mu_E = \mu_E$ $\mu_I = \mu_I$ $\eta_I = \eta_I$	$\mu_E = \mu_1 \left( 1 + \frac{\mu_1}{\mu_e} \right)^{-1}$ $\mu_I = \mu_e \left( 1 + \frac{\mu_1}{\mu_e} \right)^{-1}$ $\eta_I = \eta_1 \left( 1 + \frac{\mu_1}{\mu_e} \right)^{-2}$	$\mu_E = \mu_s \frac{3(2 - \nu_s)}{3(2 - \nu_s) + 16d(1 - \nu_s)}$ $\mu_I = \mu_s \frac{16d(1 - \nu_s)}{3(2 - \nu_s) + 16d(1 - \nu_s)}$ $\eta_I = \frac{a \eta 128 d (1 - \nu_s)^2}{\pi [3(2 - \nu_s) + 16d(1 - \nu_s)]^2}$
	$\mu_e = \mu_I + \mu_E$ $\mu_1 = \frac{\mu_E}{\mu_I} \left( \mu_I + \mu_E \right)$ $\eta_1 = \eta_I \left( \frac{\mu_I + \mu_E}{\mu_I} \right)^2$	$\mu_e = \mu_e$ $\mu_1 = \mu_1$ $\eta_1 = \eta_1$	$\mu_e = \mu_s$ $\mu_1 = \mu_s \frac{3(2 - \nu_s)}{16d(1 - \nu_s)}$ $\eta_1 = \frac{a \eta}{2 \pi d}$

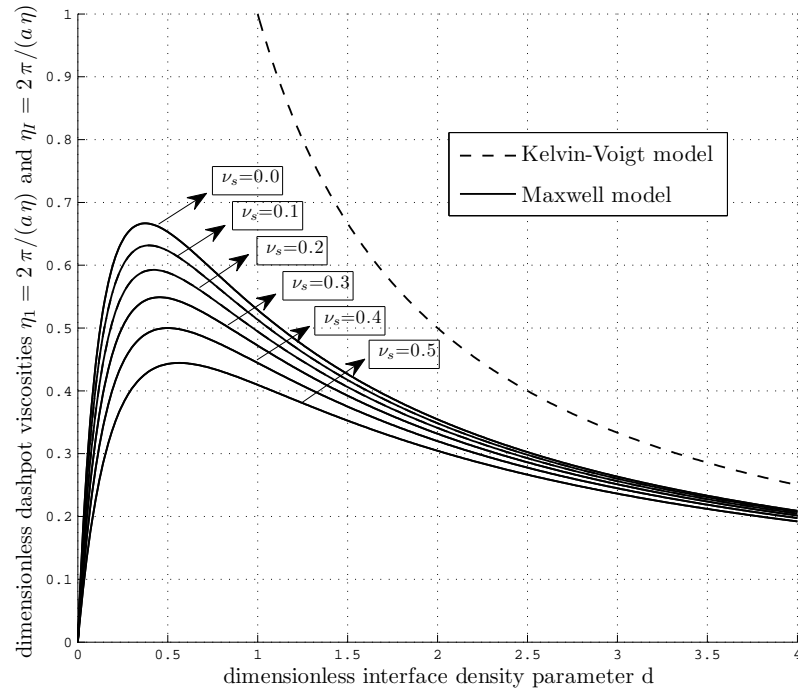


Figure 3.4: Dimensionless dashpot viscosity of Kelvin-Voigt and Maxwell models,  $\eta_I$  and  $\eta_I$ , over the dimensionless interface density parameter  $d$

Then this relation (3.54) is compared to  $\tau = \tau_1^\eta + \tau_1^\mu$ . Under consideration of (3.51) and (3.53), it follows that

$$\tau_1^\eta = T_1 \quad (3.55)$$

As for the Maxwell representation of the standard linear solid model, we seek micromechanical analogons for the stress acting on the Maxwell unit,  $\tau_I$ , the stress acting on the additional spring,  $\tau_E$ , the strain in the Maxwell spring,  $\gamma_I^\mu$ , and the strain in the dashpot,  $\gamma_I^\eta$ . As for a micromechanics-based expression for  $\tau_E$ , we first specify the spring law  $\tau_E = \mu_E \gamma$  for  $\mu_E = \mu_E(\mu_s, \nu_s, d)$  according to Table 3.1, and for  $\gamma = 2 E_{13}$ , see (3.51),

$$\tau_E = \mu_E \gamma = \frac{\mu_s 3 (2 - \nu_s)}{3 (2 - \nu_s) + 16 d (1 - \nu_s)} 2 E_{13} \quad (3.56)$$

As for expressing  $\tau_I$ , we first solve (3.32) for  $E_{13}$ , and we then insert the resulting expression into (3.56); this yields

$$\tau_E = \Sigma_{13} - \frac{16 d (1 - \nu_s)}{3 (2 - \nu_s) + 16 d (1 - \nu_s)} T_1 \quad (3.57)$$

Comparing this relation with  $\tau_E = \tau - \tau_I$ , yields, under consideration of (3.51),

$$\tau_I = \frac{16 d (1 - \nu_s)}{3 (2 - \nu_s) + 16 d (1 - \nu_s)} T_1 \quad (3.58)$$

In order to provide a micromechanical analogon for  $\gamma_I^\mu$ , we specify the spring law  $\gamma_I^\mu = \tau_I / \mu_I$ , see (3.20), for  $\tau_I$  from (3.58), and for  $\mu_I$  from Table 3.1, yielding

$$\gamma_I^\mu = \frac{T_3}{\mu_s} \quad (3.59)$$

Similarly, we specify the dashpot law  $\dot{\gamma}_I^\eta = \tau_I / \eta_I$ , see (3.20), for  $\tau_I$  from (3.58), and for  $\eta_I$  from Table 3.1, leading to

$$\dot{\gamma}_I^\eta = \frac{\pi [3 (2 - \nu_s) + 16 d (1 - \nu_s)] T_1}{8 a (1 - \nu_s) \eta} \quad (3.60)$$

Specifying (3.60) for  $T_1 / \eta = \llbracket \dot{\xi}_1 \rrbracket$ , see (3.30), and omitting the dots indicating time derivatives, i.e. integrating over time, finally yields

$$\gamma_I^\eta = \frac{\pi [3 (2 - \nu_s) + 16 d (1 - \nu_s)]}{8 a (1 - \nu_s)} \llbracket \xi_1 \rrbracket \quad (3.61)$$

### 3.4.3 Micromechanical illustration of energy dissipating in dashpots of the rheological models

The relation between rheological parameters and micromechanical quantities, as derived in the previous two subsections, allow us to illustrate the dashpot-associated dissipation in terms of micromechanical quantities. Specification of the Kelvin-Voigt-related dissipation according to (3.16), for  $\tau_1^\eta$  according to (3.55), and for  $\dot{\gamma}_1$  according to the time derivative of (3.52), delivers

$$\mathcal{D} = \tau_1^\eta \dot{\gamma}_1 = \frac{2 d \pi}{a} \llbracket \dot{\xi}_1 \rrbracket T_1 \quad (3.62)$$

Similarly, specification of the Maxwell-related dissipation according to (3.28), for  $\tau_I$  according to (3.58), and for  $\dot{\gamma}_I^\eta$  according to the time derivative of (3.61), delivers

$$\mathcal{D} = \tau_I \dot{\gamma}_I^\eta = \frac{2d\pi}{a} \llbracket \dot{\xi}_1 \rrbracket T_1 \quad (3.63)$$

Notably, both (3.62) and (3.63) result in the same expression for the dissipation of the matrix-interface composite. This clearly illustrates that the dissipation happening in the dashpots of the two rheological models is related to the dissipation happening in the viscous interfaces of the micromechanical representation. In addition, the analogy-derived micromechanical expressions (3.62) and (3.63) are identical to the directly derived dissipation relation (3.50). This proves that all our derivations were correct. This is because the analogy-defining formula for  $\tau_1^\eta$ ,  $\dot{\gamma}_1$ ,  $\tau_I$  and  $\dot{\gamma}_I^\eta$  were obtained from comparison of the differential equations (3.12), (3.24), as well as (3.38), and hence their derivation was *independent* of the derivation of dissipation relation (3.16), (3.28), and (3.50).

### 3.5 Discussion and conclusion

The standard linear solid models, both in the Kelvin-Voigt and in the Maxwell representations, can perfectly describe the rheological behavior of a matrix-interface composite whose time-dependent material properties result from the linear viscosity of the interfaces behavior, i.e. they are compatible with traction-dislocation relations originating from liquid crystal interface physics, and multiscale homogenization of eigenstressed interfaces. The relations listed in Table 3.1 establish the links between spring stiffnesses as well as dashpot viscosities, on the one hand, and micromechanical quantities of the matrix-interface composite, on the other hand, the latter ones being interface size, density, and viscosity, as well as shear modulus and Poisson's ratio of the isotropic solid matrix material.

When subjecting the matrix-interface composite to sudden loading, either in terms of stresses or of strains, the effective stiffness of the material is equal to the stiffness of the solid matrix, because, according to (3.30), dislocations would need time to develop, so that, without time passing, the interfaces are locked, which results in an uniform microscopic stress field [31]. The same is true for the dashpot in the rheological models, being blocked upon sudden loading. Accordingly, the then observed effective stiffness of Kelvin-Voigt model is equal to the additional spring stiffness, and the effective stiffness of the Maxwell model is equal to the sum of the spring stiffnesses. These effective stiffnesses are directly related to how the

stiffness of the solid matrix manifests itself in the two rheological models: In the Kelvin-Voigt representation, the additional elastic spring simply represents the solid matrix material, while in the Maxwell representation, the sum of the two spring stiffnesses is equal to the one of the solid matrix, see Table 3.1.

The time-dependent evolution of interfacial dislocations increases the effective compliance of the matrix-interface composite. Given a constant (time-independent) loading, the stiffness-reducing effect is fully developed, once the asymptotic state of the material is reached, i.e. once the interface tractions have decayed to zero and the interface dislocations have grown to their maximum [31]. The additional time-dependent material compliance is the larger, the larger the interface density. As for the Kelvin-Voigt model, the additional compliance is simply equal to the compliance of the Kelvin-Voigt spring, see Table 3.1. In the Maxwell representation, in turn, the interface density appears in the expressions of both spring constants, and the compliance of the additional spring is equal to the compliance of the solid matrix plus the additional compliance stemming from the interfacial dislocations, see Table 3.1.

The characteristic time of rheological processes shown by a matrix-interface composite are triggered, in general, by interface size  $a$ , viscosity  $\eta$ , and density  $d$ . This becomes apparent from the fact that the dashpot viscosities of both rheological models are directly proportional to interface size and viscosity, but the role of interface density deserves special attention, see Table 3.1. The Kelvin-Voigt dashpot viscosity is simply indirectly proportional to the interface density, see Table 3.1. Due to a more intricate mode of spring-dashpot interaction, however, the Maxwell dashpot viscosity depends in a non-trivial fashion on the interface density, and the dashpot viscosity is the smaller, the larger the Poisson's ratio of the solid matrix, see Table 3.1 and Fig. 3.4.

When it comes to discussing the rheological counterparts of interface tractions and interface dislocations, the Kelvin-Voigt model again allows for a more straightforward mode of interpretation of the underlying interface-micromechanics: the interface traction is simply equal to the stress acting on the Kelvin-Voigt dashpot, see (3.55), and the strain in the Kelvin-Voigt unit is directly proportional to both the interfacial dislocations and the interface density, while it is indirectly proportional to the interface size, see (3.52). In the Maxwell model, in turn, the stress acting on the Maxwell unit is also proportional to the interface tractions, but the proportionality factor depends, again in a non-trivial fashion, on both the interface density and on the Poisson's ratio of the solid matrix, see (3.58). Also

the relation between interfacial dislocations and the strain of the Maxwell dashpot is of increased mathematical complexity, with the interface density not any more exhibiting the nature of a simple proportionality factor, and also the Poisson's ratio of the solid entering the picture, see (3.61).

We conclude that the Kelvin-Voigt representation of the standard linear solid model is a more natural and elegant choice for modeling a hydrated matrix-interface composite containing viscous interfaces of identical size and viscosity, because the relations between spring-dashpot properties and micromechanical quantities turn out as very simple. Nonetheless, exactly the same model features can be achieved through a Maxwell-type representation, based on an appropriate choice of the spring stiffnesses and dashpot viscosities; their relations to micromechanics quantities, however, are significantly less intuitive when compared to the Kelvin-Voigt model. It is interesting to generalize this conclusion towards consideration of multiple interface sizes and viscosities, and corresponding chain models of the Kelvin-Voigt or Maxwell type. This is the topic of the companion paper [79].

### 3.6 Nomenclature

$a$	radius of the interface
$\underline{\underline{B}}$	fourth-order Biot tensor
$\underline{\underline{C}}_s$	fourth-order stiffness tensor of solid
$\underline{\underline{C}}_s^{-1}$	inverse of fourth-order stiffness tensor of solid
$\underline{\underline{C}}_{hom}$	fourth-order homogenized stiffness tensor
$d$	interface density parameter
$\mathcal{D}$	dissipation
$\underline{e}_1, \underline{e}_3$	unit base vectors of Cartesian coordinate system
$\underline{\underline{E}}$	macroscopic strain
$E_{13}$	shear component of macroscopic strain
$i$	index for interface phase
$\underline{\underline{I}}$	symmetric fourth-order identity tensor
$\underline{\underline{I}}_{dev}$	deviatoric part of $\underline{\underline{I}}$
$\underline{\underline{I}}_{vol}$	volumetric part of $\underline{\underline{I}}$
$k_s$	bulk modulus of solid phase
$\ell$	characteristic size of RVE
$\mathcal{L}_s^{ext}$	external power supplied to elastic matrix

---

$\underline{\underline{N}}^{-1}$	inverse of fourth-order tensor of Biot moduli
RVE	Representative of Volume Element
$s$	index for solid phase
$t$	time
$\underline{T}$	interface traction vector
$\underline{\underline{T}}_i$	fourth-order morphology tensor for 2D interface inclusion (shape of a “sharp crack”)
$T_1$	shear component of interface traction vector
$V_i$	volume of inclusion
$V_s$	volume of solid
$V_{RVE}$	volume of RVE
$x, y, z$	Cartesian coordinates
$\underline{x}$	position vector
$\dot{W}_{ext}$	rate of work of external forces
$\gamma$	shear strain
$\gamma_h$	solution of homogeneous differential equation for shear strain
$\gamma_p$	particulate integral
$\gamma_e$	shear strain of elastic spring of Kelvin-Voigt representation of standard linear solid (Zener model)
$\gamma_E$	shear strain of elastic spring of Maxwell representation of standard linear solid
$\gamma_I$	shear strain of Maxwell unit
$\gamma_I^\mu$	shear strain of spring in Maxwell unit
$\gamma_I^\eta$	shear strain of dashpot in Maxwell unit
$\delta$	Kronecker delta
$\underline{\underline{\varepsilon}}$	second-order tensor of microscopic strain
$\eta$	viscosity of the interfaces
$\eta_1$	viscosity constant of dashpot in Kelvin-Voigt unit
$\eta_I$	viscosity constant of dashpot in Maxwell unit
$\mu_e$	shear modulus of elastic spring in Kelvin-Voigt representation of standard linear solid (Zener model)
$\mu_E$	shear modulus of spring in Maxwell representation of standard linear solid
$\mu_1$	shear modulus of spring in Kelvin-Voigt unit
$\mu_I$	shear modulus of spring in Maxwell unit
$\mu_s$	shear modulus of isotropic solid matrix
$\nu_s$	Poisson’s ratio of isotropic solid matrix
$\underline{\xi}$	displacement vector

---

$[[\xi]]_1$	in-plane component of interfacial dislocation vector
$[[\xi]]_3$	out-of-plane component of interfacial dislocation vector
$\underline{\underline{\sigma}}$	second-order tensor of microscopic stress
$\underline{\underline{\sigma}}_i^E$	second-order tensor of interface eigenstress
$\underline{\underline{\Sigma}}$	second-order tensor of macroscopic stress
$\Sigma_{13}$	shear component of macroscopic stress
$\tau$	shear stress
$\tau_h$	solution of homogeneous differential equation for shear stress
$\tau_p$	particulate integral
$\tau_e$	shear stress in elastic spring in Kelvin-Voigt representation of standard linear solid (Zener model)
$\tau_E$	shear stress in elastic spring in Maxwell representation of standard linear solid
$\tau_I$	shear stress acting on Maxwell unit
$\tau_1$	shear stress acting on Kelvin-Voigt unit
$\tau_1^\mu$	shear stress in spring of Kelvin-Voigt unit
$\tau_1^\eta$	shear stress in dashpot of Kelvin-Voigt unit
$\underline{\underline{\Phi}}$	second-order tensor accounting for interfacial geometry changes
$\Phi_{13}$	shear component of $\underline{\underline{\Phi}}$
$\Psi$	elastic energy of matrix-interface composites
$\psi_s$	elastic internal energy of solid
$\partial$	partial derivative
:	second-order tensor contraction
$\dot{\bullet}$	partial derivative with respect to time (“rate”), of quantity “ $\bullet$ ”
$\otimes$	dyadic product

## Chapter 4

# Interfacial micromechanics assessment of classical rheological models II: Multiple interface sizes and viscosities

### 4.1 Introduction

While the rheological models of the Maxwell and the Kelvin-Voigt type, which combine, in different ways, two spring and one dashpot element, are often helpful to illustrate principal features of the creep and relaxation characteristics of various materials, they often appear as too simple when it comes to the representation of the actual material behavior. This was realized already in the 19th century when the field of creep mechanics was initiated [43]; and the problem was tackled by the introduction of rheological chain models, such as (i) Maxwell chains, representing a parallel arrangement of several Maxwell units [76] and an additional spring, and (ii) Kelvin-Voigt chains, representing a serial arrangement of several Kelvin-Voigt units [74, 75] and an additional spring. Ever since, these models and/or combination of them, have enjoyed great popularity in a variety of applications, concerning, e.g. the creep of aging cementitious materials [44], of soft biomaterials such as intervertebral discs [45], or of different types of polymers and plastics [46]. Extending the discussion developed in the companion paper [80], we here ask the question whether also the aforementioned chain models can be directly related to the mechanics of microstructural systems consisting of an elastic solid matrix and

viscous interfaces embedded therein. This requires, notably, the consideration of interfaces with differing viscosities and differing sizes. In more detail, we compare (i) coefficients of macroscopic stress-strain relations of rheological chains models with  $N$  Maxwell units (or  $N$  Kelvin-Voigt units, respectively), with (ii) coefficients of stress-strain relations characterizing a matrix-interface composite consisting of a contiguous, isotropic, and linear elastic solid matrix, as well as of  $N$  families of parallel interfaces. By analogy to the companion paper [80], our focus lies on time-dependent behavior under pure shear. Given interfaces with normals pointing in  $\underline{e}_3$  direction, the composite is susceptible to time-dependent behavior when subjected to shear in the  $\underline{x}_1, \underline{x}_3$ -plane and/or in the  $\underline{x}_2, \underline{x}_3$ -plane. Without loss of generality, we here focus on the former case, i.e. we study the relation between macroscopic stresses

$$\underline{\underline{\Sigma}} = \Sigma_{13} (\underline{e}_1 \otimes \underline{e}_3 + \underline{e}_3 \otimes \underline{e}_1) \quad (4.1)$$

and strains

$$\underline{\underline{E}} = E_{13} (\underline{e}_1 \otimes \underline{e}_3 + \underline{e}_3 \otimes \underline{e}_1) \quad (4.2)$$

As for the structure of this paper, we devote the two following sections to rheological chain models (of the Kelvin-Voigt and the Maxwell type, respectively), and to matrix-interface composites, respectively. In each of these sections, we use specific mathematical schemes for the derivation of stress-strain relations which link shear stresses and their time-derivatives, to shear strains and their time-derivatives. We start with two rheological units or two interface families, respectively, before we then extend the derivation to three rheological units or three interface families, respectively. Finally, we tackle the case of  $N$  rheological units or  $N$  interface families, respectively. Therefore, we compare the  $2N + 1$  independent coefficients occurring in the constitutive equations derived for the Kelvin-Voigt chain models, the Maxwell chain models, and the micromechanics models with different viscous interfaces families, respectively. This allows for a micromechanical interpretation of Maxwell chain models and Kelvin-Voigt chain models. The paper closes with a discussion of the results and conclusions.

## 4.2 Review of rheological chain models: derivation of governing differential equations

### 4.2.1 Kelvin-Voigt chain models

Kelvin-Voigt chain models consist of  $N$  Kelvin-Voigt units in series with an additional elastic spring (see Fig. 4.1). Here, such chain models are considered to represent a piece of material subjected to pure shear, such that the stress and strain states read as

$$\underline{\underline{\Sigma}} = \tau (\underline{e}_1 \otimes \underline{e}_3 + \underline{e}_3 \otimes \underline{e}_1) \quad \text{and} \quad \underline{\underline{E}} = \frac{1}{2} \gamma (\underline{e}_1 \otimes \underline{e}_3 + \underline{e}_3 \otimes \underline{e}_1) \quad (4.3)$$

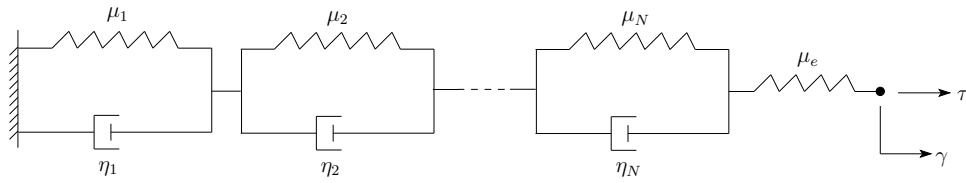


Figure 4.1: Kelvin-Voigt representation of standard linear solid, used to model time-dependent behavior under pure shear

The overall shear deformation of the rheological model,  $\gamma$ , can be decomposed additively into the contributions of the individual Kelvin-Voigt units ( $\gamma_1, \gamma_2, \dots, \gamma_N$ ) and into the one of the elastic spring ( $\gamma_e$ ),

$$\gamma = \gamma_e + \sum_{i=1}^N \gamma_i \quad (4.4)$$

The overall shear stress  $\tau$ , in turn, is transferred through all  $N$  Kelvin-Voigt units ( $\tau_1 = \tau_2 = \tau_N = \tau$ ) and through the elastic spring ( $\tau_e = \tau$ ), such that

$$\tau = \tau_1 = \tau_2 = \dots = \tau_N = \tau_e \quad (4.5)$$

The shear stress acting on the  $i$ -th Kelvin-Voigt unit can be decomposed into the shear stress acting on the spring,  $\tau_i^\mu$ , and into the shear stress acting on the dashpot,  $\tau_i^\eta$

$$\tau = \tau_i^\mu + \tau_i^\eta \quad i = 1, 2, \dots, N \quad (4.6)$$

where indexes  $\mu$  and  $\eta$  refer to the spring and to the dashpot, respectively.

The derivation of a constitutive relation between shear stress  $\tau$  and shear strain  $\gamma$ , see Eq. (4.3) and Fig. 4.1, requires individual constitutive laws for all involved rheological devices. Denoting the spring stiffness of the additional elastic spring as  $\mu_e$ , and the ones of the Kelvin-Voigt springs as  $\mu_1, \mu_2, \dots, \mu_N$ , as well as the

dashpot viscosities as  $\eta_1, \eta_2, \dots, \eta_N$ , see Fig. 4.1, the individual constitutive laws read as

$$\left. \begin{aligned} \tau_i^\mu &= \mu_i \gamma_i \\ \tau_i^\eta &= \eta_i \dot{\gamma}_i \end{aligned} \right\} \quad i = 1, 2, \dots, N \quad \tau_e = \mu_e \gamma_e \quad (4.7)$$

where a dot stands for a time-derivative.

$$\dot{\gamma}_i = \frac{\partial \gamma_i}{\partial t} \quad (4.8)$$

The sought constitutive relation-between  $\tau$  and  $\gamma$  is obtained by constructing linear combinations between Eqs. (4.4) to (4.7) and their time-derivatives, yielding, for a chain model with one Kelvin-Voigt unit ( $N = 1$ ) [80]

$$\tau \left( \frac{1}{\mu_e} + \frac{1}{\mu_1} \right) + \dot{\tau} \frac{\eta_1}{\mu_1} \left( \frac{1}{\mu_e} \right) = \gamma + \frac{\eta_1}{\mu_1} \dot{\gamma} \quad (4.9)$$

In agreement with our current focus on more than one interface size and/or viscosity, we continue with the derivation of the constitutive  $\tau, \gamma$ -relation for a chain model with two Kelvin-Voigt units ( $N = 2$ ). In this context, it is beneficial to derive elementary stress-strain relations for the individual Kelvin-Voigt units by specifying Eqs. (4.6) for the spring and dashpot laws (4.7), and dividing the resulting expressions by the shear moduli of the involved spring, yielding

$$\frac{\tau}{\mu_1} = \frac{\eta_1}{\mu_1} \dot{\gamma}_1 + \gamma_1 \quad (4.10)$$

$$\frac{\tau}{\mu_2} = \frac{\eta_2}{\mu_2} \dot{\gamma}_2 + \gamma_2 \quad (4.11)$$

By analogy, the shear stress  $\tau_e$  appearing in the spring law of the additional spring, see (4.7), can be set equal to  $\tau$ , see (4.5), and the resulting expression can be solved for  $\gamma_e$ , in order to deliver

$$\frac{\tau}{\mu_e} = \gamma_e \quad (4.12)$$

Summing up Eqs. (4.10) – (4.12) and considering of (4.4), allow for elimination of  $\gamma_1, \gamma_2$ , and  $\gamma_e$

$$\tau \left( \frac{1}{\mu_e} + \frac{1}{\mu_1} + \frac{1}{\mu_2} \right) = \frac{\eta_1}{\mu_1} \dot{\gamma}_1 + \frac{\eta_2}{\mu_2} \dot{\gamma}_2 + \gamma \quad (4.13)$$

The next step consists of eliminating from (4.13), the first-order derivatives  $\dot{\gamma}_1$  and  $\dot{\gamma}_2$ . Therefore, the first-order time-derivatives of (4.10), (4.11), and (4.12) are

multiplied with  $\eta_2/\mu_2$ , with  $\eta_1/\mu_1$ , and with  $\eta_1/\mu_1 + \eta_2/\mu_2$ , respectively, yielding

$$\frac{\dot{\tau} \eta_2}{\mu_1 \mu_2} = \frac{\eta_1 \eta_2}{\mu_1 \mu_2} \ddot{\gamma}_1 + \frac{\eta_2}{\mu_2} \dot{\gamma}_1 \quad (4.14)$$

$$\frac{\dot{\tau} \eta_1}{\mu_2 \mu_1} = \frac{\eta_1 \eta_2}{\mu_1 \mu_2} \ddot{\gamma}_2 + \frac{\eta_1}{\mu_1} \dot{\gamma}_2 \quad (4.15)$$

$$\frac{\dot{\tau}}{\mu_e} \left( \frac{\eta_1}{\mu_1} + \frac{\eta_2}{\mu_2} \right) = \left( \frac{\eta_1}{\mu_1} + \frac{\eta_2}{\mu_2} \right) \dot{\gamma}_e \quad (4.16)$$

Subsequent summation of Eqs. (4.13) – (4.16), together with consideration of (4.4) in form of  $\dot{\gamma} = \dot{\gamma}_e + \dot{\gamma}_1 + \dot{\gamma}_2$ , yields an expression free from  $\dot{\gamma}_1$  and  $\dot{\gamma}_2$ , namely

$$\tau \left( \frac{1}{\mu_e} + \frac{1}{\mu_1} + \frac{1}{\mu_2} \right) + \dot{\tau} \left[ \frac{\eta_1}{\mu_1} \left( \frac{1}{\mu_2} + \frac{1}{\mu_e} \right) + \frac{\eta_2}{\mu_2} \left( \frac{1}{\mu_1} + \frac{1}{\mu_e} \right) \right] = \gamma + \left( \frac{\eta_1}{\mu_1} + \frac{\eta_2}{\mu_2} \right) \dot{\gamma} + \frac{\eta_1 \eta_2}{\mu_1 \mu_2} (\ddot{\gamma}_1 + \ddot{\gamma}_2) \quad (4.17)$$

Finally, second-order derivatives  $\ddot{\gamma}_1$  and  $\ddot{\gamma}_2$  are eliminated from (4.17). Therefore, the second-order time-derivative of (4.12) is multiplied with  $\left( \frac{\eta_1 \eta_2}{\mu_1 \mu_2} \right)$ , yielding

$$\frac{\ddot{\tau} \eta_1 \eta_2}{\mu_e \mu_1 \mu_2} = \frac{\eta_1 \eta_2}{\mu_1 \mu_2} \ddot{\gamma}_e \quad (4.18)$$

Summing up Eqs. (4.17) and (4.18) and consideration of (4.4) in form of  $\ddot{\gamma} = \ddot{\gamma}_e + \ddot{\gamma}_1 + \ddot{\gamma}_2$  then yield the sought constitutive relation between  $\tau$  and  $\gamma$ ,

$$\begin{aligned} \tau \left( \frac{1}{\mu_e} + \frac{1}{\mu_1} + \frac{1}{\mu_2} \right) + \dot{\tau} \left[ \frac{\eta_1}{\mu_1} \left( \frac{1}{\mu_2} + \frac{1}{\mu_e} \right) + \frac{\eta_2}{\mu_2} \left( \frac{1}{\mu_1} + \frac{1}{\mu_e} \right) \right] + \ddot{\tau} \frac{\eta_1 \eta_2}{\mu_1 \mu_2} \left( \frac{1}{\mu_e} \right) = \\ \gamma + \left( \frac{\eta_1}{\mu_1} + \frac{\eta_2}{\mu_2} \right) \dot{\gamma} + \frac{\eta_1 \eta_2}{\mu_1 \mu_2} \ddot{\gamma} \end{aligned} \quad (4.19)$$

The same strategy can be applied in order to derive a constitutive relation between  $\tau$  and  $\gamma$  for a chain model containing three Kelvin-Voigt units ( $N = 3$ ). The elementary stress-strain relations of the Kelvin-Voigt units and the one of the additional spring are combined, such that  $\gamma_1$ ,  $\gamma_2$ ,  $\gamma_3$ , and  $\gamma_e$  are eliminated. The resulting expression contains terms containing  $\dot{\gamma}_1$ ,  $\dot{\gamma}_2$ ,  $\dot{\gamma}_3$ , and  $\dot{\gamma}_e$ . They are eliminated by constructing a suitable linear combination of the aforementioned expression and the first-order time-derivatives of the elementary stress-strain relations. This will introduce terms containing  $\ddot{\gamma}_1$ ,  $\ddot{\gamma}_2$ , and  $\ddot{\gamma}_3$ , into the new expression arising from the aforementioned linear combination. By constructing a suitable linear combination of this new expression and the second-order time-derivatives of the aforementioned stress-strain relations,  $\ddot{\gamma}_1$ ,  $\ddot{\gamma}_2$ , and  $\ddot{\gamma}_3$  can be eliminated as well, but third-order terms appear,  $\ddot{\gamma}_1$ ,  $\ddot{\gamma}_2$ , and  $\ddot{\gamma}_3$ . They can be eliminated by constructing a suitable linear combination with the third-order time-derivative of the elementary stress-strain relation of the additional spring. In the end, the following

third-order differential equation in  $\tau$  and  $\gamma$  is obtained

$$\begin{aligned} & \tau \left( \frac{1}{\mu_e} + \frac{1}{\mu_1} + \frac{1}{\mu_2} + \frac{1}{\mu_3} \right) + \dot{\tau} \left[ \frac{\eta_1}{\mu_1} \left( \frac{1}{\mu_2} + \frac{1}{\mu_3} + \frac{1}{\mu_e} \right) + \frac{\eta_2}{\mu_2} \left( \frac{1}{\mu_1} + \frac{1}{\mu_3} + \frac{1}{\mu_e} \right) + \frac{\eta_3}{\mu_3} \left( \frac{1}{\mu_1} + \frac{1}{\mu_2} + \frac{1}{\mu_e} \right) \right] \\ & + \ddot{\tau} \left[ \frac{\eta_1 \eta_2}{\mu_1 \mu_2} \left( \frac{1}{\mu_e} + \frac{1}{\mu_3} \right) + \frac{\eta_1 \eta_3}{\mu_1 \mu_3} \left( \frac{1}{\mu_e} + \frac{1}{\mu_2} \right) + \frac{\eta_2 \eta_3}{\mu_2 \mu_3} \left( \frac{1}{\mu_e} + \frac{1}{\mu_1} \right) \right] + \dddot{\tau} \frac{\eta_1 \eta_2 \eta_3}{\mu_1 \mu_2 \mu_3} \left( \frac{1}{\mu_e} \right) \\ & = \\ & \gamma + \left( \frac{\eta_1}{\mu_1} + \frac{\eta_2}{\mu_2} + \frac{\eta_3}{\mu_3} \right) \dot{\gamma} + \left[ \frac{\eta_1 \eta_2}{\mu_1 \mu_2} + \frac{\eta_2 \eta_3}{\mu_2 \mu_3} + \frac{\eta_1 \eta_3}{\mu_1 \mu_3} \right] \ddot{\gamma} + \frac{\eta_1 \eta_2 \eta_3}{\mu_1 \mu_2 \mu_3} \ddot{\gamma} \end{aligned} \quad (4.20)$$

The general structure of constitutive  $\tau, \gamma$ -relations for chain models containing  $N$  Kelvin Voigt units can be identified by comparing the  $\tau, \gamma$ -relations for one, two, and three Kelvin Voigt units, respectively, see Eqs. (4.9), (4.19) and (4.20). Accordingly, it appears that the first-order derivative of the strain,  $\dot{\gamma}$ , is always multiplied with the sum over all characteristic times  $\eta_i/\mu_i$ , with  $i = 1, 2, \dots, N$ . The second-order derivative of the strain,  $\ddot{\gamma}$ , is always multiplied with the sum over all possible products of two different characteristic times. The third-order derivative of the strain,  $\ddot{\gamma}$ , is always multiplied with the sum over all possible products of three different characteristic times. This clarifies the general structure: the  $n^{\text{th}}$ -order derivative of the strain is multiplied with the sum over all possible products of  $n$  different characteristic times. The coefficients multiplied with the stress and stress derivatives are just slightly more complex: The stress,  $\tau$ , is always multiplied with the sum over all reciprocal shear modulus values. The first-order derivative of the stress,  $\dot{\tau}$ , is always multiplied with the sum over all products of each characteristic time  $\eta_i/\mu_i$  and a corresponding constant being equal to the sum over all reciprocal shear modulus values minus  $1/\mu_i$ . The second-order derivative of the stress,  $\ddot{\tau}$ , is always multiplied with the sum over all possible products of two different characteristic times,  $\eta_i \eta_j / (\mu_i \mu_j)$ , whereby  $i \neq j$ , and corresponding constants being equal to the sum over all reciprocal shear modulus values minus  $(1/\mu_i + 1/\mu_j)$ . The third-order derivative of the stress,  $\ddot{\tau}$ , is always multiplied with the sum over all possible products of three different characteristic times,  $\eta_i \eta_j \eta_k / (\mu_i \mu_j \mu_k)$ , whereby  $i \neq j, i \neq k, j \neq k$ , and corresponding constants which are equal to the sum over all reciprocal shear modulus values minus  $(1/\mu_i + 1/\mu_j + 1/\mu_k)$ . This clarifies the general structure: the  $n^{\text{th}}$ -order derivative of the stress is multiplied with the sum over all possible products of  $n$  different characteristic times, and corresponding constants being equal to the sum over all reciprocal shear modulus values minus the sum over all those reciprocal shear modulus values which also show up in the products of the characteristic times. In conclusion, the



The overall shear deformation  $\gamma$ , in turn, is the same for all  $N$  Maxwell units ( $\gamma_I = \gamma_{II} = \gamma_N = \gamma$ ) and for the elastic spring ( $\gamma_E = \gamma$ ), such that

$$\gamma = \gamma_I = \gamma_{II} = \cdots = \gamma_N = \gamma_E \quad (4.23)$$

The shear deformation of the  $i$ -th Maxwell unit can be decomposed into the shear deformation of the spring,  $\gamma_I^\mu$ , and into the shear deformation of the dashpot,  $\gamma_I^\eta$

$$\gamma = \gamma_i^\mu + \gamma_i^\eta \quad i = I, II, \dots, N \quad (4.24)$$

The derivation of a constitutive relation between shear stress  $\tau$  and shear strain  $\gamma$ , see Eq. (4.3) and Fig. 4.2, requires individual constitutive laws for all involved rheological devices. Denoting the stiffness of the additional elastic spring as  $\mu_E$ , the stiffnesses of the Maxwell springs as  $\mu_I, \mu_{II}, \dots, \mu_N$ , and the dashpot viscosities as  $\eta_I, \eta_{II}, \dots, \eta_N$ , see Fig. 4.2, the individual constitutive laws read, in analogy to (4.7), as

$$\left. \begin{array}{l} \tau_i = \mu_i \gamma_i^\mu \\ \tau_i = \eta_i \dot{\gamma}_i^\eta \end{array} \right\} \quad i = I, II, \dots, N \quad \tau_E = \mu_E \gamma_E \quad (4.25)$$

The sought constitutive relation between  $\tau$  and  $\gamma$  is obtained by constructing linear combinations of Eqs. (4.22) to (4.25) and their time-derivatives, yielding, for a chain model with one Maxwell unit ( $N = I$ ), see [80]

$$\tau + \dot{\tau} \frac{\eta_I}{\mu_I} = \gamma \mu_E + \dot{\gamma} \frac{\eta_I}{\mu_I} \left( \mu_E + \mu_I \right) \quad (4.26)$$

In agreement with our current focus on more than one interface size and/or viscosity, we continue with the derivation of the constitutive  $\tau, \gamma$ -relation for a chain model with two Maxwell units ( $N = II$ ). In this context, it is beneficial to derive elementary stress-strain relations for the individual Maxwell units by specifying the time-derivative of Eqs. (4.24) for the spring and dashpot laws (4.25), and by multiplying the resulting expressions with the viscosity of the involved dashpot, yielding

$$\tau_I + \dot{\tau}_I \frac{\eta_I}{\mu_I} = \dot{\gamma} \eta_I \quad (4.27)$$

$$\tau_{II} + \dot{\tau}_{II} \frac{\eta_{II}}{\mu_{II}} = \dot{\gamma} \eta_{II} \quad (4.28)$$

By analogy, the shear deformation  $\gamma_E$  appearing in the spring law of the additional spring, see (4.25), can be set equal to  $\gamma$ , according to (4.23), so that we obtain

$$\tau_E = \mu_E \gamma \quad (4.29)$$

Summing up Eqs. (4.27) – (4.29) and consideration of (4.22) allows for elimination of  $\tau_I$ ,  $\tau_{II}$ , and  $\tau_E$ , yielding

$$\tau + \dot{\tau}_I \frac{\eta_I}{\mu_I} + \dot{\tau}_{II} \frac{\eta_{II}}{\mu_{II}} = \gamma \mu_E + \dot{\gamma} (\eta_I + \eta_{II}) \quad (4.30)$$

Next, first-order time-derivatives  $\dot{\tau}_I$  and  $\dot{\tau}_{II}$  are eliminated, by constructing linear combinations of Eq. (4.30) with the first-order time-derivatives of (4.27), (4.28), and (4.29), whereby the latter derivatives are multiplied with  $\eta_{II}/\mu_{II}$ , with  $\eta_I/\mu_I$ , and with  $\eta_I/\mu_I + \eta_{II}/\mu_{II}$ , respectively

$$\dot{\tau}_I \frac{\eta_{II}}{\mu_{II}} + \ddot{\tau}_I \frac{\eta_I \eta_{II}}{\mu_I \mu_{II}} = \ddot{\gamma} \frac{\eta_I \eta_{II}}{\mu_{II}} \quad (4.31)$$

$$\dot{\tau}_{II} \frac{\eta_I}{\mu_I} + \ddot{\tau}_{II} \frac{\eta_I \eta_{II}}{\mu_I \mu_{II}} = \ddot{\gamma} \frac{\eta_I \eta_{II}}{\mu_I} \quad (4.32)$$

$$\dot{\tau}_E \left( \frac{\eta_I}{\mu_I} + \frac{\eta_{II}}{\mu_{II}} \right) = \dot{\gamma} \mu_E \left( \frac{\eta_I}{\mu_I} + \frac{\eta_{II}}{\mu_{II}} \right) \quad (4.33)$$

Summing up Eqs. (4.30) – (4.33) and consideration of (4.22) in form of  $\dot{\tau} = \dot{\tau}_E + \dot{\tau}_I + \dot{\tau}_{II}$ , yields

$$\begin{aligned} & \tau + \dot{\tau} \left( \frac{\eta_I}{\mu_I} + \frac{\eta_{II}}{\mu_{II}} \right) + (\ddot{\tau}_I + \ddot{\tau}_{II}) \frac{\eta_I \eta_{II}}{\mu_I \mu_{II}} \\ &= \\ & \gamma \mu_E + \dot{\gamma} \left[ \frac{\eta_I}{\mu_I} (\mu_E + \mu_I) + \frac{\eta_{II}}{\mu_{II}} (\mu_E + \mu_{II}) \right] + \ddot{\gamma} \frac{\eta_I \eta_{II}}{\mu_I \mu_{II}} (\mu_I + \mu_{II}) \end{aligned} \quad (4.34)$$

Finally, the second-order time-derivatives  $\ddot{\tau}_I$  and  $\ddot{\tau}_{II}$  are eliminated by constructing a linear combination of (4.34) with the second-order time-derivative of (4.29), whereby the latter is multiplied by  $(\frac{\eta_I \eta_{II}}{\mu_I \mu_{II}})$ , i.e.

$$\ddot{\tau}_E \frac{\eta_I \eta_{II}}{\mu_I \mu_{II}} = \ddot{\gamma} \mu_E \frac{\eta_I \eta_{II}}{\mu_I \mu_{II}} \quad (4.35)$$

Summing up Eqs. (4.34) and (4.35) and consideration of (4.24) in form of  $\dot{\tau} = \ddot{\tau}_E + \ddot{\tau}_I + \ddot{\tau}_{II}$  yields the sought constitutive relation between  $\tau$  and  $\gamma$ ,

$$\begin{aligned} \tau + \dot{\tau} \left( \frac{\eta_I}{\mu_I} + \frac{\eta_{II}}{\mu_{II}} \right) + \ddot{\tau} \frac{\eta_I \eta_{II}}{\mu_I \mu_{II}} \\ = \\ \gamma \mu_E + \dot{\gamma} \left[ \frac{\eta_I}{\mu_I} (\mu_E + \mu_I) + \frac{\eta_{II}}{\mu_{II}} (\mu_E + \mu_{II}) \right] + \ddot{\gamma} \frac{\eta_I \eta_{II}}{\mu_I \mu_{II}} (\mu_E + \mu_I + \mu_{II}) \end{aligned} \quad (4.36)$$

The same strategy can be applied to derive a constitutive relation between  $\tau$  and  $\gamma$  for a chain model containing three Maxwell units ( $N = III$ ). The elementary stress-strain relations of the Maxwell units and the one of the additional spring are combined, such that  $\tau_I$ ,  $\tau_{II}$ ,  $\tau_{III}$ , and  $\tau_E$  are eliminated. The resulting expression contains terms in  $\dot{\tau}_I$ ,  $\dot{\tau}_{II}$ ,  $\dot{\tau}_{III}$ , and  $\dot{\tau}_E$ . They are eliminated by constructing a suitable linear combination with the first-order time-derivatives of the elementary stress-strain relations. This will introduce terms containing  $\ddot{\tau}_I$ ,  $\ddot{\tau}_{II}$ , and  $\ddot{\tau}_{III}$ . They are eliminated by constructing a suitable linear combination with the second-order time-derivatives of the aforementioned stress-strain relations. This will introduce terms containing  $\dddot{\tau}_I$ ,  $\dddot{\tau}_{II}$ , and  $\dddot{\tau}_{III}$ , and they can be eliminated by constructing a suitable linear combination with the third-order time-derivative of the elementary stress-strain relation of the additional spring. In the end, the following third-order differential equation in  $\tau$  and  $\gamma$  is obtained

$$\begin{aligned} \tau + \dot{\tau} \left( \frac{\eta_I}{\mu_I} + \frac{\eta_{II}}{\mu_{II}} + \frac{\eta_{III}}{\mu_{III}} \right) + \ddot{\tau} \left( \frac{\eta_I \eta_{II}}{\mu_I \mu_{II}} + \frac{\eta_I \eta_{III}}{\mu_I \mu_{III}} + \frac{\eta_{II} \eta_{III}}{\mu_{II} \mu_{III}} \right) + \ddot{\tau} \left( \frac{\eta_I \eta_{II} \eta_{III}}{\mu_I \mu_{II} \mu_{III}} \right) \\ = \\ \gamma \mu_E + \dot{\gamma} \left[ \frac{\eta_I}{\mu_I} (\mu_E + \mu_I) + \frac{\eta_{II}}{\mu_{II}} (\mu_E + \mu_{II}) + \frac{\eta_{III}}{\mu_{III}} (\mu_E + \mu_{III}) \right] \\ + \\ \ddot{\gamma} \left[ \frac{\eta_I \eta_{II}}{\mu_I \mu_{II}} (\mu_E + \mu_I + \mu_{II}) + \frac{\eta_I \eta_{III}}{\mu_I \mu_{III}} (\mu_E + \mu_I + \mu_{III}) + \frac{\eta_{II} \eta_{III}}{\mu_{II} \mu_{III}} (\mu_E + \mu_{II} + \mu_{III}) \right] \\ + \\ \ddot{\gamma} \frac{\eta_I \eta_{II} \eta_{III}}{\mu_I \mu_{II} \mu_{III}} (\mu_E + \mu_I + \mu_{II} + \mu_{III}) \end{aligned} \quad (4.37)$$

The general structure of constitutive  $\tau, \gamma$ -relations for chain models containing  $N$  Maxwell units can be identified from comparing the  $\tau, \gamma$ -relations of one, two, and three Maxwell units, respectively, see Eqs. (4.26), (4.36), and (4.37). Accordingly, it appears that the first-order derivative of the stress,  $\dot{\tau}$ , is always multiplied with the sum over all characteristic times  $\eta_i/\mu_i$ ,  $i = I, II, \dots, N$ . The second-order derivative of the stress,  $\ddot{\tau}$ , is always multiplied with the sum over all possible products of two different characteristic times. The third-order derivative of the stress,  $\dddot{\tau}$ , is always multiplied with the sum over all possible products of three different characteristic times. This clarifies the general structure: the  $n^{th}$ -order derivative of the stress is multiplied with the sum over all possible products of  $n$  different characteristic times. The strain,  $\gamma$ , is always multiplied with the shear

modulus of the additional spring. The first-order derivative of the strain,  $\dot{\gamma}$ , is always multiplied with the sum over all products of each characteristic time,  $\eta_i/\mu_i$ , and a corresponding sum of stiffnesses ( $\mu_E + \mu_i$ ). The second-order derivative of the strain,  $\ddot{\gamma}$ , is always multiplied with the sum over all possible products of two different characteristic times,  $\eta_i \eta_j / (\mu_i \mu_j)$ , whereby  $i \neq j$ , and corresponding sums of stiffnesses reading as  $(\mu_E + \mu_i + \mu_j)$ . The third-order derivative of the stress,  $\dddot{\gamma}$ , is always multiplied with the sum over all possible products of three different characteristic times,  $\eta_i \eta_j \eta_k / (\mu_i \mu_j \mu_k)$ , whereby  $i \neq j$ ,  $i \neq k$ , and  $j \neq k$ , and factors in the form of stiffnesses sums,  $(\mu_E + \mu_i + \mu_j + \mu_k)$ . This clarifies the general structure: the  $n^{\text{th}}$ -order derivative of the strain is multiplied with the sum over all possible products of  $n$  different characteristic times and corresponding constants being equal to the sum of the shear modulus of the additional spring plus all shear moduli which also show up in the products of the characteristic times. Accordingly, the mathematical format of the general  $\tau, \gamma$ -relation for a chain model with  $N$  Maxwell units reads as

$$\begin{aligned} \tau + \sum_{n=I}^N \left( \sum_{i_I=I}^{N-n+I} \dots \left( \sum_{i_a=i_{a-I}+I}^{N-(n-a)+I} \dots \left( \sum_{i_n=i_{n-I}+I}^N \left( \prod_{j \in \{i_I, \dots, i_n\}} \frac{\eta_j}{\mu_j} \right) \right) \dots \right) \dots \right) \frac{\partial^n \tau}{\partial t^n} = \mu_E \gamma + \\ \sum_{n=I}^N \left( \sum_{i_I=I}^{N-n+I} \dots \left( \sum_{i_a=i_{a-I}+I}^{N-(n-a)+I} \dots \left( \sum_{i_n=i_{n-I}+I}^N \left( \left( \mu_E + \sum_{j \in \{i_I, \dots, i_n\}} \mu_j \right) \left( \prod_{k \in \{i_I, \dots, i_n\}} \frac{\eta_k}{\mu_k} \right) \right) \right) \dots \right) \dots \right) \frac{\partial^n \gamma}{\partial t^n} \end{aligned} \quad (4.38)$$

see also Eq. (E.2) in Appendix E.2 for a more expanded form of (4.38).

### 4.3 Matrix-interface representation and constitutive relations

Here, we consider matrix-inclusion composites consisting of one solid phase and of  $N$  parallel interface phases, differing by viscosity and size, representing together the entity of all viscous fluid layers within the investigated material volume (Fig. 4.3). These composite materials are subjected to pure shear, which is aligned with the interface orientation, see (4.1) and (4.2), and the solid phase exhibits linear elastic behavior characterized by an isotropic stiffness tensor  $\underline{\underline{C}}_s$ .

In more symbolic detail, each interface phase is characterized by a specific interface radius  $a_i$  and a specific interface viscosity  $\eta_{i,1}$ , with  $i = 1, 2, \dots, N$ . In addition, we consider that molecular ordering-related joining forces may prevent the interfaces from opening, so that displacement jumps in interface normal direction  $\underline{e}_3$  vanish. The component of the traction vector acting in the interface plane,  $T_i$ , is related,

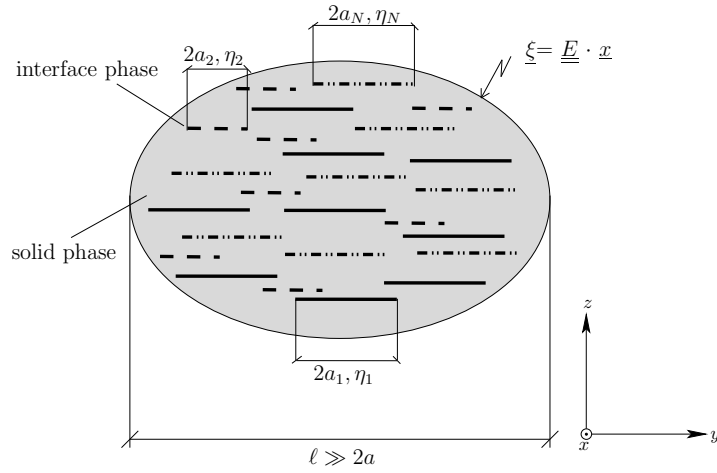


Figure 4.3: 2D flat, parallel, spherical interfaces; 2D sketch of 3D representative volume elements

by a linear viscous law, to the rate of the average in-plane displacement jump,  $[[\dot{\xi}]]_i$

$$T_i = \eta_{i,1} [[\dot{\xi}]]_i \quad i = 1, 2, \dots, N \quad (4.39)$$

The derivation of a differential equation describing the constitutive behavior of the studied composite in terms of macroscopic stress  $\Sigma_{13}$  and strain  $E_{13}$ , is based on the macroscopic poromechanical state equation and on concentration-influence relations, as described next.

- The macroscopic state equation, expressing the macrostress  $\underline{\underline{\Sigma}}$  as a function of the macrostrain  $\underline{\underline{E}}$  and of the interface traction vector  $\underline{T}_i$  reads as [31]

$$\underline{\underline{\Sigma}} = \underline{\underline{C}}_{hom} : \underline{\underline{E}} + \sum_{i=1}^N \underline{\underline{B}}_i \cdot \underline{T}_i \quad (4.40)$$

where  $\underline{\underline{C}}_{hom}$  denotes the homogenized stiffness tensor of the studied composite and  $\underline{\underline{B}}_i$  denotes a Biot-type tensor quantifying the influence of interface traction vector  $\underline{T}_i$  on the macrostress  $\underline{\underline{\Sigma}}$ , provided that the macrostrain  $\underline{\underline{E}}$  and all the other interface families traction are equal to zero. Specifying (4.40) for the matrix-interface composite shown in Fig. 4.3 and for loading in terms of pure macroscopic shear according to (4.1) and (4.2), allows for extracting the following scalar equation linking shear stress  $\Sigma_{13}$ , shear strain  $E_{13}$  and

the in-plane interface traction vector components  $T_{i,1}$ ,  $i = 1, 2, \dots, N$  [31]

$$\Sigma_{13} = \frac{3\mu_s(2-\nu_s)}{3(2-\nu_s) + 16(1-\nu_s)\sum_{i=1}^N d_i} 2E_{13} + \frac{16(1-\nu_s)\sum_{i=1}^N T_{i,1}d_i}{3(2-\nu_s) + 16(1-\nu_s)\sum_{i=1}^N d_i} \quad (4.41)$$

In (4.41),  $\mu_s$  and  $\nu_s$  stand for the shear modulus and for Poisson's ratio of the isotropic solid matrix.

- The concentration-influence relation expressing the dislocation vector  $[\underline{\xi}]_i$  as a function of the macrostrain  $\underline{\underline{E}}$  and of the interface traction vector  $\underline{T}_j$ , reads as [31]

$$[\underline{\xi}]_i = \underline{\underline{A}}_i : \underline{\underline{E}} + \sum_{j=1}^N \underline{\underline{D}}_{ij} \cdot \underline{T}_j \quad (4.42)$$

where  $\underline{\underline{A}}_i$  denotes a concentration tensor quantifying the influence of macrostrain  $\underline{\underline{E}}$  on the dislocation vector  $[\underline{\xi}]_i$ , provided that the interface traction vector  $\underline{T}_j$  vanishes; and  $\underline{\underline{D}}_{ij}$  stands for an influence tensor quantifying the influence of the interface traction vector  $\underline{T}_j$  on the dislocation vector  $[\underline{\xi}]_i$ , provided that macrostrain  $\underline{\underline{E}}$  and all the other interface families traction vanish. Specifying (4.42) for the matrix-interface composite shown in Fig. 4.3 and for loading in terms of pure macroscopic shear according to (4.1) and (4.2), allows for extracting a scalar equation linking in-plane dislocation  $[\underline{\xi}]_{i,1}$ , the shear strain  $E_{13}$ , and the in-plane interface traction vector component  $T_{1,i}$  [31], it reads as

$$[\underline{\xi}]_{i,1} = \frac{8(1-\nu_s)a_i}{\pi \left[ 3(2-\nu_s) + 16(1-\nu_s)\sum_{j=1}^N d_j \right]} \left[ 2E_{13} - \frac{T_{i,1}}{\mu_s} + \frac{16(1-\nu_s)}{3\mu_s(2-\nu_s)} \sum_{j=1}^N d_j (T_{j,1} - T_{i,1}) \right] \quad (4.43)$$

The sought differential equation in  $\Sigma_{13}$  and  $E_{13}$  is derived by means of linearly combining Eqn. (4.39), (4.41), and (4.43), as well as their time-derivatives. For the special case of one interface phase,  $N = 1$ , macroscopic state equation (4.41) and concentration-influence relation (4.43) are given in Eqs. (32) and (33) of the companion paper [80], and the sought differential equation is obtained as

$$\dot{\Sigma}_{13} \frac{8a\eta(1-\nu_s)}{3\pi(2-\nu_s)\mu_s} \left( \frac{1}{\mu_s} \right) + \Sigma_{13} \left( \frac{1}{\mu_s} + \frac{1}{\mu_s} \frac{16d(1-\nu_s)}{3(2-\nu_s)} \right) = 2\dot{E}_{13} \frac{8a\eta(1-\nu_s)}{3\pi(2-\nu_s)\mu_s} \left( \frac{1}{\mu_s} \right) + 2E_{13} \quad (4.44)$$

Next, we analyze the more general case of two interface phases ( $N = 2$ ). Specifying the macroscopic state equation (4.41) for  $N = 2$  yields

$$\Sigma_{13} = \frac{3\mu_s(2-\nu_s)}{3(2-\nu_s) + 16(d_1+d_2)(1-\nu_s)} 2E_{13} + \frac{16(1-\nu_s)(T_{1,1}d_1 + T_{2,1}d_2)}{3(2-\nu_s) + 16(d_1+d_2)(1-\nu_s)} \quad (4.45)$$

and specifying the concentration-influence relation (4.43) for  $N = 2$  delivers

$$\llbracket \xi \rrbracket_{1,1} = \frac{8(1-\nu_s)a_1}{\pi[3(2-\nu_s) + 16(1-\nu_s)(d_1+d_2)]} \left[ 2E_{13} - \frac{T_{1,1}}{\mu_s} + \frac{16(1-\nu_s)}{3\mu_s(2-\nu_s)} d_2(T_{1,2} - T_{1,1}) \right] \quad (4.46)$$

$$\llbracket \xi \rrbracket_{2,1} = \frac{8(1-\nu_s)a_2}{\pi[3(2-\nu_s) + 16(1-\nu_s)(d_1+d_2)]} \left[ 2E_{13} - \frac{T_{2,1}}{\mu_s} + \frac{16(1-\nu_s)}{3\mu_s(2-\nu_s)} d_1(T_{1,1} - T_{2,1}) \right] \quad (4.47)$$

In order to derive the sought relation between  $\Sigma_{13}$  and  $E_{13}$ , we construct a linear combination of (4.45), (4.46), and (4.47), whereby (4.46) and (4.47) are multiplied with  $2\mu_s\pi d_1/a_1$  and with  $2\mu_s\pi d_2/a_2$ , respectively, such that the interface tractions  $T_{1,1}$  and  $T_{2,1}$  are eliminated:

$$\frac{2\mu_s\pi d_1}{a_1} \llbracket \xi \rrbracket_{1,1} + \frac{2\mu_s\pi d_2}{a_2} \llbracket \xi \rrbracket_{2,1} + \Sigma_{13} = 2\mu_s E_{13} \quad (4.48)$$

Interface tractions are re-introduced by taking the time-derivative of (4.48) and considering (4.39), i.e.  $\llbracket \dot{\xi} \rrbracket_{1,1} = T_{1,1}/\eta_{i,1}$  as well as  $\llbracket \dot{\xi} \rrbracket_{2,1} = T_{2,1}/\eta_{i,2}$

$$\frac{2\mu_s\pi d_1}{a_1\eta_{i,1}} T_{1,1} + \frac{2\mu_s\pi d_2}{a_2\eta_{i,2}} T_{2,1} + \dot{\Sigma}_{13} = 2\mu_s \dot{E}_{13} \quad (4.49)$$

Next, we construct a linear combination of (4.49), (4.46), (4.47), whereby (4.46) and (4.47), respectively, are multiplied with

$$\frac{d_1 \left[ 16(1-\nu_s)(a_1\eta_{i,1}d_2 + a_2\eta_{i,2}d_1) + 3a_2\eta_{i,2}(2-\nu_s) \right] \mu_s^2 \pi^2}{4a_1^2\eta_{i,1}a_2\eta_{i,2}(1-\nu_s)} \quad (4.50)$$

and

$$\frac{d_2 \left[ 16(1-\nu_s)(a_1\eta_{i,1}d_2 + a_2\eta_{i,2}d_1) + 3a_1\eta_{i,1}(2-\nu_s) \right] \mu_s^2 \pi^2}{4a_1\eta_{i,1}a_2^2\eta_{i,2}(1-\nu_s)} \quad (4.51)$$

respectively, such that again, interface tractions  $T_{1,1}$  and  $T_{2,1}$  are eliminated, yielding

$$\begin{aligned} \dot{\Sigma}_{13} &= \frac{d_1 \left[ 16 (1 - \nu_s) (a_1 \eta_{i,1} d_2 + a_2 \eta_{i,2} d_1) + 3 a_2 \eta_{i,2} (2 - \nu_s) \right] \mu_s^2 \pi^2}{4 a_1^2 \eta_{i,1} a_2 \eta_{i,2} (1 - \nu_s)} \llbracket \dot{\xi} \rrbracket_{1,1} \\ &\quad - \frac{d_2 \left[ 16 (1 - \nu_s) (a_1 \eta_{i,1} d_2 + a_2 \eta_{i,2} d_1) + 3 a_1 \eta_{i,1} (2 - \nu_s) \right] \mu_s^2 \pi^2}{4 a_1 \eta_{i,1} a_2^2 \eta_{i,2} (1 - \nu_s)} \llbracket \dot{\xi} \rrbracket_{2,1} \\ &= 2 \mu_s \dot{E}_{13} - \frac{4 (a_1 \eta_{i,1} d_2 + a_2 \eta_{i,2} d_1) \pi \mu_s^2}{a_1 \eta_{i,1} a_2 \eta_{i,2}} E_{13} \end{aligned} \quad (4.52)$$

Interface tractions are re-introduced by taking the time-derivative of (4.52) and considering (4.39), i.e.  $\llbracket \dot{\xi} \rrbracket_{1,1} = T_{1,1}/\eta_{i,1}$  as well as  $\llbracket \dot{\xi} \rrbracket_{2,1} = T_{2,1}/\eta_{i,2}$

$$\begin{aligned} \ddot{\Sigma}_{13} &= \frac{d_1 \left[ 16 (1 - \nu_s) (a_1 \eta_{i,1} d_2 + a_2 \eta_{i,2} d_1) + 3 a_2 \eta_{i,2} (2 - \nu_s) \right] \mu_s^2 \pi^2}{4 a_1^2 \eta_{i,1}^2 a_2 \eta_{i,2} (1 - \nu_s)} T_{1,1} \\ &\quad - \frac{d_2 \left[ 16 (1 - \nu_s) (a_1 \eta_{i,1} d_2 + a_2 \eta_{i,2} d_1) + 3 a_1 \eta_{i,1} (2 - \nu_s) \right] \mu_s^2 \pi^2}{4 a_1 \eta_{i,1} a_2^2 \eta_{i,2}^2 (1 - \nu_s)} T_{2,1} \\ &= 2 \mu_s \ddot{E}_{13} - \frac{4 (a_1 \eta_{i,1} d_2 + a_2 \eta_{i,2} d_1) \pi \mu_s^2}{a_1 \eta_{i,1} a_2 \eta_{i,2}} \dot{E}_{13} \end{aligned} \quad (4.53)$$

The sought differential equation is finally obtained by constructing a linear combination of (4.45), (4.49), and (4.53), whereby (4.45) and (4.49), respectively, are multiplied with

$$\frac{\left[ 16 (1 - \nu_s) (a_1 d_2 \eta_{i,1} + a_2 d_1 \eta_{i,2}) + 3 a_1 \eta_{i,1} (2 - \nu_s) + 3 a_2 \eta_{i,2} (2 - \nu_s) \right] \mu_s \pi}{8 a_1 a_2 \eta_{i,1} \eta_{i,2} (1 - \nu_s)} \quad (4.54)$$

and

$$\frac{3 \left[ 16 (1 - \nu_s) (d_1 + d_2) + 3 (2 - \nu_s) \right] \pi^2 \mu_s^2 (2 - \nu_s)}{64 a_1 a_2 \eta_{i,1} \eta_{i,2} (1 - \nu_s)^2} \quad (4.55)$$

respectively. Re-arranging terms in the resulting expression, such that  $2E_{13}$  is multiplied with a coefficient being equal to 1, delivers

$$\begin{aligned}
 & \ddot{\Sigma}_{13} \left[ \frac{8a_1\eta_{i,1}(1-\nu_s)}{3\pi(2-\nu_s)\mu_s} \frac{8a_2\eta_{i,2}(1-\nu_s)}{3\pi(2-\nu_s)\mu_s} \left( \frac{1}{\mu_s} \right) \right] + \dot{\Sigma}_{13} \left[ \frac{8a_1\eta_{i,1}(1-\nu_s)}{3\pi(2-\nu_s)\mu_s} \left( \frac{1}{\mu_s} + \frac{1}{\mu_s} \frac{16d_2(1-\nu_s)}{3(2-\nu_s)} \right) \right. \\
 & \left. + \frac{8a_2\eta_{i,2}(1-\nu_s)}{3\pi(2-\nu_s)\mu_s} \left( \frac{1}{\mu_s} + \frac{1}{\mu_s} \frac{16d_1(1-\nu_s)}{3(2-\nu_s)} \right) \right] + \Sigma_{13} \left( \frac{1}{\mu_s} + \frac{1}{\mu_s} \frac{16d_1(1-\nu_s)}{3(2-\nu_s)} + \frac{1}{\mu_s} \frac{16d_2(1-\nu_s)}{3(2-\nu_s)} \right) \\
 & = \\
 & 2\ddot{E}_{13} \left[ \frac{8a_1\eta_{i,1}(1-\nu_s)}{3\pi(2-\nu_s)\mu_s} \frac{8a_2\eta_{i,2}(1-\nu_s)}{3\pi(2-\nu_s)\mu_s} \right] + 2\dot{E}_{13} \left[ \frac{8a_1\eta_{i,1}(1-\nu_s)}{3\pi(2-\nu_s)\mu_s} + \frac{8a_2\eta_{i,2}(1-\nu_s)}{3\pi(2-\nu_s)\mu_s} \right] + 2E_{13}
 \end{aligned} \tag{4.56}$$

The same strategy can be applied to derive a constitutive relation between  $\Sigma_{13}$  and  $2E_{13}$  for a matrix-inclusion composite containing three interface phases ( $N = 3$ ). The macroscopic poroelastic state equation (4.41) and the concentration-influence relations (4.43) are combined, such that interface tractions  $T_{1,1}$ ,  $T_{2,1}$ , and  $T_{3,1}$  are eliminated. This results in an equation containing  $\Sigma_{13}$ ,  $2E_{13}$ ,  $[\xi]_{1,1}$ ,  $[\xi]_{2,1}$ , and  $[\xi]_{3,1}$ . Taking the time-derivative of this equation and using the viscous law (4.39) delivers an equation containing  $\dot{\Sigma}_{13}$ ,  $2\dot{E}_{13}$ ,  $T_{1,1}$ ,  $T_{2,1}$ , and  $T_{3,1}$ . From this equation, the interface tractions are eliminated by constructing a suitable linear combination with the concentration-influence relations. The result is an expression containing  $\dot{\Sigma}_{13}$ ,  $\Sigma_{13}$ ,  $2\dot{E}_{13}$ ,  $2E_{13}$ ,  $[\xi]_{1,1}$ ,  $[\xi]_{2,1}$ , and  $[\xi]_{3,1}$ . Taking the time-derivative of this equation and using the viscous law (4.39) delivers an equation containing  $\ddot{\Sigma}_{13}$ ,  $\dot{\Sigma}_{13}$ ,  $2\ddot{E}_{13}$ ,  $2\dot{E}_{13}$ ,  $T_{1,1}$ ,  $T_{2,1}$ , and  $T_{3,1}$ . From this equation, the interface tractions are eliminated by constructing a suitable linear combination with the concentration-influence relations. The result is an expression containing  $\ddot{\Sigma}_{13}$ ,  $\dot{\Sigma}_{13}$ ,  $\Sigma_{13}$ ,  $2\ddot{E}_{13}$ ,  $2\dot{E}_{13}$ ,  $2E_{13}$ ,  $[\xi]_{1,1}$ ,  $[\xi]_{2,1}$ , and  $[\xi]_{3,1}$ . Taking the time-derivative of this equation and using the viscous law (4.39) delivers an equation containing  $\ddot{\Sigma}_{13}$ ,  $\dot{\Sigma}_{13}$ ,  $\dot{\Sigma}_{13}$ ,  $2\ddot{E}_{13}$ ,  $2\dot{E}_{13}$ ,  $2\dot{E}_{13}$ ,  $T_{1,1}$ ,  $T_{2,1}$ , and  $T_{3,1}$ . The sought differential equation is obtained from construction a linear combination the derived equations containing (i)  $\Sigma_{13}$ ,  $2E_{13}$ ,  $T_{1,1}$ ,  $T_{2,1}$ , and  $T_{3,1}$ , (ii)  $\dot{\Sigma}_{13}$ ,  $\Sigma_{13}$ ,  $2\dot{E}_{13}$ ,  $2E_{13}$ ,  $T_{1,1}$ ,  $T_{2,1}$ , and  $T_{3,1}$ , and (iii)  $\ddot{\Sigma}_{13}$ ,  $\ddot{\Sigma}_{13}$ ,  $\dot{\Sigma}_{13}$ ,  $2\ddot{E}_{13}$ ,  $2\dot{E}_{13}$ ,  $2\dot{E}_{13}$ ,  $T_{1,1}$ ,  $T_{2,1}$ , and  $T_{3,1}$ , with the aim to eliminate the

interface tractions. This delivers

$$\begin{aligned}
 & \ddot{\Sigma}_{13} \left[ \frac{8 a_1 \eta_{i,1} (1 - \nu_s)}{3 \pi (2 - \nu_s) \mu_s} \frac{8 a_2 \eta_{i,2} (1 - \nu_s)}{3 \pi (2 - \nu_s) \mu_s} \frac{8 a_3 \eta_{i,3} (1 - \nu_s)}{3 \pi (2 - \nu_s) \mu_s} \left( \frac{1}{\mu_s} \right) \right] + \\
 & \dot{\Sigma}_{13} \left[ \frac{8 a_1 \eta_{i,1} (1 - \nu_s)}{3 \pi (2 - \nu_s) \mu_s} \frac{8 a_2 \eta_{i,2} (1 - \nu_s)}{3 \pi (2 - \nu_s) \mu_s} \left( \frac{1}{\mu_s} + \frac{1}{\mu_s} \frac{16 d_3 (1 - \nu_s)}{3 (2 - \nu_s)} \right) \right. \\
 & \quad + \frac{8 a_1 \eta_{i,1} (1 - \nu_s)}{3 \pi (2 - \nu_s) \mu_s} \frac{8 a_3 \eta_{i,3} (1 - \nu_s)}{3 \pi (2 - \nu_s) \mu_s} \left( \frac{1}{\mu_s} + \frac{1}{\mu_s} \frac{16 d_2 (1 - \nu_s)}{3 (2 - \nu_s)} \right) \\
 & \quad \left. + \frac{8 a_2 \eta_{i,2} (1 - \nu_s)}{3 \pi (2 - \nu_s) \mu_s} \frac{8 a_3 \eta_{i,3} (1 - \nu_s)}{3 \pi (2 - \nu_s) \mu_s} \left( \frac{1}{\mu_s} + \frac{1}{\mu_s} \frac{16 d_1 (1 - \nu_s)}{3 (2 - \nu_s)} \right) \right] + \\
 & \dot{\Sigma}_{13} \left[ \frac{8 a_1 \eta_{i,1} (1 - \nu_s)}{3 \pi (2 - \nu_s) \mu_s} \left( \frac{1}{\mu_s} + \frac{1}{\mu_s} \frac{16 d_2 (1 - \nu_s)}{3 (2 - \nu_s)} + \frac{1}{\mu_s} \frac{16 d_3 (1 - \nu_s)}{3 (2 - \nu_s)} \right) \right. \\
 & \quad + \frac{8 a_2 \eta_{i,2} (1 - \nu_s)}{3 \pi (2 - \nu_s) \mu_s} \left( \frac{1}{\mu_s} + \frac{1}{\mu_s} \frac{16 d_1 (1 - \nu_s)}{3 (2 - \nu_s)} + \frac{1}{\mu_s} \frac{16 d_3 (1 - \nu_s)}{3 (2 - \nu_s)} \right) \\
 & \quad \left. + \frac{8 a_3 \eta_{i,3} (1 - \nu_s)}{3 \pi (2 - \nu_s) \mu_s} \left( \frac{1}{\mu_s} + \frac{1}{\mu_s} \frac{16 d_1 (1 - \nu_s)}{3 (2 - \nu_s)} + \frac{1}{\mu_s} \frac{16 d_2 (1 - \nu_s)}{3 (2 - \nu_s)} \right) \right] \tag{4.57} \\
 & \Sigma_{13} \left[ \frac{1}{\mu_s} + \frac{1}{\mu_s} \frac{16 d_1 (1 - \nu_s)}{3 (2 - \nu_s)} + \frac{1}{\mu_s} \frac{16 d_2 (1 - \nu_s)}{3 (2 - \nu_s)} + \frac{1}{\mu_s} \frac{16 d_3 (1 - \nu_s)}{3 (2 - \nu_s)} \right] \\
 & = \\
 & 2 \ddot{E}_{13} \left[ \frac{8 a_1 \eta_{i,1} (1 - \nu_s)}{3 \pi (2 - \nu_s) \mu_s} \frac{8 a_2 \eta_{i,2} (1 - \nu_s)}{3 \pi (2 - \nu_s) \mu_s} \frac{8 a_3 \eta_{i,3} (1 - \nu_s)}{3 \pi (2 - \nu_s) \mu_s} \right] + \\
 & 2 \ddot{E}_{13} \left[ \frac{8 a_1 \eta_{i,1} (1 - \nu_s)}{3 \pi (2 - \nu_s) \mu_s} \frac{8 a_2 \eta_{i,2} (1 - \nu_s)}{3 \pi (2 - \nu_s) \mu_s} + \frac{8 a_2 \eta_{i,2} (1 - \nu_s)}{3 \pi (2 - \nu_s) \mu_s} \frac{8 a_3 \eta_{i,3} (1 - \nu_s)}{3 \pi (2 - \nu_s) \mu_s} \right. \\
 & \quad \left. + \frac{8 a_1 \eta_{i,1} (1 - \nu_s)}{3 \pi (2 - \nu_s) \mu_s} \frac{8 a_3 \eta_{i,3} (1 - \nu_s)}{3 \pi (2 - \nu_s) \mu_s} \right] + \\
 & 2 \dot{E}_{13} \left[ \frac{8 a_1 \eta_{i,1} (1 - \nu_s)}{3 \pi (2 - \nu_s) \mu_s} + \frac{8 a_2 \eta_{i,2} (1 - \nu_s)}{3 \pi (2 - \nu_s) \mu_s} + \frac{8 a_3 \eta_{i,3} (1 - \nu_s)}{3 \pi (2 - \nu_s) \mu_s} \right] + 2 E_{13}
 \end{aligned}$$

The general structure of constitutive  $\Sigma_{13}, E_{13}$ -relations for a matrix-inclusion composite containing  $N$  interface phases can be identified from comparing the  $\Sigma_{13}, E_{13}$ -relations of one, two, and three interface phases, respectively, see Eqs. (4.44), (4.56) and (4.57). Accordingly, it appears that the first-order derivative of the strain,  $2\dot{E}_{13}$ , is always multiplied with the sum over all expressions of the form  $8a_i\eta_{i,1}(1-\nu_s)/[3\pi(2-\nu_s)\mu_s]$ , with  $i = 1, 2, \dots, N$ . The second-order derivative of the strain,  $2\ddot{E}_{13}$ , is always multiplied with the sum over all possible products of two different characteristic times. The third-order derivative of the strain,  $2\ddot{E}_{13}$ , is always multiplied with the sum over all possible products of three different characteristic times. This clarifies the general structure: the  $n^{th}$ -order derivative of the strain is multiplied with the sum over all possible products of  $n$  different characteristic times. The coefficients multiplied with the stress and stress derivatives are just slightly more complex: The stress,  $\Sigma_{13}$ , is always multiplied with a coefficient being equal to  $1/\mu_s$  plus the sum over all expressions  $16d_r(1-\nu_s)/[\mu_s 3(2-\nu_s)]$  with  $r = 1, 2, \dots, N$ . The first-order derivative

of the stress,  $\dot{\Sigma}_{13}$ , is always multiplied with the sum over all the products of characteristic times,  $8a_i\eta_{i,1}(1-\nu_s)/[3\pi(2-\nu_s)\mu_s]$ , and corresponding constants being equal to  $1/\mu_s$  plus the sum over all expressions  $16d_r(1-\nu_s)/[\mu_s 3(2-\nu_s)]$ , with  $r = 1, 2, \dots, N$ , minus  $16d_i(1-\nu_s)/[\mu_s 3(2-\nu_s)]$ . The second-order derivative of the stress,  $\ddot{\Sigma}_{13}$ , is always multiplied with the sum over all possible products of two different characteristic times,  $8^2 a_i \eta_{i,1} a_j \eta_{j,1} (1-\nu_s)^2 / [3\pi(2-\nu_s)\mu_s]^2$ , whereby  $i \neq j$ , and corresponding constants being equal to  $1/\mu_s$  plus the sum over all expressions  $16d_r(1-\nu_s)/[\mu_s 3(2-\nu_s)]$ , with  $r = 1, 2, \dots, N$ , minus  $16(d_i + d_j)(1-\nu_s)/[\mu_s 3(2-\nu_s)]$ . The third-order derivative of the stress,  $\dddot{\Sigma}_{13}$ , is always multiplied with the sum over all possible products of three different characteristic times,  $8^3 a_i \eta_{i,1} a_j \eta_{j,1} a_k \eta_{k,1} (1-\nu_s)^3 / [3\pi(2-\nu_s)]^3$ , whereby  $i \neq j$ ,  $i \neq k$ ,  $j \neq k$ , and corresponding constants which are equal to  $1/\mu_s$  plus the sum over all expressions  $16d_r(1-\nu_s)/[\mu_s 3(2-\nu_s)]$ , with  $r = 1, 2, \dots, N$ , minus  $16(d_i + d_j + d_k)(1-\nu_s)/[\mu_s 3(2-\nu_s)]$ . This clarifies the general structure: the  $n^{\text{th}}$ -order derivative of the stress is multiplied with the sum over all possible products of  $n$  different characteristic times and constants being equal to the sum over  $1/\mu_s$  plus the sum over all expressions  $16d_r(1-\nu_s)/[\mu_s 3(2-\nu_s)]$ , with  $r = 1, 2, \dots, N$ , minus all expressions  $16d_l(1-\nu_s)/[\mu_s 3(2-\nu_s)]$  with indexes  $l$  running over all those values which show up in the products of the characteristic times. In conclusion, mathematical forms of the general  $\Sigma_{13}, E_{13}$ -relation for a matrix-inclusion composite with  $N$  interface phases reads as

$$\begin{aligned}
 & \left( \frac{1}{\mu_s} + \sum_{l=1}^N \frac{1}{\mu_s} \frac{16 d_l (1 - \nu_s)}{3 (2 - \nu_s)} \right) \Sigma_{13} + \sum_{n=1}^N \left( \sum_{i_1=1}^{N-n+1} \dots \right. \\
 & \dots \left( \sum_{i_a=i_{a-1}+1}^{N-(n-a)+1} \dots \left( \sum_{i_n=i_{n-1}+1}^N \left( \left( \left( \frac{1}{\mu_s} + \sum_{l=1}^N \frac{1}{\mu_s} \frac{16 d_l (1 - \nu_s)}{3 (2 - \nu_s)} \right) - \sum_{j \in \{i_1, \dots, i_n\}} \frac{16 d_j (1 - \nu_s)}{3 (2 - \nu_s)} \right) \right) \right. \right. \\
 & \left. \left. \left( \prod_{k \in \{i_1, \dots, i_n\}} \frac{8 a_k \eta_{k,1} (1 - \nu_s)}{3 \pi (2 - \nu_s) \mu_s} \right) \right) \dots \right) \dots \right) \frac{\partial^n \Sigma_{13}}{\partial t^n} \\
 & = \\
 & 2 E_{13} + \sum_{n=1}^N \left( \sum_{i_1=1}^{N-n+1} \dots \left( \sum_{i_a=i_{a-1}+1}^{N-(n-a)+1} \dots \left( \sum_{i_n=i_{n-1}+1}^N \left( \prod_{j \in \{i_1, \dots, i_n\}} \frac{8 a_j \eta_{j,1} (1 - \nu_s)}{3 \pi (2 - \nu_s) \mu_s} \right) \right) \dots \right) \dots \right) \frac{\partial^n 2 E_{13}}{\partial t^n}
 \end{aligned} \tag{4.58}$$

#### 4.4 Interface micromechanics assessment of rheological models

Here, we establish relations between the Kelvin-Voigt chain-related and the Maxwell chain-related spring and dashpot parameters, as well as between these

parameters and the micromechanics-related quantities of the matrix-interface composites, namely the shear modulus and Poisson's ratio of the solid matrix, as well as the sizes, viscosities, and densities of the embedded 2D interfaces. To this end, we compare the Kelvin-Voigt chain-related, Maxwell chain-related, and micromechanics-related coefficients occurring in the differential equations comprising stresses, strains, and their temporal derivatives; see Eqs. (4.21), (4.38), and (4.58).

#### 4.4.1 Relations between Kelvin Voigt chain parameters and micromechanical quantities

Links between spring stiffnesses and damper viscosities of Kelvin Voigt chains, on the one hand, and micromechanical properties, on the other hand, are obtained from comparing the coefficients appearing in the two  $N - th$  order differential equations (4.21) and (4.58). This leads to the identities

$$\left( \frac{1}{\mu_e} + \sum_{l=1}^N \frac{1}{\mu_l} \right) = \left( \frac{1}{\mu_s} + \sum_{l=1}^N \frac{1}{\mu_s} \frac{16 d_l (1 - \nu_s)}{3 (2 - \nu_s)} \right) \quad (4.59)$$

as well as

$$\begin{aligned} & \sum_{n=1}^N \left( \sum_{i_1=1}^{N-n+1} \cdots \left( \sum_{i_a=i_{a-1}+1}^{N-(n-a)+1} \cdots \left( \sum_{i_n=i_{n-1}+1}^N \left( \left( \left( \frac{1}{\mu_e} + \sum_{l=1}^N \frac{1}{\mu_l} \right) - \sum_{j \in \{i_1, \dots, i_n\}} \frac{1}{\mu_j} \right) \right. \right. \right. \right. \\ & \quad \left. \left. \left. \left. \left( \prod_{k \in \{i_1, \dots, i_n\}} \frac{\eta_k}{\mu_k} \right) \right) \right) \right) \right) \cdots \right) \cdots \\ & = \\ & \sum_{n=1}^N \left( \sum_{i_1=1}^{N-n+1} \cdots \left( \sum_{i_a=i_{a-1}+1}^{N-(n-a)+1} \cdots \left( \sum_{i_n=i_{n-1}+1}^N \left( \left( \left( \frac{1}{\mu_s} + \sum_{l=1}^N \frac{1}{\mu_s} \frac{16 d_l (1 - \nu_s)}{3 (2 - \nu_s)} \right) \right. \right. \right. \right. \right. \\ & \quad \left. \left. \left. \left. \left( \sum_{j \in \{i_1, \dots, i_n\}} \frac{16 d_j (1 - \nu_s)}{3 (2 - \nu_s)} \right) \left( \prod_{k \in \{i_1, \dots, i_n\}} \frac{8 a_k \eta_{k,1} (1 - \nu_s)}{3 \pi (2 - \nu_s) \mu_s} \right) \right) \right) \right) \right) \cdots \right) \cdots \end{aligned} \quad (4.60)$$

and finally

$$\begin{aligned} & \sum_{n=1}^N \left( \sum_{i_1=1}^{N-n+1} \cdots \left( \sum_{i_a=i_{a-1}+1}^{N-(n-a)+1} \cdots \left( \sum_{i_n=i_{n-1}+1}^N \left( \prod_{j \in \{i_1, \dots, i_n\}} \frac{\eta_j}{\mu_j} \right) \right) \cdots \right) \cdots \right) \\ &= \\ & \sum_{n=1}^N \left( \sum_{i_1=1}^{N-n+1} \cdots \left( \sum_{i_a=i_{a-1}+1}^{N-(n-a)+1} \cdots \left( \sum_{i_n=i_{n-1}+1}^N \left( \prod_{j \in \{i_1, \dots, i_n\}} \frac{8 a_j \eta_{j,1} (1 - \nu_s)}{3 \pi (2 - \nu_s) \mu_s} \right) \right) \cdots \right) \cdots \right) \end{aligned} \quad (4.61)$$

Eqs. (4.59), (4.60), and (4.61) represent  $2N + 1$  algebraic equations, with the following solutions

$$\left. \begin{aligned} \mu_e &= \mu_s, \\ \mu_i &= \frac{3\mu_s(2 - \nu_s)}{16d_i(1 - \nu_s)} \\ \eta_{i,1} &= \frac{a_i \eta_{i,1}}{2\pi d_i} \end{aligned} \right\} \quad i = 1, 2, \dots, N \quad (4.62)$$

We observe that Eq. (4.62) is formally identical to the relations derived for the special case  $N = 1$  in the companion paper, see [80].

#### 4.4.2 Relations between Maxwell chain parameters and viscosities as well as micromechanical quantities

Links between spring stiffnesses and damper viscosities of Maxwell chains, on the one hand, and micromechanical properties, on the other hand, are obtained from comparing the coefficients appearing in the two  $N - th$  order differential equations (4.38) and (4.58). This leads to the identities

$$\frac{1}{\mu_E} = \left( \frac{1}{\mu_s} + \sum_{l=1}^N \frac{1}{\mu_s} \frac{16 d_l (1 - \nu_s)}{3 (2 - \nu_s)} \right) \quad (4.63)$$

as well as

$$\begin{aligned}
 & \frac{1}{\mu_E} \sum_{n=I}^N \left( \sum_{i_I=I}^{N-n+I} \cdots \left( \sum_{i_a=i_{a-I}+I}^{N-(n-a)+I} \cdots \left( \sum_{i_n=i_{n-I}+I}^N \left( \prod_{j \in \{i_I, \dots, i_n\}} \frac{\eta_j}{\mu_j} \right) \right) \cdots \right) \cdots \right) \\
 & = \\
 & \sum_{n=1}^N \left( \sum_{i_1=1}^{N-n+1} \cdots \left( \sum_{i_a=i_{a-1}+1}^{N-(n-a)+1} \cdots \left( \sum_{i_n=i_{n-1}+1}^N \left( \left( \left( \frac{1}{\mu_s} + \sum_{l=1}^N \frac{1}{\mu_s} \frac{16 d_l (1 - \nu_s)}{3 (2 - \nu_s)} \right) \right. \right. \right. \right. \\
 & \quad \left. \left. \left. \left. - \sum_{j \in \{i_1, \dots, i_n\}} \frac{16 d_j (1 - \nu_s)}{3 (2 - \nu_s)} \right) \right) \left( \prod_{k \in \{i_1, \dots, i_n\}} \frac{8 a_k \eta_{k,1} (1 - \nu_s)}{3 \pi (2 - \nu_s) \mu_s} \right) \right) \right) \cdots \right) \cdots \right)
 \end{aligned} \tag{4.64}$$

and finally

$$\begin{aligned}
 & \frac{1}{\mu_E} \sum_{n=I}^N \left( \sum_{i_I=I}^{N-n+I} \cdots \left( \sum_{i_a=i_{a-I}+I}^{N-(n-a)+I} \cdots \left( \sum_{i_n=i_{n-I}+I}^N \left( \left( \mu_E + \sum_{j \in \{i_I, \dots, i_n\}} \mu_j \right) \left( \prod_{k \in \{i_I, \dots, i_n\}} \frac{\eta_k}{\mu_k} \right) \right) \right) \right) \cdots \right) \cdots \right) \\
 & = \\
 & \sum_{n=1}^N \left( \sum_{i_1=1}^{N-n+1} \cdots \left( \sum_{i_a=i_{a-1}+1}^{N-(n-a)+1} \cdots \left( \sum_{i_n=i_{n-1}+1}^N \left( \prod_{j \in \{i_1, \dots, i_n\}} \frac{8 a_j \eta_{j,1} (1 - \nu_s)}{3 \pi (2 - \nu_s) \mu_s} \right) \right) \right) \cdots \right) \cdots \right)
 \end{aligned} \tag{4.65}$$

Eqs. (4.63), (4.64), and (4.65) represent a system of  $2N + 1$  non-linear, coupled algebraic equations. The analytical solution for  $N = 1$  is presented in the companion paper, see Eq. (25) in [80], but already for  $N = 2$ , analytical solutions involve complicated terms involving square root-expressions, for  $N = 3$  cubic roots are found, and so on. We conclude that for the general situation of  $N$  interface phases and  $N$  Maxwell chains, Eqs. (4.63)-(4.65) have to be solved numerically.

#### 4.4.3 Relation between parameters characterizing Kelvin-Voigt and Maxwell chains, respectively

The link between the spring dashpot constants of the Kelvin-Voigt chain model and of the Maxwell chain model can be expressed as

$$\frac{1}{\mu_E} = \left( \frac{1}{\mu_e} + \sum_{l=1}^N \frac{1}{\mu_l} \right) \tag{4.66}$$

as well as

$$\begin{aligned}
 & \frac{1}{\mu_E} \sum_{n=I}^N \left( \sum_{i_I=I}^{N-n+I} \cdots \left( \sum_{i_a=i_{a-I}+I}^{N-(n-a)+I} \cdots \left( \sum_{i_n=i_{n-I}+I}^N \left( \prod_{j \in \{i_I, \dots, i_n\}} \frac{\eta_j}{\mu_j} \right) \right) \cdots \right) \cdots \right) \\
 & \qquad \qquad \qquad = \\
 & \sum_{n=1}^N \left( \sum_{i_1=1}^{N-n+1} \cdots \left( \sum_{i_a=i_{a-1}+1}^{N-(n-a)+1} \cdots \left( \sum_{i_n=i_{n-1}+1}^N \left( \left( \left( \frac{1}{\mu_e} + \sum_{l=1}^N \frac{1}{\mu_l} \right) - \sum_{j \in \{i_1, \dots, i_n\}} \frac{1}{\mu_j} \right) \right) \right) \right) \right) \\
 & \qquad \qquad \qquad \left( \prod_{k \in \{i_1, \dots, i_n\}} \frac{\eta_k}{\mu_k} \right) \right) \cdots \right) \cdots
 \end{aligned} \tag{4.67}$$

and

$$\begin{aligned}
 & \frac{1}{\mu_E} \sum_{n=I}^N \left( \sum_{i_I=I}^{N-n+I} \cdots \left( \sum_{i_a=i_{a-I}+I}^{N-(n-a)+I} \cdots \left( \sum_{i_n=i_{n-I}+I}^N \left( \left( \mu_E + \sum_{j \in \{i_I, \dots, i_n\}} \mu_j \right) \left( \prod_{k \in \{i_I, \dots, i_n\}} \frac{\eta_k}{\mu_k} \right) \right) \right) \right) \cdots \right) \cdots \right) \\
 & \qquad \qquad \qquad = \\
 & \sum_{n=1}^N \left( \sum_{i_1=1}^{N-n+1} \cdots \left( \sum_{i_a=i_{a-1}+1}^{N-(n-a)+1} \cdots \left( \sum_{i_n=i_{n-1}+1}^N \left( \prod_{j \in \{i_1, \dots, i_n\}} \frac{\eta_j}{\mu_j} \right) \right) \right) \cdots \right) \cdots
 \end{aligned} \tag{4.68}$$

## 4.5 Discussion and conclusion

Both Kelvin-Voigt and Maxwell chain models are well suited to describe the time-dependent behavior of matrix-interface composites with  $N$  different interface families, exhibiting different sizes and viscosities. Still, the chosen type of the rheological representation matters significantly when it comes to the mathematical complexity of the relations between the microstructural quantities of matrix-interface composites and the rheological parameters such as spring stiffnesses and dashpot viscosities. As for Kelvin-Voigt chain-models, the “intuitive” relations identified for one interface family and one Kelvin-Voigt unit, see the companion paper [80], are conceptually identical with the relations found for  $N$  interface families and  $N$  Kelvin-Voigt units, see Eqs. (4.59) – (4.62). As for Maxwell chain models, however, the mathematical complexity of the relations increases with increasing number of interface families and number of Maxwell units, see Eq. (4.63) – (4.65). In other words, from the viewpoint of interface micromechanics, Kelvin-Voigt chain models are conceptually preferable to the (fully equivalent) Maxwell chain models.

The herein derived results suggest that observation of rather complex macroscopic creep behavior, which raises the need for introduction of several rheological chain units when it comes to modeling of measured macroscopic creep functions, is an indicator for microscopic interface size distributions. Different sizes of interfaces, located at the microstructure of a creeping material, namely, manifest themselves at the macroscale of the materials as different characteristic creep times. In other words, interface micromechanics suggests that continuous interface size distributions relate to continuous spectra of macroscopic characteristic creep times.

The herein presented developments also allow for an interesting interpretation of the Maxwell chain models typically used for modeling aging creep of concrete, see [44] and follow-up publications. Such models are based on spring stiffnesses and dashpot viscosities which evolve with increasing maturity of concrete. Assessment of these evolutions from the viewpoint of the herein established relations between interface micromechanics and rheological models propose that the chemical hardening reaction between water and cement as well as the related transformation of the microstructure of the material induces evolutions of (i) microstructural interface sizes and densities, as well as of (ii) the stress concentration properties from the macroscale of concrete down to the creeping calcium-silicate-hydrates.

Accordingly, the following extensions of the underlying interface micromechanics framework are desirable in the sense of an outlook to the future: Firstly, it will be interesting to consider materials with isotropic orientations of viscous interfaces, i.e. a materials containing a great number of the here investigated transversely-isotropic matrix-inclusion composites, whereby these building block are randomly orientated in space. Secondly, it will be desirable to gain access to physical values of interface viscosities, in order to develop predictive multiscale creep models for hydrated materials such as hydroxyapatite in bone and biomimetic materials. Given that viscous interfaces are expected on diameter length scales as small as some hundreds of nanometers up to a few micrometers, and of thicknesses which may even be below 1 nanometer, together with technological difficulties to perform “microshear tests” at such microscales, molecular dynamics simulation [1, 18, 81, 82] appears as the interesting candidates for direct interface viscosity identification; in addition to downscaled viscosity values from various independent macroscopic test, as done e.g. in [21]

## 4.6 Nomenclature

---

$a$	radius of the interface
$\underline{\underline{B}}$	fourth-order Biot tensor
$\underline{\underline{C}}_s$	fourth-order stiffness tensor of solid
$\underline{\underline{C}}_s^{-1}$	inverse of fourth-order stiffness tensor of solid
$\underline{\underline{C}}_{hom}$	fourth-order homogenized stiffness tensor
$d$	interface density parameter
$\underline{e}_1, \underline{e}_3$	unit base vectors of Cartesian coordinate system
$\underline{E}$	macroscopic strain
$E_{13}$	shear component of macroscopic strain
$i$	index for interface phase
$\underline{\underline{I}}$	symmetric fourth-order identity tensor
$\underline{\underline{I}}_{dev}$	deviatoric part of $\underline{\underline{I}}$
$\underline{\underline{I}}_{vol}$	volumetric part of $\underline{\underline{I}}$
$k_s$	bulk modulus of solid phase
$\ell$	characteristic size of RVE
$N$	number of Maxwell or Kelvin-Voigt units
RVE	Representative of Volume Element
$s$	index for solid phase
$\underline{T}$	interface traction vector
$\underline{\underline{T}}_i$	fourth-order morphology tensor for 2D interface inclusion (“sharp crack” morphology)
$T_{i,1}$	shear component of traction vector in the $i$ -th interface phase
$x, y, z$	Cartesian coordinates
$\underline{x}$	position vector
$\gamma$	shear strain
$\gamma_e$	shear strain of elastic spring of Kelvin-Voigt representation of standard linear solid
$\gamma_h$	solution for homogeneous differential equation for shear strain
$\gamma_p$	particulate integral shear strain
$\gamma_E$	shear strain of elastic spring of Maxwell representation of standard linear solid
$\gamma_I$	shear strain of Maxwell unit
$\gamma_I^\mu$	shear strain of spring in Maxwell unit
$\gamma_I^\eta$	shear strain of dashpot in Maxwell unit
$\delta$	Kronecker delta
$\underline{\underline{\varepsilon}}$	microscopic strain

---

$\eta_{i,1}$	viscosity of the interfaces
$\eta_1$	viscosity constant of dashpot in Kelvin-Voigt unit
$\eta_I$	viscosity constant of dashpot in Maxwell unit
$\mu_e$	shear modulus of elastic spring in Zener model
$\mu_E$	shear modulus of spring in Kelvin-Voigt model
$\mu_1$	shear modulus of spring in Kelvin-Voigt unit
$\mu_I$	shear modulus of spring in Maxwell unit
$\mu_s$	shear modulus of isotropic solid matrix
$\nu_s$	Poisson's ratio of isotropic solid matrix
$\underline{\xi}$	displacement vector
$\llbracket \xi \rrbracket_{i,1}$	shear component of dislocation of interfaces in shear direction
$\underline{\underline{\sigma}}$	microscopic stress
$\underline{\underline{\sigma}}_i^E$	interface eigenstress tensor
$\underline{\underline{\Sigma}}$	macroscopic stress
$\Sigma_{13}$	shear component of macroscopic stress
$\tau$	shear stress
$\tau_h$	solution for homogeneous differential equation for shear stress
$\tau_p$	particulate integral for shear stress
$\tau_e$	shear stress in elastic spring for Kelvin-Voigt representation of standard linear solid
$\tau_E$	shear stress in elastic spring for Maxwell representation of standard linear solid
$\tau_I$	shear stress for Maxwell unit
$\tau_1$	shear stress for Kelvin-Voigt unit
$\tau_1^\mu$	shear stress in spring for Kelvin-Voigt unit
$\tau_1^\eta$	shear stress in dashpot for Kelvin-Voigt unit
$\partial$	partial derivative
:	second-order tensor contraction
$\dot{\bullet}$	partial derivative with respect to time ("rate"), of quantity " $\bullet$ "
$\otimes$	dyadic product

## Chapter 5

# Viscosity of water interfaces adjacent to Hydroxyapatite crystals: Shear thinning as source for significant viscosity change

### 5.1 Introduction

“Universal” mechanical properties of bone’s elementary constituents (hydroxyapatite, collagen, and water with non-collagenous organics), their “universal” interaction patterns across multiple length scales, and corresponding “universal” composition rules for extracellular bone matrices allow for the prediction of the large variety of mechanical properties of different bone tissues observed at the macroscopic scale, see, e. g. [47, 48, 49, 50]. In this context, the viscoelasticity of interface-penetrated extrafibrillar mineral clusters were identified from downscaling of different, independent macroscopic creep and relaxation tests. They can be quantified by isotropic Kelvin-Voigt parameters, in terms of a viscosity amounting to  $\eta_{KV,iso} = 1.34 \cdot 10^5$  GPs, and a spring constant (= a viscous shear stiffness) amounting to  $\mu_{KV,iso} = 179$  MPa. We here expand on how to downscale this bulk viscosity value further, i. e. down to the level of the individual interfaces.

To this end, we first use so-called Reuss bounds in order to derive, from knowledge on anisotropic creep tensors of matrix-interface composites with parallel interfaces, the *isotropic* creep tensor of a new material system which comprises *randomly oriented* RVEs of matrix-interface composites with parallel interfaces

(Section 5.2). This opens the door to top-down identification of interface density, interface viscosity, and bulk viscosity of “glassy” water filling interfaces between hydroxyapatite crystals (Section 5.3). As for the comparison of the top-down identified bulk viscosity with a corresponding quantity derived in a bottom-up approach resting on molecular dynamics simulations, it turns out to be useful to estimate the dislocation speed from macroscopic relaxation experiments on bone (Section 5.4). Top-down identified and bottom-up identified bulk viscosity of adsorbed water and speeds of interfacial dislocations, respectively, differ by several orders of magnitude. This allows for identifying the pronounced thixotropic behavior of “glassy water”, the viscosity of which decreases with increasing dislocation rate (Section 5.5).

## 5.2 Reuss bound-based estimation of creep tensor for interfaced materials with random orientation of interfaced building blocks

We here envision a new material system consisting of randomly arranged and randomly oriented building blocks which are RVEs of the matrix-interface composites with one family of parallel interfaces. Our first aim is to derive the corresponding isotropic creep tensor of such a material system. To this end, we recall that a matrix-interface composite with parallel interfaces exhibits an *anisotropic* creep compliance tensor  $\underline{\underline{J}}$  which reads as, see also (1.119)

$$\underline{\underline{J}}_{aniso} = \underline{\underline{C}}_s^{-1} + \frac{(1 + \nu_s)}{2 E_s} \frac{16 d (1 - \nu_s)}{3 (2 - \nu_s)} \left[ 1 - \exp \left( \frac{-t}{\tau_{creep}} \right) \right] \underline{\underline{I}}_{aniso} \quad (5.1)$$

In Eq. (5.1),  $\underline{\underline{J}}_{aniso}$  stands for the anisotropic fourth-order creep compliance tensor,  $\underline{\underline{C}}_s^{-1}$  stands for the inversion of fourth-order elastic stiffness tensor of the solid matrix,  $\underline{\underline{I}}_{aniso}$  stands for the anisotropic fourth-order identity tensor, and  $\tau_{creep}$  is the creep characteristic time, see (1.108). Given interfaces with normals pointing in  $\underline{e}_z$  direction, the anisotropic fourth-order identity tensor reads as

$$\begin{aligned} \underline{\underline{I}}_{aniso} = & \underline{e}_x \otimes \underline{e}_z \otimes \underline{e}_x \otimes \underline{e}_z + \underline{e}_x \otimes \underline{e}_z \otimes \underline{e}_z \otimes \underline{e}_x \\ & + \underline{e}_z \otimes \underline{e}_x \otimes \underline{e}_x \otimes \underline{e}_z + \underline{e}_z \otimes \underline{e}_x \otimes \underline{e}_z \otimes \underline{e}_x \\ & + \underline{e}_y \otimes \underline{e}_z \otimes \underline{e}_y \otimes \underline{e}_z + \underline{e}_y \otimes \underline{e}_z \otimes \underline{e}_z \otimes \underline{e}_y \\ & + \underline{e}_z \otimes \underline{e}_y \otimes \underline{e}_y \otimes \underline{e}_z + \underline{e}_z \otimes \underline{e}_y \otimes \underline{e}_z \otimes \underline{e}_y \end{aligned} \quad (5.2)$$

A material which is constituted by a random arrangement of building blocks with parallel interfaces, i. e. a material hosting randomly oriented matrix-interface composites, exhibits isotropic homogenized properties. In order to derive from the anisotropic creep functions  $\underline{\underline{J}}_{aniso}$  of the individual building blocks, see (5.1) the isotropic creep compliance tensor  $\underline{\underline{J}}_{iso}$  of the described isotropic material, we use the rule of mixture for creep compliance, or “Reuss bound”, i. e. we consider simply a spatial average over all possible orientations of matrix-interface composites

$$\underline{\underline{J}}_{iso} = \int_{\phi=0}^{\phi=2\pi} \int_{\theta=0}^{\theta=\pi} \underline{\underline{J}}_{aniso} \frac{\sin \theta d\theta d\phi}{4\pi} \quad (5.3)$$

In (5.3),  $\theta$  and  $\phi$  denote the polar angle (= “zenith angle” or “colatitude”) and the azimuthal angle, respectively. Specifying (5.3) for (5.1), rewriting the integral as a sum of two integrals (the first extending over  $\underline{\underline{C}}_s^{-1}$  and the second over the time-dependent part of  $\underline{\underline{J}}_{aniso}$ ), and consideration that the complete three-dimensional space average of isotropic compliance tensor  $\underline{\underline{C}}_s^{-1}$  is equal to  $\underline{\underline{C}}_s^{-1}$ , finally yields

$$\underline{\underline{J}}_{iso} = \underline{\underline{C}}_s^{-1} + \frac{(1 + \nu_s)}{2 E_s} \frac{16 d (1 - \nu_s)}{3 (2 - \nu_s)} \left[ 1 - \exp \left( \frac{-t}{\tau_{creep}} \right) \right] \int_{\phi=0}^{\phi=2\pi} \int_{\theta=0}^{\theta=\pi} \underline{\underline{I}}_{aniso} \frac{\sin \theta d\theta d\phi}{4\pi} \quad (5.4)$$

Evaluation of the double integral in Eq. (5.4) yields

$$\underline{\underline{J}}_{iso} = \underline{\underline{C}}_s^{-1} + \frac{1}{4 \mu_s} \frac{16 d (1 - \nu_s)}{3 (2 - \nu_s)} \left[ 1 - \exp \left( \frac{-t}{\tau_{creep}} \right) \right] \frac{4}{5} \underline{\underline{I}}_{dev} \quad (5.5)$$

Noting that the inverse of the fourth-order elastic stiffness tensor can be expressed as a function of bulk modulus  $k_s$  and shear modulus  $\mu_s$ ,

$$\underline{\underline{C}}_s^{-1} = \frac{1}{3 k_s} \underline{\underline{I}}_{vol} + \frac{1}{2 \mu_s} \underline{\underline{I}}_{dev}, \quad (5.6)$$

the creep function expression (5.5) can be re-written as

$$\underline{\underline{J}}_{iso} = \frac{1}{3 k_s} \underline{\underline{I}}_{vol} + \frac{1}{2} \left[ \frac{1}{\mu_s} + \frac{32 d (1 - \nu_s)}{15 \mu_s (2 - \nu_s)} \left\{ 1 - \exp \left( \frac{-t}{\tau_{creep}} \right) \right\} \right] \underline{\underline{I}}_{dev} \quad (5.7)$$

with the characteristic creep time  $\tau_{creep}$  given in (5.8) as

$$\tau_{creep} = \frac{a \eta_i}{\mu_s} \frac{8 (1 - \nu_s)}{3 \pi (2 - \nu_s)} \quad (5.8)$$

### 5.3 Top-down identification of interface density, interface viscosity, and bulk viscosity of adsorbed water filling interfaces between hydroxyapatite crystals

Comparing Eq. (5.7) with the “Kelvin-Voigt” form of an isotropic creep tensor for interfaced hydroxyapatite

$$\underline{\underline{J}}_{iso} = \frac{1}{3 k_s} \underline{\underline{I}}_{vol} + \frac{1}{2} \left[ \frac{1}{\mu_s} + \frac{1}{\mu_{KV,iso}} \left\{ 1 - \exp \left( \frac{-t}{\tau_{creep,KV,iso}} \right) \right\} \right] \underline{\underline{I}}_{dev} \quad (5.9)$$

allows for identification of a relation between the isotropic Kelvin-Voigt properties and corresponding micromechanical counterparts: Comparing the terms multiplied in (5.9) and (5.7), respectively, with the angled brackets containing the exponential delivers

$$\frac{1}{\mu_{KV,iso}} = \frac{32 d (1 - \nu_s)}{15 \mu_s (2 - \nu_s)} \Rightarrow d = \frac{\mu_s}{\mu_{KV,iso}} \frac{15 (2 - \nu_s)}{32 (1 - \nu_s)} \quad (5.10)$$

Noting that the characteristic time of a Kelvin Voigt model reads, according to (D.13), as

$$\tau_{creep,KV,iso} = \frac{\eta_{KV,iso}}{\mu_{KV,iso}} \quad (5.11)$$

and comparing the characteristic times in (5.9) and (5.7), respectively, i. e. setting equal Eqs. (5.8) and (5.11) delivers, under consideration of (5.10)<sub>1</sub>

$$\frac{\eta_{KV,iso}}{\mu_{KV,iso}} = \frac{a \eta_i}{\mu_s} \frac{8 (1 - \nu_s)}{3 \pi (2 - \nu_s)} \Rightarrow \eta_i = \frac{4 \pi d}{5 a} \eta_{KV,iso} \quad (5.12)$$

Eqs. (5.10) and (5.12) allow for identification of the interface density  $d$  and for the interface viscosity  $\eta_i$  as described next. To this end, we recall that the shear modulus of hydroxyapatite amounts to [21]

$$\mu_s = 44.9 \text{ GPa} \quad (5.13)$$

that the Poisson’s ratio of hydroxyapatite amounts to [21]

$$\nu_s = 0.24 \quad (5.14)$$

that the creep modulus of interfaced hydroxyapatite amounts to [21]

$$\mu_{KV,iso} = 179.52 \text{ GPa} \quad (5.15)$$

and that the isotropic Kelvin Voigt viscosity of interfaced hydroxyapatite amounts to [21]

$$\eta_{KV,iso} = 1.34 \cdot 10^5 \text{ GPa s} \quad (5.16)$$

The interface density  $d$  is identified from specifying (5.10) for (5.13), (5.14), and (5.15) as

$$d = \frac{\mu_s}{\mu_{KV,iso}} \frac{15(2 - \nu_s)}{32(1 - \nu_s)} = 0.271 \quad (5.17)$$

As for identification of the correct order of magnitude of the interface viscosity, we envision the interfaces to exhibit a diameter amounting to 100 nm, i. e. an interface radius amounting to

$$a = 50 \text{ nm} \quad (5.18)$$

The interface viscosity  $\eta_i$  is identified from specifying (5.12) for (5.17), (5.18), and (5.15) as

$$\eta_i = \frac{4\pi d}{5a} \eta_{KV,iso} = 1.83 \cdot 10^{12} \text{ GPa s/m} \quad (5.19)$$

The bulk velocity  $\eta_b$  of “glassy water” is equal to the product of the interface viscosity  $\eta_i$  and the thickness  $c$  of of the interfaces, which is envisioned to amount to

$$c = 1 \text{ nm} \quad (5.20)$$

This yields

$$\eta_b = \eta_i c = 1.83 \cdot 10^{12} \text{ Pa s} \quad (5.21)$$

The bulk viscosity  $\eta_b$  given in Eq. (5.21) is on the same order of magnitude as the bulk viscosity of *molten glass*. This is another indicator for the “glassy” nature of adsorbed water filling interfaces between hydroxyapatite crystals.

## 5.4 Top-down identification of typical interfacial dislocation speeds in relaxation tests on bone, starting from macroscopic three-point bedding tests

The typical interface dislocation speeds can be determined from relaxation experiments on bone, starting from three-point bending tests on bone [68]. The initial maximum normal stress in these tests amounts to [21] to

$$\max \Sigma_{bone,axial} = 32.6 \text{ MPa} \quad (5.22)$$

The corresponding maximum shear stresses act in planes that are inclined by 45° with respect to the cross-sections of the beam, and they are by a factor of 2 smaller than the maximum normal stress [83], i.e. maximum shear stresses amount to

$$\max \Sigma_{bone, shear} = 16.3 \text{ MPa} \quad (5.23)$$

and they refer to the tissue scale. Typical stress concentration factors from the tissue scale down to the mineral scale range from 1.5 to 2.8 [48, 84, 85, 86]. This yields matrix-interface composite-related shear stresses ranging in the following interval

$$\max \Sigma_{shear} \in [24, 45] \text{ MPa} \quad (5.24)$$

Microscopic interface shear tractions  $T$  are equal to the shear stresses imposed on the matrix-interface composite, at the time instant of sudden loading, see Chapter 1:

$$\max T \in [24, 45] \text{ MPa} \quad (5.25)$$

The interface tractions  $T$  are related to dislocation rates  $[\dot{\xi}]$  via the viscous interface law

$$T = \eta_i [\dot{\xi}] \quad (5.26)$$

Eq. (5.26) specified for interface tractions  $T$  from (5.25) and for the interface viscosity  $\eta_i$  from (5.19) suggests that the maximum dislocation rates range in the following interval

$$\max[\dot{\xi}] \in [5.3, 8.3] \cdot 10^{-15} \text{ m/s} \quad (5.27)$$

## 5.5 Thixotropy of adsorbed water allows for explaining differences in top-down and bottom-up identified viscosities: an outlook to bridging continuum micromechanics and molecular dynamics simulations

We here compare the identified bulk viscosity of adsorbed water, see (5.21), and the identified speed of interfacial dislocations in macroscopic relaxation experiments on bone, see (5.27), with corresponding counterparts obtained from molecular dynamics simulations performed by colleagues at Purdue University, IN, USA.

- The bulk viscosity of adsorbed water, which was identified based on a top-down approach, amounts to  $1.83 \cdot 10^{12}$  Pa.s, and this by 14 orders of magnitude larger than the bulk viscosity quantified in the molecular dynamics simulations, see Appendix G.
- The interfacial dislocation rates, which was identified based on a top-down approach, range from  $5.3 \cdot 10^{-15}$  m/s to  $8.3 \cdot 10^{-15}$  m/s, and this is by 16 orders of magnitude smaller than the bulk viscosity quantified in the molecular dynamics simulations, see Appendix G.

The effect of such huge differences in corresponding shear rates felt by the viscous fluid inside the interfaces qualifies as the main candidate for explaining the viscosity changes: In fact, it is experimentally known for a number of different materials [87, 88, 89, 90] that increasing shear rates lead to decreased viscosities (or thinning) of viscous materials. Hence, the mismatch between MD and downscaled results for the viscosity of water trapped between hydroxyapatite crystals does not reveal any fundamental shortcomings of any of these methods, but rather elucidates the low speed-enhanced, very “glassy” state of the water interfaces under physiological loading conditions.

## 5.6 Nomenclature

$a$	interface radius
$c$	interface thickness
$\underline{\underline{C}}_s$	fourth-order elastic stiffness tensor of solid
$\underline{\underline{C}}_s^{-1}$	inverse of $\underline{\underline{C}}_s$
$d$	interface density parameter
$E_s$	Young’s modulus of the solid
$\underline{e}_x, \underline{e}_y, \underline{e}_z$	unit base vectors of Cartesian coordinate system
$\underline{\underline{I}}_{aniso}$	symmetric fourth-order identity tensor
$\underline{\underline{I}}_{dev}$	deviatoric part of $\underline{\underline{I}}$
$\underline{\underline{I}}_{vol}$	volumetric part of $\underline{\underline{I}}$
$\underline{\underline{J}}$	creep tensor
$J_{aniso}$	anisotropic creep function
$J_{iso}$	isotropic creep function
$k_s$	bulk modulus of isotropic solid matrix

---

$\mathcal{N}$	number of interfaces per unit volume of a matrix-interface composite
$s$	index for solid phase
$t$	time
$t$	interface traction
$\eta_i$	viscosity of the interfaces
$\eta_b$	bulk viscosity of the interfaces
$\eta_{KV,iso}$	viscosity of Kelvin-Voigt model
$\theta$	spherical (latitudinal) integration variable, $\theta = 0 \cdots \pi$
$\mu_s$	shear modulus of isotropic solid matrix
$\mu_{KV,iso}$	shear modulus of Kelvin-Voigt model
$\nu_s$	Poisson's ratio of isotropic solid matrix
$[[\xi]]$	dislocation of the interfaces
$[[\dot{\xi}]]$	time derivative of dislocation of the interfaces
$\Sigma_{shear}$	shear macroscopic stress
$\Sigma_{bone,axial}$	bone axial macroscopic stress
$\Sigma_{bone,shear}$	bone shear macroscopic stress
$\tau_{creep}$	characteristic time of creep function
$\phi$	spherical (longitudinal) integration variable, $\phi = 0 \cdots 2\pi$
$\in$	dyadic product
$\otimes$	dyadic product

## Outlook

The presented thesis has opened a virtually new topic in continuum (micro-)mechanics - allowing for the explicit consideration of microscopic interface viscosities on the overall macroscopic material behavior. Therefore, it holds the promise for great impact in the understanding of any material where such interfaces occur, namely in almost any hydrated bio or geomaterial. Still, it is interesting to further inspect some more specific next steps which are of immediate interest, or whose realization is imminent:

- Consideration of interfaces oriented in different direction, mutually penetrating each other: Instead of using the Reuss bound as in the chapter devoted to the hydroxyapatite crystals, one could realize the mathematical description of an RVE hosting interfaces oriented in different directions. In fact, major steps in this directions have been made during the last three years, and key results are given in Appendix F. While the derivation of the governing differential equations is still quite straightforward in this case (it depends, however, already on a certain discretization of a uniform distribution of infinite many interfaces; so as not to obtain infinitely many unknowns . . . ), the solution of such systems of differential equations requires a level of mathematical involvement, which clearly exceeded the scope of the present thesis (particularly, when considering all the other tasks fulfilled).
- Modeling of interface spreading: In Chapter 1, interface spreading was suggested as a phenomenon which could explain that many hydrated geomaterials (such as concrete) exhibit logarithmic, rather than exponential creep behavior. Accordingly, it would be interesting to let the interfaces evolve during the creep process. One major problem in this context, however, is the appropriate representation of traction states during interface growth. This challenge awaits deeper scrutiny - however, some crude first guesses already resulted in differential equations with solutions deviating significantly from the exponential shape - which is of course a good sign.
- The most straightforward next step consists in repeating the exercise for bone given in Chapter 5, for other material systems for which hierarchical micromechanical representations are ready, in particular for concrete [91, 92]. Related research activities are in progress - and again, effects of shear thinning or thixotropy seem probable.

## Appendix A

# Proof of limit case of strain concentration tensor of inclusion at infinity

To start with, we consider  $\underline{\underline{A}}_i^\infty$  according to (1.18), and we invert the tensor product  $\underline{\underline{A}}_i^\infty : \underline{\underline{P}}_i$

$$\left(\underline{\underline{A}}_i^\infty : \underline{\underline{P}}_i\right)^{-1} = \underline{\underline{P}}_i^{-1} : \left[\underline{\underline{I}} - \underline{\underline{P}}_i : \underline{\underline{C}}_s\right] = \left[\underline{\underline{I}} - \underline{\underline{C}}_s : \underline{\underline{P}}_i\right] : \underline{\underline{P}}_i^{-1} \quad (\text{A.1})$$

such that re-inversion yields under consideration of (1.20)

$$\underline{\underline{A}}_i^\infty : \underline{\underline{P}}_i = \underline{\underline{C}}_s^{-1} : \underline{\underline{S}}^t : \left[\underline{\underline{I}} - \underline{\underline{S}}^t\right]^{-1} \quad (\text{A.2})$$

Multiplication of (A.2) by  $\omega$ , expansion by  $+\underline{\underline{I}} - \underline{\underline{I}} = (\underline{\underline{I}} - \underline{\underline{S}}^t) : (\underline{\underline{I}} - \underline{\underline{S}}^t)^{-1} - \underline{\underline{I}}$ , and taking the limit  $\omega \rightarrow 0$ , yields under consideration of (1.44) and of  $\lim_{\omega \rightarrow 0} \omega \underline{\underline{I}} = 0$

$$\lim_{\omega \rightarrow 0} \omega \underline{\underline{A}}_i^\infty : \underline{\underline{P}}_i = \lim_{\omega \rightarrow 0} \omega \underline{\underline{C}}_s^{-1} : \left\{ \underline{\underline{S}}^t : \left(\underline{\underline{I}} - \underline{\underline{S}}^t\right)^{-1} \pm \underline{\underline{I}} \right\} = \underline{\underline{C}}_s^{-1} : \underline{\underline{T}}_i^t \quad (\text{A.3})$$

## Appendix B

# Consideration of two parallel interface phases exhibiting *different sizes*

We here consider two parallel interface phases (also called “interface families”), which are characterized by two different interface radii, denoted by  $a_1$  and  $a_2$ , respectively, and by two different interface density parameters,  $d_1$  and  $d_2$ . These two families exhibit different average displacement jumps  $[[\xi]]_1$  and  $[[\xi]]_2$ , and different average traction forces  $\underline{T}_1$  and  $\underline{T}_2$ . Corresponding extension of the auxiliary material system of Section 1.3 to two inclusion phases (with eigenstresses  $\underline{\underline{\sigma}}_1^E$  and  $\underline{\underline{\sigma}}_2^E$ , respectively) yields the following influence-concentration relations [as extension of Eq. (1.9)],

$$\underline{\underline{\varepsilon}}_1 = \underline{\underline{A}}_1 : \underline{\underline{E}} + \underline{\underline{D}}_{11} : \underline{\underline{\sigma}}_1^E + \underline{\underline{D}}_{12} : \underline{\underline{\sigma}}_2^E \quad (\text{B.1})$$

$$\underline{\underline{\varepsilon}}_2 = \underline{\underline{A}}_2 : \underline{\underline{E}} + \underline{\underline{D}}_{21} : \underline{\underline{\sigma}}_1^E + \underline{\underline{D}}_{22} : \underline{\underline{\sigma}}_2^E \quad (\text{B.2})$$

with  $\underline{\underline{A}}_1$  and  $\underline{\underline{A}}_2$ , as the concentration tensors of inclusion phases 1 and 2, respectively; with influence tensor  $\underline{\underline{D}}_{12}$  ( $\underline{\underline{D}}_{21}$ ) quantifying the effect of eigenstresses  $\underline{\underline{\sigma}}_2^E$  ( $\underline{\underline{\sigma}}_1^E$ ) on inclusion phase strains  $\underline{\underline{\varepsilon}}_1$  ( $\underline{\underline{\varepsilon}}_2$ ); and with influence tensor  $\underline{\underline{D}}_{22}$  quantifying the effect of eigenstresses  $\underline{\underline{\sigma}}_2^E$  on phase strains  $\underline{\underline{\varepsilon}}_2$ . Application of Levin’s theorem to our extended material system delivers the macroscopic stress state equation in the form,

$$\underline{\underline{\Sigma}} = \underline{\underline{C}}_{hom} : \underline{\underline{E}} + f_1 \underline{\underline{\sigma}}_1^E : \underline{\underline{A}}_1 + f_2 \underline{\underline{\sigma}}_2^E : \underline{\underline{A}}_2 \quad (\text{B.3})$$

with  $f_1$  and  $f_2$  as the volume fractions of inclusion phases 1 and 2. In order to arrive at analytical expressions for the aforementioned influence and concentration relations, the two inclusion phases are assigned two matrix-inclusion problems as the one depicted in Figure 1.3, subjected to the *same* strains at the infinite boundary. Combination of respective relations analogous to Eqs. (1.18) - (1.22) yields the strains at the infinite boundary of the auxiliary matrices, originally given by Eq. (1.23), now in the format:

$$\underline{\underline{E}}_\infty = \left[ f_s \underline{\underline{I}} + f_1 \underline{\underline{A}}_1^\infty + f_2 \underline{\underline{A}}_2^\infty \right]^{-1} : \left( \underline{\underline{E}} + f_1 \underline{\underline{A}}_1^\infty : \underline{\underline{P}}_1 : \underline{\underline{\sigma}}_1^E + f_2 \underline{\underline{A}}_2^\infty : \underline{\underline{P}}_2 : \underline{\underline{\sigma}}_2^E \right) \quad (\text{B.4})$$

Backsubstitution of (B.4) into the matrix-inclusion problems related to the now two inclusion phases yields the phase strains in inclusion phase 1 and 2, respectively, as

$$\begin{aligned} \underline{\underline{\varepsilon}}_1 = \underline{\underline{A}}_1^\infty : \left[ f_s \underline{\underline{I}} + f_1 \underline{\underline{A}}_1^\infty + f_2 \underline{\underline{A}}_2^\infty \right]^{-1} : \\ \left( \underline{\underline{E}} + f_1 \underline{\underline{A}}_1^\infty : \underline{\underline{P}}_1 : \underline{\underline{\sigma}}_1^E + f_2 \underline{\underline{A}}_2^\infty : \underline{\underline{P}}_2 : \underline{\underline{\sigma}}_2^E \right) - \underline{\underline{A}}_1^\infty : \underline{\underline{P}}_1 : \underline{\underline{\sigma}}_1^E \end{aligned} \quad (\text{B.5})$$

$$\begin{aligned} \underline{\underline{\varepsilon}}_2 = \underline{\underline{A}}_2^\infty : \left[ f_s \underline{\underline{I}} + f_1 \underline{\underline{A}}_1^\infty + f_2 \underline{\underline{A}}_2^\infty \right]^{-1} : \\ \left( \underline{\underline{E}} + f_1 \underline{\underline{A}}_1^\infty : \underline{\underline{P}}_1 : \underline{\underline{\sigma}}_1^E + f_2 \underline{\underline{A}}_2^\infty : \underline{\underline{P}}_2 : \underline{\underline{\sigma}}_2^E \right) - \underline{\underline{A}}_2^\infty : \underline{\underline{P}}_2 : \underline{\underline{\sigma}}_2^E \end{aligned} \quad (\text{B.6})$$

Comparison of (B.1) and (B.2) with (B.5) and (B.6) allows for identification of the following concentration and influence tensors,

$$\begin{aligned} \underline{\underline{A}}_1 = \underline{\underline{A}}_1^\infty : \left[ f_s \underline{\underline{I}} + f_1 \underline{\underline{A}}_1^\infty + f_2 \underline{\underline{A}}_2^\infty \right]^{-1}, \quad \underline{\underline{A}}_2 = \underline{\underline{A}}_2^\infty : \left[ f_s \underline{\underline{I}} + f_1 \underline{\underline{A}}_1^\infty + f_2 \underline{\underline{A}}_2^\infty \right]^{-1} \\ \underline{\underline{D}}_{11} = \left( f_1 \underline{\underline{A}}_1 - \underline{\underline{I}} \right) : \underline{\underline{A}}_1^\infty : \underline{\underline{P}}_1, \quad \underline{\underline{D}}_{12} = \underline{\underline{A}}_1 : f_2 \underline{\underline{A}}_2^\infty : \underline{\underline{P}}_2 \\ \underline{\underline{D}}_{21} = \underline{\underline{A}}_2 : f_1 \underline{\underline{A}}_1^\infty : \underline{\underline{P}}_1, \quad \underline{\underline{D}}_{22} = \left( f_2 \underline{\underline{A}}_2 - \underline{\underline{I}} \right) : \underline{\underline{A}}_2^\infty : \underline{\underline{P}}_2 \end{aligned} \quad (\text{B.7})$$

We restrict the present discussion to creep boundary conditions, i.e. to evolving strains due to prescribed stresses: Therefore, we use the state equation (B.3) in order to express the macroscopic strains as functions of the macroscopic stresses and the phase eigenstresses, and insert the corresponding result into (B.5) and

(B.6). When taking, thereafter, as described for one inclusion phase in Section 1.4, the limit that the aspect ratio of both inclusion phases tends to zero, then phase strains (B.5) and (B.6) are transformed to displacement jumps, and we arrive at expressedly simple extensions of the concentration-influence relation Eq. (1.72), reading as

$$\begin{aligned} \llbracket \underline{\xi} \rrbracket_1 &= \underline{\underline{A}}_1^{\Sigma,lim} : \underline{\underline{\Sigma}} + \underline{\underline{D}}_{11}^{\Sigma,lim} \cdot \underline{\underline{T}}_1^E + \underline{\underline{D}}_{12}^{\Sigma,lim} \cdot \underline{\underline{T}}_2^E \\ \llbracket \underline{\xi} \rrbracket_2 &= \underline{\underline{A}}_2^{\Sigma,lim} : \underline{\underline{\Sigma}} + \underline{\underline{D}}_{21}^{\Sigma,lim} \cdot \underline{\underline{T}}_1^E + \underline{\underline{D}}_{22}^{\Sigma,lim} \cdot \underline{\underline{T}}_2^E \end{aligned} \quad (\text{B.8})$$

whereby the non-zero components of the concentration and influence tensors read as

$$\begin{aligned} A_{1,xxz}^{\Sigma,lim} &= A_{1,xzx}^{\Sigma,lim} = A_{1,yyz}^{\Sigma,lim} = A_{1,yzy}^{\Sigma,lim} = \frac{16 a_1 (1 - \nu_s^2)}{3 \pi E_s (2 - \nu_s)}, \\ A_{1,zzz}^{\Sigma,lim} &= \frac{16 a_1 (1 - \nu_s^2)}{3 \pi E_s} \\ D_{11,xx}^{\Sigma,lim} &= D_{11,yy}^{\Sigma,lim} = -\frac{16 a_1 (1 - \nu_s^2)}{3 \pi E_s (2 - \nu_s)}, \quad D_{11,zz}^{\Sigma,lim} = -\frac{16 a_1 (1 - \nu_s^2)}{3 \pi E_s} \end{aligned} \quad (\text{B.9})$$

as well as

$$\begin{aligned} A_{2,xxz}^{\Sigma,lim} &= A_{2,xzx}^{\Sigma,lim} = A_{2,yyz}^{\Sigma,lim} = A_{2,yzy}^{\Sigma,lim} = \frac{16 a_2 (1 - \nu_s^2)}{3 \pi E_s (2 - \nu_s)}, \\ A_{2,zzz}^{\Sigma,lim} &= \frac{16 a_2 (1 - \nu_s^2)}{3 \pi E_s} \\ D_{22,xx}^{\Sigma,lim} &= D_{22,yy}^{\Sigma,lim} = -\frac{16 a_2 (1 - \nu_s^2)}{3 \pi E_s (2 - \nu_s)}, \quad D_{22,zz}^{\Sigma,lim} = -\frac{16 a_2 (1 - \nu_s^2)}{3 \pi E_s} \end{aligned} \quad (\text{B.10})$$

Remarkably, there are no direct cross effects between the traction forces in the first interface family and the dislocations in the second family, and vice versa ( $\underline{\underline{D}}_{12}^{\Sigma,lim} = \underline{\underline{D}}_{21}^{\Sigma,lim} = 0$ ). Specifying (B.8) for the extended glueing condition  $\llbracket \underline{\xi}_z \rrbracket_1 = \llbracket \underline{\xi}_z \rrbracket_2 = 0$  yields, by analogy to (1.105),

$$T_{1,z} = T_{2,z} = \Sigma_{zz} \quad (\text{B.11})$$

Combining (B.8) with in-plane viscous behavior of the interface families according to (1.78), i.e. with  $\eta \llbracket \dot{\underline{\xi}}_\alpha \rrbracket_1 = T_{1,\alpha}$  and  $\eta \llbracket \dot{\underline{\xi}}_\alpha \rrbracket_2 = T_{2,\alpha}$ , with  $\alpha = x, y$ , delivers by

analogy to (1.106) - (1.108) the following displacement jump evolutions

$$\begin{aligned} \llbracket \xi_\alpha \rrbracket_1(t) &= \frac{16(1-\nu_s^2)a_1\Sigma_{\alpha z}}{3\pi E_s(2-\nu_s)} \times \left[ 1 - \exp\left(-\frac{3\pi(2-\nu_s)}{16(1-\nu_s^2)} \frac{E_s t}{a_1 \eta}\right) \right], \alpha = x, y \\ \llbracket \xi_\alpha \rrbracket_2(t) &= \frac{16(1-\nu_s^2)a_2\Sigma_{\alpha z}}{3\pi E_s(2-\nu_s)} \times \left[ 1 - \exp\left(-\frac{3\pi(2-\nu_s)}{16(1-\nu_s^2)} \frac{E_s t}{a_2 \eta}\right) \right], \alpha = x, y \end{aligned} \quad (\text{B.12})$$

Notably, the characteristic times of the two interface families are different, since they explicitly depend on the size of the interfaces, see  $a_1$  and  $a_2$  appearing in the exponential expressions of (B.12). The time evolution of interface tractions  $T_{1,\alpha}$  and  $T_{2,\alpha}$  follow from specifying the viscosity relations  $\eta \llbracket \dot{\xi}_\alpha \rrbracket_1 = T_{1,\alpha}$  and  $\eta \llbracket \dot{\xi}_\alpha \rrbracket_2 = T_{2,\alpha}$  for (B.12) as

$$\begin{aligned} T_{1,\alpha}(t) &= \Sigma_{\alpha z} \exp\left(-\frac{3\pi(2-\nu_s)}{16(1-\nu_s^2)} \frac{E_s t}{a_1 \eta}\right), \alpha = x, y \\ T_{2,\alpha}(t) &= \Sigma_{\alpha z} \exp\left(-\frac{3\pi(2-\nu_s)}{16(1-\nu_s^2)} \frac{E_s t}{a_2 \eta}\right), \alpha = x, y \end{aligned} \quad (\text{B.13})$$

These interface tractions also appear in the macroscopic state equation providing access to the macroscopic creep strains:

$$\underline{\underline{E}} = (\underline{\underline{C}}_{hom}^{lim})^{-1} : \underline{\underline{\Sigma}} - \underline{\underline{B}}_1^{\Sigma,lim} \cdot \underline{\underline{T}}_1 - \underline{\underline{B}}_2^{\Sigma,lim} \cdot \underline{\underline{T}}_2 \quad (\text{B.14})$$

Specification of (B.14) for (B.13) delivers, strain components  $E_{xx}$ ,  $E_{yy}$ ,  $E_{zz}$ , and  $E_{xy}$  according to (1.110) - (1.113), as well as

$$\begin{aligned} E_{\alpha z}(t) &= \frac{(1+\nu_s)}{E_s} \Sigma_{\alpha z} \times \left( 1 + \frac{16d_1(1-\nu_s)}{3(2-\nu_s)} \left[ 1 - \exp\left(-\frac{3\pi(2-\nu_s)}{16(1-\nu_s^2)} \frac{E_s t}{a_1 \eta}\right) \right] + \right. \\ &\quad \left. + \frac{16d_2(1-\nu_s)}{3(2-\nu_s)} \left[ 1 - \exp\left(-\frac{3\pi(2-\nu_s)}{16(1-\nu_s^2)} \frac{E_s t}{a_2 \eta}\right) \right] \right), \alpha = x, y \end{aligned} \quad (\text{B.15})$$

Eq. (B.15) underlines that consideration of different interface sizes yields creep spectra [93], because the characteristic time of each interface size depends on its size. Only the spontaneous shear strain observed right after sudden macroscopic load increases and the asymptotically reached final creep strains do not depend

on the interface sizes:

$$\begin{aligned}
 E_{\alpha z}(t = 0) &= \frac{(1 + \nu_s)}{E_s} \Sigma_{\alpha z}, \quad \alpha = x, y \\
 E_{\alpha z}(t = \infty) &= \frac{(1 + \nu_s)}{E_s} \Sigma_{\alpha z} \frac{3(2 - \nu_s) + 16(d_1 + d_2)(1 - \nu_s)}{3(2 - \nu_s)}, \quad \alpha = x, y
 \end{aligned} \tag{B.16}$$

## Appendix C

# Components of homogenized elastic stiffness tensor, interface morphology tensor, as well as concentration and influence tensors

### C.1 Components of homogenized elastic stiffness tensor, interface morphology tensor, as well as concentration and influence tensors

Eq. (2.2) contains the fourth-order tensors  $\underline{\underline{I}}_{vol}$  and  $\underline{\underline{I}}_{dev}$  which are defined as  $\underline{\underline{I}}_{vol} = \frac{1}{3} \underline{\underline{1}} \otimes \underline{\underline{1}}$  and  $\underline{\underline{I}}_{dev} = \underline{\underline{I}} - \underline{\underline{I}}_{vol}$ , respectively. They denote the volumetric and the deviatoric part of the symmetric fourth-order identity tensor  $\underline{\underline{I}}$ , with components  $I_{ijkl} = \frac{1}{2}(\delta_{ik} \delta_{jl} + \delta_{il} \delta_{kj})$ , and with  $\delta_{ij}$  denoting the Kronecker delta being equal to 1 if  $i = j$  and 0 otherwise. In addition,  $\underline{\underline{1}}$  is the second-order identity tensor with components being equal to the Kronecker delta.

Eqs. (2.7) and (2.11) contain  $\underline{\underline{C}}_{hom}$ , the homogenized elastic stiffness tensor of the studied matrix-interface composites, which is defined as [63]

$$\underline{\underline{C}}_{hom} = \underline{\underline{C}}_s : \left[ \underline{\underline{I}} + \frac{4\pi(d_1 + d_2)}{3} \underline{\underline{T}}_i \right]^{-1} \quad (\text{C.1})$$

In (C.1),  $\underline{\underline{T}}_i$  denotes a fourth-order mophology tensor for flat parallel interfaces. For interfaces parallel to the  $x,y$ -plane, the non-vanishing non-vanishing components of  $\underline{\underline{T}}_i$  read as [63]

$$\left. \begin{aligned} T_{i,xzxz} = T_{i,zxxz} = T_{i,xzzx} = T_{i,zxzx} \\ T_{i,yzyz} = T_{i,zyyz} = T_{i,yzzz} = T_{i,zyzy} \end{aligned} \right\} = \frac{2(1-\nu_s)}{\pi(2-\nu_s)} \quad (\text{C.2})$$

$$\left. \begin{aligned} T_{i,zzxx} \\ T_{i,zzyy} \end{aligned} \right\} = \frac{4\nu_s(1-\nu_s)}{\pi(1-2\nu_s)} \quad (\text{C.3})$$

$$T_{i,zzzz} = \frac{4(1-\nu_s)^2}{\pi(1-2\nu_s)} \quad (\text{C.4})$$

Eq. (2.7) contains Biot-type influence tensors  $\underline{\underline{B}}_1$  and  $\underline{\underline{B}}_2$ . Their non-vanishing components read as

$$B_{1,zzx} = B_{1,xzx} = B_{1,zyy} = B_{1,yzy} = \frac{16d_1(1-\nu_s)}{3(2-\nu_s) + 16(d_1+d_2)(1-\nu_s)} \quad (\text{C.5})$$

$$B_{1,xxz} = B_{1,yyz} = -\frac{16d_1\nu_s(1-\nu_s)}{3(1-2\nu_s) + 16(d_1+d_2)(1-\nu_s)^2} \quad (\text{C.6})$$

$$B_{1,zzz} = \frac{16d_1(1-\nu_s)^2}{3(1-2\nu_s) + 16(d_1+d_2)(1-\nu_s)^2} \quad (\text{C.7})$$

and

$$B_{2,zzx} = B_{2,xzx} = B_{2,zyy} = B_{2,yzy} = \frac{16d_2(1-\nu_s)}{3(2-\nu_s) + 16(d_1+d_2)(1-\nu_s)} \quad (\text{C.8})$$

$$B_{2,xxz} = B_{2,yyz} = -\frac{16d_2\nu_s(1-\nu_s)}{3(1-2\nu_s) + 16(d_1+d_2)(1-\nu_s)^2} \quad (\text{C.9})$$

$$B_{2,zzz} = \frac{16d_2(1-\nu_s)^2}{3(1-2\nu_s) + 16(d_1+d_2)(1-\nu_s)^2} \quad (\text{C.10})$$

Eqs. (2.8) and (2.9) contain concentration tensors  $\underline{\underline{A}}_1$  and  $\underline{\underline{A}}_2$ . Their non-vanishing components read as

$$A_{1,xxz} = A_{1,xzx} = A_{1,yyz} = A_{1,yzy} = \frac{8(1-\nu_s)a_1}{\pi[3(2-\nu_s) + 16(d_1+d_2)(1-\nu_s)]} \quad (\text{C.11})$$

$$A_{1,zzx} = A_{1,zyy} = \frac{16\nu_s(1-\nu_s)a_1}{\pi[3(1-2\nu_s) + 16(d_1+d_2)(1-\nu_s)^2]} \quad (\text{C.12})$$

$$A_{1,zzz} = \frac{1-\nu_s}{\nu_s} A_{1,zzx} \quad (\text{C.13})$$

and

$$A_{2,xxz} = A_{2,xzx} = A_{2,yyz} = A_{2,yzy} = \frac{8(1-\nu_s)a_2}{\pi[3(2-\nu_s)+16(d_1+d_2)(1-\nu_s)]} \quad (\text{C.14})$$

$$A_{2,zxx} = A_{2,zyy} = \frac{16\nu_s(1-\nu_s)a_2}{\pi[3(1-2\nu_s)+16(d_1+d_2)(1-\nu_s)^2]} \quad (\text{C.15})$$

$$A_{2,zzz} = \frac{1-\nu_s}{\nu_s} A_{2,zxx} \quad (\text{C.16})$$

Eqs. (2.8) and (2.9) contain influence tensors  $\underline{\underline{D}}_{11}$ ,  $\underline{\underline{D}}_{12}$ ,  $\underline{\underline{D}}_{21}$ , and  $\underline{\underline{D}}_{22}$ . Their non-vanishing components read as

$$D_{11,xx} = D_{11,yy} = -\frac{16(1-\nu_s^2)[3(2-\nu_s)+16d_2(1-\nu_s)]a_1}{3E_s\pi(2-\nu_s)[3(2-\nu_s)+16(d_1+d_2)(1-\nu_s)]}$$

$$D_{11,zz} = -\frac{16(1-\nu_s^2)[3(1-2\nu_s)+16d_2(1-\nu_s)^2]a_1}{3E_s\pi[3(1-2\nu_s)+16(d_1+d_2)(1-\nu_s)^2]} \quad (\text{C.17})$$

$$D_{12,xx} = D_{12,yy} = \frac{256}{3} \frac{a_1 d_2 (1-\nu_s^2)(1-\nu_s)}{E_s \pi (2-\nu_s)[3(2-\nu_s)+16(d_1+d_2)(1-\nu_s)]}$$

$$D_{12,zz} = \frac{256}{3} \frac{a_1 d_2 (1-\nu_s^2)(1-\nu_s)^2}{E_s \pi [3(1-2\nu_s)+16(d_1+d_2)(1-\nu_s)^2]} \quad (\text{C.18})$$

$$D_{21,xx} = D_{21,yy} = \frac{256}{3} \frac{a_2 d_1 (1-\nu_s^2)(1-\nu_s)}{E_s \pi (2-\nu_s)[3(2-\nu_s)+16(d_1+d_2)(1-\nu_s)]}$$

$$D_{21,zz} = \frac{256}{3} \frac{a_2 d_1 (1-\nu_s^2)(1-\nu_s)^2}{E_s \pi [3(1-2\nu_s)+16(d_1+d_2)(1-\nu_s)^2]} \quad (\text{C.19})$$

and

$$D_{22,xx} = D_{22,yy} = -\frac{16(1-\nu_s^2)[3(2-\nu_s)+16d_1(1-\nu_s)]a_2}{3E_s\pi(2-\nu_s)[3(2-\nu_s)+16(d_1+d_2)(1-\nu_s)]}$$

$$D_{22,zz} = -\frac{16(1-\nu_s^2)[3(1-2\nu_s)+16d_1(1-\nu_s)^2]a_2}{3E_s\pi[3(1-2\nu_s)+16(d_1+d_2)(1-\nu_s)^2]} \quad (\text{C.20})$$

Eq. (2.11) contains influence tensors  $\underline{\underline{B}}_1^\Sigma$  and  $\underline{\underline{B}}_2^\Sigma$ . Their non-vanishing components read as

$$B_{1,zzx}^\Sigma = B_{1,xzx}^\Sigma = B_{1,zyy}^\Sigma = B_{1,yzy}^\Sigma = \frac{16 d_1 (1 - \nu_s^2)}{3 E_s (2 - \nu_s)} \quad (\text{C.21})$$

$$B_{1,zzz}^\Sigma = \frac{16 d_1 (1 - \nu_s^2)}{3 E_s} \quad (\text{C.22})$$

and

$$B_{2,zzx}^\Sigma = B_{2,xzx}^\Sigma = B_{2,zyy}^\Sigma = B_{2,yzy}^\Sigma = \frac{16 d_2 (1 - \nu_s^2)}{3 E_s (2 - \nu_s)} \quad (\text{C.23})$$

$$B_{2,zzz}^\Sigma = \frac{16 d_2 (1 - \nu_s^2)}{3 E_s} \quad (\text{C.24})$$

Eqs. (2.12) and (2.13) contain concentration tensors  $\underline{\underline{A}}_1^\Sigma$  and  $\underline{\underline{A}}_2^\Sigma$ . Their non-vanishing components read as

$$A_{1,xxz}^\Sigma = A_{1,xzx}^\Sigma = A_{1,yyz}^\Sigma = A_{1,yzy}^\Sigma = \frac{16 a_1 (1 - \nu_s^2)}{3 \pi E_s (2 - \nu_s)} \quad \text{and} \quad A_{1,zzz}^\Sigma = \frac{16 a_1 (1 - \nu_s^2)}{3 \pi E_s} \quad (\text{C.25})$$

and

$$A_{2,xxz}^\Sigma = A_{2,xzx}^\Sigma = A_{2,yyz}^\Sigma = A_{2,yzy}^\Sigma = \frac{16 a_2 (1 - \nu_s^2)}{3 \pi E_s (2 - \nu_s)} \quad \text{and} \quad A_{2,zzz}^\Sigma = \frac{16 a_2 (1 - \nu_s^2)}{3 \pi E_s} \quad (\text{C.26})$$

Eqs. (2.12) and (2.13) contain influence tensors  $\underline{\underline{D}}_{11}^\Sigma$  and  $\underline{\underline{D}}_{22}^\Sigma$ . Their non-vanishing components read as

$$D_{11,xx}^\Sigma = D_{11,yy}^\Sigma = -\frac{16 a_1 (1 - \nu_s^2)}{3 \pi E_s (2 - \nu_s)}, \quad D_{11,zz}^\Sigma = -\frac{16 a_1 (1 - \nu_s^2)}{3 \pi E_s} \quad (\text{C.27})$$

and

$$D_{22,xx}^\Sigma = D_{22,yy}^\Sigma = -\frac{16 a_2 (1 - \nu_s^2)}{3 \pi E_s (2 - \nu_s)}, \quad D_{22,zz}^\Sigma = -\frac{16 a_2 (1 - \nu_s^2)}{3 \pi E_s} \quad (\text{C.28})$$

## Appendix D

# Creep and relaxation study of rheological models, as well as matrix-interfaces composites

### D.1 Defintion of elastic stiffness of solid, identity tensor, and so-called T-tensor

The isotropic elastic stiffness of solid in matrix-interface composite read as

$$\underline{\underline{\underline{C}}}_s = 3 k_s \underline{\underline{\underline{I}}}_{vol} + 2 \mu_s \underline{\underline{\underline{I}}}_{dev} \quad (\text{D.1})$$

where  $\underline{\underline{\underline{I}}}_{vol} = \frac{1}{3} \underline{\underline{\underline{1}}} \otimes \underline{\underline{\underline{1}}}$  and  $\underline{\underline{\underline{I}}}_{dev} = \underline{\underline{\underline{I}}} - \underline{\underline{\underline{I}}}_{vol}$ , respectively, denote the volumetric and the deviatoric part of the symmetric fourth-order identity tensor  $\underline{\underline{\underline{I}}}$ , with components  $I_{ijkl} = \frac{1}{2}(\delta_{ik} \delta_{jl} + \delta_{il} \delta_{kj})$ , and with  $\delta_{ij}$  denoting the Kronecker delta being equal to 1 if  $i = j$  and 0 otherwise. In addition,  $\underline{\underline{\underline{1}}}$  is the second-order identity tensor with components being equal to the Kronecker delta. In (D.1),  $k_s$  and  $\mu_s$  denote the bulk modulus and the shear modulus of the solid phase, respectively. Bulk modulus  $k_s$  is related to Poisson's ratio  $\nu_s$  and the shear modulus  $\mu_s$  as

$$k_s = \frac{2 \mu_s (1 + \nu_s)}{3(1 - 2 \nu_s)} \quad (\text{D.2})$$

The non-vanishing components of  $\underline{\underline{T}}_i$  are functions of Poisson's ratio of the solid, and they read as [63]

$$\left. \begin{aligned} T_{i,xzxz} = T_{i,zxxz} = T_{i,xzzx} = T_{i,zxzx} \\ T_{i,yzyz} = T_{i,zyyz} = T_{i,yzzz} = T_{i,zyzy} \end{aligned} \right\} = \frac{2(1-\nu_s)}{\pi(2-\nu_s)} \quad (\text{D.3})$$

$$\left. \begin{aligned} T_{i,zzxx} \\ T_{i,zzyy} \end{aligned} \right\} = \frac{4\nu_s(1-\nu_s)}{\pi(1-2\nu_s)} \quad (\text{D.4})$$

$$T_{i,zzzz} = \frac{4(1-\nu_s)^2}{\pi(1-2\nu_s)} \quad (\text{D.5})$$

## D.2 Kelvin-Voigt formulation: Creep and relaxation study

### D.2.1 Creep test

In a creep study, the system is suddenly subjected to a force  $\tau$  which is kept constant afterwards:

$$\tau(t) = \text{constant} = \tau, \quad \dot{\tau} = 0 \quad (\text{D.6})$$

Specification of (3.12) for (D.6) delivers the governing differential equation for creep as

$$\tau \left( \frac{1}{\mu_e} + \frac{1}{\mu_1} \right) \frac{\mu_1}{\eta_1} = \frac{\mu_1}{\eta_1} \gamma(t) + \dot{\gamma}(t) \quad (\text{D.7})$$

The solution of (D.7) contains two parts: the solution of the homogeneous differential equation, called complementary function  $\gamma_h$ , and one particulate integral  $\gamma_p$

$$\gamma(t) = \gamma_h(t) + \gamma_p \quad (\text{D.8})$$

The particulate solution turns out to be constant and reads as

$$\gamma_p = \tau \left( \frac{1}{\mu_e} + \frac{1}{\mu_1} \right) \quad (\text{D.9})$$

The sought complementary function follows as

$$\gamma_h(t) = C \exp \left( - \frac{\mu_1}{\eta_1} t \right) \quad (\text{D.10})$$

The total solution is obtained from specification of (D.8) for (D.9) and for (D.10), reading as

$$\gamma(t) = C \exp \left( - \frac{\mu_1}{\eta_1} t \right) + \frac{\tau}{\mu_e} + \frac{\tau}{\mu_1} \quad (\text{D.11})$$

The integration constant  $C$  follows from the initial condition  $\gamma(t = 0) = \frac{\tau}{\mu_e}$  as

$$C = -\frac{\tau}{\mu_1} \quad (\text{D.12})$$

Backsubstitution of (D.12) into (D.11), and simplifying the corresponding result, finally yields

$$\gamma(t) = \frac{\tau}{\mu_e} + \frac{\tau}{\mu_1} \left[ 1 - \exp\left(-\frac{\mu_1}{\eta_1} t\right) \right] \quad (\text{D.13})$$

### D.2.2 Relaxation test

In a relaxation study, the system is suddenly subjected to an elongation  $\gamma$  which is kept constant afterwards.

$$\gamma(t) = \text{constant} = \gamma, \quad \dot{\gamma} = 0 \quad (\text{D.14})$$

Specifying (3.12) for (D.14) delivers the governing differential equation for relaxation as

$$\dot{\tau}(t) + \tau(t) \frac{\mu_e}{\eta_1} \left( 1 + \frac{\mu_1}{\mu_e} \right) = \gamma \left( \frac{\mu_e \mu_1}{\eta_1} \right) \quad (\text{D.15})$$

The solution of (D.15) contains two parts: the solution of the homogeneous differential equation, called complementary function  $\tau_h(t)$ , and one particulate integral  $\tau_p$

$$\tau(t) = \tau_h(t) + \tau_p \quad (\text{D.16})$$

The particulate solution turns out to be time-independent, and reads as

$$\tau_p = \gamma \frac{\mu_1}{\left( 1 + \frac{\mu_1}{\mu_e} \right)} = \frac{\gamma}{\left( \frac{1}{\mu_1} + \frac{1}{\mu_e} \right)} \quad (\text{D.17})$$

The sought complementary function reads as

$$\tau_h(t) = C \exp \left[ -\frac{\mu_e}{\eta_1} \left( 1 + \frac{\mu_1}{\mu_e} \right) t \right] \quad (\text{D.18})$$

Specifying (D.16) for (D.17) and (D.18), yields the force history

$$\tau(t) = C \exp \left[ -\frac{\mu_e}{\eta_1} \left( 1 + \frac{\mu_1}{\mu_e} \right) t \right] + \frac{\gamma}{\left( \frac{1}{\mu_1} + \frac{1}{\mu_e} \right)} \quad (\text{D.19})$$

The integration constant  $C$  is identified from the initial condition  $\tau(t = 0) = \gamma \mu_e$  as

$$C = \gamma \frac{\mu_e}{\left(1 + \frac{\mu_1}{\mu_e}\right)} \quad (\text{D.20})$$

Backsubstitution of (D.20) into (D.19) gives access to the final solution which reads as

$$\tau(t) = \gamma \frac{\mu_e}{\left(1 + \frac{\mu_1}{\mu_e}\right)} \exp \left[ -\frac{\mu_e}{\eta_1} \left(1 + \frac{\mu_1}{\mu_e}\right) t \right] + \frac{\gamma}{\left(\frac{1}{\mu_1} + \frac{1}{\mu_e}\right)} \quad (\text{D.21})$$

### D.3 Maxwell formulation: Creep and relaxation study

#### D.3.1 Creep study

In a creep study, the system is suddenly subjected to a force  $\tau$  which is kept constant afterwards: see (D.6). Specification of (3.24) for (D.6) delivers the governing differential equation for creep as

$$\dot{\gamma}(t) + \frac{\mu_I \mu_E}{(\mu_I + \mu_E) \eta_I} \gamma(t) = \frac{\mu_I}{(\mu_I + \mu_E) \eta_I} \tau \quad (\text{D.22})$$

The solution of (D.22) contains two parts: the solution of the homogeneous differential equation, called complementary function  $\gamma_h$ , and one particulate integral  $\gamma_p$

$$\gamma(t) = \gamma_h(t) + \gamma_p \quad (\text{D.23})$$

The particulate solution turns out to be constant and reads as

$$\gamma_p = \frac{\tau}{\mu_E} \quad (\text{D.24})$$

The sought complementary function follows as

$$\gamma_h(t) = C \exp \left( -\frac{\mu_I \mu_E}{\mu_I + \mu_E} \frac{t}{\eta_I} \right) \quad (\text{D.25})$$

The total solution is obtained from specification of (D.23) for (D.24) and for (D.25), as

$$\gamma(t) = C \exp \left( -\frac{\mu_I \mu_E}{\mu_I + \mu_E} \frac{t}{\eta_I} \right) + \frac{\tau}{\mu_E} \quad (\text{D.26})$$

In order to solve for the integration constant  $C$ , we consider the initial condition  $\gamma(t = 0) = \frac{\tau}{\mu_I + \mu_E}$ , yielding

$$C = -\frac{\mu_I \tau}{\mu_E(\mu_I + \mu_E)} \quad (\text{D.27})$$

Specifying (D.26) for (D.27), delivers the deformation history of the system as

$$\gamma(t) = \frac{\tau}{\mu_E} - \frac{\mu_I \tau}{\mu_E(\mu_I + \mu_E)} \exp\left(-\frac{\mu_I \mu_E}{\mu_I + \mu_E} \frac{t}{\eta_I}\right) \quad (\text{D.28})$$

### D.3.2 Relaxation study

In a relaxation study, the system is suddenly subjected to an elongation  $\gamma$  which is kept constant afterwards, see (D.14). Specification of (3.24) for (D.14) delivers the governing differential equation for relaxation as

$$\dot{\tau}(t) + \frac{\mu_I}{\eta_I} \tau(t) = \frac{\mu_I \mu_E}{\eta_I} \gamma \quad (\text{D.29})$$

The solution of (D.29) contains two parts: the solution of the homogeneous differential equation, called complementary function  $\tau_h(t)$ , and one particulate integral  $\tau_p$

$$\tau(t) = \tau_h(t) + \tau_p \quad (\text{D.30})$$

where the particulate solution turns out to be time-independent, and reads as

$$\tau_p = \gamma \mu_E \quad (\text{D.31})$$

The sought complementary function follows as

$$\tau_h(t) = C \exp\left[-\frac{\mu_I}{\eta_I} t\right] \quad (\text{D.32})$$

Specification of (D.30) for (D.31) and for (D.32), yields

$$\tau(t) = C \exp\left[-\frac{\mu_I}{\eta_I} t\right] + \gamma \mu_E \quad (\text{D.33})$$

In order to solve for the integration constant  $C$ , we apply the initial condition ( $\tau(t = 0) = \gamma(\mu_E + \mu_I)$ ), which yields

$$C = \gamma \mu_I \quad (\text{D.34})$$

Specification of (D.33) for (D.34) delivers the stress history of the system as

$$\tau(t) = \gamma \mu_E + \gamma \mu_I \exp \left[ -\frac{\mu_I}{\eta_I} t \right] \quad (\text{D.35})$$

## D.4 Micromechanics formulation: Creep and relation study

### D.4.1 Creep test

In a creep study, the RVE is suddenly subjected to a shear stress  $\Sigma_{13}$  which is kept constant afterwards:

$$\Sigma_{13}(t) = \text{constant} = \Sigma_{13}, \quad \dot{\Sigma}_{13} = 0 \quad (\text{D.36})$$

Specification of the governing differential equation of interface micromechanics (4.44) for (D.36), yields the governing equation for the macrostrain reads as

$$\dot{E}_{13} + \mu_s \frac{3(2 - \nu_s) \pi}{8(1 - \nu_s) a \eta} E_{13} = \frac{\pi [3(2 - \nu_s) + 16 d (1 - \nu_s)]}{16 a \eta (1 - \nu_s)} \Sigma_{13} \quad (\text{D.37})$$

The solution of (D.37) contains two parts: the solution of homogeneous differential equation, called complementary function  $E_{13,h}(t)$ , and one particular integral  $E_{13,p}$

$$E_{13}(t) = E_{13,h}(t) + E_{13,p} \quad (\text{D.38})$$

The particular solution turns out to be time-independent, and reads as

$$E_{13,p} = \frac{3(2 - \nu_s) + 16 d (1 - \nu_s)}{2 \mu_s 3(2 - \nu_s)} \Sigma_{13} \quad (\text{D.39})$$

The sought complementary function reads as

$$E_{13,h}(t) = C \exp \left( -\frac{\mu_s 3(2 - \nu_s) \pi}{8(1 - \nu_s)} \frac{t}{a \eta} \right) \quad (\text{D.40})$$

The total solution is obtained from specification of (D.38) for (D.39) and for (D.40), yielding

$$E_{13}(t) = C \exp \left( -\frac{\mu_s 3(2 - \nu_s) \pi}{8(1 - \nu_s)} \frac{t}{a \eta} \right) + \frac{3(2 - \nu_s) + 16 d (1 - \nu_s)}{2 \mu_s 3(2 - \nu_s)} \Sigma_{13} \quad (\text{D.41})$$

In order to solve for the integration constant  $C$ , we consider the initial condition  $E_{13}(t = 0) = \frac{1}{2\mu_s} \Sigma_{13}$ , yielding

$$C = -\frac{16d(1-\nu_s)}{2\mu_s 3(2-\nu_s)} \Sigma_{13} \quad (\text{D.42})$$

Specifying (D.41) for the integration constant (D.42) allows us to write the time evolution of the macroscopic strain as

$$E_{13}(t) = \frac{\Sigma_{13}}{2\mu_s} \frac{3(2-\nu_s) + 16d(1-\nu_s) \left[ 1 - \exp\left(-\frac{3\pi(2-\nu_s)}{16(1-\nu_s^2)} \frac{E_s t}{a\eta}\right) \right]}{3(2-\nu_s)} \quad (\text{D.43})$$

#### D.4.2 Relaxation test

In a relaxation study, the RVE is suddenly subjected to a shear deformation  $E_{13}$  which is kept constant afterwards:

$$E_{13}(t) = \text{constant} = E_{13}, \quad \dot{E}_{13} = 0 \quad (\text{D.44})$$

Specification of the governing differential equation of interface micromechanics (4.44) for (D.44), yields the following differential equation in  $\Sigma_{13}$

$$\dot{\Sigma}_{13} + \mu_s \frac{\pi [3(2-\nu_s) + 16d(1-\nu_s)]}{8a\eta(1-\nu_s)} \Sigma_{13} = 2\mu_s^2 \frac{3(2-\nu_s)\pi}{8a\eta(1-\nu_s)} E_{13} \quad (\text{D.45})$$

The solution of (D.45) contains two parts: the solution of homogeneous differential equation, called complementary function  $\Sigma_{13,h}(t)$ , and one particular integral  $\Sigma_{13,p}$

$$\Sigma_{13}(t) = \Sigma_{13,h}(t) + \Sigma_{13,p} \quad (\text{D.46})$$

The particular solution turns out to be time-independent, and reads as

$$\Sigma_{13,p} = \frac{2\mu_s 3(2-\nu_s)}{3(2-\nu_s) + 16d(1-\nu_s)} E_{13} \quad (\text{D.47})$$

The sought complementary function reads as

$$\Sigma_{13,h}(t) = C \exp\left(-\frac{\mu_s \pi [3(2-\nu_s) + 16d(1-\nu_s)]}{8(1-\nu_s)} \frac{t}{a\eta}\right) \quad (\text{D.48})$$

Specification of (D.46) for the particular solution (D.47) and for the complementary function (D.48), yields

$$\Sigma_{13}(t) = C \exp\left(-\frac{\mu_s \pi [3(2 - \nu_s) + 16d(1 - \nu_s)]}{8(1 - \nu_s)} \frac{t}{a\eta}\right) + \frac{2\mu_s 3(2 - \nu_s)}{3(2 - \nu_s) + 16d(1 - \nu_s)} E_{13} \quad (\text{D.49})$$

In order to solve for the integration constant  $C$ , we consider the initial condition ( $\Sigma_{13}(t = 0) = 2\mu_s E_{13}$ ), delivering

$$C = 2\mu_s \frac{16d(1 - \nu_s)}{3(2 - \nu_s) + 16d(1 - \nu_s)} E_{13} \quad (\text{D.50})$$

Specification of (D.49) for (D.50), yields stress history as

$$\Sigma_{13}(t) = 2\mu_s E_{13} \frac{3(2 - \nu_s) + 16d(1 - \nu_s) \exp\left(-\frac{\pi [3(2 - \nu_s) + 16d(1 - \nu_s)]}{16(1 - \nu_s^2)} \frac{E_s t}{a\eta}\right)}{3(2 - \nu_s) + 16d(1 - \nu_s)} \quad (\text{D.51})$$

## Appendix E

# Expanded version of generalized chain models

### E.1 Expanded version of generalized Kelvin-Voigt model

Eq. (4.21), can be understood easier in the expanded form as

$$\begin{aligned}
& \gamma + \left( \sum_{i=1}^N \frac{\eta_i}{\mu_i} \right) \frac{\partial \gamma}{\partial t} + \left( \sum_{i=1}^{N-1} \left( \sum_{j=i+1}^N \frac{\eta_i \eta_j}{\mu_i \mu_j} \right) \frac{\partial^2 \gamma}{\partial t^2} + \dots + \right. \\
& \left. \left( \sum_{i_1=1}^{N-n+1} \dots \left( \sum_{i_a=i_{a-1}+1}^{N-(n-a)+1} \dots \left( \sum_{i_n=i_{n-1}+1}^N \left( \prod_{j \in \{i_1, \dots, i_n\}} \frac{\eta_j}{\mu_j} \right) \dots \right) \dots \right) \right) \frac{\partial^n \gamma}{\partial t^n} + \dots + \left( \prod_{i=1}^N \frac{\eta_i}{\mu_i} \right) \frac{\partial^N \gamma}{\partial t^N} \right) \\
& = \\
& \left( \frac{1}{\mu_e} + \sum_{l=1}^N \frac{1}{\mu_l} \right) \tau + \left( \sum_{i=1}^N \left( \left( \frac{1}{\mu_e} + \sum_{l=1}^N \frac{1}{\mu_l} \right) - \frac{1}{\mu_i} \right) \frac{\eta_i}{\mu_i} \right) \frac{\partial \tau}{\partial t} + \\
& \left( \sum_{i=1}^{N-1} \left( \sum_{j=i+1}^N \left( \left( \frac{1}{\mu_e} + \sum_{l=1}^N \frac{1}{\mu_l} \right) - \frac{1}{\mu_i} - \frac{1}{\mu_j} \right) \frac{\eta_i \eta_j}{\mu_i \mu_j} \right) \right) \frac{\partial^2 \tau}{\partial t^2} + \dots + \\
& \left( \sum_{i_1=1}^{N-n+1} \dots \left( \sum_{i_a=i_{a-1}+1}^{N-(n-a)+1} \dots \left( \sum_{i_n=i_{n-1}+1}^N \left( \left( \left( \frac{1}{\mu_e} + \sum_{l=1}^N \frac{1}{\mu_l} \right) - \sum_{j \in \{i_1, \dots, i_n\}} \frac{1}{\mu_j} \right) \right. \right. \right. \right. \\
& \left. \left. \left. \left. \left( \prod_{k \in \{i_1, \dots, i_n\}} \frac{\eta_k}{\mu_k} \right) \right) \dots \right) \dots \right) \frac{\partial^n \tau}{\partial t^n} + \dots + \frac{1}{\mu_e} \left( \prod_{i=1}^N \frac{\eta_i}{\mu_i} \right) \frac{\partial^N \tau}{\partial t^N} \right)
\end{aligned} \tag{E.1}$$

## E.2 Expanded version of generalized Maxwell model

Eq. (4.38), can be understood easier in the expanded form as

$$\begin{aligned}
& \tau + \left( \sum_{i=1}^N \frac{\eta_i}{\mu_i} \right) \frac{\partial \tau}{\partial t} + \left( \sum_{i=1}^{N-1} \left( \sum_{j=i+1}^N \frac{\eta_i \eta_j}{\mu_i \mu_j} \right) \frac{\partial^2 \tau}{\partial t^2} + \dots + \right. \\
& \left. \left( \sum_{i_1=1}^{N-n+1} \dots \left( \sum_{i_a=i_{a-1}+1}^{N-(n-a)+1} \dots \left( \sum_{i_n=i_{n-1}+1}^N \left( \prod_{j \in \{i_1, \dots, i_n\}} \frac{\eta_j}{\mu_j} \right) \right) \dots \right) \dots \right) \frac{\partial^n \tau}{\partial t^n} + \dots + \left( \prod_{i=1}^N \frac{\eta_i}{\mu_i} \right) \frac{\partial^N \tau}{\partial t^N} \right. \\
& = \\
& \mu_E \gamma + \left( \sum_{i=1}^N (\mu_E + \mu_i) \frac{\eta_i}{\mu_i} \right) \frac{\partial \gamma}{\partial t} + \left( \sum_{i=1}^{N-1} \left( \sum_{j=i+1}^N (\mu_E + \mu_i + \mu_j) \frac{\eta_i \eta_j}{\mu_i \mu_j} \right) \right) \frac{\partial^2 \gamma}{\partial t^2} + \dots + \\
& \left( \sum_{i_1=1}^{N-n+1} \dots \left( \sum_{i_a=i_{a-1}+1}^{N-(n-a)+1} \dots \left( \sum_{i_n=i_{n-1}+1}^N \left( \left( \mu_E + \sum_{j \in \{i_1, \dots, i_n\}} \mu_j \right) \left( \prod_{k \in \{i_1, \dots, i_n\}} \frac{\eta_k}{\mu_k} \right) \right) \right) \dots \right) \dots \right) \frac{\partial^n \gamma}{\partial t^n} \\
& + \dots + \left( \mu_E + \sum_{j=1}^N \mu_j \right) \left( \prod_{i=1}^N \frac{\eta_i}{\mu_i} \right) \frac{\partial^N \gamma}{\partial t^N}
\end{aligned}$$

(E.2)

## Appendix F

# Interpenetration of randomly oriented viscous interfaces

### F.1 Micromechanics of polycrystals with eigenstressed interface phases of isotropic orientation

Extending the work described in Chapter. 2, we now consider a representative volume  $\Omega$  of a polycrystalline material (fulfilling the standard separation-of-scales requirement [32] of being much smaller than the structure built up by this material, and much larger than the inhomogeneities found within this material), which hosts the following material phases (i.e. subdomains with homogeneous mechanical properties), see Fig. F.1: (i) one solid phase and (ii) an *infinite amount* of almost flat oblate interface phases being isotropically oriented in  $\mathbb{R}^3$ . The term “polycrystalline” expresses that all phases are considered to be in direct mutual interaction, and this implies that the differently oriented interfaces are actually envisioned to interpenetrate one each other. Every interface phase is characterized by a specific orientation (labelled by  $(\vartheta, \varphi)$ , see Fig. F.2), by an eigenstress  $\underline{\underline{\sigma}}_{(\vartheta, \varphi)}^V$  (which is “free” from elastic effects, and which will be connected to viscous effects in Section 1.5), and by a vanishing stiffness

$$\underline{\underline{\sigma}}_{(\vartheta, \varphi)} = \underline{\underline{\sigma}}_{(\vartheta, \varphi)}^V, \quad \underline{\underline{C}}_{(\vartheta, \varphi)} = 0, \quad \forall \begin{cases} \vartheta \in [0; \pi], \\ \varphi \in [0; 2\pi] \end{cases} \quad (\text{F.1})$$

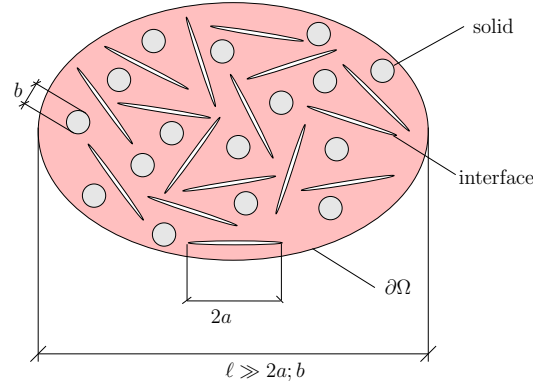


Figure F.1: Polycrystalline material comprising one spherical solid phase and an infinite amount of almost flat, circular interface phases with isotropic spatial orientation; 2D sketch of a 3D representative material volume  $\Omega$

The solid phase is characterized by an elastic stiffness tensor  $\underline{\underline{C}}_s$  and no eigenstress, such that the elasticity law reads as

$$\underline{\underline{\sigma}}_s = \underline{\underline{C}}_s : \underline{\underline{\varepsilon}}_s \quad (\text{F.2})$$

with  $\underline{\underline{\sigma}}_s$  and  $\underline{\underline{\varepsilon}}_s$  as the average microstresses and the average microstrains in the solid. We here consider an isotropic solid stiffness

$$\underline{\underline{C}}_s = 3 k_s \underline{\underline{J}} + 2 \mu_s \underline{\underline{K}} \quad (\text{F.3})$$

where  $\underline{\underline{J}} = \frac{1}{3} \underline{\underline{1}} \otimes \underline{\underline{1}}$  and  $\underline{\underline{K}} = \underline{\underline{I}} - \underline{\underline{J}}$ , respectively, denote the volumetric and the deviatoric part of the symmetric fourth-order identity tensor  $\underline{\underline{I}}$ , with components  $I_{ijkl} = \frac{1}{2}(\delta_{ik} \delta_{jl} + \delta_{il} \delta_{kj})$ , and with  $\delta_{ij}$  denoting the Kronecker delta being equal to 1 if  $i = j$  and 0 otherwise. In addition,  $\underline{\underline{1}}$  is the second-order identity tensor with components being equal to the Kronecker delta. In (F.3),  $k_s$  and  $\mu_s$  denote the bulk modulus and the shear modulus of the solid phase, respectively.

The volume fractions of the solid and the interfaces respectively, are considered as

$$f_{(\vartheta, \varphi)} = \frac{\mathcal{N}_{(\vartheta, \varphi)}}{\Omega} \frac{4\pi}{3} a^2 c = \frac{4\pi d_{(\vartheta, \varphi)}}{3} \omega, \quad f_s = 1 - \int_{\varphi=0}^{\varphi=2\pi} \int_{\vartheta=0}^{\vartheta=\pi} f_{(\vartheta, \varphi)} \frac{\sin \vartheta d\vartheta d\varphi}{4\pi} \quad (\text{F.4})$$

In Eq. (F.4),  $\mathcal{N}_{(\vartheta, \varphi)}$  denotes the number of interfaces constituting phase  $(\vartheta, \varphi)$ , and where  $d_{(\vartheta, \varphi)}$  denotes the interface density parameter defined as [65]

$$d_{(\vartheta, \varphi)} = \frac{\mathcal{N}_{(\vartheta, \varphi)} a^3}{\Omega}, \quad \forall \begin{cases} \vartheta \in [0; \pi], \\ \varphi \in [0; 2\pi] \end{cases} \quad (\text{F.5})$$

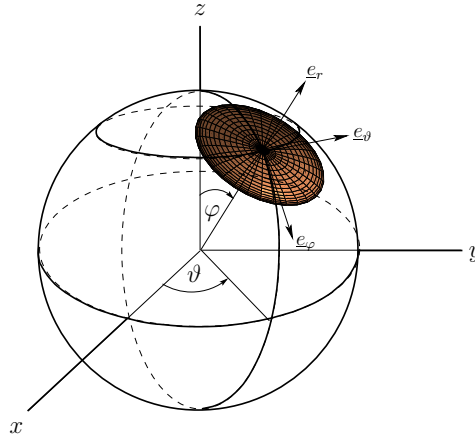


Figure F.2: Orientation of an interface phase as well as interface-related base vectors

The double integral in (F.4) refers to a summation of all (infinity many) interface orientations. The material volume of Fig. 2 is subjected, at its boundary  $\partial\Omega$ , to macroscopic strains being applied in terms of displacements

$$\underline{\xi}(\underline{x}) = \underline{E} \cdot \underline{x} \quad \forall \underline{x} \in \partial\Omega \quad (\text{F.6})$$

with  $\underline{x}$  as the position vector. Furthermore, we consider the resulting microscopic strain field inside the material volume  $\Omega$

$$\underline{\underline{\varepsilon}}(\underline{x}) = \frac{1}{2} \left[ \underline{\underline{\nabla}}\underline{\xi}(\underline{x}) + {}^t\underline{\underline{\nabla}}\underline{\xi}(\underline{x}) \right] \quad \forall \underline{x} \in \Omega \quad (\text{F.7})$$

to be kinematically compatible, which entails the validity of the strain averaging rule [55] in the form

$$\underline{E} = f_s \underline{\underline{\varepsilon}}_s + \int_{\varphi=0}^{\varphi=2\pi} \int_{\vartheta=0}^{\vartheta=\pi} f_{(\vartheta,\varphi)} \underline{\underline{\varepsilon}}_{(\vartheta,\varphi)} \frac{\sin \vartheta d\vartheta d\varphi}{4\pi} \quad (\text{F.8})$$

with  $\underline{\underline{\varepsilon}}_{(\vartheta,\varphi)}$  as the average strains in the  $(\vartheta, \varphi)$ -oriented interface phase and  $f_{(\vartheta,\varphi)}$  as its volume fraction; while  $\underline{\underline{\varepsilon}}_s$  and  $f_s$  denote the average strain and the volume fraction of the solid material. The linear elasticity law of the solid (F.2), the eigenstresses of the interfaces (F.1), the linear strain-displacement relation (F.7), and the uniform strain boundary conditions (F.6) imply the following linear

concentration-influence relations [52, 54]

$$\underline{\underline{\varepsilon}}_{(\vartheta, \varphi)} = \underline{\underline{A}}_{(\vartheta, \varphi)} : \underline{\underline{E}} + \int_{\phi=0}^{\phi=2\pi} \int_{\theta=0}^{\theta=\pi} \underline{\underline{D}}_{(\vartheta, \varphi, \theta, \phi)} : \underline{\underline{\sigma}}_{(\theta, \phi)}^V \frac{\sin \theta d\theta d\phi}{4\pi} \quad \forall \begin{cases} \vartheta \in [0; \pi], \\ \varphi \in [0; 2\pi] \end{cases} \quad (\text{F.9})$$

$$\underline{\underline{\varepsilon}}_s = \underline{\underline{A}}_s : \underline{\underline{E}} + \int_{\phi=0}^{\phi=2\pi} \int_{\theta=0}^{\theta=\pi} \underline{\underline{D}}_s(\theta, \phi) : \underline{\underline{\sigma}}_{(\theta, \phi)}^V \frac{\sin \theta d\theta d\phi}{4\pi} \quad (\text{F.10})$$

with  $\underline{\underline{A}}_{(\vartheta, \varphi)}$  and  $\underline{\underline{A}}_s$  as the strain concentration tensors of the  $(\vartheta, \varphi)$ -oriented interface phase and of the solid, respectively, as well as with  $\underline{\underline{D}}_{(\vartheta, \varphi, \theta, \phi)}$  and  $\underline{\underline{D}}_s(\theta, \phi)$  as the influence tensors quantifying the effect of eigen-microstresses  $\underline{\underline{\sigma}}_{(\theta, \phi)}^V$  of a  $(\theta, \phi)$ -oriented interface phase on the microstrains of the  $(\vartheta, \varphi)$ -oriented interface phase and on the microstrains of the solid, respectively.

For defining the macroscopic stress  $\underline{\underline{\Sigma}}$ , we consider that the work done by the RVE-related macrostress  $\underline{\underline{\Sigma}}$  on the macrostrain  $\underline{\underline{E}}$ , is equal to the work done by all microstresses *within* the RVE, on all microstrains:

$$\underline{\underline{\Sigma}} : \underline{\underline{E}} = \frac{1}{\Omega} \int_{\Omega} \underline{\underline{\sigma}}(\underline{\underline{x}}) : \underline{\underline{\varepsilon}}(\underline{\underline{x}}) d\Omega \quad (\text{F.11})$$

When considering the strain average rule (F.8) and an equilibrated microscopic stress field ( $\text{div } \underline{\underline{\sigma}}(\underline{\underline{x}}) = 0 \underline{\underline{x}} \in \Omega$ ), the integral in (F.11) can be transformed into [59]

$$\frac{1}{\Omega} \int_{\Omega} \underline{\underline{\sigma}}(\underline{\underline{x}}) : \underline{\underline{\varepsilon}}(\underline{\underline{x}}) d\Omega = \frac{1}{\Omega} \int_{\Omega} \underline{\underline{\sigma}}(\underline{\underline{x}}) d\Omega : \frac{1}{\Omega} \int_{\Omega} \underline{\underline{\varepsilon}}(\underline{\underline{x}}) d\Omega \quad (\text{F.12})$$

which is standardly referred to as Hill's lemma. From combination of (F.11), (F.12), and (F.8) it follows that the macrostress is the average of the microstresses over the RVE,

$$\underline{\underline{\Sigma}} = \frac{1}{\Omega} \int_{\Omega} \underline{\underline{\sigma}}(\underline{\underline{x}}) d\Omega \quad \Rightarrow \quad \underline{\underline{\Sigma}} = f_s \underline{\underline{\sigma}}_s + \int_{\varphi=0}^{\varphi=2\pi} \int_{\vartheta=0}^{\vartheta=\pi} f_{(\vartheta, \varphi)} \underline{\underline{\sigma}}_{(\vartheta, \varphi)} \frac{\sin \vartheta d\vartheta d\varphi}{4\pi} \quad (\text{F.13})$$

Eq. (F.13) is standardly referred to as the stress average rule. As to arrive at an elegant alternative expression for the macroscopic stress, we follow Dormieux [59] in splitting the loading of the RVE into two separate parts, namely (i) the macroscopic strains  $\underline{\underline{E}}$  and (ii) the interface eigenstresses  $\underline{\underline{\sigma}}_{(\vartheta, \varphi)}^V$ , labelling corresponding physical quantities with “I” and “II”, respectively. Accordingly,  $\underline{\underline{E}}_I = \underline{\underline{E}}$ ,  $\underline{\underline{E}}_{II} = 0$ ,

$\underline{\underline{\sigma}}_{(\vartheta,\varphi),I}^V = 0$ , and  $\underline{\underline{\sigma}}_{(\vartheta,\varphi),II}^V = \underline{\underline{\sigma}}_{(\vartheta,\varphi)}^V$ . Insertion of Eqs. (F.1), (F.2), and (F.10) into Eq. (F.13), and specifying the result for load case  $I$ , yields

$$\underline{\underline{\Sigma}}_I = \underline{\underline{C}}_{hom} : \underline{\underline{E}} \quad (\text{F.14})$$

with the so-called homogenized stiffness tensor

$$\underline{\underline{C}}_{hom} = f_s \underline{\underline{C}}_s : \underline{\underline{A}}_s \quad (\text{F.15})$$

Because the solid is isotropic, see (F.3), and because we envision the interface phases to be isotropically oriented and distributed in  $\mathbb{R}^3$ , also the homogenized stiffness is isotropic

$$\underline{\underline{C}}_{hom} = 3 k_{hom} \underline{\underline{J}} + 2 \mu_{hom} \underline{\underline{K}} \quad (\text{F.16})$$

As for calculation of the macrostress in load case  $II$ , we let microscopic stresses  $\underline{\underline{\sigma}}_{s,II}$  and  $\underline{\underline{\sigma}}_{(\vartheta,\varphi),II}^V$  do work on microscopic strains  $\underline{\underline{\varepsilon}}_{s,I}$  and  $\underline{\underline{\varepsilon}}_{(\vartheta,\varphi),I}$ , which, upon twofold application of Hill's lemma (F.11) and (F.12), yields [59]

$$\underline{\underline{\Sigma}}_{II} = \int_{\varphi=0}^{\varphi=2\pi} \int_{\vartheta=0}^{\vartheta=\pi} f_{(\vartheta,\varphi)} \underline{\underline{\sigma}}_{(\vartheta,\varphi)}^V : \underline{\underline{A}}_{(\vartheta,\varphi)} \frac{\sin \vartheta d\vartheta d\varphi}{4\pi} \quad (\text{F.17})$$

which is referred to as Levin's theorem [60]. Adding (F.14) and (F.17) yields the sought alternative expression for the macroscopic stresses,

$$\underline{\underline{\Sigma}} = \underline{\underline{C}}_{hom} : \underline{\underline{E}} + \underline{\underline{\Sigma}}_{hom}^f \quad (\text{F.18})$$

with

$$\underline{\underline{\Sigma}}_{hom}^f = \int_{\varphi=0}^{\varphi=2\pi} \int_{\vartheta=0}^{\vartheta=\pi} f_{(\vartheta,\varphi)} \underline{\underline{\sigma}}_{(\vartheta,\varphi)}^V : \underline{\underline{A}}_{(\vartheta,\varphi)} \frac{\sin \vartheta d\vartheta d\varphi}{4\pi} \quad (\text{F.19})$$

## F.2 Determination of concentration and influence tensors from matrix-inclusion problems

For the described polycrystalline material (Fig. F.1), the so-called self-consistent scheme is appropriate. Accordingly, we estimate the solid strains  $\underline{\underline{\varepsilon}}_s$  and the interface phase strains  $\underline{\underline{\varepsilon}}_{(\vartheta,\varphi)}$  by means of auxiliary matrix-inclusion problems (see Fig. F.3), namely we set them equal to the uniform strains in an ellipsoidal inclusion (exhibiting phase properties in terms of shape, orientation, elastic stiffness, and

eigenstress), embedded in an infinite matrix of isotropic stiffness  $\underline{\underline{C}}_{hom}$  and eigenstress  $\underline{\underline{\Sigma}}_{hom}^f$ , subjected to fictitious strains  $\underline{\underline{E}}^\infty$  at its infinitely remote boundary. The latter strains are chosen in a way which allows for fulfillment of the strain average rule (F.8).

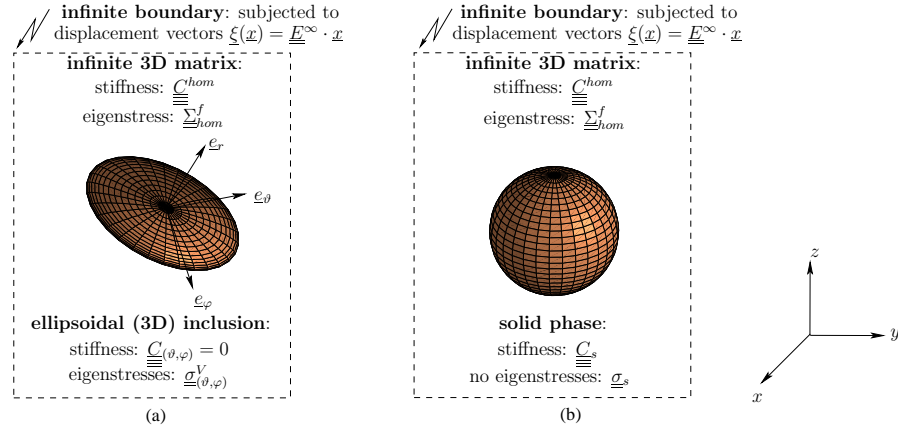


Figure F.3: Eshelby-type matrix-inclusion problems including infinite 3D matrices with isotropic stiffness, and eigenstress as well as one inclusion (a): oriented, almost flat spheroid with vanishing solid stiffness and eigenstresses, and (b): spherical inclusion with isotropic solid stiffness and vanishing eigenstresses

In detail, for every interface phase, the corresponding inclusion is a  $(\vartheta, \varphi)$ -oriented, almost flat oblate inclusion which exhibits vanishing solid stiffness  $\underline{\underline{C}}_{(vartheta, varphi)} = 0$  and eigenstress  $\underline{\underline{\sigma}}_{(vartheta, varphi)}^V$  [Fig. F.3(a)], and the inclusion strains follow the analytical relation [32, 62]

$$\underline{\underline{\varepsilon}}_{(vartheta, varphi)} = \underline{\underline{A}}_{(vartheta, varphi)}^\infty : \left\{ \underline{\underline{E}}^\infty - \underline{\underline{P}}_{(vartheta, varphi)} : \left[ \underline{\underline{\sigma}}_{(vartheta, varphi)}^V - \underline{\underline{\Sigma}}_{hom}^f \right] \right\} \quad (\text{F.20})$$

$$\underline{\underline{A}}_{(vartheta, varphi)}^\infty = \left\{ \underline{\underline{I}} - \underline{\underline{P}}_{(vartheta, varphi)} : \underline{\underline{C}}_{hom} \right\}^{-1} \quad \forall \begin{cases} \vartheta \in [0; \pi], \\ \varphi \in [0; 2\pi] \end{cases} \quad (\text{F.21})$$

The Hill tensor  $\underline{\underline{P}}_{(vartheta, varphi)}$  in (F.20) and (F.21) is standardly derived from the Eshelby tensor  $\underline{\underline{S}}_{(vartheta, varphi)}$ , through

$$\underline{\underline{P}}_{(vartheta, varphi)} = \underline{\underline{S}}_{(vartheta, varphi)} : \underline{\underline{C}}_{hom}^{-1} \quad \forall \begin{cases} \vartheta \in [0; \pi], \\ \varphi \in [0; 2\pi] \end{cases} \quad (\text{F.22})$$

and the Eshelby tensor components for oblate spheroidal inclusions with radius  $a$  and half-opening  $c$  (see Fig. 1.4), can be found in [62]. Given our interest in almost flat spheroids, characterized by very small aspect ratio  $\omega = c/a \ll 1$ , we develop these components into Taylor series around  $\omega = 0$ , which we then truncate after

the terms which are linear in  $\omega$ , leading to the following non-vanishing components, provided that the normal to the mid-plane of the almost flat spheroid is pointing in  $z$ -direction:

$$\begin{aligned}
S_{(\varphi=0,\vartheta=0),xxxx} &= \frac{13 - 8\nu_{hom}}{32(1 - \nu_{hom})} \pi \omega, \\
S_{(\varphi=0,\vartheta=0),xxyy} &= \frac{8\nu_{hom} - 1}{32(1 - \nu_{hom})} \pi \omega, \\
S_{(\varphi=0,\vartheta=0),xxzz} &= \frac{2\nu_{hom} - 1}{8(1 - \nu_{hom})} \pi \omega, \\
S_{(\varphi=0,\vartheta=0),zzxx} &= \frac{\nu_{hom}}{(1 - \nu_{hom})} \left( 1 - \frac{4\nu_{hom} + 1}{8\nu_{hom}} \pi \omega \right), \\
S_{(\varphi=0,\vartheta=0),xyxy} &= \frac{7 - 8\nu_{hom}}{32(1 - \nu_{hom})} \pi \omega, \\
S_{(\varphi=0,\vartheta=0),yzyz} &= \frac{1}{2} \left( 1 + \frac{(\nu_{hom} - 2)}{(1 - \nu_{hom})} \frac{\pi}{4} \omega \right), \\
S_{(\varphi=0,\vartheta=0),zzzz} &= 1 - \frac{1 - 2\nu_{hom}}{1 - \nu_{hom}} \frac{\pi}{4} \omega
\end{aligned} \tag{F.23}$$

with symmetries  $S_{(\varphi=0,\vartheta=0),ijkl} = S_{(\varphi=0,\vartheta=0),jikl} = S_{(\varphi=0,\vartheta=0),ijlk}$ . In Eq. (F.23),  $\nu_{hom}$  stands for Poisson's ratio of the homogenized polycrystal. For the solid phase, in turn, the considered matrix inclusion problem involves a spherical inclusion with isotropic elastic stiffness  $\underline{\underline{C}}_s$  and vanishing eigenstress [Fig. F.3(b)], such that the inclusion strains read as [32, 62]

$$\underline{\underline{\varepsilon}}_s = \underline{\underline{A}}_s^\infty : \left[ \underline{\underline{E}}^\infty + \underline{\underline{P}}_s : \underline{\underline{\Sigma}}_{hom}^f \right] \tag{F.24}$$

$$\underline{\underline{A}}_s^\infty = \left[ \underline{\underline{I}} + \underline{\underline{P}}_s : (\underline{\underline{C}}_s - \underline{\underline{C}}_{hom}) \right]^{-1} \tag{F.25}$$

The Hill tensor for the solid phase  $\underline{\underline{P}}_s$  in (F.24) and (F.25) is related through

$$\underline{\underline{P}}_s = \underline{\underline{S}}_s : \underline{\underline{C}}_{hom}^{-1} \tag{F.26}$$

to the Eshelby tensor  $\underline{\underline{S}}_s$  of a spherical inclusion [62]

$$\underline{\underline{S}}_s = \frac{1 + \nu_{hom}}{3(1 - \nu_{hom})} \underline{\underline{J}} + \frac{2}{15} \frac{4 - 5\nu_{hom}}{1 - \nu_{hom}} \underline{\underline{K}} \tag{F.27}$$

Now we treat (F.20) and (F.24) as estimates of interface strains  $\underline{\underline{\varepsilon}}_{(\vartheta,\varphi)}$  and of solid

strains  $\underline{\underline{\varepsilon}}_s$ , respectively, and we insert them into the strain average rule (F.8), in order to obtain a relation between the strains  $\underline{\underline{E}}$  imposed at the boundary of the RVE and the (fictitious) strains  $\underline{\underline{E}}^\infty$  acting at the infinitely remote boundaries of the auxiliary matrix of the problems shown in Fig. F.3,

$$\begin{aligned} \underline{\underline{E}}^\infty = & \left[ f_s \underline{\underline{A}}_s^\infty + \int_{\varphi=0}^{\varphi=2\pi} \int_{\vartheta=0}^{\vartheta=\pi} f(\vartheta, \varphi) \underline{\underline{A}}_{(\vartheta, \varphi)}^\infty \frac{\sin \vartheta d\vartheta d\varphi}{4\pi} \right]^{-1} : \\ & \left\{ \underline{\underline{E}} - f_s \underline{\underline{A}}_s^\infty : \underline{\underline{P}}_s : \underline{\underline{\Sigma}}_{hom}^f + \right. \\ & \left. \int_{\varphi=0}^{\varphi=2\pi} \int_{\vartheta=0}^{\vartheta=\pi} f(\vartheta, \varphi) \underline{\underline{A}}_{(\vartheta, \varphi)}^\infty : \underline{\underline{P}}_{(\vartheta, \varphi)} : \left[ \underline{\underline{\sigma}}_{(\vartheta, \varphi)}^V - \underline{\underline{\Sigma}}_{hom}^f \right] \frac{\sin \vartheta d\vartheta d\varphi}{4\pi} \right\} \end{aligned} \quad (\text{F.28})$$

RVE-related phase strain which are kinematically admissible with the imposed macrostrains  $\underline{\underline{E}}$  follow from backsubstitution of (F.28) into (F.20) and into (F.24), respectively, as

$$\begin{aligned} \underline{\underline{\varepsilon}}_{(\vartheta, \varphi)} = & \underline{\underline{A}}_{(\vartheta, \varphi)}^\infty : \left[ f_s \underline{\underline{A}}_s^\infty + \int_{\phi=0}^{\phi=2\pi} \int_{\theta=0}^{\theta=\pi} f(\theta, \phi) \underline{\underline{A}}_{(\theta, \phi)}^\infty \frac{\sin \theta d\theta d\phi}{4\pi} \right]^{-1} : \\ & \left( \underline{\underline{E}} - f_s \underline{\underline{A}}_s^\infty : \underline{\underline{P}}_s : \underline{\underline{\Sigma}}_{hom}^f + \int_{\phi=0}^{\phi=2\pi} \int_{\theta=0}^{\theta=\pi} f(\theta, \phi) \underline{\underline{A}}_{(\theta, \phi)}^\infty : \underline{\underline{P}}_{(\theta, \phi)} : (\underline{\underline{\sigma}}_{(\theta, \phi)}^V - \underline{\underline{\Sigma}}_{hom}^f) \right. \\ & \left. \frac{\sin \theta d\theta d\phi}{4\pi} \right) - \underline{\underline{A}}_{(\vartheta, \varphi)}^\infty : \underline{\underline{P}}_{(\vartheta, \varphi)} : (\underline{\underline{\sigma}}_{(\vartheta, \varphi)}^V - \underline{\underline{\Sigma}}_{hom}^f) \quad \forall \begin{cases} \vartheta \in [0; \pi], \\ \varphi \in [0; 2\pi] \end{cases} \end{aligned} \quad (\text{F.29})$$

and

$$\begin{aligned} \underline{\underline{\varepsilon}}_s = & \underline{\underline{A}}_s^\infty : \left[ f_s \underline{\underline{A}}_s^\infty + \int_{\varphi=0}^{\varphi=2\pi} \int_{\vartheta=0}^{\vartheta=\pi} f(\vartheta, \varphi) \underline{\underline{A}}_{(\vartheta, \varphi)}^\infty \frac{\sin \vartheta d\vartheta d\varphi}{4\pi} \right]^{-1} : \left( \underline{\underline{E}} - f_s \underline{\underline{A}}_s^\infty : \underline{\underline{P}}_s : \underline{\underline{\Sigma}}_{hom}^f \right. \\ & \left. + \int_{\varphi=0}^{\varphi=2\pi} \int_{\vartheta=0}^{\vartheta=\pi} f(\vartheta, \varphi) \underline{\underline{A}}_{(\vartheta, \varphi)}^\infty : \underline{\underline{P}}_{(\vartheta, \varphi)} : (\underline{\underline{\sigma}}_{(\vartheta, \varphi)}^V - \underline{\underline{\Sigma}}_{hom}^f) \frac{\sin \vartheta d\vartheta d\varphi}{4\pi} \right) + \underline{\underline{A}}_s^\infty : \underline{\underline{P}}_s : \underline{\underline{\Sigma}}_{hom}^f \end{aligned} \quad (\text{F.30})$$

In order to identify estimates of phase strains concentration tensors  $\underline{\underline{A}}_{(\vartheta, \varphi)}^\infty$  and  $\underline{\underline{A}}_s^\infty$  as well as of influence tensors  $\underline{\underline{D}}_{(\vartheta, \varphi, \theta, \phi)}^\infty$  and  $\underline{\underline{D}}_{s(\theta, \phi)}^\infty$ , we compare (F.29) and (F.30)

with (F.9) and (F.10). This yields

$$\underline{\underline{A}}_{(\vartheta, \varphi)} = \underline{\underline{A}}_{(\vartheta, \varphi)}^\infty : \left[ f_s \underline{\underline{A}}_s^\infty + \int_{\phi=0}^{\phi=2\pi} \int_{\theta=0}^{\theta=\pi} f(\theta, \phi) \underline{\underline{A}}_{(\theta, \phi)}^\infty \frac{\sin \theta d\theta d\phi}{4\pi} \right]^{-1} \quad \forall \begin{cases} \vartheta \in [0; \pi], \\ \varphi \in [0; 2\pi] \end{cases} \quad (\text{F.31})$$

and

$$\underline{\underline{A}}_s = \underline{\underline{A}}_s^\infty : \left[ f_s \underline{\underline{A}}_s^\infty + \int_{\varphi=0}^{\varphi=2\pi} \int_{\vartheta=0}^{\vartheta=\pi} f(\vartheta, \varphi) \underline{\underline{A}}_{(\vartheta, \varphi)}^\infty \frac{\sin \vartheta d\vartheta d\varphi}{4\pi} \right]^{-1} \quad (\text{F.32})$$

as well as under consideration of (F.19)

$$\begin{aligned} \underline{\underline{D}}_{(\vartheta, \varphi, \theta, \phi)} &= -\underline{\underline{A}}_{(\vartheta, \varphi)}^\infty : \underline{\underline{P}}_{(\vartheta, \varphi)} \delta_{\vartheta\theta} \delta_{\varphi\phi} + \underline{\underline{A}}_{(\vartheta, \varphi)} : \underline{\underline{f}}_{(\theta, \phi)} \underline{\underline{A}}_{(\theta, \phi)}^\infty : \underline{\underline{P}}_{(\theta, \phi)} - \\ &\left( \underline{\underline{A}}_{(\vartheta, \varphi)} : \left[ f_s \underline{\underline{A}}_s^\infty : \underline{\underline{P}}_s + \int_{\Phi=0}^{\Phi=2\pi} \int_{\Theta=0}^{\Theta=\pi} f(\Theta, \Phi) \underline{\underline{A}}_{(\Theta, \Phi)}^\infty : \underline{\underline{P}}_{(\Theta, \Phi)} \frac{\sin \Theta d\Theta d\Phi}{4\pi} \right] - \right. \\ &\left. \underline{\underline{A}}_{(\vartheta, \varphi)}^\infty : \underline{\underline{P}}_{(\vartheta, \varphi)} \right) : f(\theta, \phi) \underline{\underline{A}}_{(\theta, \phi)}^t \quad \forall \begin{cases} \vartheta, \theta \in [0; 2\pi], \\ \varphi, \phi \in [0; \pi] \end{cases} \end{aligned} \quad (\text{F.33})$$

and

$$\begin{aligned} \underline{\underline{D}}_s(\vartheta, \varphi) &= \underline{\underline{A}}_s : \underline{\underline{f}}_{(\vartheta, \varphi)} \underline{\underline{A}}_{(\vartheta, \varphi)}^\infty : \underline{\underline{P}}_{(\vartheta, \varphi)} - \left( \underline{\underline{A}}_s : \left[ f_s \underline{\underline{A}}_s^\infty : \underline{\underline{P}}_s + \right. \right. \\ &\left. \left. \int_{\phi=0}^{\phi=2\pi} \int_{\theta=0}^{\theta=\pi} f(\theta, \phi) \underline{\underline{A}}_{(\theta, \phi)}^\infty : \underline{\underline{P}}_{(\theta, \phi)} \frac{\sin \theta d\theta d\phi}{4\pi} \right] - \underline{\underline{A}}_s^\infty : \underline{\underline{P}}_s \right) : f(\vartheta, \varphi) \underline{\underline{A}}_{(\vartheta, \varphi)}^t \\ &\quad \forall \begin{cases} \vartheta \in [0; \pi], \\ \varphi \in [0; 2\pi] \end{cases} \end{aligned} \quad (\text{F.34})$$

The homogenized polycrystal is identified under consideration of Eqs. (F.15), (1.26), (F.25), (F.26), (F.27), and (F.23), and reads as

$$\begin{aligned} \underline{\underline{C}}_{hom} &= \underline{\underline{C}}_s : \left[ \underline{\underline{I}} + \underline{\underline{P}}_s : (\underline{\underline{C}}_s - \underline{\underline{C}}_{hom}) \right]^{-1} : \left( \left[ \underline{\underline{I}} + \underline{\underline{P}}_s : \right. \right. \\ &\left. \left. (\underline{\underline{C}}_s - \underline{\underline{C}}_{hom}) \right]^{-1} + \int_{\varphi=0}^{\varphi=2\pi} \int_{\vartheta=0}^{\vartheta=\pi} f(\vartheta, \varphi) \underline{\underline{A}}_{(\vartheta, \varphi)}^\infty \frac{\sin \vartheta d\vartheta d\varphi}{4\pi} \right)^{-1} \end{aligned} \quad (\text{F.35})$$

In Eq. (F.35),  $\underline{\underline{C}}_{hom}$  appears in both sides of equation, therefore, the implicit homogenized polycrystal needs to be computed by iterating.

### F.2.1 Transition from almost flat oblate spheroids to 2D interfaces

Next, we discuss the transition from almost oblate spheroidal inclusions to perfectly *flat*, i.e. 2D, circular interfaces, extending the idea of Pensée et al. [51] to (zero-stiffness) inclusions *with eigenstresses*. Given an inclusion radius  $a$  and an initial half-opening  $c$  (see Fig. 1.4), this transition refers to the limit of the aspect ratio  $\omega = c/a$  going to zero. The displacement field across the resulting 2D interface is discontinuous, and can be quantified as follows.

We start from the displacement field in an spheroidal interface inclusion (see Fig. 1.4), which, given the linear strain-displacement relations (F.7), can be derived from the uniform strains  $\underline{\underline{\varepsilon}}_{(\vartheta, \varphi)}$  prevailing in this inclusion, through

$$\underline{\underline{\xi}}(\underline{x}) = \underline{\underline{\varepsilon}}_{(\vartheta, \varphi)} \cdot \underline{x} \quad \forall \underline{x} \in \Omega_{(\vartheta, \varphi)} \quad (\text{F.36})$$

where  $\Omega_{(\vartheta, \varphi)}$  refers to the volume of the inclusion. In order to label the boundary of such an inclusion, we choose cylindrical coordinates for expressing corresponding location vectors  $\underline{x}$  (see Fig. 1.4),

$$\underline{x} = \rho \cos \varphi \underline{e}_\varphi + \rho \sin \vartheta \underline{e}_\vartheta + r \underline{e}_r \quad (\text{F.37})$$

so that all points of the upper boundary of the inclusion, denoted as  $\underline{x}^+$ , fulfill

$$\forall \underline{x}^+ \in \partial\Omega_{(\vartheta, \varphi)}^+ : \quad r = \omega \sqrt{a^2 - \rho^2} \quad (\text{F.38})$$

while those at the lower boundary of the inclusion, denoted as  $\underline{x}^-$ , fulfill

$$\forall \underline{x}^- \in \partial\Omega_{(\vartheta, \varphi)}^- : \quad r = -\omega \sqrt{a^2 - \rho^2} \quad (\text{F.39})$$

Relations (F.37), (F.38), and (F.39) allow us to express the displacement increment  $\Delta\underline{\underline{\xi}}_{(\vartheta, \varphi)}$  between the upper and the lower inclusion boundary, as

$$\Delta\underline{\underline{\xi}}_{(\vartheta, \varphi)} = \underline{\underline{\varepsilon}}_{(\vartheta, \varphi)} \cdot (\underline{x}^+ - \underline{x}^-) = 2\omega \underline{\underline{\varepsilon}}_{(\vartheta, \varphi)} \cdot \underline{n}_{(\vartheta, \varphi)} \sqrt{a^2 - \rho^2} \quad (\text{F.40})$$

where  $\underline{n}_{(\vartheta, \varphi)}$  is the unit vector in  $\underline{e}_r$ -direction (see Fig. 1.4). Eq. (F.40) underlines that the displacement increment depends on the radial coordinate  $\rho$ , i.e. on the distance from the inclusion center. In order to come up with one constant value characterizing the displacement increment across in the inclusion, we introduce

the average displacement increment of the interface phase as

$$\Delta \underline{\underline{\xi}}_{(\vartheta, \varphi)} = \frac{1}{a^2 \pi} \int_0^a 2 \omega \underline{\underline{\xi}}_{(\vartheta, \varphi)} \cdot \underline{\underline{n}}_{(\vartheta, \varphi)} \sqrt{a^2 - \rho^2} 2\pi \rho d\rho = \frac{4a}{3} \omega \underline{\underline{\xi}}_{(\vartheta, \varphi)} \cdot \underline{\underline{n}}_{(\vartheta, \varphi)} \quad (\text{F.41})$$

Finally, we insert the concentration-influence relation (F.9) into displacement increment expression (F.41), yielding

$$\Delta \underline{\underline{\xi}}_{(\vartheta, \varphi)} = \frac{4a}{3} \omega \left( \underline{\underline{A}}_{(\vartheta, \varphi)} : \underline{\underline{E}} + \int_{\phi=0}^{\phi=2\pi} \int_{\theta=0}^{\theta=\pi} \underline{\underline{D}}_{(\vartheta, \varphi, \theta, \phi)} : \underline{\underline{\sigma}}_{(\theta, \phi)}^V \frac{\sin \theta d\theta d\phi}{4\pi} \right) \cdot \underline{\underline{n}}_{(\vartheta, \varphi)} \\ \forall \begin{cases} \vartheta \in [0; \pi], \\ \varphi \in [0; 2\pi] \end{cases} \quad (\text{F.42})$$

We now consider the transition from spheroidal inclusions to flat, “sharp” interfaces, through the limit case  $\omega \rightarrow 0$ , so that displacement increment  $\Delta \underline{\underline{\xi}}_{(\vartheta, \varphi)}$  becomes a displacement jump (“dislocation”) across the infinitely thin interface,

$$\lim_{\omega \rightarrow 0} \Delta \underline{\underline{\xi}}_{(\vartheta, \varphi)} = \llbracket \underline{\underline{\xi}} \rrbracket_{(\vartheta, \varphi)} = \frac{4a}{3} \left( \lim_{\omega \rightarrow 0} \omega \underline{\underline{A}}_{(\vartheta, \varphi)} : \underline{\underline{E}} + \int_{\phi=0}^{\phi=2\pi} \int_{\theta=0}^{\theta=\pi} \lim_{\omega \rightarrow 0} \omega \underline{\underline{D}}_{(\vartheta, \varphi, \theta, \phi)} : \underline{\underline{\sigma}}_{(\theta, \phi)}^V \frac{\sin \theta d\theta d\phi}{4\pi} \right) \cdot \underline{\underline{n}}_{(\vartheta, \varphi)} \quad (\text{F.43})$$

Eq. (F.43) highlights the need for calculating the limits  $\lim_{\omega \rightarrow 0} \omega \underline{\underline{A}}_{(\vartheta, \varphi)}$  and  $\lim_{\omega \rightarrow 0} \omega \underline{\underline{D}}_{(\vartheta, \varphi, \theta, \phi)}$ . Both  $\underline{\underline{A}}_{(\vartheta, \varphi)}$  and  $\underline{\underline{D}}_{(\vartheta, \varphi, \theta, \phi)}$  depend on  $\underline{\underline{C}}_{hom}$  which is only implicitly defined see Eq. (F.35). Therefore, the limit case of Eq. (F.35), read as

$$\lim_{\omega \rightarrow 0} \omega \underline{\underline{C}}_{hom} = \underline{\underline{C}}_{hom}^{lim} = \underline{\underline{C}}_s : \underline{\underline{A}}_s^{\infty, lim} : \left[ \underline{\underline{A}}_s^{\infty, lim} + \int_{\Phi=0}^{\Phi=2\pi} \int_{\Theta=0}^{\Theta=\pi} \frac{4\pi d(\Theta, \Phi)}{3} \underline{\underline{T}}_{(\Theta, \Phi)} \frac{\sin \Theta d\Theta d\Phi}{4\pi} \right]^{-1} \quad (\text{F.44})$$

where  $\underline{\underline{A}}_s^{\infty, lim}$  is read as

$$\lim_{\omega \rightarrow 0} \omega \underline{\underline{A}}_s^{\infty} = \underline{\underline{A}}_s^{\infty, lim} = \left[ \underline{\underline{I}} + \underline{\underline{P}}_s : (\underline{\underline{C}}_s - \underline{\underline{C}}_{hom}^{lim}) \right]^{-1} \quad (\text{F.45})$$

where we followed [94] in introducing the notation

$$\underline{\underline{T}}_{(\vartheta, \varphi)} = \lim_{\omega \rightarrow 0} \omega \underline{\underline{A}}_{(\vartheta, \varphi)}^{\infty} = \lim_{\omega \rightarrow 0} \omega \left[ \underline{\underline{I}} - \underline{\underline{S}}_{(\vartheta, \varphi)}(\omega) \right]^{-1}, \quad \forall \begin{cases} \vartheta \in [0; \pi], \\ \varphi \in [0; 2\pi] \end{cases} \quad (\text{F.46})$$

Given an interface with normal pointing in  $z$ -direction, ( $\vartheta = 0, \varphi = 0$ ) the non-vanishing components of  $\underline{\underline{T}}_{(\vartheta, \varphi)}$  follow from specification of (F.46) for (F.23) as

$$\left. \begin{aligned} T_{(\varphi=0, \vartheta=0), zzzx} \\ T_{(\varphi=0, \vartheta=0), zzyy} \end{aligned} \right\} = \frac{4 \nu_{hom} (1 - \nu_{hom})}{\pi (1 - 2 \nu_{hom})}, \quad \left. \begin{aligned} T_{(\varphi=0, \vartheta=0), xzxx} \\ T_{(\varphi=0, \vartheta=0), yzyz} \end{aligned} \right\} = \frac{2 (1 - \nu_{hom})}{\pi (2 - \nu_{hom})}$$

$$T_{(\varphi=0, \vartheta=0), zzzz} = \frac{4 (1 - \nu_{hom})^2}{\pi (1 - 2 \nu_{hom})}$$
(F.47)

with symmetries  $T_{(\varphi=0, \vartheta=0), ijkl} = T_{(\varphi=0, \vartheta=0), jikl} = T_{(\varphi=0, \vartheta=0), ijlk}$ . The limit  $\lim_{\omega \rightarrow 0} \omega \underline{\underline{A}}_{(\vartheta, \varphi)}$  follows from (F.31), under consideration of (F.21)-(F.23), and (F.4) as well as of the limit rule of (tensor) products as

$$\lim_{\omega \rightarrow 0} \omega \underline{\underline{A}}_{(\vartheta, \varphi)} = \underline{\underline{A}}_{(\vartheta, \varphi)}^{lim} = \underline{\underline{T}}_{(\vartheta, \varphi)} : \left( \underline{\underline{A}}_s^{\infty, lim} + \int_{\Phi=0}^{\Phi=2\pi} \int_{\Theta=0}^{\Theta=\pi} \frac{4 \pi d(\Theta, \Phi)}{3} \underline{\underline{T}}_{(\Theta, \Phi)} \frac{\sin \Theta d\Theta d\Phi}{4 \pi} \right)^{-1}$$

$$\forall \begin{cases} \vartheta \in [0; \pi], \\ \varphi \in [0; 2\pi] \end{cases}$$
(F.48)

The limit,  $\lim_{\omega \rightarrow 0} \omega \underline{\underline{D}}_{(\vartheta, \varphi, \theta, \phi)}$  describes the influence of interfacial eigenstresses  $\underline{\underline{\sigma}}_{(\theta, \phi)}^V$  on the average displacement jump  $[\underline{\underline{\xi}}]_{(\vartheta, \varphi)}$ . The limit rules for tensor products together with (F.4), (F.48), and (F.46) yield

$$\lim_{\omega \rightarrow 0} \omega \underline{\underline{D}}_{(\vartheta, \varphi, \theta, \phi)} = - \lim_{\omega \rightarrow 0} \omega \underline{\underline{A}}_{(\vartheta, \varphi)}^{\infty} : \underline{\underline{P}}_{(\vartheta, \varphi)} \delta_{\vartheta\theta} \delta_{\varphi\phi} + \underline{\underline{A}}_{(\vartheta, \varphi)}^{lim} : \frac{4 \pi d(\theta, \phi)}{3} \lim_{\omega \rightarrow 0} \omega \underline{\underline{A}}_{(\theta, \phi)}^{\infty} : \underline{\underline{P}}_{(\theta, \phi)}$$

$$- \left[ \underline{\underline{A}}_{(\vartheta, \varphi)}^{lim} : \left( \underline{\underline{A}}_s^{\infty, lim} : \underline{\underline{P}}_s + \int_{\Phi=0}^{\Phi=2\pi} \int_{\Theta=0}^{\Theta=\pi} \frac{4 \pi d(\Theta, \Phi)}{3} \lim_{\omega \rightarrow 0} \omega \underline{\underline{A}}_{(\Theta, \Phi)}^{\infty} : \underline{\underline{P}}_{(\Theta, \Phi)} \frac{\sin \Theta d\Theta d\Phi}{4 \pi} \right) \right.$$

$$\left. - \lim_{\omega \rightarrow 0} \omega \underline{\underline{A}}_{(\vartheta, \varphi)}^{\infty} : \underline{\underline{P}}_{(\vartheta, \varphi)} \right] : \frac{4 \pi d(\theta, \phi)}{3} \underline{\underline{A}}_{(\theta, \phi)}^{lim, t} \quad \forall \begin{cases} \vartheta, \theta \in [0; \pi], \\ \varphi, \phi \in [0; 2\pi] \end{cases}$$
(F.49)

## F.2.2 Introduction of eigentraction vector for flat interfaces

The described transition from three-dimensional oblates to two-dimensional interfaces implies that the interfacial displacement jumps (F.43) as well as the macrostress (F.18) are only influenced by three components of the eigenstress tensor [31], i.e. the ones forming the eigentraction vector  $\underline{\underline{T}}_{(\theta, \phi)}^V$  which is acting on

the interface plane

$$\underline{\underline{T}}_{(\theta,\phi)}^V = \underline{\underline{\sigma}}_{(\theta,\phi)}^V \cdot \underline{\underline{n}}_{(\theta,\phi)} \quad \forall \begin{cases} \theta \in [0; \pi], \\ \phi \in [0; 2\pi] \end{cases} \quad (\text{F.50})$$

reformulate (F.43) and (1.17) as

$$\llbracket \underline{\underline{\xi}} \rrbracket_{(\vartheta,\varphi)} = \underline{\underline{A}}_{(\vartheta,\varphi)}^{lim} : \underline{\underline{E}} + \int_{\phi=0}^{\phi=2\pi} \int_{\theta=0}^{\theta=\pi} \underline{\underline{D}}_{(\vartheta,\varphi,\theta,\phi)}^{lim} \cdot \underline{\underline{T}}_{(\theta,\phi)}^V \frac{\sin \theta d\theta d\phi}{4\pi} \quad \forall \begin{cases} \vartheta \in [0; \pi], \\ \varphi \in [0; 2\pi] \end{cases} \quad (\text{F.51})$$

and

$$\underline{\underline{\Sigma}} = \underline{\underline{C}}_{hom}^{lim} : \underline{\underline{E}} + \int_{\phi=0}^{\phi=2\pi} \int_{\theta=0}^{\theta=\pi} \underline{\underline{B}}_{(\theta,\phi)}^{lim} \cdot \underline{\underline{T}}_{(\theta,\phi)}^V \frac{\sin \theta d\theta d\phi}{4\pi} \quad (\text{F.52})$$

While  $\underline{\underline{C}}_{hom}^{lim}$  is already defined in (F.44), the third-order concentration tensor  $\underline{\underline{A}}_{(\vartheta,\varphi)}^{lim}$ , the second-order influence tensor  $\underline{\underline{D}}_{(\vartheta,\varphi,\theta,\phi)}^{lim}$ , and the third-order influence tensor  $\underline{\underline{B}}_{(\theta,\phi)}^{lim}$  are defined as

$$\frac{4a}{3} \left( \lim_{\omega \rightarrow 0} \omega \underline{\underline{A}}_{(\vartheta,\varphi)}^{lim} : \underline{\underline{E}} \right) \cdot \underline{\underline{n}}_{(\vartheta,\varphi)} = \underline{\underline{A}}_{(\vartheta,\varphi)}^{lim} : \underline{\underline{E}} \quad \forall \begin{cases} \vartheta \in [0; \pi], \\ \varphi \in [0; 2\pi] \end{cases} \quad (\text{F.53})$$

$$\frac{4a}{3} \left( \lim_{\omega \rightarrow 0} \omega \underline{\underline{D}}_{(\vartheta,\varphi,\theta,\phi)}^{lim} : \underline{\underline{\sigma}}_{(\theta,\phi)}^V \right) \cdot \underline{\underline{n}}_{(\theta,\phi)} = \underline{\underline{D}}_{(\vartheta,\varphi,\theta,\phi)}^{lim} \cdot \underline{\underline{T}}_{(\theta,\phi)}^V, \quad \forall \begin{cases} \theta \in [0; \pi], \\ \phi \in [0; 2\pi] \end{cases} \quad (\text{F.54})$$

$$\lim_{\omega \rightarrow 0} \left[ \frac{4\pi d(\theta,\phi)}{3} \omega \underline{\underline{A}}_{(\theta,\phi)}^t : \underline{\underline{\sigma}}_{(\theta,\phi)}^V \right] = \underline{\underline{B}}_{(\theta,\phi)}^{lim} \cdot \underline{\underline{T}}_{(\theta,\phi)}^V \quad \forall \begin{cases} \vartheta \in [0; \pi], \\ \varphi \in [0; 2\pi] \end{cases} \quad (\text{F.55})$$

### F.2.3 Remarks on macroscopic loading in form of controlled stress

We now consider that a material with eigenstressed interfaces is subjected to a given macroscopic stress state  $\underline{\underline{\Sigma}}$ , such that the macrostrain  $\underline{\underline{E}}$  is a dependent quantity. This is the motivation for solving state equation (F.52) for  $\underline{\underline{E}}$

$$\begin{aligned} \underline{\underline{E}} &= (\underline{\underline{C}}_{hom}^{lim})^{-1} : \underline{\underline{\Sigma}} - (\underline{\underline{C}}_{hom}^{lim})^{-1} : \int_{\phi=0}^{\phi=2\pi} \int_{\theta=0}^{\theta=\pi} \underline{\underline{B}}_{(\theta,\phi)}^{lim} \cdot \underline{\underline{T}}_{(\theta,\phi)}^V \frac{\sin \theta d\theta d\phi}{4\pi} \\ &= (\underline{\underline{C}}_{hom}^{lim})^{-1} : \underline{\underline{\Sigma}} - \int_{\phi=0}^{\phi=2\pi} \int_{\theta=0}^{\theta=\pi} \underline{\underline{B}}_{(\theta,\phi)}^{\Sigma,lim} \cdot \underline{\underline{T}}_{(\theta,\phi)}^V \frac{\sin \theta d\theta d\phi}{4\pi} \end{aligned} \quad (\text{F.56})$$

where we introduced a third-order influence tensor  $\underline{\underline{B}}_{(\theta,\phi)}^{\Sigma,lim}$ , as

$$\underline{\underline{B}}_{(\theta,\phi)}^{\Sigma,lim} = (\underline{\underline{C}}_{hom}^{lim})^{-1} : \underline{\underline{B}}_{(\theta,\phi)}^{lim} \quad (\text{F.57})$$

Subsequently, we use the expression (F.56) to replace  $\underline{\underline{E}}$ , in the concentration-influence relation (F.51), by  $\underline{\underline{\Sigma}}$ , which results in the relation

$$\begin{aligned} \llbracket \xi \rrbracket_{(\vartheta,\varphi)} &= \underline{\underline{A}}_{(\vartheta,\varphi)}^{lim} : (\underline{\underline{C}}_{hom}^{lim})^{-1} : \underline{\underline{\Sigma}} + \int_{\phi=0}^{\phi=2\pi} \int_{\theta=0}^{\theta=\pi} (\underline{\underline{D}}_{(\vartheta,\varphi,\theta,\phi)}^{lim} - \underline{\underline{A}}_{(\vartheta,\varphi)}^{lim} : \underline{\underline{B}}_{(\theta,\phi)}^{\Sigma,lim}) \cdot \underline{\underline{T}}_{(\theta,\phi)}^V \frac{\sin \theta d\theta d\phi}{4\pi} \\ &= \underline{\underline{A}}_{(\vartheta,\varphi)}^{\Sigma,lim} : \underline{\underline{\Sigma}} + \int_{\phi=0}^{\phi=2\pi} \int_{\theta=0}^{\theta=\pi} \underline{\underline{D}}_{(\vartheta,\varphi,\theta,\phi)}^{\Sigma,lim} \cdot \underline{\underline{T}}_{(\theta,\phi)}^V \frac{\sin \theta d\theta d\phi}{4\pi} \quad \forall \begin{cases} \vartheta \in [0; \pi], \\ \varphi \in [0; 2\pi] \end{cases} \end{aligned} \quad (\text{F.58})$$

where we introduced the third-order influence tensor  $\underline{\underline{A}}_{(\vartheta,\varphi)}^{\Sigma,lim}$  and the second-order influence tensor  $\underline{\underline{D}}_{(\vartheta,\varphi,\theta,\phi)}^{\Sigma,lim}$  as

$$\underline{\underline{A}}_{(\vartheta,\varphi)}^{\Sigma,lim} = \underline{\underline{A}}_{(\vartheta,\varphi)}^{lim} : (\underline{\underline{C}}_{hom}^{lim})^{-1} \quad (\text{F.59})$$

and

$$\underline{\underline{D}}_{(\vartheta,\varphi,\theta,\phi)}^{\Sigma,lim} = \underline{\underline{D}}_{(\vartheta,\varphi,\theta,\phi)}^{lim} - \underline{\underline{A}}_{(\vartheta,\varphi)}^{lim} : \underline{\underline{B}}_{(\theta,\phi)}^{\Sigma,lim} \quad (\text{F.60})$$

### F.3 Constitutive behavior of viscous interfaces in local, interface-related components

The fluid filling the interfaces is envisioned to exhibit the following behavior. Once fluid sheets start to glide along each other, viscous shear tractions are activated. They are envisioned to be proportional to the time-derivative of the displacement jumps

$$\eta \llbracket \dot{\xi}_t \rrbracket = T_t \quad (\text{F.61})$$

where  $t$  is an index denoting any in-plane component orthogonal to the interface normal  $\underline{\underline{n}}$ , where  $\eta$  denotes a viscosity constant with physical dimension [Stress×Time/Length], and where the partial derivative with respect to time is indicated with a dot

$$\dot{\bullet} = \frac{\partial \bullet}{\partial t} \quad (\text{F.62})$$

In interface normal direction, the fluid is envisioned to prevent the interface from significant opening/closing deformations, accounted for by means of the following glueing conditions

$$[[\xi_n]] = 0 \quad (\text{F.63})$$

#### F.4 Specification of eigtraction-based micromechanics model for viscous interface behavior

As for actual computations, it is beneficial to replace double integrals over all interface orientations by so-called weighted Stroud sums [6]

$$\int_{\varphi=0}^{\varphi=2\pi} \int_{\vartheta=0}^{\vartheta=\pi} \bullet(\vartheta, \varphi) \frac{\sin \vartheta d\vartheta d\varphi}{4\pi} = \sum_{i=1}^{n_o} \omega_i \bullet_i \quad \text{with} \quad \bullet_i = \bullet(\varphi_i, \vartheta_i) \quad (\text{F.64})$$

where  $\omega_i$  with  $i = 1, 2, \dots, n_o$  denotes scalar weights related to  $n_o$  specific orientations, see Tables F.1 and F.2 for orientation angles  $\varphi_i$  and  $\vartheta_i$  as well as for weights  $\omega_i$  related to 15 and to 28 directions, respectively.

Table F.1: 15 Stroud orientations [6]

i	$\vartheta_i$	$\varphi_i$	$\omega_i$
1	$\vartheta_1=1.256637$	$\varphi_1=1.017221$	1/15
2	$\vartheta_2=1.256637$	$\varphi_2=-1.017221$	1/15
3	$\vartheta_3=1.256637$	$\varphi_3=2.124370$	1/15
4	$\vartheta_4=1.256637$	$\varphi_4=-2.124370$	1/15
5	$\vartheta_5=0.628318$	$\varphi_5=1.017221$	1/15
6	$\vartheta_6=0.628318$	$\varphi_6=-1.017221$	1/15
7	$\vartheta_7=0.628318$	$\varphi_7=2.124370$	1/15
8	$\vartheta_8=0.628318$	$\varphi_8=-2.124370$	1/15
9	$\vartheta_9=1.047197$	$\varphi_9=0.364863$	1/15
10	$\vartheta_{10}=1.047197$	$\varphi_{10}=-0.364863$	1/15
11	$\vartheta_{11}=1.047197$	$\varphi_{11}=2.776728$	1/15
12	$\vartheta_{12}=1.047197$	$\varphi_{12}=-2.77672$	1/15
13	$\vartheta_{13}=1.570796$	$\varphi_{13}=0$	1/15
14	$\vartheta_{14}=1.570796$	$\varphi_{14}=1.570796$	1/15
15	$\vartheta_{15}=0$	$\varphi_{15}=0$	1/15

Table F.2: 28 Stroud orientations [6]

i	$\vartheta_i$	$\varphi_i$	$\omega_i$
1	$\vartheta_1=0.955316$	$\varphi_1=0.785398$	$9/280$
2	$\vartheta_2=0.955316$	$\varphi_2=-0.785398$	$9/280$
3	$\vartheta_3=0.955316$	$\varphi_3=2.356194$	$9/280$
4	$\vartheta_4=0.955316$	$\varphi_4=-2.356194$	$9/280$
5	$\vartheta_5=1.317534$	$\varphi_5=0.261799$	$(122+9\sqrt{3})/3360$
6	$\vartheta_6=1.317534$	$\varphi_6=-0.261799$	$(122+9\sqrt{3})/3360$
7	$\vartheta_7=1.317534$	$\varphi_7=2.879793$	$(122+9\sqrt{3})/3360$
8	$\vartheta_8=1.317534$	$\varphi_8=-2.879793$	$(122+9\sqrt{3})/3360$
9	$\vartheta_9=1.317534$	$\varphi_9=1.308996$	$(122+9\sqrt{3})/3360$
10	$\vartheta_{10}=1.317534$	$\varphi_{10}=-1.308996$	$(122+9\sqrt{3})/3360$
11	$\vartheta_{11}=1.317534$	$\varphi_{11}=1.832595$	$(122+9\sqrt{3})/3360$
12	$\vartheta_{12}=1.317534$	$\varphi_{12}=-1.832595$	$(122+9\sqrt{3})/3360$
13	$\vartheta_{13}=0.362218$	$\varphi_{13}=0.785398$	$(122+9\sqrt{3})/3360$
14	$\vartheta_{14}=0.362218$	$\varphi_{14}=-0.785398$	$(122+9\sqrt{3})/3360$
15	$\vartheta_{15}=0.362218$	$\varphi_{15}=2.356194$	$(122+9\sqrt{3})/3360$
16	$\vartheta_{16}=0.362218$	$\varphi_{16}=-2.356194$	$(122+9\sqrt{3})/3360$
17	$\vartheta_{17}=0.802728$	$\varphi_{17}=1.308996$	$(122-9\sqrt{3})/3360$
18	$\vartheta_{18}=0.802728$	$\varphi_{18}=-1.308996$	$(122-9\sqrt{3})/3360$
19	$\vartheta_{19}=0.802728$	$\varphi_{19}=1.832595$	$(122-9\sqrt{3})/3360$
20	$\vartheta_{20}=0.802728$	$\varphi_{20}=-1.832595$	$(122-9\sqrt{3})/3360$
21	$\vartheta_{21}=0.802728$	$\varphi_{21}=0.261799$	$(122-9\sqrt{3})/3360$
22	$\vartheta_{22}=0.802728$	$\varphi_{22}=-0.261799$	$(122-9\sqrt{3})/3360$
23	$\vartheta_{23}=0.802728$	$\varphi_{23}=2.879793$	$(122-9\sqrt{3})/3360$
24	$\vartheta_{24}=0.802728$	$\varphi_{24}=-2.879793$	$(122-9\sqrt{3})/3360$
25	$\vartheta_{25}=1.383547$	$\varphi_{25}=0.785398$	$(122-9\sqrt{3})/3360$
26	$\vartheta_{26}=1.383547$	$\varphi_{26}=-0.785398$	$(122-9\sqrt{3})/3360$
27	$\vartheta_{27}=1.383547$	$\varphi_{27}=2.356194$	$(122-9\sqrt{3})/3360$
28	$\vartheta_{28}=1.383547$	$\varphi_{28}=-2.356194$	$(122-9\sqrt{3})/3360$

## Appendix G

# **Mechanics of organic-inorganic bio-interfaces – Implications for strength and creep properties**

Manuscript prepared for possible publication publication in MRS Bulletin.

**MECHANICS OF ORGANIC-INORGANIC BIO-INTERFACES – IMPLICATIONS FOR STRENGTH AND CREEP PROPERTIES**

Tao Qu, Devendra Verma, Vikas Tomar\*, Mehran Shahidi, Bernhard Pichler, Christian Hellmich

From the biological/chemical perspective, interface concepts related to cell surface/synthetic biomaterial interface and extracellular matrix/biomolecule interface have wide applications in medical and biological technology. Interfaces control biological reactions, provide unique organic microenvironments that can enhance specific affinities, provide self-assembly in the interface plane that can be used to orient and space molecules with precision etc. Interfaces also play a significant role in determining structural integrity and mechanical creep and strength properties of biomaterials. Structural arrangement of interfaces combined with interfacial interaction between organic and inorganic phases in the biomaterial interfaces significantly determines mechanical properties of biological materials, especially the aspect that leads to a unique combination of seemingly “in-consistent” properties, such as fracture strength and tensile strength *both* being high - as opposed to traditional engineering materials, which have high fracture strength linked to low tensile strength and vice-versa. While there has been a tremendous amount of work focused on the effect of structural arrangements on biomaterial properties, both experimental and computational studies of the strength, the deformation, and the viscosity of the interface itself are limited to just a few systems. Even in such studies, the actual interface stress is rarely analyzed, and correlated to the overall material strength. This review provides a focused overview of such studies in hard biological materials, but then provides a new vision on how the results of interfacial molecular studies could be consistently linked to high – scale, micromechanics based perceptions of hierarchical biological materials.

**Keywords:** Biological, stress/strain relationship, bone, strength, creep

**§1 Introduction**

Biological materials have evolved over millions of years and are often found as complex composites with superior properties compared to their relatively weak original constituents. The toughness of spider silk, the strength and lightweight of bamboos, self-healing of bone, high toughness of nacre, and the adhesion abilities of the gecko’s feet are a few of the many examples of high performance biological materials. Hard biomaterials such as bone, nacre, and dentin have

intrigued researchers for decades for their high stiffness, toughness, and self-healing capabilities. Such biological materials have been reviewed in appreciable detail, in the context of their hierarchical structure, material properties, and failure mechanisms.<sup>1-5</sup> Such hard biological materials are not only light weight but also possess high toughness and mechanical strength. In particular, such materials combine two properties which are usually quite contradictory, but essential for the function of these materials. A unique feature that determines properties of such materials is interfacial interaction between organic and inorganic phases in the form of protein (e.g. chitin (CHI) or tropocollagen (TC))-mineral (e.g. calcite (CAL) or hydroxyapatite (HAP)) interfaces. The volume fraction of the protein-mineral interfaces can be enormous as the mineral bits have nanoscale size. For example, in a raindrop size volume of a nanocomposite, the area of interfacial region can be as large as a football field.<sup>6</sup>

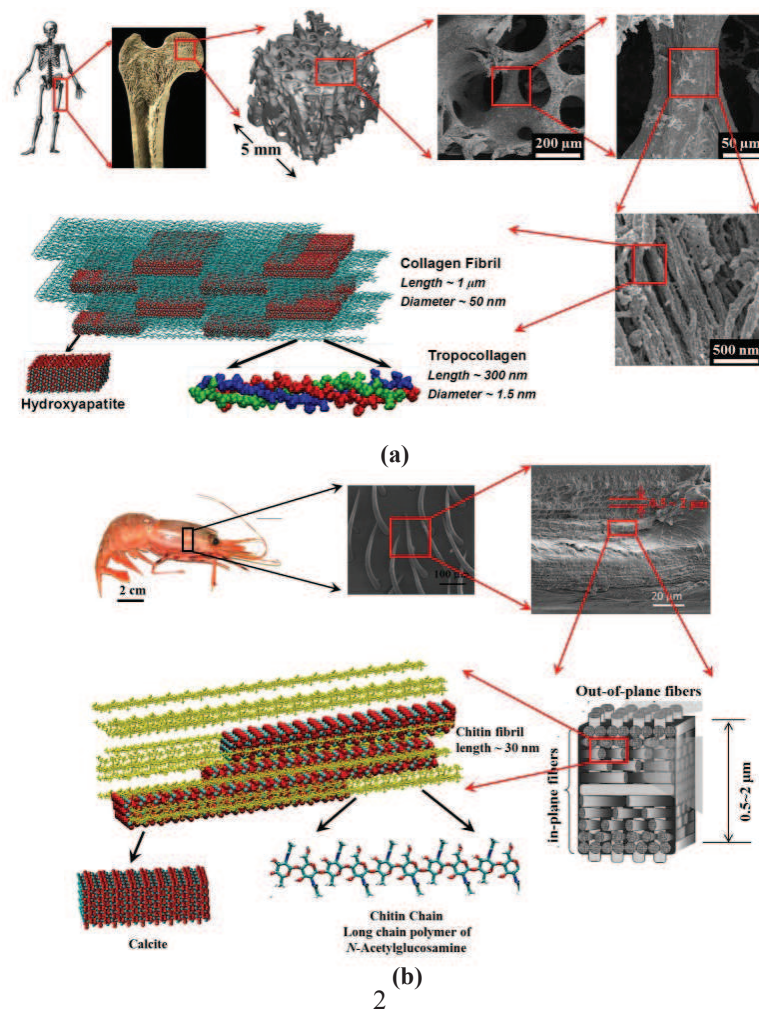


**Figure 1.** A schematic of the hierarchical structure of (a) bone and (b) shrimp exoskeleton

In the structural studies of such biological materials, it is observed that at the mesoscale (~100 nm to few  $\mu\text{m}$ ), the mineral crystals are preferentially aligned along the length of the organic phase polypeptide molecules in a hierarchical (e.g. staggered or Bouligand pattern) arrangement, Fig. 1.<sup>7-11</sup> Interfaces are perceived to play a significant role in the stress transfer and the consequent improvements in stiffness and strength of such material systems. However, how exactly the change in interfacial chemical configuration leads to change in mechanical properties in such materials is a big subject of debate. The length scale and complexity of microstructure of hybrid interfaces in biological materials makes it difficult to study them and understand the underlying mechanical principles, which are responsible for their extraordinary mechanical performance. For this reason the governing mechanisms for the mechanical behavior for such biomaterials is not understood completely. At the same time such building block level understanding is not only important for the evolution of biological materials science but vital to the development of bio-inspired materials. One of the most important aspects of understanding the influence of interfaces on natural material properties is the knowledge of how stress transfer occurs across the organic-inorganic interfaces. Multi-component hierarchical structure of biomaterials results in the organic-inorganic interfaces involved at different length scales, i.e., between the basic components at the nano-scale, between the mineralized fibrils at the micro-scale, and between the layers of the multi-layered structures at micro- or macro-scale. While considerable progress has been made as concerns elastic, poroelastic, strength, or viscoelastic *bulk* properties from the basic constituent scale up to the macroscopic scale of bone<sup>79-82</sup> or invertebrate exoskeleton<sup>83</sup>, the authors are not aware of any studies that have been able to quantify the magnitude of interfacial stress in such materials and its correlation with material strength and creep. However, recent progress in materials science and mechanics which we will review in the following, brings us very close to identification of the aforementioned interfacial properties. The article will then culminate in the probably first bottom-up and top-down estimations of interfacial stresses occurring in the extrafibrillar matrix of bone, revealing a pronounced thixotropy of this hierarchical biological composite behavior – a property described for many material systems<sup>79-83</sup>, but only rarely described in biological materials so far.

## §2 Understanding Interface Mechanics by means of Molecular Simulations – Review

Several experimental studies have been performed to understand mechanical behavior of bone and similar hard biological materials at nanoscale.<sup>15,27,51-54</sup> However, till date experiments have not yet measured interface strength at the nanoscale interfaces in such materials as a function of interface deformation properties. As pointed out in the earlier section, such measurements are extremely important for reliable material behavior prediction at macroscale. In the absence of such experiments, molecular simulation based models can play an important role in predicting interface deformation and interface strength affected material behavior. The mechanical behavior of bone with a view to understand the role of TC molecules and HAP mineral has been earlier analyzed using experiments, modeling, and simulations based on Molecular dynamics (MD) based schemes. Molecular simulation based studies to explicitly calculate interface stress in biological materials are limited. Dubey and Tomar<sup>55</sup> have performed 3-D *ab initio* MD (AIMD) simulations to understand atomic interactions in selected TC-HAP interfaces under tensile loading. However, AIMD simulations have limited length scales. Recent work by Dubey and Tomar<sup>56-60</sup>, presents a mechanistic understanding of interfacial interactions in idealized TC and HAP interfacial biomaterials as a function of hierarchy. A three dimensional atomistic modeling framework is developed which combines both organic and inorganic cells together to form supercells as shown in Fig. 4. Both tensile and compressive loading directions were considered. For failure analysis, TSC model<sup>45,61</sup> was used to estimate the interfacial shear strength and fracture localization zone width.

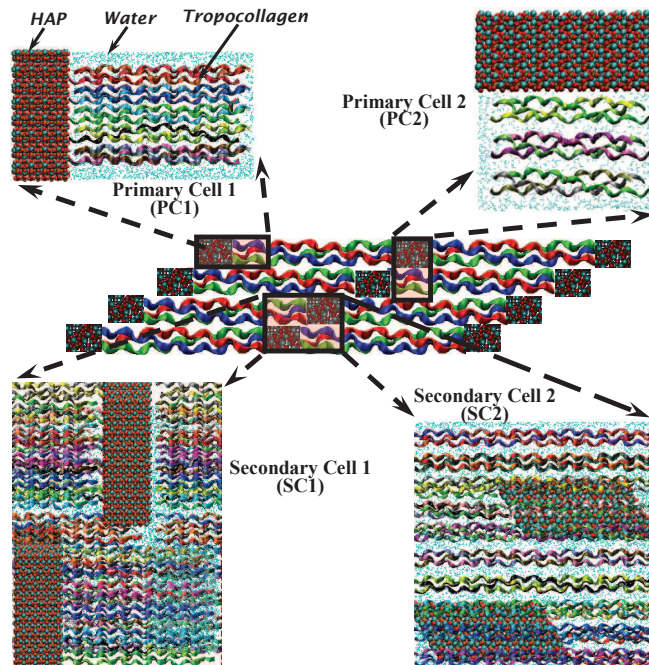


**Figure 2.** A schematic showing the derivation of PC1, PC2, SC1, and SC2 cells from the staggered and layered assembly. In PC1 and SC1 cells, tropocollagen molecules are aligned in a direction parallel to the c-axis of hydroxyapatite crystals. In PC2 and SC2 cells, tropocollagen molecules are aligned in a direction normal to the longitudinal c-axis of hydroxyapatite super cell. Dimensions of hydroxyapatite crystals are approximately the same in all cells. Tropocollagen molecules are all shown in multi-color segments and water molecules are shown in cyan.

The analyses confirm that relative alignment of TC molecules with respect to the HAP mineral surface such that the interfacial contact area is maximized, along with optimal direction of applied loading with respect to the TC-HAP interface orientation are important factors that contribute to making nanoscale staggered arrangement a preferred structural configuration in such biological materials. The analyses also point out that such an arrangement results in higher interfacial strength as well as higher fracture strength. In addition, such TC-HAP nanocomposite shows toughening and strain hardening behavior, which is attributed to the reconstitution of Columbic interactions between TC and HAP at the interface during sliding. The dominant tensile

failure mechanism at the HAP-TC interface is simply the interfacial separation of TC and HAP without significant initial HAP deformation, Fig. 5.

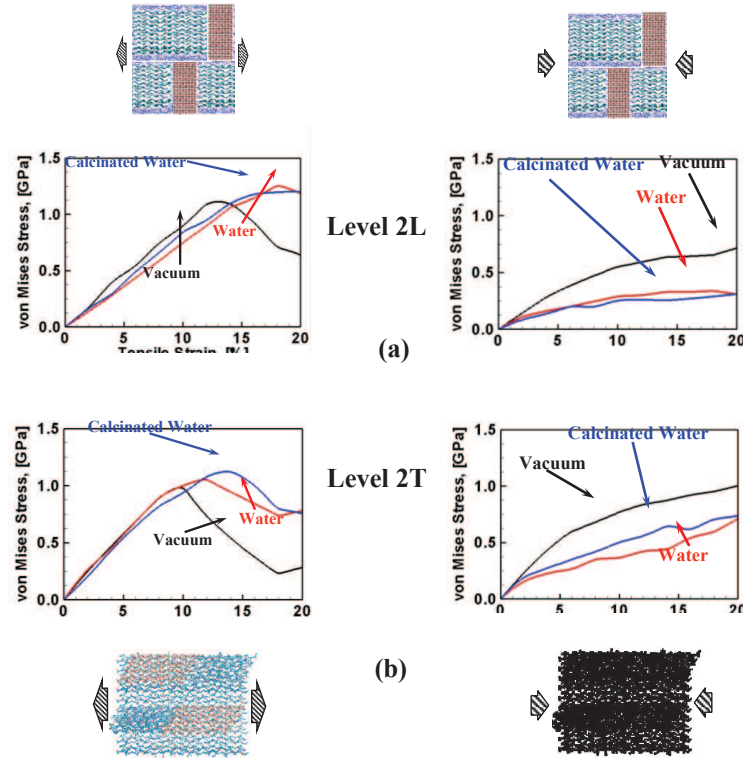


**Figure 3.** Tensile and compressive von Mises stress Vs. strain plots as a function of chemical environment in the case of (a) supercell Layer 2L loaded in longitudinal direction, (b) supercell Level 2T loaded in transverse direction

The  $\text{NH}_3^+$  and  $\text{COO}^-$  groups in TC molecules are strongly attracted to the ions in HAP surface ( $\text{Ca}^{2+}$ ,  $\text{PO}_4^{3-}$  and  $\text{OH}^-$  ions) <sup>(62)</sup>. Since TC is a flexible chain like molecule it elongates on applied deformation but cleaves off after the point when it is fully stretched. Such cleavage results in local nanoscale interfacial failure. Most biological materials in physiological systems contain water as one of their constituents. It has been observed that the presence of water molecules in the TC-HAP biocomposites enhanced overall composite mechanical strength (Fig. 5 (a)), <sup>(57)</sup>. This is attributed to water molecule's affinity for charged surfaces, such as HAP surface, <sup>(62)</sup>, and  $\text{NH}_3^+$  and  $\text{COO}^-$  groups in TC, owing to its polar nature and capability of make strong hydrogen bonds. As a result, water acts as an electrostatic bridge between HAP surface

and TC molecules and strengthens the TC-HAP interface. This strengthening especially plays an important role whenever there is a relative sliding occurs between HAP surface and TC molecules at the interface. Previous studies have shown that hydration has a stabilizing effect on the collagen triple helix<sup>63</sup>, and solvated TC molecule requires more energy to untie from the HAP surface.<sup>64</sup> Similar interaction behavior of water at protein-mineral interface is found in nacre as well.<sup>65,66</sup> It also acts as glue between TC-TC interactions<sup>67</sup>, and thereby, delays the failure of the overall system. Another interesting finding emerged out of a comparison between stress-strain curves for two different hierarchical levels is that the failure of such biocomposites is predominantly strain dependent and not a function of ultimate strength.

Bone diseases such as Osteogenesis Imperfecta are marked by extreme bone fragility and are associated with point mutations in the tropocollagen molecule. Also, there is been a debate as to whether the HAP crystals in bone tissues are plate shaped or needle shaped. Hence, a further investigation into the effect of change in mineral crystal shape and effect of change in TC residue sequences on the mechanical strength of TC-HAP biomaterials was performed. Results show that TC-HAP interface shear strength increases as the side group complexity and heterogeneity of residues increases in the TC-HAP nanocomposite, and the plate shaped crystals are overall better in resisting load as compared to needle shaped HAP crystals case.<sup>68</sup> However, the effect of change in mineral crystal morphology has a stronger effect on the mechanical strength of the TC-HAP biocomposites, as compared to change in TC residue sequences.<sup>60</sup> This suggests that probably mutations in TC manifest its effect by changing the mineral crystal morphology and distribution during nucleation and growth period over the lifetime of the animal.

### **§3 Molecular Mechanics targeting at interface stresses – novel results**

While the studies discussed so far have focused on role of interface related mechanisms in determining overall mechanical deformation properties, the real aspect of stresses at interfaces while the mechanical deformation is going on still remains unaddressed. As pointed out earlier, important questions are: For a given peak tensile strength of a given material how much is attributed to interface strength? What is the contribution of interface sliding in time dependent deformation observed in a simple tension test of a given material sample? Recently simulation performed by Qu and Tomar<sup>44</sup> have pointed out some important aspects in answering such

questions. Figure 6 shows a schematic of the type of interfacial systems analyzed. CHI and TC molecules are embedded in-between CAL and HAP platelets, respectively. Such interfaces are then deformed under tensile and shear modes using established non-equilibrium molecular dynamics (NEMD) and steered molecular dynamics (SMD) schemes with focus on measuring their shear strength in two separate deformation modes.

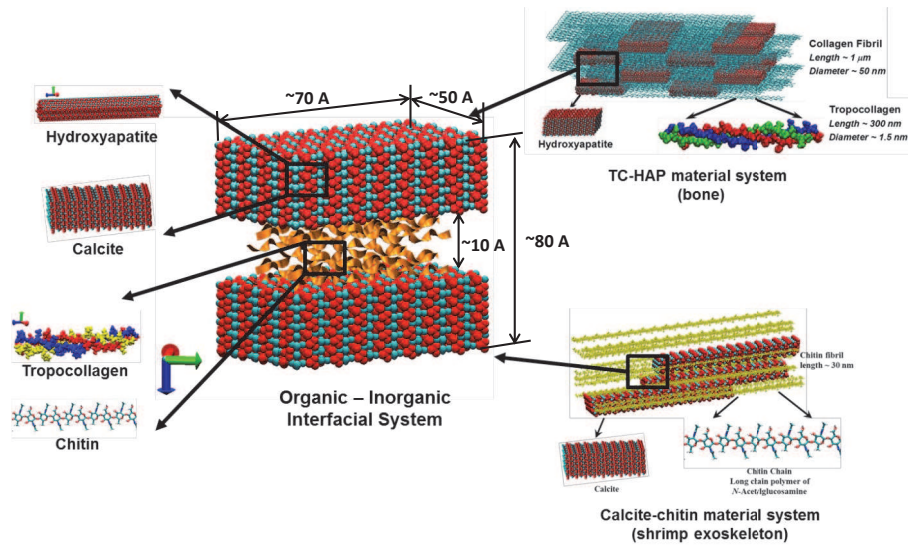


**Figure 4.** A schematic showing configuration of TC-HAP and CHI-CAL interfaces analyzed

In order to analyze the effect of hydration on interface stress, water (WT) molecules are added to the interface region. The interface separation in Figs. 3-(c) and 3-(d) is chosen so as to have one layer of TC (or CHI) molecules in the interface region. Due to computational infeasibility of performing atomistic analysis of supercells with full-length TC (or CHI) molecules, only a segment of TC (or CHI) full-length molecule is used in the supercells. Stress-strain curve information is generated based on the well-known virial stress formulation using NEMD simulations. There are 2 loading directions (Fig. 6): direction along the molecule length ( $x$ -axis) and direction transverse to molecule length ( $y$ -axis). The simulated supercells are divided into slabs and three diagonal components of the pressure tensor in each slab are given in output, Fig. 7. The virial stress tensor of each slab and the overall system at the end of the equilibration is recorded as the stress tensor up to the point 20 % strain is achieved. The procedures make it possible to estimate how the measured stress of the loaded material system is

distributed inside its interfacial regions and the stress between the interfaces can be obtained according to the behavior of the corresponding slab of the simulation system, Fig. 7-(b).

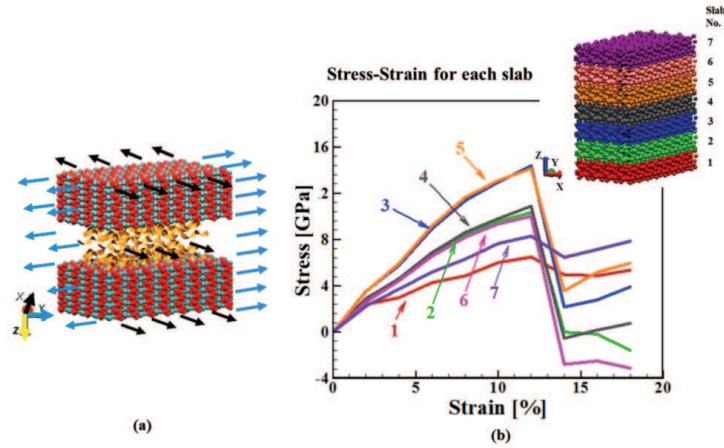


**Figure 5.** (a) A schematic showing of loading condition of the interfacial material system, (b) stress-strain curve for each slab of the system from the bottom to the top layer.

NEMD simulations using the procedure shown in Fig. 7 predict interface strength by way of measuring stress-strain behavior of a thin block of atoms that are contained in the interfacial region. Such simulations cannot predict the effect of interface strength on interface separation mechanism. In order to understand such SMD simulations are performed. SMD simulations in the constant speed mode<sup>69</sup>, were used to pull out the upper inorganic crystals (HAP or CAL) from the substrate inorganic crystals (HAP or CAL) in order to replicate the interfacial sliding process. Similar to the case of NEMD simulations, there are 2 loading directions: direction along the molecule length ( $x$ -axis) and direction transverse to molecule length ( $y$ -axis). SMD force was applied to the center of mass of upper inorganic crystals in a chosen direction. The organic molecules (TC or CHI) and water molecules in the interface region were not under constraint. The substrate inorganic crystals were fixed on the bottom. In order to quantify the interface sliding process and failure in the interface region, a viscoplastic model<sup>70</sup>, for interfacial sliding is introduced. The viscoplastic failure of the interfaces relates to the applied shear stress,  $\tau$ , and to the shear velocity gradient (rate of shear deformation),  $\frac{\partial V}{\partial d}$ , after the yield stress,  $\tau_0$ , is reached, as

$$\tau = \tau_0 + \mu \frac{\partial V}{\partial d} . \quad (1)$$

Here,  $\mu$  is the shear viscosity of interfacial sliding and  $d$  is defined in Fig. 8.

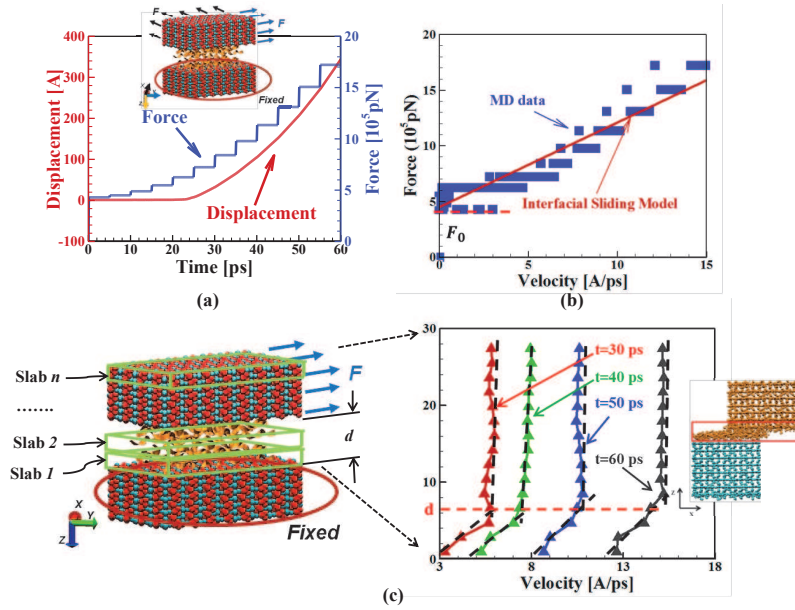


**Figure 6.** (a) SMD force and displacement of the SMD structure as a function of time with a schematic showing of loading condition of the SMD in constant force pulling mode, (b) curve fitting of the MD data with the viscoplastic model, (c) velocity profile at different time steps.

In order to study the effect of shear rate on the viscous behavior of the interfacial systems, different magnitude of force increment was only applied to the HAP-TC-HAP (and CAL-CHI-CAL) system with one layer of TC (and CHI) molecules due to the limited space to perform the interfacial sliding with different shear rate. The shear viscosity of the HAP-HAP interface (Fig. 6) is calculated as  $0.0232 \text{ Pa s}$ . The viscosity of the slurries of HAP was reported as  $\sim 0.01 - 1.6 \text{ Pa s}$  earlier by experiments performed<sup>71</sup>, and the viscosity of montmorillonite hydrate was reported as  $\sim 0.008 \text{ Pa s}$  by MD simulations.<sup>72</sup> The thickness of the interface region,  $d$ , can be determined from the plot. The yield shear stress,  $\tau_Y$ , is calculated from the critical force,  $F_0$ , obtained by the curve fitting, and the interfacial area,  $A$ . The failure shear stress,  $\tau_F$ , is calculated from the interface separation force divided by the interfacial area,  $A$ .

Shear stress plays an important role in the failure of examined TC-HAP and CAL-CHI composite supercells. The lower and the upper bound of the shear strength of the interfacial material systems with organic interfaces or water interfaces could be defined by the yield shear stress,  $\tau_Y$ , and the failure stress,  $\tau_F$ , which are used to characterize the plastic shear deformation, where  $\tau_Y < \tau_F$ . Fig. 9-(a) displays the yield shear stress ( $\tau_Y$ ) calculated using SMD, failure stress ( $\tau_F$ ) calculated using SMD, interfacial shear strength of each of the TC-HAP interfacial material system shown in figure calculated using NEMD ( $\sigma_I$ ), shear strength of the organic TC phase region (or region of HAP cells with WT) ( $\sigma_3$ ) calculated using NEMD, and tensile mechanical strength of the organic phase region (or region of HAP cells with WT) ( $\sigma_4$ ) calculated using NEMD, as a function of the interfacial components.

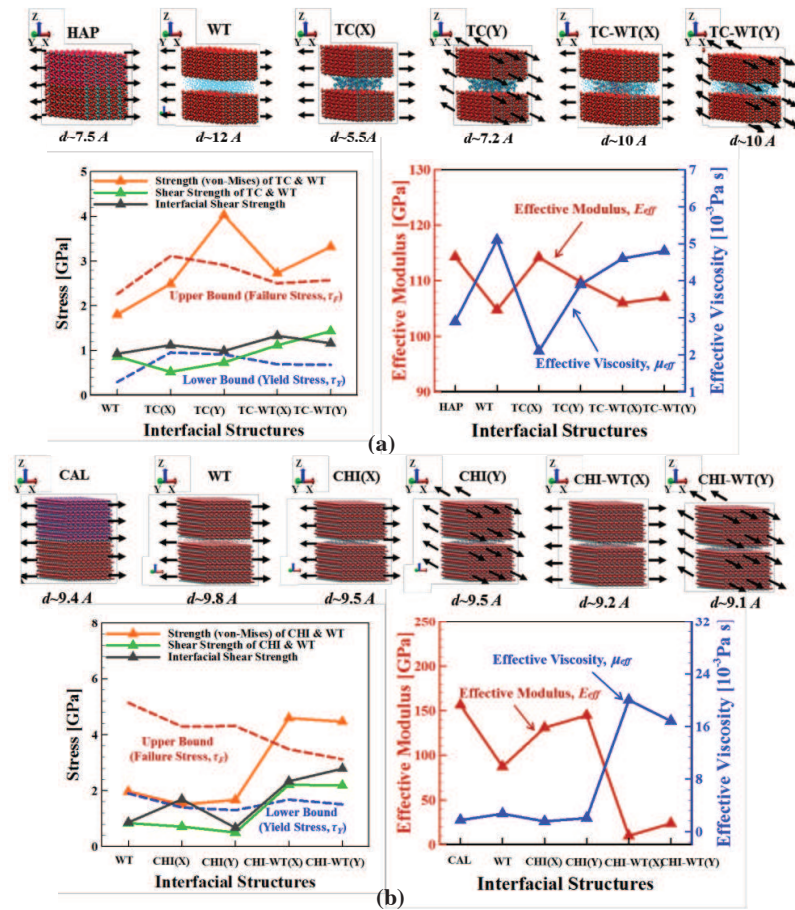


**Figure 7.** Stress, Young’s modulus and effective viscosity as function of interfacial structures in the case of **(a)** TC-HAP interfaces and **(b)** CAL-CHI interfaces.

Fig. 9-(a) also compares effective viscosity and Young’s moduli as a function on type of interfaces. The HAP supercell consists of two HAP cells placed over each other separated by layer distance corresponding to  $\text{PO}_4$  using in planes (7.5 Angstroms). The WT supercell consists of the same HAP supercells but with now water molecules separating the two. Fig. 9-(b) shows similar results in the case of CHI-CAL interfaces. In this case, the CAL supercell consists of two CAL cells placed over each other separated by layer distance corresponding to  $\text{PO}_4$  using in planes (9.4 Angstroms). The WT supercell consists of the same CAL supercells but with now water molecules separating the two.

Perhaps not surprisingly, the behavior of the two types of interfacial systems is quite similar to each other. The shear strength of organic phase (green line,  $\sigma_3$ ) lies around the lower bounded line of the yield shear stress (blue dotted line,  $\tau_y$ ). The organic phases is the main contributor of the interfacial shear strength based on Fig. 9-(a) where the interfacial shear strength (grey line,  $\sigma_I$ ) matches closely with, sometimes a little higher than, the shear strength of the organic phases (green line,  $\sigma_3$ ). However, it is always below the upper bounded line defined by the failure stress (red dotted line,  $\tau_F$ ) which initiating the “catastrophic failure” of the interfaces. The mechanical strength of the organic phases (yellow line,  $\sigma_4$ ) usually lies between the lower and upper bounded line because shear deformation is usually the main contributor of the mechanical behavior of organic phases. Those points which are beyond the upper bound are in the cases of the hydrated organic interfaces (i.e. TC-WT or CHI-WT). This could be attributed to the much higher contribution of the shear interaction to the overall behavior as well as the higher shear viscosity of the interfacial material systems.

Whatever differing mechanisms observable in the different investigated systems, all interfacial shear viscosities reported for the HAP-TC-HAP system are on the order of  $10^{-2} \text{ Pa s}$ . The question arises whether this value is realistic – or how it may be checked or validated by independent computational or experimental results. This is dealt with next.

#### **§4 Continuum micromechanics top-down access to interface viscosity of HAP-water-HAP system**

In a series of papers<sup>79-82</sup>, it has been shown how “universal” mechanical properties of bone’s elementary constituents (hydroxyapatite, collagen, water with non-collagenous organics), their “universal” interaction patterns across multiple length scales, and corresponding “universal” composition rules for extracellular bone matrices allow for the prediction of the large variety of mechanical properties of different bone tissues observed at the macroscopic scale. In this context, the viscoelasticity of interface-penetrated extrafibrillar mineral clusters (see Figure 8© for the mineral cluster phases, where each of them is envisioned as interface-penetrated continuum as seen in Figure 9) were identified from downscaling of different, independent macroscopic creep tests: they can be characterized by Kelvin-Voigt parameters: a viscosity of  $\eta_{KV} = 1.34 \times 10^5$  GP.s, and spring constant of  $\mu_{KV} = 179$  MPa. We here expand on how to further downscale this bulk viscosity value further, to the level of the individual interfaces (appearing as phases in Figure 9).

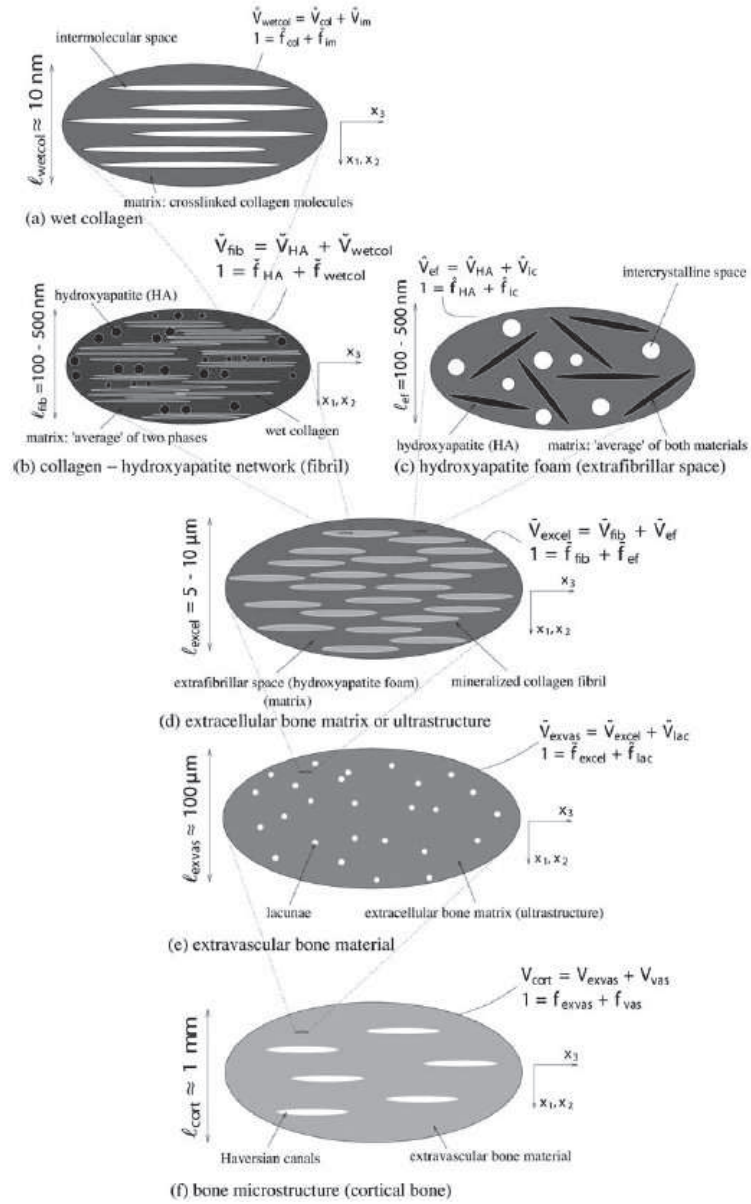


**Figure 8.** Micromechanical representation of bone material by means of a six-step homogenization scheme<sup>80</sup>

Therefore, we employ the recently established matrix-interface representation of hydrated creeping materials depicted in Figure 2<sup>84</sup>. Such materials are transversely isotropic, exhibiting the following creep function tensor

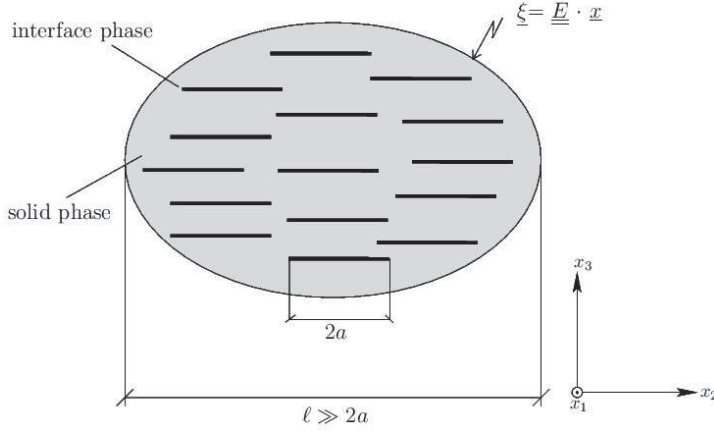


**Figure 9.** 2D flat, parallel, spherical interfaces embedded in a linear elastic solid matrix; 2D sketch of a 3D representative volume element

$$\underline{\underline{J}}_{\text{aniso}} = \underline{\underline{C}}^{-1} + \frac{4d(1-\nu_s)}{3\mu_s(2-\nu_s)} \left[ 1 - \exp\left(\frac{-t}{\tau_{\text{creep}}}\right) \right] \underline{\underline{I}}_{\text{aniso}} \quad (2)$$

with  $\underline{\underline{J}}_{\text{aniso}}$  standing for an anisotropic fourth-order creep compliance tensor,  $\underline{\underline{C}}^{-1}$  standing for the inversion of fourth-order elastic solid matrix,  $\underline{\underline{I}}_{\text{aniso}}$  standing for an anisotropic fourth-order identity tensor,  $\mu_s$  standing for shear modulus of elastic solid matrix,  $\nu_s$  standing for the Poisson's ratio of elastic solid matrix, and  $(\tau_{\text{creep}} = a\eta_i 8(1-\nu_s)/(\mu_s 3\pi(2-\nu_s)))$  standing for the creep characteristic time. Interaction of various such polycrystals is considered through the Reuss average over all spatial orientations, leading to the following isotropic creep function

$$\underline{\underline{J}}_{\text{iso}} = \int_{\phi=0}^{\phi=2\pi} \int_{\theta=0}^{\theta=\pi} \underline{\underline{J}}_{\text{aniso}} \frac{\sin\theta d\theta d\phi}{4\pi} = \frac{1}{3k_s} \underline{\underline{I}}_{\text{vol}} + \frac{1}{2} \left[ \frac{1}{\mu_s} + \frac{32d(1-\nu_s)}{15\mu_s(2-\nu_s)} \left\{ 1 - \exp\left(\frac{-t}{\tau_{\text{creep}}}\right) \right\} \right] \underline{\underline{I}}_{\text{dev}} \quad (3)$$

$\underline{\underline{I}}_{vol}$  and  $\underline{\underline{I}}_{dev}$  denote the volumetric and the deviatoric part of the symmetric fourth-order identity tensor. Analogy between this matrix-interface creep function and the standard Kelvin-Voigt creep function, reveals the following identities,

$$\frac{1}{\mu_{KV}} = \frac{32d(1-\nu_s)}{15\mu_s(2-\nu_s)} \Rightarrow d = \frac{\mu_s}{\mu_{KV}} \frac{15(2-\nu_s)}{32(1-\nu_s)}, \quad \eta_{KV} = \frac{5a\eta_i}{4\pi d} \Rightarrow \eta_i = \frac{4\pi d\eta_{KV}}{5a}$$

(4)

Accounting, in addition, for the shear modulus and the Poisson's ratio of hydroxyapatite,  $\mu_s = 44.9$  GPa and  $\nu_s = 0.24$ , yields the interface density parameter as  $d = 0.271$  and the interface viscosity as  $\eta_i = 1.83 \times 10^{12}$  GPa·s·m<sup>-1</sup>. In order to finally retrieve the bulk viscosity related to the fluid *within* the interfaces, we multiply  $\eta_i$  by the interface thickness of 1 nm, yielding  $\eta_{WT} = 1.83 \times 10^{12}$  Pa·s. This value is by 14 orders of magnitude larger than the corresponding value obtained from the MD simulations.

How can this be explained? The most straightforward answer relates to the sliding speed of the involved crystals, with the water interface in between: The MD-based dislocation speed amounts to  $4 \times 10^1$  m/s, while the typical interface dislocation speeds can be determined from relaxation experiments carried out in the framework of three-point bending tests on bone<sup>91</sup>. The initial maximum normal stress in these tests amounts to 32.6 MPa<sup>81</sup>. The corresponding maximum shear stresses act in planes that are inclined by 45° with respect to the cross-sections of the beam, and they are by a factor of 2 smaller than the maximum normal stress<sup>88</sup>, i.e. maximum shear stresses amount to 16.3 MPa and they refer to the tissue scale. Typical stress concentration factors from the tissue scale down to the mineral scale range from 1.5 to 2.8<sup>90,89,14,80</sup>. This yields matrix-interface composite-related shear stresses ranging from 24 MPa to 45 MPa. At the time instant of sudden loading, microscopic interface shear tractions  $T$  are *equal* to the shear stresses imposed on the matrix-interface composite, at the time instant of sudden loading<sup>84</sup>. The interface tractions  $T$  are related to dislocation rates  $[\dot{\xi}]$  via the following viscous interface law

$$T = \eta_i[\dot{\xi}] \Rightarrow [\dot{\xi}] = \frac{T}{\eta_i} \quad (5)$$

Eq. (5) specified for interface tractions  $T$  ranging from 24 MPa to 45 MPa and for the interface viscosity amounting to  $\eta_i = 1.83 \times 10^{12} \text{ GPa}\cdot\text{s}\cdot\text{m}^{-1}$  suggests that the maximum dislocation rates range from  $5.3 \times 10^{-15} \text{ m/s}$  to  $8.3 \times 10^{-15} \text{ m/s}$ , and this is by 16 orders of magnitude smaller than the dislocation rate in the MD simulations. The effect of such huge difference in corresponding shear rates felt by the viscous fluid inside the interfaces qualifies as the main candidate for explaining the viscosity changes: In fact, it is experimentally known for a number of different materials<sup>85, 86, 87</sup>, that increasing shear rates lead to decreased viscosities (or thinning) of viscous materials. Hence, the mismatch between MD and downscaled results for the viscosity of water trapped between hydroxyapatite crystals does not reveal any fundamental shortcomings of any of these methods, but rather elucidates the low speed-enhanced, very “glassy” state of the water interfaces under physiological loading conditions.

#### §6 Comparison of MD results to experimental interface data

The viscosities obtained from our MD simulations are much lower than the experimental results; those could be on the order of  $10^5 \text{ Pa}\cdot\text{s}$ <sup>73,74</sup> for the material of collagen gels. The much higher shear rates in MD simulation lead to the measured lower viscosity values. Considered as the Newtonian fluid behavior, the shear rate ( $\dot{\gamma}$ ) dependency of the viscosity ( $\mu$ ) of polymeric molecular structure is quite sensitive, i.e. increasing sharply as the shear rate decreases.<sup>75,76</sup> Due to the computational capability of MD simulation, different shear rates varying from  $10^7$  to  $10^9$  1/sec were performed on the HAP-TC-HAP system with one layer of TC molecules. Fitting with the widely used power law relation

$$\mu = B\dot{\gamma}^{n-1}, \quad (2)$$

with the parameters  $B=42.49 \text{ Pa}\cdot\text{s}$  and  $n=0.7034$ , however, it is still not enough to capture the full picture of the viscosity-shear relationship because shear rate is still much higher than that used in creep or stress relaxation experiments (i.e.  $10^{-6}$  to  $10^{-2}$  1/sec<sup>75,77</sup> which is too low to be generated using MD simulation). The current study reports the viscous behavior of the bio interface systems at the infinite shear rate which can be used to estimate the properties beyond

the observation range together with the material intrinsic property, i.e. zero-shear viscosity,  $\mu_0$ , using the extrapolation methods, such as the cross model<sup>75,77</sup>,

$$\mu = \mu_{\infty} + \frac{\mu_0 - \mu_{\infty}}{1 + (C\dot{\gamma})^m} \quad (7)$$

Where  $\mu_{\infty}$  is the infinite shear viscosity obtained from the MD simulation, C is the cross time constant and m is known as the cross rate constant. With the viscosities of collagen materials at the lower shear rate from previous studies<sup>73,74,78</sup> and our infinity shear rate viscosity, the cross model parameters are obtained as C=3845.7 s and m=2.002. Fig. 10 displays the viscosity versus shear rate behavior as a plot of  $\log(\mu)$  versus  $\log(\dot{\gamma})$ . The cross model extrapolation captures the significant shear thinning behavior of the material within the low shear rate region and gives the idea of upscaling the MD viscosity results with the decreasing of the shear rate. The overall shear rate dependent viscous behavior of the material is predicted with the combination of the cross model and MD simulations.

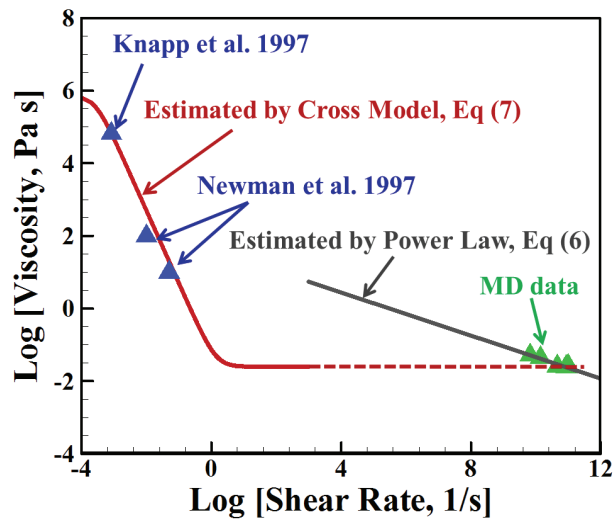


**Figure 10.** Plot showing viscosity as a function of shear rate

## §5 Summary

Hard biological materials such as nacre, bone, and marine crustacean exoskeletons exhibit remarkable mechanical performance despite the fact that they are made up of relatively weaker constituents. In terms of the underlying mechanical principles for structural design of such materials, quite a few have been suggested. For example, one principle is the alignment of mineral-protein interfaces along the loading directions. MD study of TC-HAP biomaterials shows that a composite is best poised to handle the load if the protein molecules are in contact with mineral crystals having their longitudinal axis parallel to the mineral surface and along the loading direction of the composite. Second principle is the staggered arrangement of hard mineral crystals in soft protein matrix, leading to a unique mechanism of load transfer where crystals bear the normal load and protein transfers the load via shear. Third principle is that the failure of such polymer-ceramic type composites is dominantly peak strain dependent instead of peak strength. Also, presence of moisture at the interface enhances the stability and strength of such biomaterials by supporting the cross linking mechanism due to polar nature of water molecule.

One common feature which strongly stands out in most hard biological materials structures presence of interfaces at multiple levels of hierarchy. It seems that nature has designed these interfaces for optimum multifunctional performance during the course of evolution. Interfacial forces play key role during deformation and failure of such biomaterials. Inorganic phases in the material systems carry the uniaxial tensile loading while the organic phases mainly carry the shear loading. Organic interfacial systems exhibit plastic shear deformation, the yield and failure shear stress define the lower and higher bound of the interfacial strength. Shear viscosity of the interfacial systems shows a highly shear rate dependent behavior, however, the full picture of this behavior cannot be captured using MD simulation without the assistance from experimental technique and the extrapolation estimation. Interfacial interaction between the soft phase and hard phase is responsible for redistribution of stresses and directly affects the toughness and strength of the natural materials. Further, the design of the organic-inorganic interface along with the critical length of mineral constituent also contributes potentially in strengthening the biomaterials against failure and in affecting their overall mechanical performance.

## 5. References

- 1 Fratzl, P. & Weinkamer, R. Nature's hierarchical materials. *Progress in Materials Science* **52**, 1263-1334 (2007).
- 2 Meyers, M. A., Chen, P. Y., Lin, A. Y. M. & Seki, Y. Biological materials: Structure and mechanical properties. *Progress in Materials Science* **53**, 1-206, doi:10.1016/j.pmatsci.2007.05.002 (2008).
- 3 Rho, J. Y., Kuhn-Spearing, L. & Zioupos, P. Mechanical properties and the hierarchical structure of bone. *Medical Engineering & Physics* **20**, 92-102 (1998).
- 4 Launey, M. E. & Ritchie, R. O. On the Fracture Toughness of Advanced Materials. *Advanced Materials* **21**, 2103-2110, doi:10.1002/adma.200803322 (2009).
- 5 Dubey, D. K. & Tomar, V. Role of molecular level interfacial forces in hard biomaterial mechanics: a review. *Annals of Biomedical Engineering* **38**, 2040-2055 (2010).
- 6 Vaia, R. Polymer nanocomposites: status and opportunities. *MRS Bulletin(USA)* **26**, 394-401 (2001).
- 7 Landis, W. J. *et al.* Mineralization of collagen may occur on fibril surfaces: evidence from conventional and high-voltage electron microscopy and three-dimensional imaging. *Journal of Structural Biology* **117**, 24-35 (1996).
- 8 Landis, W. J., Hodgens, K. J., Arena, J., Song, M. J. & McEwen, B. F. Structural relations between collagen and mineral in bone as determined by high voltage electron microscopic tomography. *Microscopy Research and Technique* **33**, 192-202 (1996).
- 9 Fratzl, P., Fratzlzelman, N., Klaushofer, K., Vogl, G. & Koller, K. Nucleation and growth of mineral crystals in bone studied by small-angle X-ray scattering. *Calcified Tissue International* **48**, 407-413 (1991).
- 10 Weiner, S., Talmon, Y. & Traub, W. Electron diffraction of mollusc shell organic matrices and their relationship to the mineral phase. *International Journal of Biological Macromolecules* **5**, 325-328 (1983).
- 11 Al-Sawalmih, A. *et al.* Microtexture and chitin/calcite orientation relationship in the mineralized exoskeleton of the American lobster. *Advanced functional materials* **18**, 3307-3314 (2008).
- 12 Peterlik, H., Roschger, P., Klaushofer, K. & Fratzl, P. From brittle to ductile fracture of bone. *Nature Materials* **5**, 52-55 (2006).
- 13 Dubey, D. K. & Tomar, V. Microstructure dependent dynamic fracture analyses of trabecular bone based on nascent bone atomistic simulations. *Mechanics Research Communications Special Issue on Multiscale Modeling* **35**, 24-31 (2008).
- 14 Gupta, H. S. *et al.* Cooperative deformation of mineral and collagen in bone at the nanoscale. *Proceedings of the National Academy of Sciences of the United States of America* **103**, 17741-17746, doi:10.1073/pnas.0604237103 (2006).
- 15 Gupta, H. S. *et al.* Nanoscale deformation mechanisms in bone. *Nano Letters* **5**, 2108-2111 (2005).
- 16 Jackson, A. P., Vincent, J. F. V. & Turner, R. M. The Mechanical Design of Nacre. *Proceedings of the Royal Society of London Series B-Biological Sciences* **234**, 415-& (1988).
- 17 Smith, B. L. *et al.* Molecular mechanistic origin of the toughness of natural adhesives, fibres and composites. *Nature* **399**, 761-763 (1999).
- 18 Sumitomo, T., Kakisawa, H., Owaki, Y. & Kagawa, Y. In situ transmission electron microscopy observation of reversible deformation in nacre organic matrix. *Journal of Materials Research* **23**, 1466-1471, doi:10.1557/jmr.2008.0184 (2008).
- 19 Wang, R. Z., Suo, Z., Evans, A. G., Yao, N. & Aksay, I. A. Deformation mechanisms in nacre. *Journal of Materials Research* **16**, 2485-2493 (2001).
- 20 Barthelat, F., Tang, H., Zavattieri, P. D., Li, C. M. & Espinosa, H. D. On the mechanics of mother-of-pearl: A key feature in the material hierarchical structure. *Journal of the Mechanics and Physics of Solids* **55**, 306-337, doi:10.1016/j.jmps.2006.07.007 (2007).

- 21 Currey, J. D. Mechanical-Properties of Mother of Pearl in Tension. *Proceedings of the Royal Society of London Series B-Biological Sciences* **196**, 443-& (1977).
- 22 Barthelat, F., Li, C. M., Comi, C. & Espinosa, H. D. Mechanical properties of nacre constituents and their impact on mechanical performance. *Journal of Materials Research* **21**, 1977-1986, doi:10.1557/jmr.2006.0239 (2006).
- 23 Menig, R., Meyers, M. H., Meyers, M. A. & Vecchio, K. S. Quasi-static and dynamic mechanical response of *Haliotis rufescens* (abalone) shells. *Acta Materialia* **48**, 2383-2398 (2000).
- 24 Bruet, B. J. F. *et al.* Nanoscale morphology and indentation of individual nacre tablets from the gastropod mollusc *Trochus niloticus*. *Journal of Materials Research* **20**, 2400-2419, doi:10.1557/jmr.2005.0273 (2005).
- 25 Li, X. D., Chang, W. C., Chao, Y. J., Wang, R. Z. & Chang, M. Nanoscale structural and mechanical characterization of a natural nanocomposite material: The shell of red abalone. *Nano Letters* **4**, 613-617, doi:10.1021/nl049962k (2004).
- 26 Thompson, J. B. *et al.* Bone indentation recovery time correlates with bond reforming time. *Nature* **414**, 773-776 (2001).
- 27 Fantner, G. E. *et al.* Sacrificial bonds and hidden length dissipate energy as mineralized fibrils separate during bone fracture. *Nature Materials* **4**, 612-616 (2005).
- 28 Katti, K. S., Katti, D. R., Pradhan, S. M. & Bhosle, A. Platelet interlocks are the key to toughness and strength in nacre. *Journal of Materials Research* **20**, 1097-1100, doi:10.1557/jmr.2005.0171 (2005).
- 29 Katti, K. S. & Katti, D. R. Why is nacre so tough and strong? *Materials Science & Engineering C-Biomimetic and Supramolecular Systems* **26**, 1317-1324, doi:10.1016/j.msec.2005.08.013 (2006).
- 30 Barthelat, F. Biomimetics for next generation materials. *Philosophical Transactions of the Royal Society a-Mathematical Physical and Engineering Sciences* **365**, 2907-2919, doi:10.1098/rsta.2007.0006 (2007).
- 31 Lian, J. & Wang, J. in *Mechanics of Biological Systems and Materials, Volume 2 Conference Proceedings of the Society for Experimental Mechanics Series* (ed Tom Proulx) Ch. 12, 93-99 (Springer New York, 2011).
- 32 Hepburn, H. R., Joffe, I., Green, N. & Nelson, K. J. Mechanical properties of a crab shell. *Comparative Biochemistry and Physiology Part A: Physiology* **50**, 551-IN513, doi:[http://dx.doi.org/10.1016/0300-9629\(75\)90313-8](http://dx.doi.org/10.1016/0300-9629(75)90313-8) (1975).
- 33 Barthelat, F., Rim, J. E. & Espinosa, H. D. in *Applied Scanning Probe Methods XIII* 17-44 (Springer, 2009).
- 34 Boßelmann, F., Romano, P., Fabritius, H., Raabe, D. & Epple, M. The composition of the exoskeleton of two crustacea: The American lobster *Homarus americanus* and the edible crab *Cancer pagurus*. *Thermochimica Acta* **463**, 65-68, doi:<http://dx.doi.org/10.1016/j.tca.2007.07.018> (2007).
- 35 Raabe, D. *et al.* Microstructure and crystallographic texture of the chitin-protein network in the biological composite material of the exoskeleton of the lobster *Homarus americanus*. *Materials Science and Engineering: A* **421**, 143-153 (2006).
- 36 Raabe, D., Sachs, C. & Romano, P. The crustacean exoskeleton as an example of a structurally and mechanically graded biological nanocomposite material. *Acta Materialia* **53**, 4281-4292, doi:<http://dx.doi.org/10.1016/j.actamat.2005.05.027> (2005).
- 37 Bouligand, Y. Twisted fibrous arrangements in biological materials and cholesteric mesophases. *Tissue and Cell* **4**, 189-217, doi:[http://dx.doi.org/10.1016/S0040-8166\(72\)80042-9](http://dx.doi.org/10.1016/S0040-8166(72)80042-9) (1972).
- 38 Giraud-Guille, M. M. Fine structure of the chitin-protein system in the crab cuticle. *Tissue and Cell* **16**, 75-92, doi:[http://dx.doi.org/10.1016/0040-8166\(84\)90020-X](http://dx.doi.org/10.1016/0040-8166(84)90020-X) (1984).

- 39 Chen, P.-Y., Lin, A. Y.-M., McKittrick, J. & Meyers, M. A. Structure and mechanical properties of crab exoskeletons. *Acta Biomaterialia* **4**, 587-596, doi:<http://dx.doi.org/10.1016/j.actbio.2007.12.010> (2008).
- 40 Chen, B., Peng, X., Wang, J. G. & Wu, X. Laminated microstructure of Bivalva shell and research of biomimetic ceramic/polymer composite. *Ceramics International* **30**, 2011-2014, doi:<http://dx.doi.org/10.1016/j.ceramint.2003.12.169> (2004).
- 41 Melnick, C. A., Chen, Z. & Mecholsky, J. J. Hardness and toughness of exoskeleton material in the stone crab, *Menippe mercenaria*. *Journal of Materials Research* **11**, 2903-2907, doi:doi:10.1557/JMR.1996.0367 (1996).
- 42 Verma, D. & Tomar, V. Structural-nanomechanical property correlation of exoskeleton of shallow water shrimp (*penaeus* spp.) at elevated temperatures. *Journal of Bionic Materials* **11**, 360-370 (2014).
- 43 Verma, D. & Tomar, V. An investigation into the environment dependent nanomechanical properties of the shallow water shrimp (*penaeus* spp.) exoskeleton. *Material Science and Engineering C* **44**, 371-379 (2014).
- 44 Qu, T. & Tomar, V. in *Proceedings of the Society of Engineering Science 51st Annual Technical Meeting, October 1-3, 2014, West Lafayette: Purdue University Libraries Scholarly Publishing Services, 2014*. (eds A. Bajaj, P. Zavattieri, M. Koslowski, & T. Siegmund).
- 45 Ji, B. & Gao, H. Mechanical properties of nanostructure of biological materials *Journal of the Mechanics and Physics of Solids* **52**, 1963-2000 (2004).
- 46 Gao, H. Application of fracture mechanics concepts to hierarchical biomechanics of bone and bone-like materials. *International Journal of Fracture* **138**, 101-137 (2006).
- 47 Gao, H. J., Ji, B. H., Jager, I. L., Arzt, E. & Fratzl, P. Materials become insensitive to flaws at nanoscale: Lessons from nature. *Proceedings of the National Academy of Sciences of the United States of America* **100**, 5597-5600, doi:10.1073/pnas.0631609100 (2003).
- 48 Hassenkam, T. *et al.* High-resolution AFM imaging of intact and fractured trabecular bone. *Bone* **35**, 4-10 (2004).
- 49 Fratzl, P., Gupta, H. S., Paschalis, E. P. & Roschger, P. Structure and mechanical quality of the collagen-mineral nano-composite in bone. *Journal of Materials Chemistry* **14**, 2115-2123 (2004).
- 50 Weiner, S. & Wagner, H. D. The material bone: Structure mechanical function relations. *Annual Review of Materials Science* **28**, 271-298 (1998).
- 51 Sasaki, N. & Odajima, S. Stress-strain curve and Young's modulus of a collagen molecule as determined by the X-ray diffraction technique. *Journal of Biomechanics* **29**, 655-658 (1996).
- 52 Eppell, S. J., Smith, B. N., Kahn, H. & Ballarini, R. Nano measurements with micro-devices: mechanical properties of hydrated collagen fibrils. *Journal of the Royal Society Interface* **3**, 117-121 (2005).
- 53 Hodge, A. J. & Petruska, J. A. in *G. N. Ramachandran, Editor. Aspects of Protein Structure. Proceedings of a Symposium* 289-300 (1963).
- 54 Thurner, P. J. *et al.* High-speed photography of compressed human trabecular bone correlates whitening to microscopic damage. *Engineering Fracture Mechanics* **74**, 1928-1941 (2007).
- 55 Dubey, D. K. & Tomar, V. Ab Initio Investigation of Strain Dependent Atomistic Interactions at Two Tropocollagen-Hydroxyapatite Interfaces. *Journal of Engineering Materials and Technology* **135**, 021015-021015, doi:10.1115/1.4023782 (2013).
- 56 Dubey, D. K. & Tomar, V. Understanding the influence of structural hierarchy and its coupling with chemical environment on the strength of idealized tropocollagen–hydroxyapatite biomaterials. *Journal of the Mechanics and Physics of Solids* **57**, 1702-1717 doi:doi:10.1016/j.jmps.2009.07.002 (2009).

- 57 Dubey, D. K. & Tomar, V. Role of the nanoscale interfacial arrangement in mechanical strength of tropocollagen-hydroxyapatite based hard biomaterials. *Acta Biomaterialia* **5**, 2704-2716, doi:doi 10.1016/j.actbio.2009.02.035 (2009).
- 58 Dubey, D. K. & Tomar, V. The effect of tensile and compressive loading on the hierarchical strength of idealized tropocollagen-hydroxyapatite biomaterials as a function of the chemical environment. *Journal of Physics-Condensed Matter* **21**, doi:10.1088/0953-8984/21/20/205103 (2009).
- 59 Dubey, D. K. & Tomar, V. Role of hydroxyapatite crystal shape in nanoscale mechanical behavior of model tropocollagen-hydroxyapatite hard biomaterials. *Materials Science & Engineering C-Materials for Biological Applications* **29**, 2133-2140, doi:10.1016/j.msec.2009.04.015 (2009).
- 60 Dubey, D. K. & Tomar, V. Effect of Osteogenesis Imperfecta Mutations in Tropocollagen Molecule on Strength of Biomimetic Tropocollagen-Hydroxyapatite Nanocomposites *Applied Physics Letters* **96**, 023703 (023701-023703) (2010).
- 61 Ji, B. H. A study of the interface strength between protein and mineral in biological materials. *Journal of Biomechanics* **41**, 259-266 (2008).
- 62 Posner, A. S. & Beebe, R. A. The surface chemistry of bone mineral and related calcium phosphates. *Semin Arthritis Rheum* **4**, 267-291 (1975).
- 63 Simone, A. D., Vitagliano, L. & Berisio, R. Role of hydration in collagen triple helix stabilization. *Biochemical and Biophysical Research Communications* **372**, 121-125 (2008).
- 64 Bhowmik, R., Katti, K. S. & Katti, D. R. Influence of mineral-polymer interactions on molecular mechanics of polymer in composite bone biomaterials. *Materials Research Society Symposia Proceedings* **978**, 6 (2007).
- 65 Barthelat, F. & Espinosa, H. D. An experimental investigation of deformation and fracture of nacre-mother of pearl. *Experimental Mechanics* **47**, 311-324, doi:10.1007/s11340-007-9040-1 (2007).
- 66 Ghosh, P., Katti, D. R. & Katti, K. S. Mineral proximity influences mechanical response of proteins in biological mineral-protein hybrid systems. *Biomacromolecules* **8**, 851-856 (2007).
- 67 Zhang, D., Chippada, U. & Jordan, K. Effect of the structural water on the mechanical properties of collagen-like microfibrils: a molecular dynamics study. *Annals of Biomedical Engineering* **35**, 1216-1230 (2007).
- 68 Dubey, D. K. & Tomar, V. Effect of changes in tropocollagen residue sequence and hydroxyapatite mineral texture on the strength of ideal nanoscale tropocollagen-hydroxyapatite biomaterials. *Journal of Materials Science-Materials in Medicine* **21**, 161-171, doi:10.1007/s10856-009-3837-7 (2010).
- 69 Phillips, J. C. *et al.* Scalable molecular dynamics with NAMD. *Journal of Computational Chemistry* **26**, 1781-1802 (2005).
- 70 Frankland, S. & Harik, V. Analysis of carbon nanotube pull-out from a polymer matrix. *Surface Science* **525**, L103-L108 (2003).
- 71 Lelievre, F., Bernache-Assollant, D. & Chartier, T. Influence of powder characteristics on the rheological behaviour of hydroxyapatite slurries. *Journal of Materials Science: Materials in Medicine* **7**, 489-494 (1996).
- 72 Ichikawa, Y., Kawamura, K., Fujii, N. & Nattavut, T. Molecular dynamics and multiscale homogenization analysis of seepage/diffusion problem in bentonite clay. *International journal for numerical methods in engineering* **54**, 1717-1749 (2002).
- 73 Knapp, D. M. *et al.* Rheology of reconstituted type I collagen gel in confined compression. *Journal of Rheology (1978-present)* **41**, 971-993 (1997).

- 74 Barocas, V. H., Moon, A. G. & Tranquillo, R. T. The fibroblast-populated collagen microsphere assay of cell traction force—Part 2: Measurement of the cell traction parameter. *Journal of Biomechanical Engineering* **117**, 161-170 (1995).
- 75 Dealy, J. M. & Wang, J. *Melt rheology and its applications in the plastics industry*. (Springer, 2013).
- 76 Bylund, G. & Pak, T. *Dairy processing handbook*. (Tetra Pak Processing Systems AB Lund, 2003).
- 77 Franck, A. Understanding Rheology of Thermoplastic Polymers. *TA Instruments* (2004).
- 78 Newman, S., Cloitre, M., Allain, C., Forgacs, G. & Beysens, D. Viscosity and elasticity during collagen assembly in vitro: Relevance to matrix-driven translocation. *Biopolymers* **41**, 337-347 (1997).
- 79 Fritsch, A. & Hellmich, C. ‘Universal’ microstructural patterns in cortical and trabecular, extracellular and extravascular bone materials: micromechanics-based prediction of anisotropic elasticity. *Journal of Theoretical Biology* **244**, 597–620 (2007).
- 80 Fritsch, A, Hellmich, C, & Dormieux, L. Ductile sliding between mineral crystals followed by rupture of collagen crosslinks: experimentally supported micromechanical explanation of bone strength. *Journal of Theoretical Biology* **260**, 230–252 (2009).
- 81 Eberhardsteiner, L., Hellmich, Ch. & Scheiner, S., Layered water in crystal interfaces as source for bone viscoelasticity: arguments from a multiscale approach, *Computer Methods in Biomechanics and Biomedical Engineering* **17**(1), 48-63 (2014).
- 82 Morin, C & Hellmich, Ch.. A multiscale poromicromechanical approach to wave propagation and attenuation in bone. *Ultrasonics* **54**, 1251–1269 (2014).
- 83 Nikolov, S, Raabe, D. Hierarchical modeling of the elastic properties of bone at submicron scales: the role of extrafibrillar mineralization. *Biophysical Journal* **94**, 4220–4232 (2008).
- 84 Shahidi, M., Pichler, B. & Hellmich, Ch. Viscous interfaces as source for material creep: a continuum micromechanics approach, *European Journal of Mechanics* **45A**, 41–58 (2014).
- 85 Wagner, N. & Brady, J. Shear thickening in colloidal dispersions. *Physics Today* October (2009)
- 86 Coussot, P. Structural similarity and transition from Newtonian to non-Newtonian behavior for clay-water suspensions. *Physical Review Letters* **74**(20), 3971-3974 (1995).
- 87 Barnes, H.A. Thixotropy-a review. *Journal of Non-Newtonian Fluid Mechanics* **70**, 1-33 (1997)
- 88 Salencon, J., *Handbook of Continuum Mechanics*. (Springer, 2001).
- 89 Borsato, K. & Sasaki, N., Measurement of partition of stress between mineral and collagen phases in bone. *Journal of Biomechanics* **30**(9), 955-957 (1997).
- 90 Almer, J. & Stock, S. Micromechanical response of mineral and collagen phases in bone. *Journal of Structural Biology* **157**(2), 365-370 (2007).
- 91 Iyo, T., Maki, Y., Sasaki, N. & Nakata, M. Anisotropic viscoelastic properties of cortical bone. *Journal of Biomechanics* **37**, 1433–1437 (2004).



# Bibliography

- [1] R. J.M. Pellenq, A. Kushima, R. Shahsavari, K. J. Van Vliet, M. J. Buehler, S. Yip, and F.J. Ulm. A realistic molecular model of cement hydrates. *Proceedings of the National Academy of Sciences of the United States of America*, 106(38):16102–16107, 2009.
- [2] H. Manzano, S. Moeini, F. Marinelli, A. C. T. van Duin, F.J. Ulm, and R. J.-M. Pellenq. Confined water dissociation in microporous defective silicates: Mechanism, dipole distribution, and impact on substrate properties. *Journal of the American Chemical Society*, 134(4):2208–2215, 2012.
- [3] K. S. Probst and S. Lees. Visualization of crystal-matrix structure. in situ demineralization of mineralized turkey leg tendon and bone. *Calcified tissue international*, 59(6):474–479, 1996.
- [4] E. A. McNally, H. P. Schwarcz, G. A. Botton, and A. L. Arsenault. A model for the ultrastructure of bone based on electron microscopy of ion-milled sections. *PLoS ONE*, 7(1), 2012.
- [5] E. McNally, F. Nan, G. A. Botton, and H. P. Schwarcz. Scanning transmission electron microscopic tomography of cortical bone using z-contrast imaging. *Micron*, 49:46–53, 2013.
- [6] A. Stroud. Approximate calculation of multiple integrals. *Prentice-Hall, Englewood Cliffs*, 1971.
- [7] L. Boltzmann. Zur Theorie der elastischen Nachwirkung [Concerning the theory of the elastic aftereffect]. *Sitzungsberichte der Mathematisch-Naturwissenschaftlichen Classe der Kaiserlichen Akademie der Wissenschaften*, 70(2):275 – 306, 1874. In German.
- [8] M.E. Gurtin and E. Sternberg. On the linear theory of viscoelasticity. *Archives of Rational Mechanics and Analysis*, 11:291 – 356, 1962.

- 
- [9] J. Salençon. *Viscoélasticité [Viscoelasticity]*. Presses de l'Ecole Nationale des Ponts et Chaussées, 1983. In French.
- [10] M. J. Leitman and M. C. Fisher. *The linear theory of viscoelasticity*. Springer-Verlag, Berlin-Heidelberg-New York, 1973.
- [11] C. A. Morrow, D. E. Moore, and D. A. Lockner. The effect of mineral bond strength and adsorbed water on fault gouge frictional strength. *Geophysical Research Letters*, 27(6):815–818, 2000.
- [12] M. Stipp, J. Tullis, and H. Behrens. Effect of water on the dislocation creep microstructure and flow stress of quartz and implications for the recrystallized grain size piezometer. *Journal of Geophysical Research B: Solid Earth*, 111: B04201, 2006.
- [13] J. Tullis and R. A. Yund. Diffusion creep in feldspar aggregates: experimental evidence. *Journal of Structural Geology*, 13(9):987–1000, 1991.
- [14] Z. P. Bažant, A. B. Hauggaard, S. Baweja, and F. J. Ulm. Microprestress-solidification theory for concrete creep. I: Aging and drying effects. *Journal of Engineering Mechanics*, 123(11):1188–1194, 1997.
- [15] R. Alizadeh, J. J. Beaudoin, and L. Raki. Viscoelastic nature of calcium silicate hydrate. *Cement and Concrete Composites*, 32(5):369–376, 2010.
- [16] A. G. Kalinichev, J. Wang, and R. J. Kirkpatrick. Molecular dynamics modeling of the structure, dynamics and energetics of mineral-water interfaces: Application to cement materials. *Cement and Concrete Research*, 37(3):337–347, 2007.
- [17] I. Vlahinić, J. J. Thomas, H. M. Jennings, and J. E. Andrade. Transient creep effects and the lubricating power of water in materials ranging from paper to concrete and kevlar. *Journal of the Mechanics and Physics of Solids*, 60(7): 1350–1362, 2012.
- [18] M. Youssef, R. J.M. Pellenq, and B. Yildiz. Glassy nature of water in an ultraconfining disordered material: The case of calcium-silicate-hydrate. *Journal of the American Chemical Society*, 133(8):2499–2510, 2011.
- [19] Z. Németh, L. Halász, J. Pálinkás, A. Bóta, and T. Horányi. Rheological behaviour of a lamellar liquid crystalline surfactant-water system. *Colloids and Surfaces A: Physicochemical and Engineering Aspects*, 145(1-3):107–119, 1998.

- [20] F. Cordobés, J. Muñoz, and C. Gallegos. Linear viscoelasticity of the hexagonal liquid-crystalline phase of a surfactant non ionic/hydrocarbon/water system. *Journal of Colloid and Interface Science*, 187(2):401–417, 1997.
- [21] L. Eberhardsteiner, Ch. Hellmich, and S. Scheiner. Layered water in crystal interfaces as source for bone viscoelasticity: arguments from a multiscale approach. *Computer Methods in Biomechanics and Biomedical Engineering*. Available online at [DOI: 10.1080/10255842.2012.670227], 2012.
- [22] J. C. Arnold and N. P. Venditti. Effects of environment on the creep properties of a poly(ethylmethacrylate) based bone cement. *Journal of Materials Science: Materials in Medicine*, 12(8):707–717, 2001.
- [23] N. Sasaki, Y. Nakayama, M. Yoshikawa, and A. Enyo. Stress relaxation function of bone and bone collagen. *Journal of Biomechanics*, 26(12):1369–1376, 1993.
- [24] P. Acker and F. . Ulm. Creep and shrinkage of concrete: Physical origins and practical measurements. *Nuclear Engineering and Design*, 203(2-3):143–158, 2001. Cited By (since 1996): 35.
- [25] T. G. Lombardo, N. Giovambattista, and P. G. Debenedetti. Structural and mechanical properties of glassy water in nanoscale confinement. *Faraday Discussions*, 141:359–376, 2009.
- [26] J. Berghausen, J. Fuchs, and W. Richtering. Rheology and shear orientation of a nematic liquid crystalline side-group polymer with laterally attached mesogenic units. *Macromolecules*, 30(24):7574–7581, 1997.
- [27] W. Brostow, N. A. D’Souza, J. Kubát, and R. Maksimov. Creep and stress relaxation in a longitudinal polymer liquid crystal: Prediction of the temperature shift factor. *Journal of Chemical Physics*, 110(19):9706–9712, 1999.
- [28] R. H. Colby, L. M. Nentwich, S. R. Clingman, and C. K. Ober. Defect-mediated creep of structured materials. *Europhysics Letters*, 54(2):269–274, 2001.
- [29] W. Jezewski, W. Kuczyński, and J. Hoffmann. Creep dynamics of structural defects in ferroelectric liquid crystals with chevron geometry. *Physical Review B - Condensed Matter and Materials Physics*, 77:094101, 2008.

- 
- [30] H. Manzano, S. Moeini, F. Marinelli, A. C. T. Van Duin, F.J. Ulm, and R. J. M. Pellenq. Confined water dissociation in microporous defective silicates: Mechanism, dipole distribution, and impact on substrate properties. *Journal of the American Chemical Society*, 134(4):2208–2215, 2012.
- [31] M. Shahidi, B. Pichler, and C. Hellmich. Viscous interfaces as source for material creep: A continuum micromechanics approach. *European Journal of Mechanics, A/Solids*, 45:41–58, 2014.
- [32] A. Zaoui. Continuum micromechanics: Survey. *Journal of Engineering Mechanics (ASCE)*, 128(8):808–816, 2002.
- [33] Y. Benveniste. A new approach to the application of Mori-Tanaka’s theory in composite materials. *Mechanics of Materials*, 6(2):147–157, 1987.
- [34] R. Luciano and J.R. Willis. FE analysis of stress and strain fields in finite random composite bodies. *Journal of the Mechanics and Physics of Solids*, 53(7):1505–1522, 2005.
- [35] C. Gruescu, A. Giraud, F. Homand, D. Kondo, and D.P. Do. Effective thermal conductivity of partially saturated porous rocks. *International Journal of Solids and Structures*, 44(3-4):811–833, 2007.
- [36] P.J. Lin and J.W. Ju. Effective elastic moduli of three-phase composites with randomly located and interacting spherical particles of distinct properties. *Acta Mechanica*, 208(1-2):11–26, 2009.
- [37] Q.-S. Zheng and D.-X. Du. An explicit and universally applicable estimate for the effective properties of multiphase composites which accounts for inclusion distribution. *Journal of the Mechanics and Physics of Solids*, 49(11):2765 – 2788, 2001.
- [38] S. Mercier and A. Molinari. Homogenization of elastic-viscoplastic heterogeneous materials: Self-consistent and Mori-Tanaka schemes. *International Journal of Plasticity*, 25(6):1024–1048, 2009.
- [39] I. Sevostianov and M. Kachanov. Normal and tangential compliances of interface of rough surfaces with contacts of elliptic shape. *International Journal of Solids and Structures*, 45(9):2723–2736, 2008.
- [40] I. Sevostianov and M. Kachanov. Homogenization of a nanoparticle with graded interface. *International Journal of Fracture*, 139(1):121–127, 2006.

- 
- [41] M. Kachanov. Elastic solids with many cracks: A simple method of analysis. *International Journal of Solids and Structures*, 23(1):23–43, 1987.
- [42] M. Kachanov. Effective elastic properties of cracked solids: critical review of some basic concepts. *Applied Mechanics Reviews*, 45(8):304–335, 1992.
- [43] O. E. Meyer. Ueber die elastische nachwirkung. *Ann. Physik u. Chemie*, 4: 249 – 267, 1878.
- [44] Z.P. Bažant. Thermodynamics of solidifying or melting viscoelastic material. *Journal of Engineering Mechanics Division (ASCE)*, 105(6):933 – 952, 1977.
- [45] B. S. Kelley, J. F. Lafferty, D. A. Bowman, and P. A. Clark. Rhesus monkey intervertebral disk viscoelastic response to shear stress. *Journal of Biomechanical Engineering*, 105(1):51–54, 1983.
- [46] H. Liu, M. A. Polak, and A. Penlidis. A practical approach to modeling time-dependent nonlinear creep behavior of polyethylene for structural applications. *Polymer Engineering and Science*, 48(1):159–167, 2008.
- [47] A. Fritsch and C. Hellmich. 'universal' microstructural patterns in cortical and trabecular, extracellular and extravascular bone materials: Micromechanics-based prediction of anisotropic elasticity. *Journal of Theoretical Biology*, 244(4):597–620, 2007.
- [48] A. Fritsch, C. Hellmich, and L. Dormieux. Ductile sliding between mineral crystals followed by rupture of collagen crosslinks: Experimentally supported micromechanical explanation of bone strength. *Journal of Theoretical Biology*, 260(2):230–252, 2009.
- [49] L. Eberhardsteiner, C. Hellmich, and S. Scheiner. Layered water in crystal interfaces as source for bone viscoelasticity: Arguments from a multiscale approach. *Computer Methods in Biomechanics and Biomedical Engineering*, 17(1):48–63, 2014.
- [50] C. Morin and C. Hellmich. A multiscale poromicromechanical approach to wave propagation and attenuation in bone. *Ultrasonics*, 54(5):1251–1269, 2014.
- [51] V. Pensée, D. Kondo, and L. Dormieux. Micromechanical analysis of anisotropic damage in brittle materials. *Journal of Engineering Mechanics*, 128(8):889–897, 2002.

- 
- [52] G.J. Dvorak and Y. Benveniste. On transformation strain and uniform fields in multiphase elastic media. *Proceedings of the Royal Society London, Series A*, 437:291–310, 1992.
- [53] G. J. Dvorak. Transformation field analysis of inelastic composite materials. *Proceedings of the Royal Society of London A*, 437:311–326, 1992.
- [54] B. Pichler and C. Hellmich. Estimation of influence tensors for eigenstressed multiphase elastic media with nonaligned inclusion phases of arbitrary ellipsoidal shape. *Journal of Engineering Mechanics*, 136(8):1043–1053, 2010.
- [55] Z. Hashin. Analysis of composite materials - a survey. *Journal of Applied Mechanics, Transactions ASME*, 50(3):481–505, 1983.
- [56] R. Hill. Elastic properties of reinforced solids: Some theoretical principles. *Journal of the Mechanics and Physics of Solids*, 11(5):357–372, 1963.
- [57] C. Huet. Application of variational concepts to size effects in elastic heterogeneous bodies. *Journal of the Mechanics and Physics of Solids*, 38(6):813–841, 1990.
- [58] W. J. Drugan and J. R. Willis. A micromechanics-based nonlocal constitutive equation and estimates of representative volume element size for elastic composites. *Journal of the Mechanics and Physics of Solids*, 44(4):497–524, 1996.
- [59] L. Dormieux. Poroelasticity and strength of fully or partially saturated porous materials. In L. Dormieux and F.-J. Ulm, editors, *Applied Micromechanics of Porous Media*, CISM courses and lecture notes No. 480, pages 109–152. Springer, 2005.
- [60] V. M. Levin. Thermal expansion coefficient of heterogeneous materials. *Mekhanika Tverdogo Tela*, 2(1):83–94, 1967.
- [61] T. Mori and K. Tanaka. Average stress in matrix and average elastic energy of materials with misfitting inclusions. *Acta Metallurgica*, 21(5):571–574, 1973.
- [62] N. Eshelby. The determination of the elastic field of an ellipsoidal inclusion, and related problems. *Proceedings of the Royal Society of London A*, 241(1226):376–396, 1957.
- [63] L. Dormieux and D. Kondo. Micromechanical approach to the coupling between permeability and damage. *Comptes Rendus - Mécanique*, 332(2):135–140, 2004.

- 
- [64] J. R. Bristow. Microcracks, and the static and dynamic elastic constants of annealed and heavily cold-worked metals. *British Journal of Applied Physics*, 11(2):81–85, 1960.
- [65] B. Budiansky and R. J. O’Connell. Elastic moduli of a cracked solid. *International Journal of Solids and Structures*, 12(2):81–97, 1976.
- [66] L. Dormieux, D. Kondo, and F.J. Ulm. *Microporomechanics*. Wiley, New York, 2006.
- [67] N. Laws and R. McLaughlin. Self-consistent estimates for the viscoelastic creep compliances of composite materials. *Proceedings of the Royal Society London, Series A*, 359:251 – 273, 1978.
- [68] T. Iyo, Y. Maki, N. Sasaki, and M. Nakata. Anisotropic viscoelastic properties of cortical bone. *Journal of Biomechanics*, 37(9):1433–1437, 2004.
- [69] M. Vandamme and F. . Ulm. Nanoindentation investigation of creep properties of calcium silicate hydrates. *Cement and Concrete Research*, 52:38–52, 2013.
- [70] Z. P. Bažant, M. H. Hubler, and Q. Yu. Pervasiveness of excessive segmental bridge deflections: Wake-up call for creep. *ACI Structural Journal*, 108(6): 766–774, 2011.
- [71] I. Vlahinić, J. J. Thomas, H. M. Jennings, and J. E. Andrade. Transient creep effects and the lubricating power of water in materials ranging from paper to concrete and kevlar. *Journal of the Mechanics and Physics of Solids*, 60(7), 2012.
- [72] I.N. Bronstein, K.A. Semendjajew, G. Musiol, and H. Mühlig. *Taschenbuch der Mathematik [Handbook of Mathematics]*. Verlag Harri Deutsch, 6 edition, 2005. In German.
- [73] S.T. Nguyen, L. Dormieux, Y.L. Pape, and J. Sanahuja. A Burger model for the effective behavior of a microcracked viscoelastic solid. *International Journal of Damage Mechanics*, 20(8):1116–1129, 2011.
- [74] W. (Lord Kelvin) Thomson. *Math. Phys.*, 4:27, 1875.
- [75] W. Voigt. Ueber die innere reibung fester koeper, insbesondere der krystalle. *Goettinger Abh*, 36:1, 1890.

- 
- [76] J. C. Maxwell. On the dynamic theory of gases. *Phil. Mag*, 35:129 – 145, 1868.
- [77] C. Zener. *Elasticity and Anelasticity of Metal*. University of Chicago Press, 1948.
- [78] B. Pichler and L. Dormieux. Cracking risk of partially saturated porous media-part I: Microporoelasticity model. *International Journal for Numerical and Analytical Methods in Geomechanics*, 34(2):135–157, 2010.
- [79] M. Shahidi, B. Pichler, and C. Hellmich. Interfacial micromechanics assessment of calassical rheological models II: Multiple interface sizes and viscosities. *Submitted for review and possible publication in Journal of Engineering Mechanics*, .
- [80] M. Shahidi, B. Pichler, and C. Hellmich. Interfacial micromechanics assessment of classical rheological models I: Single interface size and viscosity. *Submitted for review and possible publication in Journal of Engineering Mechanics*, .
- [81] D. K. Dubey and V. Tomar. Understanding the influence of structural hierarchy and its coupling with chemical environment on the strength of idealized tropocollagen-hydroxyapatite biomaterials. *Journal of the Mechanics and Physics of Solids*, 57(10):1702–1717, 2009.
- [82] T. Qu and V. Tomar. An analysis of the effects of temperature and structural arrangements on the thermal conductivity and thermal diffusivity of tropocollagen-hydroxyapatite interfaces. *Materials Science and Engineering C*, 38(1):28–38, 2014.
- [83] J. Salençon. *Handbook of Continuum Mechanics*. Springer-Verlag Berlin Heidelberg, 2001.
- [84] H.S. Gupta, J. Seto, W. Wagermaier, P. Zaslansky, P. Boesecke, and P. Fratzl. Cooperative deformation of mineral and collagen in bone at the nanoscale. *Proceedings of the National Academy of Sciences of the United States of America*, 103(47):17741–17746, 2006.
- [85] K. S. Borsato and N. Sasaki. Measurement of partition of stress between mineral and collagen phases in bone using x-ray diffraction techniques. *Journal of Biomechanics*, 30(9):955–957, 1997.

- 
- [86] J. D. Almer and S. R. Stock. Internal strains and stresses measured in cortical bone via high-energy x-ray diffraction. *Journal of structural biology*, 152(1):14–27, 2005. Cited By (since 1996):80.
- [87] N. J. Wagner and J. F. Brady. Shear thickening in colloidal dispersions. *Physics Today*, 62(10):27–32, 2009.
- [88] P. Coussot. Structural similarity and transition from newtonian to non-newtonian behavior for clay-water suspensions. *Physical Review Letters*, 74(20):3971–3974, 1995.
- [89] H. A. Barnes. Thixotropy - a review. *Journal of Non-Newtonian Fluid Mechanics*, 70(1-2):1–33, 1997.
- [90] J. Mewis. Thixotropy - a general review. *Journal of Non-Newtonian Fluid Mechanics*, 6(1):1–20, 1979.
- [91] S. Scheiner and C. Hellmich. Continuum microviscoelasticity model for aging basic creep of early-age concrete. *Journal of Engineering Mechanics*, 135(4):307–323, 2009.
- [92] B. Pichler and C. Hellmich. Upscaling quasi-brittle strength of cement paste and mortar: A multi-scale engineering mechanics model. *Cement and Concrete Research*, 41(5):467–476, 2011.
- [93] R. M. Christensen. *theory of Viscoelasticity - an Introduction, 2nd edn.* Academic Press, New York, 1982.
- [94] L. Dormieux and D. Kondo. Micromechanical approach to the coupling between permeability and damage. *Comptes Rendus - Mecanique*, 332(2):135–140, 2004.